

**PHOTONIC BANDSTRUCTURE IN SEMICONDUCTOR SLAB
WAVEGUIDES WITH STRONG TWO-DIMENSIONAL TEXTURE**

by

Vighen Pacradouni

B.Sc., McGill University, 1989

B.Eng., McGill University, 1991

M.Sc., University of British Columbia, 1993

A THESIS SUBMITTED IN PARTIAL FULFILLMENT OF
THE REQUIREMENTS FOR THE DEGREE OF

Doctor of Philosophy

in

THE FACULTY OF GRADUATE STUDIES

(Physics)

THE UNIVERSITY OF BRITISH COLUMBIA

April 2006

© Vighen Pacradouni, 2006

Abstract

Fabrication techniques were developed and used to realize sub-100 nm-thick semiconductor membranes that contain two-dimensional (2D) square arrays of holes that completely penetrate the membrane. With the pitch of the arrays on the order of 500 nm, broadband optical reflectivity spectra obtained from these “2D planar photonic crystal membranes” reveal resonant features with energies and linewidths that disperse as the in-plane momentum (angle of incidence) of the exciting radiation is varied in the near-infrared. A numerical solution of Maxwell’s equations was developed to interpret these reflectivity spectra in terms of a “photonic bandstructure” for electromagnetic modes localized in the vicinity of the porous membrane. A complete understanding of the complex (energy and lifetime) dispersion and polarization properties of this interesting new class of optical materials was obtained. It is shown that this bandstructure can be largely explained by applying symmetry considerations to the renormalization of slab waveguide modes by the high index contrast 2D scattering potential.

Table of Contents

Abstract	ii
Table of Contents	iii
List of Tables	vii
List of Figures	viii
Acknowledgements	xxiii
Dedication	xxiv
1 Introduction	1
2 Modelling	19
2.1 Introduction	19
2.2 Description of Finite Difference Real Space Approach	20
2.2.1 Scattering from a periodically textured layer	20
2.2.2 Discretization and Integration of Maxwell's Equations in Real Space	27
2.2.3 Eigenmodes on a Discrete Mesh	34
2.2.4 Significance of Using Pendry Modes	39
2.2.5 Computation of Reflection and Transmission Coefficients	42
2.2.6 Buried Gratings	48
2.3 Results	51
2.3.1 Introduction	51
2.3.2 Near-Normal Incidence Reflectivity from Untextured Uniform Slab	51

2.3.3	Bound Modes of Untextured Slab	52
2.3.4	Slab Waveguide with 1D Grating	55
2.3.5	Waveguide with 2D weak 2nd order grating	62
2.3.6	2D Strong Texture	69
2.4	Convergence	75
2.4.1	Convergence of the Integration Scheme Alone	77
2.4.2	Overall Convergence Behaviour for Textured Structures	78
2.5	Comparison with Green's Function Based Model	87
2.6	Significance of Modification to Pendry's Method	92
2.7	Summary	96
3	Fabrication	98
3.1	Introduction and Overview	98
3.2	Processing Techniques and Equipment	102
3.2.1	Electron Beam Lithography	102
3.2.2	Etching	106
3.2.3	Oxidation	111
3.2.4	Optical Microscopy	113
3.2.5	Atomic Force Microscope	114
3.3	Fabrication Procedure	115
3.3.1	SEM measurement of Layer Structure	115
3.3.2	Cleaving	115
3.3.3	Lithography	117
3.3.4	Etching	119
3.3.5	Oxidation	120
3.4	Fabrication Results	121

4	Optical Experiments	127
4.1	Introduction	127
4.2	Experimental Apparatus	128
4.2.1	Fourier Transform Spectrometer	131
4.3	Alignment	132
4.4	Angular Resolution	135
4.5	Experimental Procedure	135
5	Results	137
5.1	Introduction	137
5.2	Resonant Reflectivity	137
5.3	Polarization Properties	139
5.4	Dispersion	140
5.5	Fitting with Model	143
5.6	Extraction of Mode Frequency and Linewidth from Spectra	145
5.6.1	Extraction of Frequency and Linewidth from Experimental Spectra	145
5.6.2	Extraction of Mode Parameters from Model Spectra	146
5.7	Bandstructure	149
5.8	Linewidths	151
5.8.1	Linewidth of Lowest Energy Band	151
5.8.2	Linewidths of 4th and 5th Bands	154
5.9	Effect of Filling Fraction	155
6	Discussion	158
6.1	Introduction	158
6.2	Resonant Features in Reflectivity	159
6.3	Polarization Properties and Basic Dispersion	160
6.4	Gaps and Symmetry Influences on Linewidths	165

6.5	Effect of Filling Fraction	166
6.6	Gaps Away from Zone-Centre	169
6.7	Extrinsic Influences on Linewidths	172
7	Summary and Conclusions	175
7.1	Summary	175
7.2	Conclusions	177
7.3	Future Directions	178
	Bibliography	180
A	Generalization of FDRS Method to an Arbitrary 2D Lattice	184

List of Tables

3.1	Nominal and measured thicknesses of layers in sample ASU 721	116
3.2	Etch conditions	120
3.3	Pitches and doses specified for e-beam lithography	123
3.4	Extent of oxidation and yield	124
3.5	Pitches and hole radii and corresponding air filling fractions estimated from AFM profiles from three gratings having nominally the same pitch but different electron beam exposure times.	126
5.1	Model, Nominal, and Measured sample structure parameters for grating 22 on sample ASU 721	145

List of Figures

1.1	Schematic diagram of 3D photonic crystal concept. \mathbf{R} is any one of the lattice vectors that define the crystal symmetry.	2
1.2	Photonic bandstructure arising from 3D face-centred-cubic photonic lattice comprised of non-spherical “atoms” and dielectric contrast of $\frac{\epsilon_2}{\epsilon_1} = 13.0$ [1].	3
1.3	2D photonic crystal “waveguide” with tight bend.	5
1.4	Scheme invented by Yablonovitch [2] for fabricating a 3D photonic crystal which exhibits a complete gap. It consists of machining three sets of cylindrical airholes separated by 120° into a block of material with sufficiently high dielectric contrast at a 35° angle on a 2D periodic grid. The resulting interconnecting network of voids forms a face-centred-cubic (FCC) lattice with non-spherical “atoms”.	7
1.5	Schematic diagram of an asymmetric 3-layer slab waveguide with 2D photonic crystal embedded in core.	9
1.6	Schematic diagram of an asymmetric 3-layer slab waveguide.	10
1.7	Schematic dispersion diagram of the modes of an asymmetric 3-layer slab waveguide. The solid line represents the light line for the core material. The dot-dashed line represents the line light-line for the superstrate, <i>i.e.</i> , top semi-infinite layer (air). The dotted line represents the light line for the substrate, <i>i.e.</i> , bottom semi-infinite layer.	10
1.8	Schematic diagram of 2D photonic crystal with defect embedded in slab waveguide.	14

2.1	Schematic diagram of a two-dimensionally periodically textured slab structure.	21
2.2	Discrete in-plane $(x-y)$ lattice on which \mathbf{E} and \mathbf{H}' fields are computed on a series of planes separated by $g/2 = \gamma$. The dielectric constant is sampled on the lattice indicated by the black dots. The fields are calculated on the sublattice indicated by the crossed squares. The planes shown span a unit cell of the periodicity in the in-plane direction. The light and dark grey shading of the planes indicates whether the \mathbf{E} or \mathbf{H}' fields are computed there. The white hole in the center schematically depicts dielectric texture comprised of a circular airhole.	33
2.3	Scheme of real-space points on which the fields and dielectric constant are sampled on the unit cell. The dielectric constant is sampled at points represented by the black dots. The electric or magnetic fields are sampled only on those points with the crossed squares.	43
2.4	Scheme of reciprocal lattice vectors corresponding to in-plane wavevector of launched modes	44
2.5	2D grating embedded in an arbitrary multilayer dielectric stack	49
2.6	Component scattering matrices for calculation of overall reflection (scattering) matrix from grating embedded in an arbitrary multilayer dielectric stack.	50
2.7	Waveguide consisting of 120 nm-thick slab of material with dielectric constant $\epsilon' = 12.25$	52
2.8	Specular reflectivity spectrum for light incident at 10^0 (from the normal) on a 120 nm-thick slab of material of dielectric constant $\epsilon' = 12.25$. The solid curve depicts the spectrum for the s polarization; the dashed curve depicts the spectrum for the p polarization.	53

2.9	Plot of mode frequency versus in-plane wavevector, β , for the lowest order TE (solid curve) and TM (dotted curve) modes of a planar waveguide consisting of a 120 nm slab of material with $\epsilon' = 12.25$, clad above and below by air ($\epsilon' = 1$). The dot-dashed lines represent the lightlines for these materials. The solid vertical line depicts the part of $\omega - \beta$ space that is explored in the calculation of the spectra shown in Figure 2.10 below. The dots at the intersection of the vertical line with the dispersion curves indicate the appearance of a resonant feature in the spectra.	54
2.10	Specular reflectivity spectrum for evanescent field incident on 120 nm slab of material with $\epsilon' = 12.25$, with in-plane wavevector of $20,000 \text{ cm}^{-1}$. The solid line is for s polarized light, the dashed line is for p polarized light. .	55
2.11	Schematic dispersion plot for single-mode slab waveguide with shallow 1D grating etched into its surface. The dashed lines represent the light lines for the low-index cladding layer (larger slope) and the high-index core layer (smaller slope). The solid lines represent the dispersion of Bloch states in the presence of the grating.	56
2.12	Slab waveguide with “weak” 1D texture: the structure consists of a 120 nm-thick slab of $\epsilon' = 12.25$ material, clad above and below by air, with a 10 nm deep 1D square-toothed grating having a pitch $\Lambda = 500 \text{ nm}$ and an air filling fraction of 25% etched into the surface.	56
2.13	Calculated specular reflectivity spectrum for evanescent light incident with in-plane wavevector $\beta = (\beta_G/2)\hat{x} = (\pi/\Lambda)\hat{x}$. The solid curve is for s polarized light, the dashed curve is for p polarized light. The corresponding waveguide structure is depicted in Figure 2.12.	57

- 2.14 (a) Calculated specular reflectivity spectrum for evanescent light incident with in-plane wavevector, $\beta = 1.01\beta_G\hat{x}$, *i.e.*, slightly detuned from the boundary between the 2nd and 3rd Brillouin zones. (b) Calculated specular reflectivity spectrum for light incident with in-plane wavevector, $\beta = 0.01\beta_G\hat{x}$, *i.e.*, slightly detuned from the Brillouin zone-centre. (c) Calculated 1st order diffraction coefficient, *i.e.*, coefficient for scattering from a field component at $\beta = 0.01\beta_G\hat{x}$ to a field component at $\beta = 1.01\beta_G\hat{x}$. The solid curves are for *s* polarized light; the dashed curves are for *p* polarized light. The waveguide structure under study is depicted in Figure 2.12. 58
- 2.15 (a) Calculated specular reflectivity spectrum for evanescent light incident with in-plane wavevector, $\beta = \beta_G\hat{x}$, at the edge of the 1st Brillouin zone. (b) Calculated specular reflectivity spectrum for radiation incident with zero in-plane wavevector, *i.e.*, at the Brillouin zone-centre. (c) Calculated 1st order diffraction coefficient, *i.e.*, coefficient for scattering from a field component at $\beta = 0.01\beta_G\hat{x}$ to a field component at $\beta = 1.01\beta_G\hat{x}$. The solid curves are for *s* polarized light; the dashed curves are for *p* polarized light. The waveguide structure under study is depicted in Figure 2.12. . . 60
- 2.16 Calculated near-normal incidence specular reflectivity spectrum for light incident with in-plane wavevector, $\beta = 0.01\beta_G\hat{x}$, for *s* polarized light. The waveguide structure is identical to the one specified in Figure 2.12 except that the grating has an air filling fraction of 75% rather than 25%. 61
- 2.17 Slab waveguide with “strong” 1D texture: the structure consists of a 120 nm thick slab of $\epsilon' = 12.25$ material, clad above and below by air, with a 1D square-toothed grating that completely penetrates the slab. The grating has a pitch, $\Lambda = 500$ nm, and an air filling fraction of 25%. . . . 62

2.18	Calculated near-normal incidence specular reflectivity spectrum for s polarized light incident with in-plane wavevector, $\beta = 0.01\beta_G\hat{x}$. The waveguide structure, depicted in Figure 2.17, consists of a 120 nm thick slab of $\epsilon' = 12.25$ material, clad above and below by air, completely penetrated by 1D square-toothed grating having a pitch, $\Lambda = 500$ nm, and an air filling fraction of 25%.	63
2.19	Slab waveguide consisting of 125 nm of $\epsilon' = 12.25$ material with air above and below, having a square lattice of cylindrical airholes, 25 nm deep, embedded at its centre. The lattice has a pitch of $\Lambda = 500$ nm, and the radius, r , of the holes is $r/\Lambda = 0.10$	64
2.20	Schematic in-plane bandstructure of resonant modes of waveguide with a square grating shown in 1st 2D Brillouin zone.	64
2.21	Symmetry directions for the square lattice.	65
2.22	Calculated specular reflectivity spectrum for light incident on a 125 nm slab waveguide of $\epsilon' = 12.25$ material with air above and below, and a square lattice of cylindrical airholes, 25 nm deep, embedded at its centre. The lattice has a pitch of $\Lambda = 500$ nm, and the radius, r , of the holes is $r/\Lambda = 0.10$. Solid lines are for the s polarization, while dashed lines depict the p polarization. The spectra were calculated for light incident with in-plane wavevector fixed at $\beta/\beta_G = 0.01$ in the $\Gamma - X$ direction, which is defined in Figure 2.21.	66
2.23	Expanded view of the spectrum depicted in Figure 2.22: (a) lowest frequency cluster (b) intermediate frequency cluster (c) high frequency cluster	67
2.24	Calculated specular reflectivity spectrum from same structure as in Figure 2.23. The spectra were calculated for light incident with zero in-plane wavevector, $\beta/\beta_G = 0.00$, corresponding to normal incidence.	68

2.25	Calculated specular reflectivity spectrum from same structure as in Figure 2.23. The spectra were calculated for light incident with in-plane wavevector fixed at $\beta/\beta_G = 0.01$ in the $[\hat{x} + \hat{y}]$ direction (<i>i.e.</i> , along the $\Gamma - M$ symmetry direction).	69
2.26	Calculated specular reflectivity spectrum for light incident on a 125 nm slab waveguide of $\epsilon' = 12.25$ material with air above and below, and a square lattice of cylindrical airholes, 25 nm deep embedded at its centre. The spectra were calculated for light incident with in-plane wavevector fixed at $\beta/\beta_G = 0.001$ in the \hat{x} direction (X symmetry direction). The lattice has a pitch of $\Lambda = 500$ nm, and the radius, r , of the holes is: (a) $r/\Lambda = 0.25$ (b) $r/\Lambda = 0.32$ (c) $r/\Lambda = 0.40$	70
2.27	Strongly 2D textured thin asymmetric slab waveguide: the structure consists of a 80 nm-thick slab of $\epsilon' = 12.25$ material which forms the guiding core, clad above by air and below by $2 \mu\text{m}$ of material with $\epsilon' = 2.25$. The semi-infinite half-plane below is composed of $\epsilon' = 12.25$ material. The core waveguide layer is penetrated by a 2D square array of holes on a pitch, $\Lambda = 500$ nm, and with hole radii given by $r/\Lambda = 0.5$	71
2.28	Calculated near-normal incidence specular reflectivity spectrum for light incident with in-plane wavevector, $\beta = 0.03\beta_G$, along the $\Gamma - X$ direction for the structure depicted in Figure 2.27 with $r/\Lambda = .2821$. The solid line represents the s polarized spectrum, the dashed line depicts the p polarized spectrum.	72
2.29	Calculated near-normal incidence specular reflectivity spectrum for light incident with in-plane wavevector, $\beta = 0.03\beta_G$, along the $\Gamma - M$ direction for the structure depicted in Figure 2.27 with $r/\Lambda = .2821$. The solid line represents the s polarized spectrum, the dashed line depicts the p polarized spectrum.	72

2.30	Calculated specular reflectivity spectra for light incident on the structure depicted in Figure 2.27 with $r/\Lambda = .2821$. (a) Normal incidence specular reflectivity, <i>i.e.</i> , light incident with $\beta = 0$. (b) Reflectivity for <i>s</i> polarized evanescent light incident with $\beta = \beta_G \hat{x}$	74
2.31	Logarithmic plot of the absolute value of the error on the bound mode frequencies of an untextured slab waveguide as calculated by the FDRS method as a function of the number of mesh points in each of the \hat{x} and \hat{y} directions included in the calculation. The (artificial) unit cell for the FDRS method was set to a square of side $\Lambda = 500$ nm, and the in-plane wave vector of the incident evanescent light was set to $\beta_{\text{inc}} = 2\pi/\Lambda$. The structure used for the calculation consisted of a 120 nm slab of material with $\epsilon' = 12.25$ clad above and below by air ($\epsilon' = 1.0$). The different curves (lines) are for increasing numbers, (specifically: 12, 22, 32, 42, 62, and 122), from top to bottom on the graph, of mesh points in the \hat{z} direction.	79
2.32	Slab waveguide with “strong” 1D texture: the structure consists of a slab of thickness d of $\epsilon' = 12.25$ material, clad above and below by air, with a 1D square-toothed grating having a pitch, $\Lambda = 500$ nm, and an air filling fraction of 25% that completely penetrates the slab.	81
2.33	Mode frequency (a) and width (b) <i>vs.</i> the “number of elements” (see text) used in FDRS calculation for the structure depicted in Figure 2.32 with $d = 80$ nm. The results are for the second-order lossy mode at the zone-centre. Plots with round markers and solid lines depict results with anti-aliasing spectral filtering of the $\epsilon' - \mu'$ profile implemented; plots with square markers and dashed lines depict results without filtering of the $\epsilon' - \mu'$ profile.	82

- 2.34 (a) Mode frequency and (b) width, *vs.* square of the $x - y$ mesh size normalized by the unit cell size (or grating pitch) used in the FDRS calculation for the structure depicted in Figure 2.32 with $d = 80$ nm. The results are for the second-order lossy mode at the zone-centre. The insets provide a magnified view of the small mesh size regions of their respective graphs. The FDRS calculation was carried out with anti-aliasing spectral filtering of the $\epsilon' - \mu'$ profile implemented. The dashed lines represent the best fit line obtained from a linear least squares fit. In (b) the rightmost three points were ignored in the fitting. 84
- 2.35 Strongly 2D textured thin asymmetric slab waveguide: the structure consists of a 80 nm-thick slab of $\epsilon' = 12.25$ material which forms the guiding core, clad above by air and below by material with $\epsilon' = 2.25$. The core waveguide layer is penetrated by a 2D square array of holes on a pitch, $\Lambda = 500$ nm, and with hole radii given by $r/\Lambda = 0.2821$ 85
- 2.36 Mode frequency (a) and width (b) *vs.* square of the $x - y$ mesh size normalized by the unit cell size (or grating pitch) used in the FDRS calculation for the structure depicted in Figure 2.35. The results are for the second-order lossy mode at the zone-centre. The FDRS calculation was carried out with anti-aliasing spectral filtering of the $\epsilon' - \mu'$ profile implemented. The mesh sizes correspond (from left to right in the graph) to 21×21 , 19×19 , 17×17 , 15×15 , 13×13 , 11×11 , and 9×9 elements used in the calculation. 86

- 2.37 Near-normal incidence specular reflectivity spectra for light incident with in-plane wavevector $\beta = 0.02\beta_G$ along the $\Gamma - X$ direction calculated with the FDRS model (lower plot) and the GF model (upper plot). The parameters used for the FDRS model are as described in section 2.4.2 using 17 elements. The GF calculation included the nine reciprocal lattice vectors at $\vec{0}$, $\pm\beta_G\hat{x}$, $\pm\beta_G\hat{y}$, $\pm\beta_G\hat{x} \pm \beta_G\hat{y}$. The solid lines represent the s polarized spectra, and the dashed lines represent the p polarized spectra. The structure being modelled is the same as the one depicted in Figure 2.27. The resonance widths and shape are in excellent agreement. The mode frequencies agree to within 1.5%. 90
- 2.38 Location of the upper and lower edge of the 2nd order gap in a 1D textured symmetric waveguide as a function of guide and grating thickness, d (see Figure 2.32). The waveguide core is made of material with $\epsilon' = 12.25$ and clad above and below by air ($\epsilon' = 1.0$). The grating, which completely penetrates the waveguide core, has an air filling fraction of 25%. The dashed lines are for the calculation with the GF model, the solid lines with the FDRS model which was verified to be converged to within 1% for the upper band and 0.2% for the lower band (using 17 “elements” in the calculations). The GF calculation included the three reciprocal lattice vectors at $\vec{0}$ and $\pm\beta_G\hat{x}$ 91

2.39	Calculated normal incidence specular reflectivity spectra for light incident with zero in-plane wavevector. The calculation is performed (a) using Pendry's original approximations for \mathbf{k} and (b) the approximations for \mathbf{k} implemented in this work. The solid and dashed lines, which overlap completely here, represent the s polarized and p polarized spectra respectively. The light is incident on a film of material having a dielectric constant of 12.25 textured with a square array of 300 nm diameter cylindrical holes filled with a material having a dielectric constant of 2.25, all on a substrate with a dielectric constant of 2.25. The pitch of the grating is 500 nm.	94
2.40	Calculated near-normal incidence specular reflectivity spectrum for light incident with in-plane wavevector, $\beta = 0.01\beta_G$, along the $\Gamma - X$ direction. The calculation is performed (a) using Pendry's original approximations for \mathbf{k} and (b) the approximations for \mathbf{k} implemented in this work. The solid lines represent the s polarized spectra, the dashed lines depict the p polarized spectra. The light is incident on a film of material having a dielectric constant of 12.25 textured with a square array of 300 nm diameter cylindrical holes filled with a material having a dielectric constant of 2.25, all on a substrate with a dielectric constant of 2.25. The pitch of the grating is 500 nm.	95
3.1	Scanning electron microscope (SEM) image of freestanding air/GaAs/air slab waveguide patterned with 2D square lattice of airholes.	99
3.2	High magnification (SEM) image of the same structure as in Figure 3.1 .	100
3.3	Schematic diagram of oxide-based high-index contrast waveguide with strong 2D texture	101

3.4	(a) Field emission scanning electron microscope column, corresponding to the column of the Hitachi S-4100 SEM: (1) Electron source (2) Beam paths showing the effect of successive apertures in the column, (3) Apertures (4) Condenser Lens (5) Deflection Coils (6) Objective lens (7) Specimen; (b) Magnetic Lens detail showing how the magnitude of the axial magnetic component B_z varies in the lens region; (c) Detail showing geometry of beam aperture angle α at the sample.	105
3.5	Schematic diagram of ECR plasma etcher	108
3.6	Oxidation Setup	112
3.7	Schematic diagram of AFM tip operation and position detection	114
3.8	As grown sample layer structure for ASU 721	116
3.9	Top view of grating 22 on sample ASU 721 as imaged by the optical microscope. The size of the grating is $90\text{ }\mu\text{m} \times 90\text{ }\mu\text{m}$. Some processing was performed on the image to enhance the contrast between the oxidized region, which extends out around the grating and is slightly darker compared to the unoxidized parts of the sample.	122
3.10	$4\text{ }\mu\text{m} \times 4\text{ }\mu\text{m}$ AFM image of grating 22.	125
3.11	Section through diameter of holes in image in Figure 3.10. The arrows indicate the leading and trailing edges of the depression in the profile, which are used to obtain a measurement of the diameter of the holes at the surface.	126
4.1	Schematic diagram of scattering geometry used in specular reflectivity measurement. The dimensions of the sample and pattern depicted are the nominal values for grating 22 on sample ASU 721.	128
4.2	Schematic diagram of experimental setup	129
4.3	Schematic diagram of sampleholder	131
4.4	Schematic diagram of FTIR spectrometer	133

5.1	Experimental (a) and calculated (b) specular reflectivity spectra on grating 22 at incidence angle of $\theta = 5^\circ$ and $\phi = 0^\circ$ for p-polarization of reflected light.	138
5.2	Experimental (a) and calculated (b) specular reflectivity spectra on grating 22 at incidence angle of $\theta = 5^\circ$ and $\phi = 0^\circ$ for s-polarization of reflected light.	139
5.3	Experimental (a) and calculated (b) specular reflectivity spectra on grating 22 at incidence angle of $\theta = 5^\circ$ and $\phi = 45^\circ$ for p-polarization of reflected light.	140
5.4	Experimental (a) and calculated (b) specular reflectivity spectra on grating 22 at incidence angle of $\theta = 5^\circ$ and $\phi = 45^\circ$ for s-polarization of reflected light.	141
5.5	Experimental specular reflectivity spectra for s polarization at various incident angles, θ , along the $\Gamma - X$ direction ($\phi = 0$). The plots have been offset from one another for the sake of clarity; the vertical scale on the reflectivity traces is linear.	142
5.6	Fit to specular reflectivity spectrum obtained from grating 22 obtained with light incident at $\theta = 50^\circ$ along the $\Gamma - X$ direction. The solid line represents the experimental spectrum while the dashed line represents the "best fit" spectrum generated by a Fano lineshape function summed with an Airy function. The initial fit to the Fabry-Perot fringes was performed over a wider range of energies (6000 cm^{-1} to $11,500 \text{ cm}^{-1}$) not shown here. The fit using a Fano lineshape and Airy function was performed using data points in the range $6000 \text{ cm}^{-1} - 9000 \text{ cm}^{-1}$	147

5.7	Fit to spectra generated by the GF model. (a) Specular reflectivity spectrum for reference (b) 1st order scattering to $-\beta_G \hat{x}$ field component (c) 1st order scattering $+\beta_G \hat{x}$ field component. In (b) and (c) the symbols correspond to the model values, and the smooth lines are the result of a fit with a Fano lineshape function. The spectra are for 10^0 angle of incidence along the $\Gamma - X$ direction.	148
5.8	Mode frequency versus magnitude of in-plane wavevector for experiment (solid lines and markers) and model (dotted lines and hollow markers) for s (circles) and p (squares) polarized radiation. The inset schematically depicts the bandstructure for the case of weak texture.	150
5.9	Experimental (filled circles and solid lines) and model (filled squares and dotted lines) linewidths of the lowest frequency band appearing along the $\Gamma - X$ direction in Figure 5.8.	152
5.10	Experimental (dots and solid lines) and model (open circles and dotted lines) linewidths of 5th lowest (a), and 4th lowest (b) bands in Figure 5.8 <i>vs.</i> in-plane wavevector along the $\Gamma - X$ direction. The crossed circle represents a zero linewidth that was inferred from the absence of any feature in the spectrum.	155
5.11	Experimental specular reflectivity spectra for s polarized light (solid lines) and p polarized lines (dotted lines) (a) grating 22 (b) grating 23 (c) grating 24 which have the same pitch but different air filling fractions of (a) 0.28 (b) 0.33 (c) 0.49. The spectra have been offset vertically from one another for the sake of clarity. The vertical scale on the reflectivity traces is linear. The dark, thick lines have been drawn in by hand to serve as a guide to the eye.	157
6.1	Schematic dispersion of resonant states attached to the core of a slab waveguide with square photonic lattice.	160

6.2	Dominant Fourier field components of eigenmodes in lowest four bands along the $\Gamma - X$ ($\theta = 0$) direction depicted in Figure 5.8: the solid black arrows represent the propagation vectors associated with the in-plane variation of the field components; dashed lines represents the electric fields and their x and y components; the grey arrows represent the incident in-plane wavevector, <i>i.e.</i> , detuning from zone-centre	161
6.3	Dominant Fourier field components of eigenmodes in the four bands along the $\Gamma - M$ direction depicted in Figure 5.8: the solid arrows represent the propagation vectors associated with the in-plane variation of the field components; the grey arrows represent the incident in-plane wavevector, <i>i.e.</i> , detuning from zone-centre; the dashed lines represents the electric fields and their x and y components.	163
6.4	Calculated specular reflectivity spectra for s polarized (solid lines) and p polarized (dotted lines) for $\theta = 2^\circ$, $\phi = 0$ with (a) $r/\Lambda = 0.29$ and (b) $r/\Lambda = 0.33$. The other parameters in the model are as the fitted results for grating 22. The curves have been shifted vertically for clarity.	167
6.5	Schematic depiction of the in plane electric field intensity distribution over the unit cell for a 1D grating of the symmetric, lossy (left) and anti-symmetric, non-lossy (right) band edge states for a grating with (a) 25% (b) 50% (c) 75% air filling fraction. In (b) the lossy and lossless modes both modes have the same fraction of their total field energy (area under the curve) in the high-index region. The dielectric profile is indicated by the dashed line.	169

6.6	Dominant Fourier field components of eigenmodes in the 4th and 5th lowest energy bands along $\Gamma - X$ direction in Figure 5.8 in the vicinity of their anti-crossing: the solid arrows represent the propagation vectors associated with the in-plane variation of the field components; the grey arrows represent the incident in-plane wavevector, <i>i.e.</i> , detuning from zone-centre; dashed lines represents the electric fields and their x and y components.	171
6.7	Scattering amplitudes calculated using the FDRS Code for s polarized light incident at $\beta_{inc} \approx 0.25\beta_G\hat{x}$ corresponding to $\theta = 25^\circ$ along the $\Gamma - X$ direction, where the anti-crossing occurs. The various plots depict the scattering amplitudes to s polarized light with in-plane wavevector: (a) β_{inc} (b) $\beta_{inc} - \beta_G\hat{x}$ (c) $\beta_{inc} \pm \beta_G\hat{y}$ (d) $\beta_{inc} + \beta_G\hat{x}$ (e) $\beta_{inc} + \beta_G[-\hat{x} \pm \hat{y}]$ (f) $\beta_{inc} + \beta_G[\hat{x} \pm \hat{y}]$. The structure is the same as that for grating 22 with the parameters as obtained from fitting with the GF code.	173
A.1	Scheme of real-space points on which the fields and dielectric constant are sampled on the unit cell. The dielectric constant is sampled at points represented by the black dots. The electric or magnetic fields are sampled only on the points with squares. \mathbf{A}_1 and \mathbf{A}_2 represent the primitive lattice vectors of the photonic crystal.	187
A.2	Scheme of reciprocal lattice vectors corresponding to in-plane wavevector of launched modes for photonic crystal with oblique 2D lattice.	188

Acknowledgements

I would like to thank my contemporaries in the Photonic Nanostructures Group at UBC, postdoctoral researchers, Manoj Kanskar, Paul Paddon, and Jennifer Watson, graduate students, Alex Busch, Jody Mandeville, Francois Sfigakis, Murray McCutcheon, and Allan Cowan, as well as UBC Advanced Materials and Process Engineering Laboratory research engineers, Jim MacKenzie and Al Schmalz, for their instruction, insights, industry, and cooperation on various scientific and technical problems relevant to this dissertation. I would also like to thank Shane Johnson, Simon Watkins, and Tom Tiedje for growing the samples used throughout the course of the research described herein. I would like to gratefully acknowledge the Natural Sciences and Engineering Research Council of Canada, the BC Science Council, and the Canadian Cable Labs Fund, for funding portions of my doctoral studies and research program. As well, I would like to thank my research supervisory committee members, Mark Halpern, Lorne Whitehead, Jochen Meyer, David Jones, and Bill McCutcheon, for their helpful advice and questions over the years. I am also very grateful to Bill McCutcheon and Jess Brewer for their detailed comments on the penultimate draft of this dissertation. Finally, I would like to thank, my research supervisor, Jeff Young, for all of his valuable advice, criticism, guidance, and mentoring, as well as for the energy, enthusiasm, and diligence he has devoted to the supervision of this dissertation.

Dedication

To my loving parents and late grandmother.

Chapter 1

Introduction

Photonic crystals are structures in which the dielectric constant is given a periodic spatial variation, or “texture”, as, for example, depicted schematically in Figure 1.1.

For electromagnetic radiation with a wavelength on the order of the spatial period of the dielectric variation, this texturing can be used to modify and control the optical properties of the photonic crystal. The one-dimensional (1D) version of this concept, the dielectric stack, has existed for some time and forms the basis of applications like Distributed Bragg Reflector (DBR) mirrors and optical filters. However, it is fair to say that the field of photonic crystals was invented by Yablonovich and John (independently) [3, 4]. They generalized the concept of dielectric texture to two dimensions (2D) and three dimensions (3D) and realized that this texturing could drastically modify the totality of allowed electromagnetic states. Further, they recast the resulting electromagnetic (EM) Maxwell’s equations for light in a periodic dielectric into the formalism of existing condensed matter band theory for electrons in a periodic atomic potential. Here, the periodic dielectric plays the role of a periodic potential that couples the freely propagating electromagnetic eigenmodes into photonic Bloch states that can be used to describe the EM excitations of the photonic crystal in analogy to the electronic Bloch states formed in “normal”, *i.e.*, atomic, crystals.

Figure 1.2 depicts the photonic bandstructure in a face-centred-cubic photonic crystal [1]. At the Brillouin zone boundaries, the superposition of forward propagating and Bragg scattered radiation results in standing wave eigenstates with zero group velocity in the direction perpendicular to the zone boundaries. For a definition of Brillouin zones, Bloch states, and their importance in solving problems involving potential functions with

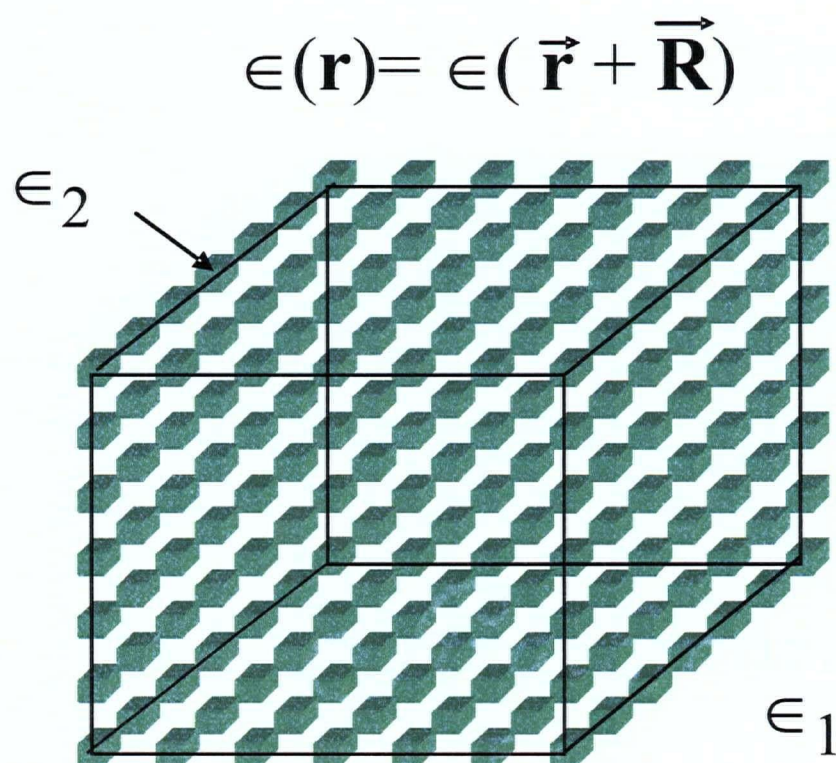


Figure 1.1: Schematic diagram of 3D photonic crystal concept. \mathbf{R} is any one of the lattice vectors that define the crystal symmetry.

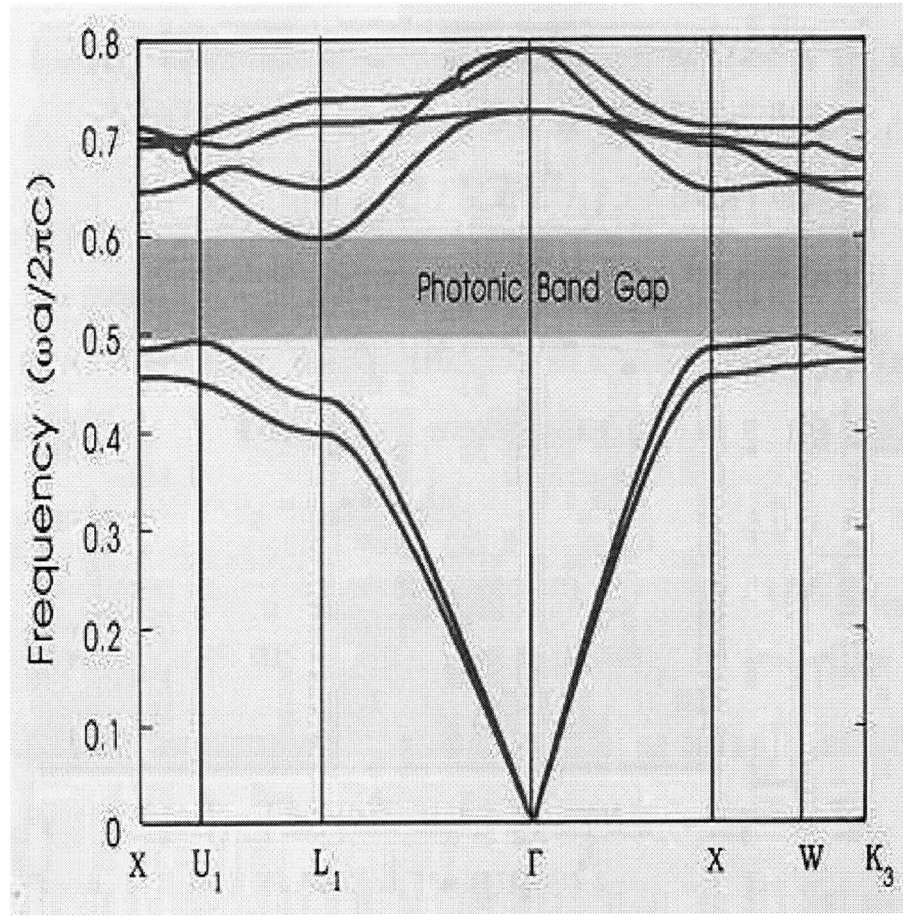


Figure 1.2: Photonic bandstructure arising from 3D face-centred-cubic photonic lattice comprised of non-spherical “atoms” and dielectric contrast of $\frac{\epsilon_2}{\epsilon_1} = 13.0$ [1].

discrete translation symmetry see [5, 6].

The periodic dielectric generally alters the dispersion and eigenstates everywhere in the Brillouin zone. The stronger the dielectric contrast, the stronger the scattering and the greater the modification to the photonic dispersion. One particular feature of this altered dispersion is that frequency gaps open up, at least along a given crystal symmetry direction, as depicted in Figure 1.2. In other words, there exists a frequency band within which there are no classical propagating electromagnetic modes with wavevectors along the given symmetry direction. Furthermore, if all of the gaps in the various

symmetry directions overlap partially, as they do here, then the region of complete overlap is said to form a complete photonic bandgap. This means that no classical propagating radiation with a frequency within the bandgap is allowed inside the crystal, and consequently, that externally impinging radiation will decay exponentially with distance into the crystal. The existence of a complete gap requires a crystal structure with a high degree of symmetry, as well as a large dielectric contrast in the texturing. The symmetry causes the energies of the modes not to vary greatly in different directions, while the high dielectric contrast causes the gaps that open up to be quite large. The combination of these two effects, then, increases the likelihood for the gaps in all of the different directions to overlap in some frequency band.

A material with a full photonic bandgap is appealing as a platform for both research as well as novel device applications. If a point defect is introduced into the otherwise infinite periodic lattice, then it is possible to localize light to the defect site and thereby trap it. Due to the full bandgap that exists within the surrounding infinite photonic lattice for some range of frequencies, the light trapped at the defect cannot propagate away. The defect site can be thought of as a high quality cavity surrounded by perfect, omnidirectionally reflecting mirrors. If an electronic resonance, such as that occurring near the bandedge of an embedded quantum well or quantum dot, is tuned to the energy of the defect mode, then there is only a single photon mode that can interact with the electronic resonance. The sub-micron size of the localized photons means that the coupling of the electronic transition and the photon can be very strong, on the order of an meV, making these structures interesting for the study of strong coupling effects [7, 8, 9]. It has been suggested that near-thresholdless lasers [3] might be realized in such systems, where there are effectively no continuum electromagnetic modes to compete with the lasing mode below threshold.

While the introduction of a point defect into a photonic crystal can create a trap for light, a *line defect* can localize light into a channel. Once again, any light having

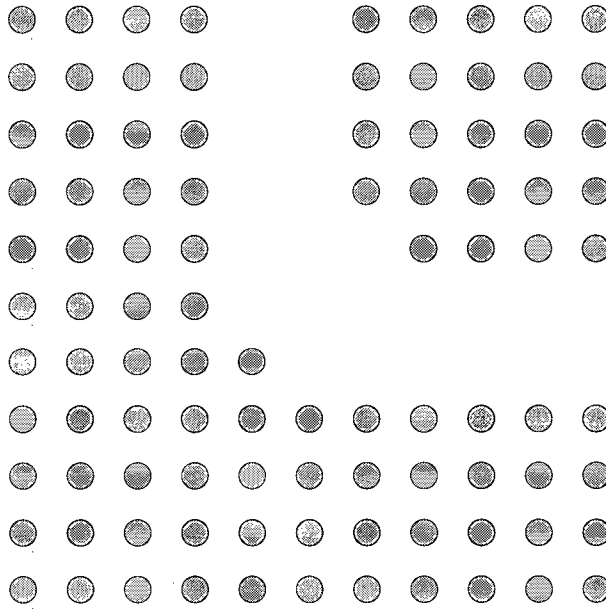


Figure 1.3: 2D photonic crystal “waveguide” with tight bend.

a frequency within the photonic bandgap of the surrounding photonic crystal cannot escape. If the defect channel is properly designed, the light can only propagate along the channel, even when the channel undergoes a tight bend, as depicted in Figure 1.3 for the case of a 2D photonic crystal. Such lossless guiding around tight bends cannot be achieved with conventional index-guided waveguides, as the critical angle of total internal reflection is exceeded if the radius of curvature becomes too small. The ability of photonic crystal waveguides to guide light nimbly around corners on a photonic chip could be an essential tool in the large scale integration of photonic circuits.

Even in the absence of a complete photonic bandgap, periodic dielectric texture confers the ability to drastically modify the dispersion of photons in a medium, beyond and separate from that attainable using composition control in untextured bulk material. This has already found application in dispersion compensation elements and compact delay components in optical fibre communication systems [10]. Furthermore, enhancement of gain in laser structures and of non-linear optical cross-sections, *e.g.*, for sum

frequency generation, have been predicted for weakly dispersive photons possessing small group velocities [11, 12].

The properties of 2D and 3D photonic crystals have been studied theoretically for pure dielectrics [1, 2, 13, 14, 15, 16, 17, 18]. They have also been verified experimentally in the microwave regime, where the lattice constants of the structures realized by assembling rods or machining slabs of polystyrene are on the order of centimeters. The bandstructure depicted in Figure 1.2 actually represents a lattice formed by machining three sets of cylindrical airholes separated by 120° into a block of material with a dielectric constant $\epsilon' = \epsilon/\epsilon_0 = 13.0$ (where ϵ_0 is the permittivity of free space) at a 35° angle on a 2D periodic grid (see Figure 1.4). The resulting interconnecting network of voids forms a face-centred-cubic (FCC) lattice with non-spherical “atoms”. Similar structures have found application in the microwave region as high-Q filters and broadband antennae platforms [19].

Semiconductors, in many ways, make ideal hosts for photonic crystals. The refractive index difference between air and several important group IV and III-V semiconductors, $\Delta n \sim 2.5$, is sufficient to allow the formation of complete optical bandgaps using appropriate lattice geometries [1]. Furthermore, artificial semiconductor quantum wells, wires and dots can be formed in a number of ways to achieve tunable electronic properties (resonant frequencies, densities of states) throughout the near-infrared part of the spectrum. In fact, it was recognized from the outset that incorporating photonic crystals into semiconductor hosts, rich in electronic resonances and ubiquitous in optical communication systems, would have even greater scientific and technological implications in the fields of quantum electronics and opto-electronics. However, the texture on the order of 200 – 500 nm required to operate in the near-infrared part of the spectrum has proven to be extremely challenging to realize in three dimensions.

Several strategies have been suggested and attempted to date. Cheng and Scherer [20] have used an ion beam to mill three sets of cylinders, as in Yablonovitch’s scheme

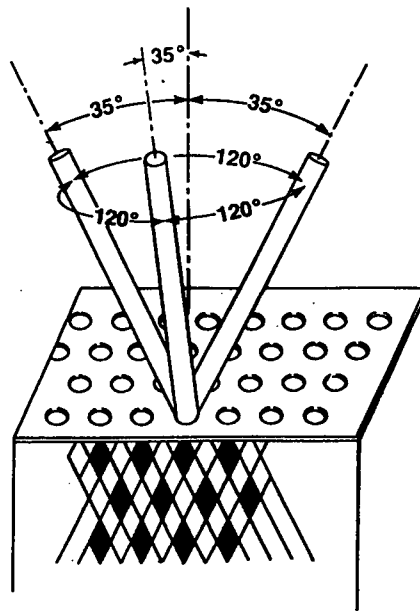


Figure 1.4: Scheme invented by Yablonovitch [2] for fabricating a 3D photonic crystal which exhibits a complete gap. It consists of machining three sets of cylindrical airholes separated by 120° into a block of material with sufficiently high dielectric contrast at a 35° angle on a 2D periodic grid. The resulting interconnecting network of voids forms a face-centred-cubic (FCC) lattice with non-spherical “atoms”.

depicted in Figure 1.4, into a GaAs/AlGaAs heterostructure through a 2D periodic mask of circular holes on a sub-micron pitch. Broadband transmission measurements did suggest that these structures exhibit an optical gap near normal incidence consistent with model calculations. However, the limitations of ion milling preclude making the structures any deeper. A more straightforward but tedious approach involves layer by layer assembly of semiconductor rods made by forming a surface grating on a sacrificial liftoff layer [21]. The textured surface is then turned upside down and fused to a previously-laid down set of rods rotated by 90° . The sacrificial layer is etched away, freeing the rods from the substrate and leaving the 1D array of rods fused to the layer previously laid down. Although this technique addresses the challenge of achieving high-contrast dielectric texture normal to the semiconductor wafer surface, it does not seem practical for reproducibly fabricating photonic crystals on a large scale. Another approach involves self-assembly of monodispersed opal or polystyrene spheres with lattice constants from $\sim 250 - 500$ nm followed by infiltration of the resulting voids with a high-index material. However, this fabrication method produces crystals with lattice imperfections that result in poor stop-bands [22]. In summary, despite considerable effort, a good-quality bulk 3D photonic crystal useful in the optical or near-infrared spectrum is still not available.

In contrast, 2D patterning of semiconductors, *via* nanolithography and etching, and epitaxial growth of multilayer semiconductor waveguides are mature technologies. It may be possible, then, to access many of the potentially useful and interesting properties of photonic crystals simply by etching a 2D array of holes in a planar semiconductor waveguide. Such a planar waveguide-based photonic crystal is depicted in Figure 1.5. An additional advantage to this approach is that it is compatible with the vast majority of existing opto-electronics components like semiconductor lasers, modulators, and couplers. The tradeoff is that it is impossible to *perfectly* localize light in this geometry because the structure cannot support *true* photonic bandgaps but, at best, pseudo-gaps.

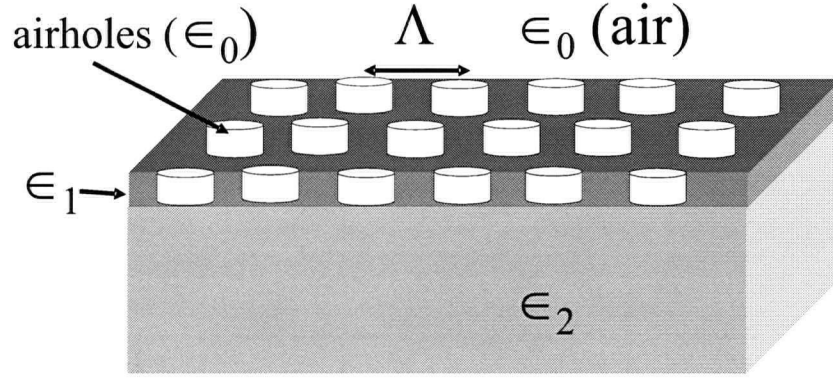


Figure 1.5: Schematic diagram of an asymmetric 3-layer slab waveguide with 2D photonic crystal embedded in core.

This is because there are always solutions to Maxwell's equations corresponding to radiation propagating in the direction perpendicular to the plane of the slab waveguide (see Figure 1.7 below).

Figure 1.6 schematically depicts an *unt textured* planar (or slab) waveguide structure along with the intensity profile of one of its guided modes. The electromagnetic excitations of the slab waveguide structures can be labelled by their in-plane wavevector, β , and frequency, ω . Figure 1.7 depicts a schematic dispersion diagram for a structure like the one shown in Figure 1.6. Three relevant light lines are also depicted on the diagram, one for each of the semi-infinite cladding layers as well as one for the guiding core. These represent the photon dispersion given by $\omega = \frac{c}{\sqrt{\epsilon/\epsilon_0}}\beta$ for propagating radiation in bulk material with an index of refraction ($=\sqrt{\epsilon/\epsilon_0}$) equal to that of their respective layers.

The three light lines on the diagram serve to delineate the boundaries between four regimes. Below the light line of the core is a “forbidden” region where there are no solutions to Maxwell's equations in the absence of external sources. The variation of the fields in the direction normal to the interfaces is necessarily exponentially growing or decaying. Between the core and substrate lightlines, there is a discrete set of guided modes bound to the guiding core. In the case of these guided modes, the fields in the

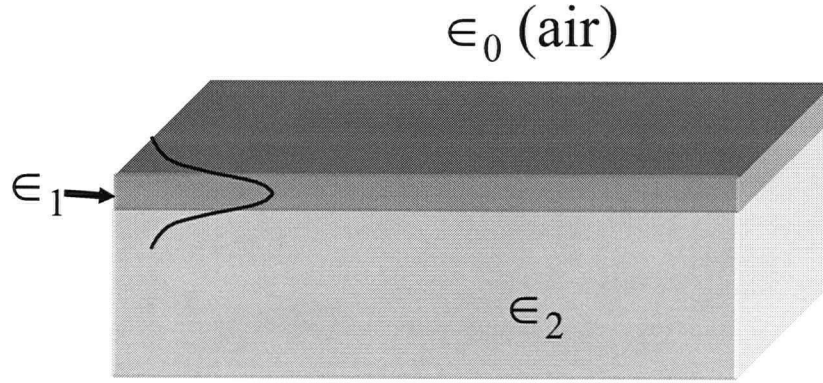


Figure 1.6: Schematic diagram of an asymmetric 3-layer slab waveguide.

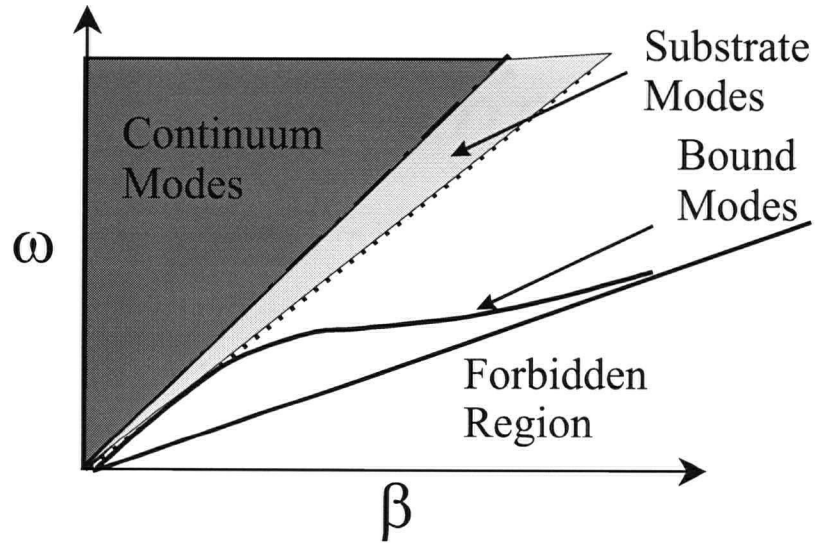


Figure 1.7: Schematic dispersion diagram of the modes of an asymmetric 3-layer slab waveguide. The solid line represents the light line for the core material. The dot-dashed line represents the line light-line for the superstrate, *i.e.*, top semi-infinite layer (air). The dotted line represents the light line for the substrate, *i.e.*, bottom semi-infinite layer.

cladding layers decay exponentially away from the core such that no energy is carried away in the transverse direction. In contrast, above the lightline of the superstrate (air), there exists a continuum of radiation modes. These modes are plane waves that propagate throughout the structure and undergo multiple reflections at the boundaries. Between the superstrate and substrate lightlines, there exists another continuum of modes with fields that decay away from the core in the superstrate but radiate down into the substrate. These are referred to as substrate modes.

Additionally, all of the electromagnetic modes can be separated into two orthogonal polarizations, transverse electric (TE) and transverse magnetic (TM), based on whether they have their electric (TE) or magnetic (TM) field completely transverse to their direction of propagation, which lies in the plane of the slab. In the case considered here, there is only one TE polarized guided mode in the region of $\omega - \beta$ space depicted in Figure 1.7. The details of planar waveguide theory can be found in reference [23].

Slab waveguides, themselves, can be classified into two types: “soft” guides and “hard” guides. “Soft” guides are comprised of a thicker ($\sim 1 \mu\text{m}$ for near-infrared wavelengths) core, and cladding layers having a relatively small difference in refractive index from that of the core ($\Delta n \approx 0.1$). “Hard” guides or membranes are comprised of a thin core ($\sim 0.1 \mu\text{m}$ for near-infrared wavelengths) with cladding layers having a larger refractive index difference ($\Delta n \sim 2$) from that of the core. “Soft” guides are found in the vast majority of opto-electronic applications, in part because they can be realized as semiconductor heterostructures which can be fabricated relatively easily using epitaxial growth techniques employing composition control in some suitably chosen alloy system (*e.g.*, GaAs/AlGaAs). Since large refractive index contrast cannot be achieved between semiconductor alloys, “hard” guides require the thin guiding core to be made freestanding, and therefore, to have air for its cladding layers, or to be clad on one or both sides by a thick oxide layer ($n \approx 1.5$).

From the point of view of embedding waveguides with planar photonic crystals, there

are advantages and drawbacks to using each of these as hosts. In order to achieve strong scattering, it is necessary that the crystal penetrate a significant portion of the core. For “soft” guides, this requires etching deep ($> 1 \mu\text{m}$) high-aspect ratio holes, which presents a considerable challenge. Moreover, the introduction of a material with dielectric constant far lower than that of the cladding layers generally reduces the volume-averaged index of the core layer enough to cut off guiding. Consequently, when planar photonic crystals are embedded in “soft” guides, the holes are made as deep as possible but placed in a cladding layer. This is done at the expense of scattering strength. Nevertheless, such “soft” guide based crystals are appealing due to their compatibility with the overwhelming majority of opto-electronic devices.

An early success in this geometry was achieved by Wendt *et al.* [24], who etched a honeycomb array of holes $\sim 1 \mu\text{m}$ deep on a sub-micron pitch into a special slab waveguide in a GaAs/AlGaAs/InGaAs heterostructure. Photoluminescence excited in the vicinity of the crystal exhibited preferential propagation along certain of its symmetry directions.

More experimental work in this area has been done by Labilloy *et al.* [25]. They have obtained evidence of a photonic bandgap and mapped dispersion by exciting broadband photoluminescence in quantum dots embedded within a 2D planar waveguide and measuring the transmission through a finite 2D photonic crystal interposed between the excited spot and a cleaved facet. They use the dropout in the transmission spectrum to determine the extent of the photonic band gap along the symmetry direction of the crystal. They then use oscillations in the spectra outside the gap, arising from the variation of the round-trip phase through the finite-sized grating as a function of the in-plane wavevector, to deduce the mode dispersion.

In contrast to “soft” waveguide-based photonic crystals, “hard” waveguide-based crystals require only shallow etches to completely penetrate the thin waveguide core. An additional advantage is that they can still support guided modes despite the introduction

of a large amount of low dielectric material into the core. On the other hand, freestanding waveguides tend to be less robust. Oxide-based structures avoid this problem; but the presence of an oxide, its quality, and the ease and reliability with which it can be incorporated pose other difficulties, especially when one attempts to make active devices. Nevertheless, these porous membranes represent the extreme, non-perturbative limit of waveguide-based photonic crystals.

The introduction of 2D in-plane periodic dielectric texture has an effect on bound modes similar to the effect on plane waves caused by the introduction of 3D periodic texture in bulk dielectrics. This can be seen in the weakly textured case by applying a perturbative method [26, 27]. The dispersion of the bound modes is modified and gaps are opened up at the boundaries of the 2D Brillouin zones, leading to a bandstructure for the slab modes.

It is interesting to address to what extent 2D planar photonic crystal waveguides can be used to implement the novel ideas mentioned above for 3D photonic crystals. For instance, point or line defects can still be introduced to create guides or cavities, but the photon confinement is achieved due to the photonic crystal in the in-plane directions, and due to the guiding properties of the slab structure in the transverse direction. Figure 1.8 schematically exemplifies a two-dimensionally textured waveguide with a point defect.

However, in any geometry that lacks translational invariance in the transverse direction there will always be some coupling to propagating modes outside of the waveguide. As is evident from Figure 1.7, at any frequency there exist modes that propagate directly through the waveguide. Consequently, although the bandstructure for modes localized to the slab waveguide core may exhibit frequency gaps, there always exist other non-resonant states at those frequencies. This geometry does not support full photonic bandgaps, but rather, at most, only pseudo-gaps.

It is of considerable importance to understand and quantify the differences between having a true gap, as opposed to only a pseudo-gap (or in-plane gap). From a practical

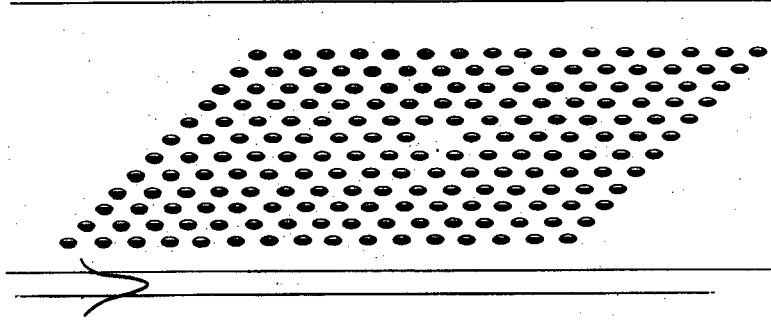


Figure 1.8: Schematic diagram of 2D photonic crystal with defect embedded in slab waveguide.

point of view this may be framed in terms of two key questions: (a) To what extent is the *total* Density of States modified ? and (b) How high are the intrinsic Q's that can be achieved ? These questions have been addressed by others to some extent.

It is known that planar photonic crystals do achieve a significant redistribution of the overall density of states in the vicinity of the pseudo-gap or the discrete defect states within the gap. Painter *et al.* [28] were able to demonstrate an optically pumped defect-mode laser in a 2D textured III-V semiconductor waveguide based photonic crystal. S. Fan *et al.* have demonstrated photon confinement by fabricating a silicon channel waveguide on an insulating substrate [29, 30]. A line of holes was then etched into the silicon channel, omitting the hole in the centre, to form a linear, 1D photonic crystal with defect for optical modes confined to the silicon channel. A localized photon was formed at the defect with an effective volume of $< 0.1 \mu\text{m}^3$. The same group has also demonstrated low losses through tight bends using photonic crystals embedded in slab waveguides [31].

Referring again to Figure 1.7, one is able to characterize the bound modes by their dispersion. It has also been shown that each such mode has a definite polarization.

Furthermore, one can see that the bound modes are discrete modes, in the sense that for any β there are no modes with a neighbouring ω . This is also the case for the modes of a 3D photonic lattice as described in Figure 1.2. The addition of 2D texture to the slab waveguide causes some of the bound modes to mix with radiative modes in the continuum. While some renormalized modes remain purely bound, the bandstructure for discrete modes now describes localized states which are generally only quasi-bound, or leaky. This leakiness can be described by an associated lifetime that has no analog in the case of pure 3D (or pure 2D) photonic crystals. It should be mentioned that such leaky modes also exist in the case of an untextured slab waveguide and are also associated with lifetimes. In this case, however, they occur in the continuum regime. Moreover, it should be emphasized that, in both cases, the lifetimes are not associated with an absorptive process. That is, the lifetimes do not describe a loss of electromagnetic energy, but rather the diminishment of its localization in the waveguide core.

The points identified above provide the main motivation for this thesis, which thoroughly characterizes the dispersion, polarization, and lifetime properties of discrete, slab modes of planar waveguides with strong 2D dielectric texture.

From a theoretical point of view, the bound and quasi-bound modes in 1D textured waveguides have been studied extensively with coupled mode theory (CMT) [32, 33, 34], which is a perturbative approach. Most of this work has been done in the context of Distributed Feedback Lasers (DFB's), which incorporate weak 1D texture in a slab waveguide geometry. This weak texture in DFB's results from particular conditions: either the index-contrast within the grating is small, or it is placed away from the waveguide core, or both. Coupled Mode Theory solves the separate scalar equations for the TE and TM modes, considering only the lowest order couplings between the modes of the waveguide.

In the case of 2D texturing of a general planar waveguide, however, the true eigenmodes of the slab can never strictly be expressed as superpositions of solely TE or solely

TM modes, and the problem is inherently one of a vector nature. In this vein, a 2D vector coupled-mode formalism has been presented by Paddon and Young [27]. Although this formalism provides a transparent understanding of the non-trivial vector coupling which occurs in 2D waveguides and insight into the polarization properties that arise from symmetry, it remains limited to weak texture.

Experimentally, we and others have shown that angle-resolved specular reflectivity measurements can be used to map out the dispersion, lifetimes, and polarization properties of these states away from the zone-centre [35, 36, 37]. In a somewhat related vein, Yablonovitch has demonstrated that coupling to radiation modes resulting from the presence of a photonic crystal can be used to enhance light extraction from light emitting diodes [2].

Our group was the first to report experimental and model results which showed that photonic bandedge states manifest themselves as Fano-like resonances [38] in normal-incidence specular reflectivity spectra taken on a strongly 2D-textured waveguide [39]. This occurred when the energy of the incident light matched that of the photonic eigenstates at zone-centre. The experiments were performed on a “hard” waveguide-based photonic crystal [39], which was fabricated by etching a periodic 2D array of holes completely through a 240 nm GaAs layer, then etching away an underlying sacrificial layer through the newly formed holes to create a freestanding, “porous waveguide”. The results were compared with a finite-element model that was developed principally by the author. The model allows for the calculation of specular reflectivity and scattering spectra, whence we may obtain the dispersion, lifetimes, and polarization properties of the modes. Qualitative agreement as well as crude quantitative agreement was obtained between the model and experiment.

These freestanding “porous waveguide” samples proved to be both difficult to fabricate and quite frail. As a result, a more robust structure and fabrication technique for “hard” waveguide-based photonic crystals was developed by the author in conjunction

with F. Sfigakis, a Master’s student in the group. In addition, the use of a new and much-improved optical scattering setup, developed by W.J. Mandeville, a doctoral student in the group, allowed for easy variation of the angle of the incident and scattered light. At the same time, a more efficient Green’s function (GF) based numerical model specific to the thin “hard” waveguide geometry, was developed by A. Cowan (another fellow doctoral student) and J.F. Young [40]. This much faster code allowed manual fitting of the model-generated bandstructures (dispersions and lifetimes) to those obtained from experiment. This entire body of work, which provides for a clear interpretation of optical scattering data in terms of the dispersion, lifetime, and polarization properties of 2D photonic crystals embedded in thin, “hard” waveguides, is the subject of this thesis.

The principal elements of this work include: (1) a numerical model for calculating specular reflectivity and scattering from an infinite 2D photonic crystal embedded in an arbitrary slab waveguide layer structure, based on integration of Maxwell’s equations through the textured layer on a discrete mesh, exploiting the discrete translational symmetry of the problem; (2) a fabrication technique for making structurally robust and robustly guiding thin semiconductor slab waveguides based on a wet oxidation technique; (3) angle-resolved specular reflectivity measurements that allow determination of mode dispersion and lifetimes, and which exhibit interesting polarization symmetries and anti-crossings away from high-symmetry points in the Brillouin zone; and (4) a comparison of these measurements with simulations based on a computationally efficient Green’s function-based (GF) model. This GF model is validated using the slower, “exact” model presented here, for the case of thin “hard” waveguides studied in this work. Resulting from this body of work is the realization that, even in this extreme non-perturbative limit of strongly textured thin waveguides, the photonic eigenstates in the vicinity of the second order TE gap can be understood qualitatively, and in some cases semi-quantitatively, as renormalized TE polarized slab modes.

The organization of the remainder of this thesis is as follows. Chapter 2 presents

the finite difference model developed by the author. Results from the model are used to introduce certain concepts related to bandstructure arising in the slab waveguide geometry as well as the approach used in this thesis for probing it. Chapter 3 presents the fabrication process used to realize the textured waveguide structures studied. Chapter 4 describes the experimental apparatus and procedure used to perform angle-resolved spectroscopy and the capabilities and limitations thereof. Chapter 5 presents the experimental data obtained, as well as a description of the fitting technique used to obtain dispersion and lifetime information. Chapter 6 provides an interpretation of the results and a qualitative explanation of the observed dispersion and polarization properties, using simple symmetry and kinematical arguments . Chapter 7 presents conclusions and some direction for future work.

Chapter 2

Modelling

2.1 Introduction

Two different techniques were used to model the linear optical scattering properties of thin porous slab waveguides in this work. The first technique, which is referred to as the Finite Difference Real Space approach (FDRS), involves the integration of Maxwell's equations through the textured layer on a discrete mesh defined on the unit cell of the photonic lattice. In our first attempt at this finite-element approach, we tried to apply an algorithm developed by J.B. Pendry [18] for calculating reflection and transmission coefficients through pure 2D and 3D photonic crystals. However, this algorithm did not converge well in our geometry. The specular reflectivity spectra did not contain the correct number of resonant features expected from symmetry considerations, nor were the polarization selection rules obeyed. The problem was traced to the use of forward differences (rather than symmetric differences) in the integration scheme, which introduced an artificial chirality into the calculation.

Consequently, a new integration scheme that converges well in our waveguide geometry was devised by the author in collaboration with P. Paddon. This new scheme was then implemented by the author. Additionally, the model was extended (by the author) to allow for efficient modelling of buried gratings. This new model is presented in detail in this chapter.

The second model used in this work was developed by J.F Young and A.R Cowan. It is referred to as the Green's Function (GF) model. This model is more computationally efficient than the FDRS approach, with its limitation being that it is only valid for

a textured layer that is thin compared to the wavelength of light therein. A detailed description of this model can be found elsewhere [40, 41] and is not given here. Due to its computational efficiency, it was used extensively for fitting to the experimental results presented in Chapter 4.

The FDRS model was developed first, and the process of its development led to most of our basic understanding of the symmetry and polarization properties of the electromagnetic modes attached to 2D photonic crystals embedded in slab waveguides. It also serves as a benchmark for more efficient codes, such as the GF code, which are based on approximations specific to a particular geometry. A comparison of the results from the GF and FDRS models is presented in section 2.5.

The remainder of this chapter provides a detailed description of the FDRS model. It also presents and discusses a number of spectra generated by the model for various relevant sample structures. Additionally, it explores the convergence behaviour of the algorithm. Finally, a discussion is presented regarding the necessity and significance of the modifications made to the original method of J.B. Pendry. A summary is given at the end of the chapter.

2.2 Description of Finite Difference Real Space Approach

2.2.1 Scattering from a periodically textured layer

We begin by considering the structure depicted in Figure 2.1. The dielectric function, $\epsilon(\mathbf{r})$ in region II is periodic in the plane of the slab:

$$\epsilon(\boldsymbol{\rho}; z) = \epsilon(\boldsymbol{\rho} + \mathbf{R}_i; z) \quad (2.1)$$

where $\boldsymbol{\rho}$ is a vector in the $x - y$ plane and \mathbf{R}_i is a 2D real-space lattice vector also in the $x - y$ plane. For simplicity, we assume that each material in the structure is linear, isotropic, and homogenous, so that it can be described in bulk form by a scalar dielectric

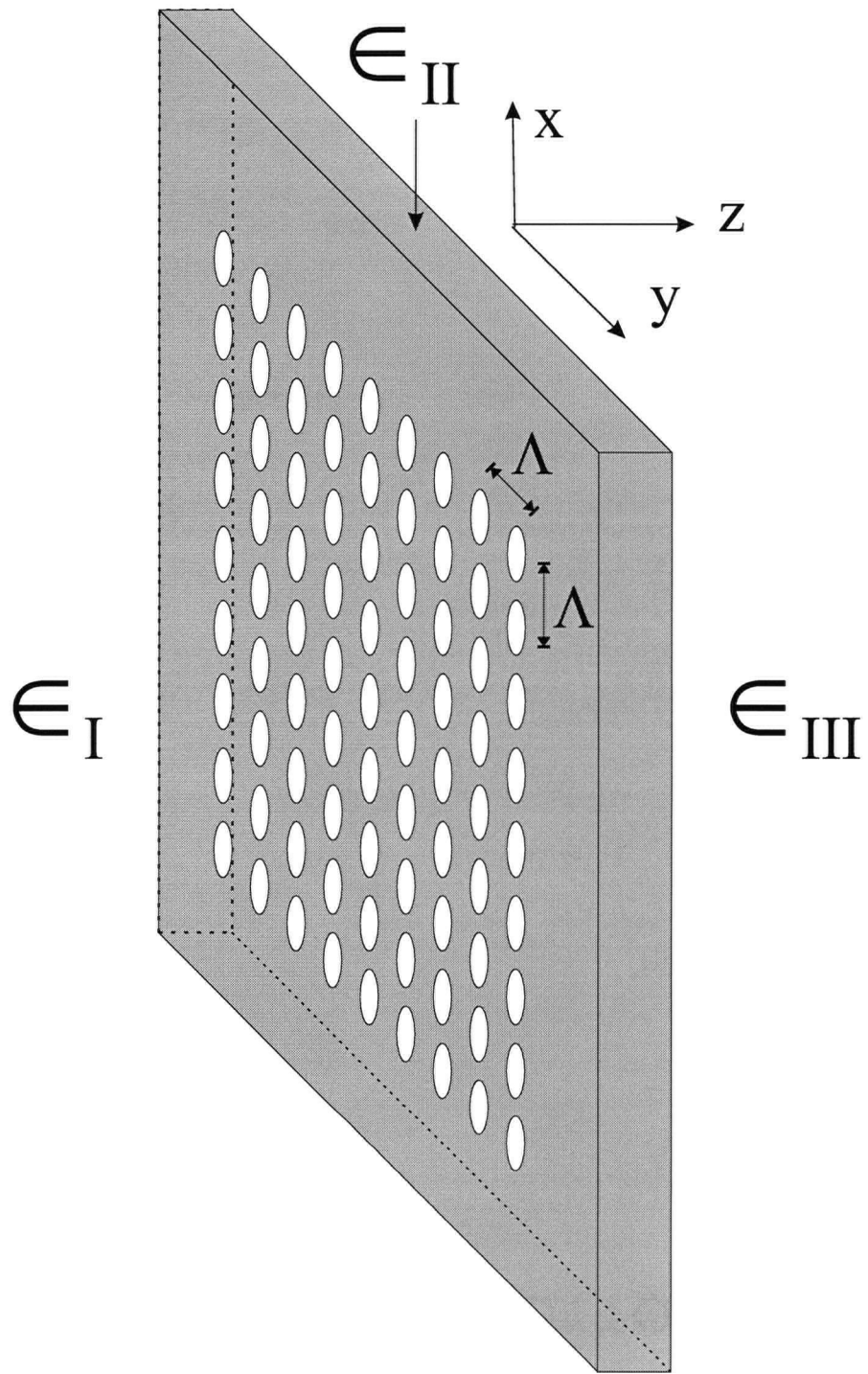


Figure 2.1: Schematic diagram of a two-dimensionally periodically textured slab structure.

constant.

Therefore, the dielectric function may be written as a Fourier series:

$$\epsilon'(\boldsymbol{\rho}; z) \triangleq \frac{\epsilon(\boldsymbol{\rho}; z)}{\epsilon_0} = \sum_{\mathbf{G}_{l,m}} \epsilon'_{\mathbf{G}_{l,m}}(z) \exp(i\mathbf{G}_{l,m} \cdot \boldsymbol{\rho}) \quad (2.2)$$

where the $\mathbf{G}_{l,m}$ are the reciprocal lattice vectors of the dielectric modulation (“photonic crystal”), *e.g.*, $\mathbf{G}_{l,m} = l\frac{2\pi}{\Lambda}\hat{x} + m\frac{2\pi}{\Lambda}\hat{y}$, for a 2D square lattice having a pitch Λ , where l and m are integers.

The harmonic solutions to Maxwell’s equations in the homogeneous regions, I and III, for a given frequency can be expanded in terms of a basis set consisting of transverse polarized plane waves (in general, a different set for each region to allow for different ϵ ’s in regions I and III) where all of the fields have a spatial-temporal variation of the form $\exp(i\mathbf{k} \cdot \mathbf{r}) \exp(-i\omega t)$ subject to the dispersion relation:

$$\epsilon'_{I/III} \frac{\omega^2}{c^2} = |\mathbf{k}|^2 = k_x^2 + k_y^2 + k_z^2 \quad (2.3)$$

and where

$$\epsilon'_{I/III} = \epsilon_{I/III}/\epsilon_0 \quad (2.4)$$

represents the dielectric constant in region I or III, which does not vary spatially, and c is the speed of light in vacuum.

There are, in general, two degenerate, orthogonal polarizations, labelled s and p according to whether the electric or magnetic field, respectively, lies completely in the plane of the slab interfaces. With the unit normal to the interfaces denoted by $\hat{\mathbf{n}}$, these plane wave modes can be written as:

$$\mathbf{E}^{(s)}(\mathbf{r}) = \frac{\hat{\mathbf{n}} \times \mathbf{k}}{|\hat{\mathbf{n}} \times \mathbf{k}|} E_0 \exp(i\mathbf{k} \cdot \mathbf{r} - i\omega t) \quad (2.5)$$

$$\mathbf{H}^{(s)}(\mathbf{r}) = \frac{\mathbf{k} \times (\hat{\mathbf{n}} \times \mathbf{k})}{|\hat{\mathbf{n}} \times \mathbf{k}|} \frac{E_0}{\mu\omega} \exp(i\mathbf{k} \cdot \mathbf{r} - i\omega t) = \frac{1}{\mu\omega} \mathbf{k} \times \mathbf{E}^{(s)}(\mathbf{r}) \quad (2.6)$$

and:

$$\mathbf{H}^{(p)}(\mathbf{r}) = \frac{\hat{\mathbf{n}} \times \mathbf{k}}{|\hat{\mathbf{n}} \times \mathbf{k}|} H_0 \exp(i\mathbf{k} \cdot \mathbf{r} - i\omega t) \quad (2.7)$$

$$\mathbf{E}^{(p)}(\mathbf{r}) = \frac{\mathbf{k} \times (\hat{\mathbf{n}} \times \mathbf{k})}{|\hat{\mathbf{n}} \times \mathbf{k}|} \frac{H_0}{\epsilon\omega} \exp(i\mathbf{k} \cdot \mathbf{r} - i\omega t) = \frac{1}{\epsilon\omega} \mathbf{k} \times \mathbf{H}^{(p)}(\mathbf{r}) \quad (2.8)$$

where ϵ and μ are the permittivity and permeability of the medium, respectively, and E_0 and H_0 are normalization constants bearing units of electric and magnetic field respectively.

For the special case of \mathbf{k} parallel to $\hat{\mathbf{n}}$ (*i.e.*, normal incidence), the fields of the polarized plane waves lie entirely in the $x - y$ plane, and hence the two independent polarizations may be defined with respect to any two orthogonal in-plane directions. For convenience, \hat{x} and \hat{y} are chosen, so our basis and the modes in this situation are defined as x or y polarized according to:

$$\mathbf{E}^{(x)}(\mathbf{r}) = E_0 \exp(i\mathbf{k} \cdot \mathbf{r} - i\omega t) \hat{x} \quad (2.9)$$

$$\mathbf{H}^{(x)}(\mathbf{r}) = \frac{k}{\mu\omega} E_0 \exp(i\mathbf{k} \cdot \mathbf{r} - i\omega t) \hat{y} = \frac{1}{\mu\omega} \mathbf{k} \times \mathbf{E}^{(x)}(\mathbf{r}) \quad (2.10)$$

and

$$\mathbf{H}^{(y)}(\mathbf{r}) = H_0 \exp(i\mathbf{k} \cdot \mathbf{r} - i\omega t) \hat{x} \quad (2.11)$$

$$\mathbf{E}^{(y)}(\mathbf{r}) = \frac{k}{\epsilon\omega} H_0 \exp(i\mathbf{k} \cdot \mathbf{r} - i\omega t) \hat{y} = \frac{1}{\epsilon\omega} \mathbf{k} \times \mathbf{H}^{(y)}(\mathbf{r}) \quad (2.12)$$

The situation we wish to consider is somewhat similar to that of a diffraction grating. We consider a plane wave of definite frequency, ω , and 3D wavevector, $\mathbf{k} = \boldsymbol{\beta} + k_z \hat{z}$, incident on the structure from the left, where $\boldsymbol{\beta}$ is the in-plane ($x - y$ plane) component of the wavevector. The incident plane wave scatters to a discrete set of plane waves travelling backward in region I as well as a discrete set of plane waves travelling forward in region III. The in-plane wavevectors of the discrete set of scattered plane waves in both regions are given by $\boldsymbol{\beta} + \mathbf{G}_{l,m}$. Physically, this arises from the fact that the periodic dielectric texture modulates the incident field, generating polarization with the same periodicity as the dielectric texture. This polarization will, in turn, generate an electric field having spatial Fourier components restricted to those described by the discrete set of reciprocal lattice vectors, $\mathbf{G}_{l,m}$, that define the dielectric texture.

Most generally, the scattering process can be described in terms of the following discrete set of transverse polarized plane waves on either side of the textured structure:

$$\mathbf{E}_{l,m}^{(s,\pm,I/III)}(\mathbf{r}) = \frac{\hat{\mathbf{n}} \times (\boldsymbol{\beta} + \mathbf{G}_{l,m})}{|\hat{\mathbf{n}} \times (\boldsymbol{\beta} + \mathbf{G}_{l,m})|} E_0 \exp[i(\boldsymbol{\beta} + \mathbf{G}_{l,m}) \cdot \boldsymbol{\rho}] \exp[iw_{l,m}^{(\pm,I/III)} z] \exp[-i\omega t] \quad (2.13)$$

$$\mathbf{H}_{l,m}^{(s,\pm,I/III)}(\mathbf{r}) = \frac{1}{\mu\omega} [(\boldsymbol{\beta} + \mathbf{G}_{l,m}) + w_{l,m}^{(\pm,I/III)} \hat{\mathbf{z}}] \times \mathbf{E}_{l,m}^{(s,\pm)}(\mathbf{r}) \quad (2.14)$$

and

$$\mathbf{H}_{l,m}^{(p,\pm,I/III)}(\mathbf{r}) = \frac{\hat{\mathbf{n}} \times (\boldsymbol{\beta} + \mathbf{G}_{l,m})}{|\hat{\mathbf{n}} \times (\boldsymbol{\beta} + \mathbf{G}_{l,m})|} H_0 \exp[i(\boldsymbol{\beta} + \mathbf{G}_{l,m}) \cdot \boldsymbol{\rho}] \exp[iw_{l,m}^{(\pm,I/III)} z] \exp[-i\omega t] \quad (2.15)$$

$$\mathbf{E}_{l,m}^{(p,\pm,I/III)}(\mathbf{r}) = \frac{1}{\epsilon\omega} [(\boldsymbol{\beta} + \mathbf{G}_{l,m}) + w_{l,m}^{(\pm,I/III)} \hat{\mathbf{z}}] \times \mathbf{H}_{l,m}^{(p,\pm)}(\mathbf{r}) \quad (2.16)$$

where

$$w_{l,m}^{(\pm,I/III)} = \pm[\epsilon'_{I/III}\omega^2/c^2 - |\boldsymbol{\beta} + \mathbf{G}_{l,m}|^2]^{1/2} \quad (2.17)$$

The quantity, $w_{l,m}^{(\pm,I/III)}$, represents the z -component of the wavevector for the particular plane wave, and equation 2.17 was obtained from the dispersion relation, equation 2.3. When $w_{l,m}^{(+/-,I/III)}$ is real-valued, we have a plane wave travelling (+) right (*i.e.*, $+\hat{\mathbf{z}}$ direction) or (−) left according to whether the positive or negative solution of the square root is selected. When $w_{l,m}^{(+/-,I/III)}$ is imaginary, then we have an evanescent plane wave that is decaying towards the (+) right or towards the (−) left. For the sake of concision, we refer to the modes simply as right-going or left-going according to the above convention regardless of whether they are actually propagating or evanescent.

We can then classify the plane waves as right- (+) or left-going (−) and order them with respect to polarization and in-plane wave-vector in a systematic manner. For the situation we are considering of a right-going (+) plane wave incident on the textured region from the left, we wish to compute the amplitudes of the scattered right-going (+) plane waves in region III, which we denote by $(a_T)_i$ for $i = 1, 2, 3, \dots$ (Transmitted), where the subscript i , now labels both the polarization and reciprocal lattice vector. We

also wish to compute the amplitudes of the scattered left-going plane waves in region I which we denote by $(a_R)_i$ (Reflected). The scattering problem can thus be written in matrix form as:

$$\mathbf{a}_T = T^{++} \mathbf{a}_{\text{inc}} \quad (2.18)$$

$$\mathbf{a}_R = T^{-+} \mathbf{a}_{\text{inc}} \quad (2.19)$$

where \mathbf{a}_{inc} contains the amplitudes of the right-going (+) plane wave modes in region I (incident). Note that for the experiment under consideration this last column matrix is all zero except for the one element corresponding to the sole plane wave incident from the left. These column matrices are of dimension $2N \times N$ where $N \times N$ is the number of reciprocal lattice vectors, in 2D, included in the calculation and the factor 2 arises from the two independent polarizations (s and p).

The matrix element T_{ij}^{++} , therefore, represents the scattering coefficient for plane wave i travelling toward the right (+) in region I to plane wave j leaving the textured layer in region III and travelling toward the right (+). The matrix element T_{ij}^{-+} , represents the scattering coefficient from plane wave i travelling toward the right (+) in region I and reflected/diffracted back to left-going (−) plane wave j in region I.

The problem, then, is to calculate the matrices T^{++} and T^{-+} . This is accomplished in the present model by integrating Maxwell's equations through the textured layer. However, in order to do so, one must perform the inverse scattering calculation using the following mathematical manipulation.

$$\mathbf{a}_{\text{inc}} = (T^{++})^{-1} \mathbf{a}_T \quad (2.20)$$

$$\mathbf{a}_R = T^{-+} (T^{++})^{-1} \mathbf{a}_T \quad (2.21)$$

Now, by specifying a single plane wave of unit amplitude travelling toward the right in region III, integrating backwards, and projecting onto the forward and backward travelling plane wave basis in region I, we obtain a column of each of the matrices

$(T^{++})^{-1}$ and $T^{-+}(T^{++})^{-1}$, respectively. The matrices may thus be constructed in their entirety by launching each of the basis plane waves in region I. The matrices T^{++} and T^{-+} are then obtained by matrix inversion and multiplication.

If we also independently consider the situation where one of the left-going modes is incident on the textured layer from region III and find the scattering amplitudes to diffracted/transmitted left-going modes in region I, $(b_T)_i$, and diffracted/reflected right-going modes in region III, $(b_R)_i$, we can define:

$$\mathbf{b}_T = T^{--}\mathbf{b}_{\text{inc}} \quad (2.22)$$

$$\mathbf{b}_R = T^{+-}\mathbf{b}_{\text{inc}} \quad (2.23)$$

where \mathbf{b}_{inc} contains the amplitudes of the left-going $(-)$ plane wave modes in region III (incident).

The matrix element T_{ij}^{--} , therefore, represents the scattering coefficient from plane wave i travelling toward the left $(-)$ in region III to plane wave j leaving the textured layer in region I and travelling toward the left $(-)$. The matrix element T_{ij}^{+-} , represents the scattering coefficient from plane wave i travelling toward the left $(-)$ in region III and reflected/diffracted back to right-going $(+)$ plane wave j in region III.

Therefore, by a similar argument, we may obtain $(T^{--})^{-1}$ and $T^{+-}(T^{--})^{-1}$ by specifying plane waves of unit amplitude travelling toward the left in region I and integrating forward, and hence obtain T^{--} and T^{+-} . The four matrices, T^{++} , T^{-+} , T^{--} , and T^{+-} completely specify the scattering properties of the textured layer.

Since the dielectric function is assumed to have the same discrete translation symmetry in the \hat{x} and \hat{y} directions for all z , Bloch's theorem may be exploited to render the computation tractable. Bloch's theorem requires that for any field component, $F(\mathbf{r}) = F(\boldsymbol{\rho}; z)$

$$F(\boldsymbol{\rho} + \mathbf{R}; z) = \exp(i\boldsymbol{\beta} \cdot \mathbf{R})F(\boldsymbol{\rho}; z) \quad (2.24)$$

Therefore, we need only compute the fields on the finite unit cell of the photonic crystal. This makes it possible to discretize Maxwell's equations on a finite number of mesh points with finite grid size so that they may be integrated forward or backward in a finite number of computational steps.

2.2.2 Discretization and Integration of Maxwell's Equations in Real Space

In order to compute the reflection and transmission matrices defined in the previous subsection, we need to be able to propagate the fields through the textured layer. That is, given the fields at one edge of the textured layer, we must compute the fields at the other boundary. This can be accomplished by stepping through the layer in the direction normal to the slab (\hat{z}) by successively computing the fields on adjacent intermediate planes lying parallel to the slab and mutually separated by some finite (z) step size. Therefore, we need to be able to calculate the fields on one plane given the fields on an adjacent plane, allowing for a spatially varying scalar permittivity, $\epsilon(\mathbf{r}) = \epsilon(\boldsymbol{\rho}; z)$.

We begin by considering Maxwell's equations in the absence of free charges and currents:

$$\nabla \times \mathbf{E}(\mathbf{r}, t) = -\partial \mathbf{B}(\mathbf{r}, t) / \partial t \quad (2.25)$$

$$\nabla \times \mathbf{H}(\mathbf{r}, t) = \partial \mathbf{D}(\mathbf{r}, t) / \partial t \quad (2.26)$$

$$\nabla \cdot \mathbf{D}(\mathbf{r}, t) = 0 \quad (2.27)$$

$$\nabla \cdot \mathbf{B}(\mathbf{r}, t) = 0 \quad (2.28)$$

and the constitutive equations:

$$\mathbf{D}(\mathbf{r}, t) = \epsilon(\mathbf{r})\mathbf{E}(\mathbf{r}, t) = \epsilon_0[1 + \chi_e(\mathbf{r})]\mathbf{E}(\mathbf{r}, t) = \epsilon_0\epsilon'(\mathbf{r})\mathbf{E}(\mathbf{r}, t) \quad (2.29)$$

$$\mathbf{B}(\mathbf{r}, t) = \mu(\mathbf{r})\mathbf{H}(\mathbf{r}, t) = \mu_0[1 + \chi_m(\mathbf{r})]\mathbf{H}(\mathbf{r}, t) = \mu_0\mu'(\mathbf{r})\mathbf{H}(\mathbf{r}, t) \quad (2.30)$$

where $\chi_e(\mathbf{r})$ and $\chi_m(\mathbf{r})$ are the electric and magnetic susceptibilities respectively, which are properties of the media, and ϵ_0 and μ_0 are the permittivity and permeability of free space, respectively.

Equations 2.25 and 2.26 may be Fourier transformed with respect to both space and time to give:

$$i\mathbf{k} \times \tilde{\mathbf{E}}(\mathbf{k}, \omega) = i\omega \tilde{\mathbf{B}}(\mathbf{k}, \omega) \quad (2.31)$$

$$i\mathbf{k} \times \tilde{\mathbf{H}}(\mathbf{k}, \omega) = -i\omega \tilde{\mathbf{D}}(\mathbf{k}, \omega) \quad (2.32)$$

As stated in the previous section, the approach we take is to solve Maxwell's equations on a finite number of spatial mesh points. As we shall see this has the effect of approximating the spatial derivatives in the equations 2.25–2.26 with difference terms between neighbouring mesh points. Consequently, we now define a rectilinear mesh with spacings a , b , and g in the \hat{x} , \hat{y} , and \hat{z} directions, respectively, and make the following approximations:

$$k_x \approx [\exp(\frac{ik_x a}{2}) - \exp(\frac{-ik_x a}{2})]/ia \triangleq \kappa_x \quad (2.33)$$

$$k_y \approx [\exp(\frac{ik_y b}{2}) - \exp(\frac{-ik_y b}{2})]/ib \triangleq \kappa_y \quad (2.34)$$

$$k_z \approx [\exp(\frac{ik_z g}{2}) - \exp(\frac{-ik_z g}{2})]/ig \triangleq \kappa_z \quad (2.35)$$

which are valid provided that:

$$k_x a \ll 1 \quad (2.36)$$

$$k_y b \ll 1 \quad (2.37)$$

$$k_z g \ll 1 \quad (2.38)$$

so that we define:

$$\boldsymbol{\kappa} \triangleq \kappa_x \hat{x} + \kappa_y \hat{y} + \kappa_z \hat{z} \approx \mathbf{k}. \quad (2.39)$$

Note that the greater the spatial frequency content in the fields, the finer the mesh required for this approximation to remain valid. It is also important to emphasize that

we have not made any assumptions here about the orientation of the coordinate system with respect to the photonic crystal.

Making the substitutions, $\mathbf{k} = \boldsymbol{\kappa}$, in equations 2.31 and 2.32, carrying out the cross-products and expanding component-by-component yields the following set of six equations:

$$\tilde{D}_x \approx -\frac{\exp(ik_y \frac{b}{2})\tilde{H}_z}{ib\omega} + \frac{\exp(-ik_y \frac{b}{2})\tilde{H}_z}{ib\omega} + \frac{\exp(ik_z \frac{g}{2})\tilde{H}_y}{ig\omega} - \frac{\exp(-ik_z \frac{g}{2})\tilde{H}_y}{ig\omega} \quad (2.40)$$

$$\tilde{D}_y \approx -\frac{\exp(ik_z \frac{g}{2})\tilde{H}_x}{ig\omega} - \frac{\exp(-ik_z \frac{g}{2})\tilde{H}_x}{ig\omega} - \frac{\exp(ik_x \frac{a}{2})\tilde{H}_z}{ia\omega} + \frac{\exp(-ik_x \frac{a}{2})\tilde{H}_z}{ia\omega} \quad (2.41)$$

$$\tilde{D}_z \approx -\frac{\exp(ik_x \frac{a}{2})\tilde{H}_y}{ia\omega} - \frac{\exp(-ik_x \frac{a}{2})\tilde{H}_y}{ia\omega} - \frac{\exp(ik_y \frac{b}{2})\tilde{H}_x}{ib\omega} + \frac{\exp(-ik_y \frac{b}{2})\tilde{H}_x}{ib\omega} \quad (2.42)$$

$$\tilde{B}_x \approx \frac{\exp(ik_y \frac{b}{2})\tilde{E}_z}{ib\omega} - \frac{\exp(-ik_y \frac{b}{2})\tilde{E}_z}{ib\omega} - \frac{\exp(ik_z \frac{g}{2})\tilde{E}_y}{ig\omega} + \frac{\exp(-ik_z \frac{g}{2})\tilde{E}_y}{ig\omega} \quad (2.43)$$

$$\tilde{B}_y \approx \frac{\exp(ik_z \frac{g}{2})\tilde{E}_x}{ig\omega} - \frac{\exp(-ik_z \frac{g}{2})\tilde{E}_x}{ig\omega} - \frac{\exp(ik_x \frac{a}{2})\tilde{E}_z}{ia\omega} + \frac{\exp(-ik_x \frac{a}{2})\tilde{E}_z}{ia\omega} \quad (2.44)$$

$$\tilde{B}_z \approx \frac{\exp(ik_x \frac{a}{2})\tilde{E}_y}{ia\omega} - \frac{\exp(-ik_x \frac{a}{2})\tilde{E}_y}{ia\omega} - \frac{\exp(ik_y \frac{b}{2})\tilde{E}_x}{ib\omega} + \frac{\exp(-ik_y \frac{b}{2})\tilde{E}_x}{ib\omega} \quad (2.45)$$

It is possible to transform the expression for the fields given above back to real-space by recognizing that the inverse Fourier transform of a field component times a phase shift is the translated real-space field. That is:

$$\begin{aligned} \exp(\pm ik_x \frac{a}{2})\tilde{F}_l &\Leftrightarrow F_l(x \mp \frac{a}{2}, y, z) = F_l(\mathbf{r} \mp \boldsymbol{\alpha}) \\ \exp(\pm ik_y \frac{b}{2})\tilde{F}_l &\Leftrightarrow F_l(x, y \mp \frac{b}{2}, z) = F_l(\mathbf{r} \mp \boldsymbol{\zeta}) \\ \exp(\pm ik_z \frac{g}{2})\tilde{F}_l &\Leftrightarrow F_l(x, y, z \mp \frac{g}{2}) = F_l(\mathbf{r} \mp \boldsymbol{\gamma}) \end{aligned} \quad (2.46)$$

where \tilde{F}_l denotes a component of the \mathbf{E} or \mathbf{H} field, and $\boldsymbol{\alpha}$, $\boldsymbol{\zeta}$, and $\boldsymbol{\gamma}$ are defined as

follows.

$$\boldsymbol{\alpha} = \frac{a}{2}\hat{x} \quad \boldsymbol{\zeta} = \frac{b}{2}\hat{y} \quad \boldsymbol{\gamma} = \frac{g}{2}\hat{z} \quad (2.47)$$

The real space fields are then given by:

$$D_x(\mathbf{r}) \approx \frac{H_z(\mathbf{r} + \boldsymbol{\zeta}) - H_z(\mathbf{r} - \boldsymbol{\zeta})}{ib\omega} - \frac{H_y(\mathbf{r} + \boldsymbol{\gamma}) - H_y(\mathbf{r} - \boldsymbol{\gamma})}{ig\omega} \quad (2.48)$$

$$D_y(\mathbf{r}) \approx \frac{H_x(\mathbf{r} + \boldsymbol{\gamma}) - H_x(\mathbf{r} - \boldsymbol{\gamma})}{ig\omega} - \frac{H_z(\mathbf{r} + \boldsymbol{\alpha}) - H_z(\mathbf{r} - \boldsymbol{\alpha})}{ia\omega} \quad (2.49)$$

$$D_z(\mathbf{r}) \approx \frac{H_y(\mathbf{r} + \boldsymbol{\alpha}) - H_y(\mathbf{r} - \boldsymbol{\alpha})}{ia\omega} - \frac{H_x(\mathbf{r} + \boldsymbol{\zeta}) - H_x(\mathbf{r} - \boldsymbol{\zeta})}{ib\omega} \quad (2.50)$$

$$B_x(\mathbf{r}) \approx -\frac{E_z(\mathbf{r} + \boldsymbol{\zeta}) - E_z(\mathbf{r} - \boldsymbol{\zeta})}{ib\omega} + \frac{E_y(\mathbf{r} + \boldsymbol{\gamma}) - E_y(\mathbf{r} - \boldsymbol{\gamma})}{ig\omega} \quad (2.51)$$

$$B_y(\mathbf{r}) \approx -\frac{E_x(\mathbf{r} + \boldsymbol{\gamma}) - E_x(\mathbf{r} - \boldsymbol{\gamma})}{ig\omega} + \frac{E_z(\mathbf{r} + \boldsymbol{\alpha}) - E_z(\mathbf{r} - \boldsymbol{\alpha})}{ia\omega} \quad (2.52)$$

$$B_z(\mathbf{r}) \approx -\frac{E_y(\mathbf{r} + \boldsymbol{\alpha}) - E_y(\mathbf{r} - \boldsymbol{\alpha})}{ia\omega} + \frac{E_x(\mathbf{r} + \boldsymbol{\zeta}) - E_x(\mathbf{r} - \boldsymbol{\zeta})}{ib\omega} \quad (2.53)$$

The constitutive equations 2.29 and 2.30 are used to eliminate the \mathbf{D} and \mathbf{B} fields to yield:

$$E_x(\mathbf{r}) \approx \frac{H_z(\mathbf{r} + \boldsymbol{\zeta}) - H_z(\mathbf{r} - \boldsymbol{\zeta})}{ib\omega\epsilon(\mathbf{r})} - \frac{H_y(\mathbf{r} + \boldsymbol{\gamma}) - H_y(\mathbf{r} - \boldsymbol{\gamma})}{ig\omega\epsilon(\mathbf{r})} \quad (2.54)$$

$$E_y(\mathbf{r}) \approx \frac{H_x(\mathbf{r} + \boldsymbol{\gamma}) - H_x(\mathbf{r} - \boldsymbol{\gamma})}{ig\omega\epsilon(\mathbf{r})} - \frac{H_z(\mathbf{r} + \boldsymbol{\alpha}) - H_z(\mathbf{r} - \boldsymbol{\alpha})}{ia\omega\epsilon(\mathbf{r})} \quad (2.55)$$

$$E_z(\mathbf{r}) \approx \frac{H_y(\mathbf{r} + \boldsymbol{\alpha}) - H_y(\mathbf{r} - \boldsymbol{\alpha})}{ia\omega\epsilon(\mathbf{r})} - \frac{H_x(\mathbf{r} + \boldsymbol{\zeta}) - H_x(\mathbf{r} - \boldsymbol{\zeta})}{ib\omega\epsilon(\mathbf{r})} \quad (2.56)$$

$$H_x(\mathbf{r}) \approx -\frac{E_z(\mathbf{r} + \boldsymbol{\zeta}) - E_z(\mathbf{r} - \boldsymbol{\zeta})}{ib\omega\mu(\mathbf{r})} + \frac{E_y(\mathbf{r} + \boldsymbol{\gamma}) - E_y(\mathbf{r} - \boldsymbol{\gamma})}{ig\omega\mu(\mathbf{r})} \quad (2.57)$$

$$H_y(\mathbf{r}) \approx -\frac{E_x(\mathbf{r} + \boldsymbol{\gamma}) - E_x(\mathbf{r} - \boldsymbol{\gamma})}{ig\omega\mu(\mathbf{r})} + \frac{E_z(\mathbf{r} + \boldsymbol{\alpha}) - E_z(\mathbf{r} - \boldsymbol{\alpha})}{ia\omega\mu(\mathbf{r})} \quad (2.58)$$

$$H_z(\mathbf{r}) \approx -\frac{E_y(\mathbf{r} + \boldsymbol{\alpha}) - E_y(\mathbf{r} - \boldsymbol{\alpha})}{ia\omega\mu(\mathbf{r})} + \frac{E_x(\mathbf{r} + \boldsymbol{\zeta}) - E_x(\mathbf{r} - \boldsymbol{\zeta})}{ib\omega\mu(\mathbf{r})} \quad (2.59)$$

Finally, the z-component of the fields are eliminated, terms containing $\mathbf{r} \pm \boldsymbol{\gamma}$ collected on the left-hand side, and the substitutions:

$$\mathbf{H}' = i\mathbf{H}/g\epsilon_0\omega \quad (2.60)$$

$$c = 1/\sqrt{\epsilon_0\mu_0} \quad (2.61)$$

$$\epsilon' = \epsilon/\epsilon_0 \quad (2.62)$$

$$\mu' = \mu/\mu_0 \quad (2.63)$$

are made, where c is the speed of light in vacuum. The substitutions are made in order to make the equations for the \mathbf{E} and \mathbf{H} fields look similar. The result is the following set of four equations:

$$\begin{aligned} E_x(\mathbf{r} + \boldsymbol{\gamma}) \approx & E_x(\mathbf{r} - \boldsymbol{\gamma}) + \frac{g^2\omega^2}{c^2}\mu'(\mathbf{r})H'_y(\mathbf{r}) + \frac{g^2}{a}\{ \\ & -\frac{H'_x(\mathbf{r} + \boldsymbol{\alpha} + \boldsymbol{\zeta}) - H'_x(\mathbf{r} + \boldsymbol{\alpha} - \boldsymbol{\zeta})}{\epsilon'(\mathbf{r} + \boldsymbol{\alpha})b} + \frac{H'_x(\mathbf{r} - \boldsymbol{\alpha} + \boldsymbol{\zeta}) - H'_x(\mathbf{r} - \boldsymbol{\alpha} - \boldsymbol{\zeta})}{\epsilon'(\mathbf{r} - \boldsymbol{\alpha})b} \\ & -\frac{H'_y(\mathbf{r}) - H'_y(\mathbf{r} - 2\boldsymbol{\alpha})}{\epsilon'(\mathbf{r} - \boldsymbol{\alpha})a} + \frac{H'_y(\mathbf{r} + 2\boldsymbol{\alpha}) - H'_y(\mathbf{r})}{\epsilon'(\mathbf{r} + \boldsymbol{\alpha})a} \} \end{aligned} \quad (2.64)$$

$$\begin{aligned} E_y(\mathbf{r} + \boldsymbol{\gamma}) \approx & E_y(\mathbf{r} - \boldsymbol{\gamma}) - \frac{g^2\omega^2}{c^2}\mu'(\mathbf{r})H'_x(\mathbf{r}) + \frac{g^2}{b}\{ \\ & +\frac{H'_y(\mathbf{r} + \boldsymbol{\alpha} + \boldsymbol{\zeta}) - H'_y(\mathbf{r} - \boldsymbol{\alpha} + \boldsymbol{\zeta})}{\epsilon'(\mathbf{r} + \boldsymbol{\zeta})a} - \frac{H'_y(\mathbf{r} + \boldsymbol{\alpha} - \boldsymbol{\zeta}) - H'_y(\mathbf{r} - \boldsymbol{\alpha} - \boldsymbol{\zeta})}{\epsilon'(\mathbf{r} - \boldsymbol{\zeta})a} \\ & +\frac{H'_x(\mathbf{r}) - H'_x(\mathbf{r} - 2\boldsymbol{\zeta})}{\epsilon'(\mathbf{r} - \boldsymbol{\zeta})b} - \frac{H'_x(\mathbf{r} + 2\boldsymbol{\zeta}) - H'_x(\mathbf{r})}{\epsilon'(\mathbf{r} + \boldsymbol{\zeta})b} \} \end{aligned} \quad (2.65)$$

$$\begin{aligned} H'_x(\mathbf{r} + \boldsymbol{\gamma}) \approx & H'_x(\mathbf{r} - \boldsymbol{\gamma}) + \epsilon'(\mathbf{r})E_y(\mathbf{r}) + \frac{c^2}{a\omega^2}\{ \\ & -\frac{E_x(\mathbf{r} + \boldsymbol{\alpha} + \boldsymbol{\zeta}) - E_x(\mathbf{r} + \boldsymbol{\alpha} - \boldsymbol{\zeta})}{\mu'(\mathbf{r} + \boldsymbol{\alpha})b} + \frac{E_x(\mathbf{r} - \boldsymbol{\alpha} + \boldsymbol{\zeta}) - E_x(\mathbf{r} - \boldsymbol{\alpha} - \boldsymbol{\zeta})}{\mu'(\mathbf{r} - \boldsymbol{\alpha})b} \\ & -\frac{E_y(\mathbf{r}) - E_y(\mathbf{r} - 2\boldsymbol{\alpha})}{\mu'(\mathbf{r} - \boldsymbol{\alpha})a} + \frac{E_y(\mathbf{r} + 2\boldsymbol{\alpha}) - E_y(\mathbf{r})}{\mu'(\mathbf{r} + \boldsymbol{\alpha})a} \} \end{aligned} \quad (2.66)$$

$$\begin{aligned} H'_y(\mathbf{r} + \boldsymbol{\gamma}) \approx & H'_y(\mathbf{r} - \boldsymbol{\gamma}) - \epsilon'(\mathbf{r})E'_x(\mathbf{r}) + \frac{c^2}{b\omega^2}\{ \\ & +\frac{E'_y(\mathbf{r} + \boldsymbol{\alpha} + \boldsymbol{\zeta}) - E'_y(\mathbf{r} - \boldsymbol{\alpha} + \boldsymbol{\zeta})}{\mu'(\mathbf{r} + \boldsymbol{\zeta})a} - \frac{E'_y(\mathbf{r} + \boldsymbol{\alpha} - \boldsymbol{\zeta}) - E'_y(\mathbf{r} - \boldsymbol{\alpha} - \boldsymbol{\zeta})}{\mu'(\mathbf{r} - \boldsymbol{\zeta})a} \\ & +\frac{E'_x(\mathbf{r}) - E'_x(\mathbf{r} - 2\boldsymbol{\zeta})}{\mu'(\mathbf{r} - \boldsymbol{\zeta})b} - \frac{E'_x(\mathbf{r} + 2\boldsymbol{\zeta}) - E'_x(\mathbf{r})}{\mu'(\mathbf{r} + \boldsymbol{\zeta})b} \} \end{aligned} \quad (2.67)$$

Given the values of the \mathbf{E} and \mathbf{H}' fields on a discrete mesh on two adjacent planes separated from one another by a distance $\gamma = g/2$ in the z direction, these equations provide for the calculation of the \mathbf{E} and \mathbf{H}' fields on a discrete mesh on two more such planes translated in the z direction by an amount g from the original planes. It applies when the spatial variation of the scalar dielectric constant is accurately described by the discrete mesh as determined by a , b , and g . In other words, this allows us to “integrate” the fields forward or backward through a given distance in the z direction in steps of g given the values of the \mathbf{E} and \mathbf{H}' fields on one pair of planes. If these planes are aligned parallel with the slab of textured material depicted in Figure 2.1, that is, the coordinate system is aligned so that \hat{z} points in the direction perpendicular to the slab, then repeated application of these equations allows us to integrate Maxwell’s equations through a textured layer. The situation is illustrated in Figure 2.2 for the case of a square photonic crystal.

Specifically, to integrate the fields forward, one begins with $\mathbf{E}(\mathbf{r}' - \gamma)$, and $\mathbf{H}'(\mathbf{r}')$, and uses equations 2.64 and 2.65 which manifestly gives the expression for $\mathbf{E}(\mathbf{r}' + \gamma)$. One then calculates $\mathbf{H}'(\mathbf{r}' + 2\gamma)$ from $\mathbf{E}(\mathbf{r}' + \gamma)$ and $\mathbf{H}'(\mathbf{r}')$ according to equations 2.66 and 2.67 making the substitution $\mathbf{r} = \mathbf{r}' + \gamma$.

It is important to note that the order in which the \mathbf{E} or \mathbf{H}' fields must be calculated is crucial and depends on the direction of integration for a given initial ordering of the \mathbf{E} and \mathbf{H}' planes. For example, in the above case, it would be impossible to calculate the \mathbf{H}' field since the value of $\mathbf{H}'(\mathbf{r}' - \gamma)$ is not known.

In order to integrate the fields backward one begins with the initially specified values $\mathbf{E}(\mathbf{r}')$, $\mathbf{H}'(\mathbf{r}' + \gamma)$, and uses equations 2.66 and 2.67 to calculate $\mathbf{H}'(\mathbf{r}' - \gamma)$. Then one calculates $\mathbf{E}(\mathbf{r}' - 2\gamma)$ from $\mathbf{E}(\mathbf{r}')$ and $\mathbf{H}'(\mathbf{r}' - \gamma)$ according to equations 2.64 and 2.65, making the substitution $\mathbf{r} = \mathbf{r}' - \gamma$.

The above expressions for the fields may be recast as a transfer matrix, \overleftrightarrow{M} , that

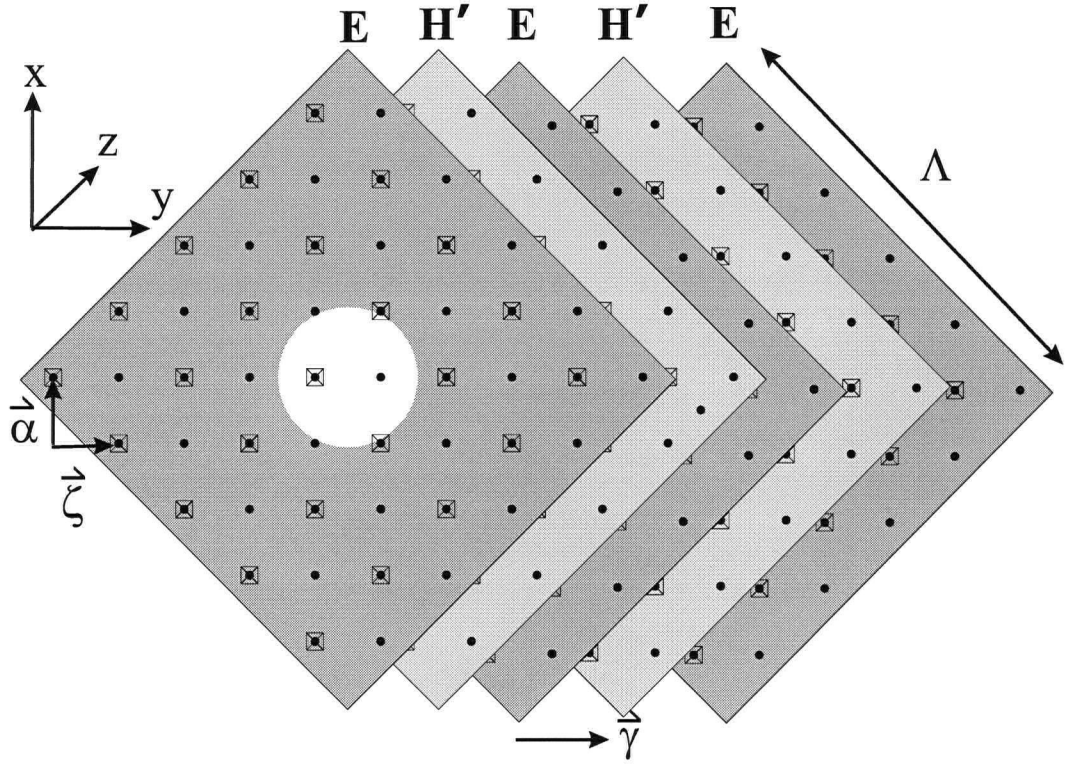


Figure 2.2: Discrete in-plane ($x-y$) lattice on which \mathbf{E} and \mathbf{H}' fields are computed on a series of planes separated by $g/2 = \gamma$. The dielectric constant is sampled on the lattice indicated by the black dots. The fields are calculated on the sublattice indicated by the crossed squares. The planes shown span a unit cell of the periodicity in the in-plane direction. The light and dark grey shading of the planes indicates whether the \mathbf{E} or \mathbf{H}' fields are computed there. The white hole in the center schematically depicts dielectric texture comprised of a circular airhole.

relates the fields on one pair of planes to the fields on a subsequent pair of planes.

$$\begin{bmatrix} \begin{bmatrix} E_x(\boldsymbol{\varrho}_{1,1}; z - \gamma) \\ E_y(\boldsymbol{\varrho}_{1,1}; z - \gamma) \\ H'_x(\boldsymbol{\varrho}_{1,1}; z) \\ H'_y(\boldsymbol{\varrho}_{1,1}; z) \\ \vdots \\ E_x(\boldsymbol{\varrho}_{N,N}; z - \gamma) \\ E_y(\boldsymbol{\varrho}_{N,N}; z - \gamma) \\ H'_x(\boldsymbol{\varrho}_{N,N}; z) \\ H'_y(\boldsymbol{\varrho}_{N,N}; z) \end{bmatrix} \\ \begin{bmatrix} E_x(\boldsymbol{\varrho}_{1,1}; z + \gamma) \\ E_y(\boldsymbol{\varrho}_{1,1}; z + \gamma) \\ H'_x(\boldsymbol{\varrho}_{1,1}; z + 2\gamma) \\ H'_y(\boldsymbol{\varrho}_{1,1}; z + 2\gamma) \\ \vdots \\ E_x(\boldsymbol{\varrho}_{N,N}; z + \gamma) \\ E_y(\boldsymbol{\varrho}_{N,N}; z + \gamma) \\ H'_x(\boldsymbol{\varrho}_{N,N}; z + 2\gamma) \\ H'_y(\boldsymbol{\varrho}_{N,N}; z + 2\gamma) \end{bmatrix} \end{bmatrix} = \overleftrightarrow{M} \begin{bmatrix} \begin{bmatrix} E_x(\boldsymbol{\varrho}_{1,1}; z + \gamma) \\ E_y(\boldsymbol{\varrho}_{1,1}; z + \gamma) \\ H'_x(\boldsymbol{\varrho}_{1,1}; z + 2\gamma) \\ H'_y(\boldsymbol{\varrho}_{1,1}; z + 2\gamma) \\ \vdots \\ E_x(\boldsymbol{\varrho}_{N,N}; z + \gamma) \\ E_y(\boldsymbol{\varrho}_{N,N}; z + \gamma) \\ H'_x(\boldsymbol{\varrho}_{N,N}; z + 2\gamma) \\ H'_y(\boldsymbol{\varrho}_{N,N}; z + 2\gamma) \end{bmatrix} \\ \begin{bmatrix} E_x(\boldsymbol{\varrho}_{1,1}; z - \gamma) \\ E_y(\boldsymbol{\varrho}_{1,1}; z - \gamma) \\ H'_x(\boldsymbol{\varrho}_{1,1}; z) \\ H'_y(\boldsymbol{\varrho}_{1,1}; z) \\ \vdots \\ E_x(\boldsymbol{\varrho}_{N,N}; z - \gamma) \\ E_y(\boldsymbol{\varrho}_{N,N}; z - \gamma) \\ H'_x(\boldsymbol{\varrho}_{N,N}; z) \\ H'_y(\boldsymbol{\varrho}_{N,N}; z) \end{bmatrix} \end{bmatrix} \quad (2.68)$$

where \overleftrightarrow{M} is a $4N^2 \times 4N^2$ matrix, and $\boldsymbol{\varrho}_{i,j}$ are the N^2 2D (in-plane) lattice vectors of the discrete *mesh* on which the fields are evaluated. Note that, in principle, the matrix \overleftrightarrow{M} may be dependent on z . Referring to Figure 2.2, the $\boldsymbol{\varrho}_{i,j}$ are depicted by the crossed squares, and taking the centre of the hole as the origin, they may be defined explicitly as:

$$\boldsymbol{\varrho}_{i,j} = (N - \frac{1}{2})\boldsymbol{\zeta} + (i - 1)(\boldsymbol{\zeta} + \boldsymbol{\alpha}) + (j - 1)(\boldsymbol{\zeta} - \boldsymbol{\alpha}) \quad i, j = 1 \dots N \quad (2.69)$$

2.2.3 Eigenmodes on a Discrete Mesh

In order to compute the matrices T^{++} , T^{-+} , T^{+-} a basis set of $4N^2$ -vectors is chosen in regions I and III. Each one of these is integrated through the textured layer and projected onto each of the basis vectors on the other side. More specifically, to construct the matrices T^{++} , T^{-+} the basis vectors that represent right-going plane waves in region III are integrated separately back through the textured layer using equations 2.64 - 2.67, and the resulting $4N^2$ -vector is projected onto each of the basis vectors in region I. Similarly, to construct the matrices T^{--} , T^{+-} the basis vectors that represent left-going plane waves in region I are integrated forward through the textured layer using equations

2.64 - 2.67 and the resulting $4N^2$ -vector is projected onto each of the basis vectors in region III.

While one might be tempted to use the basis vectors defined in equations 2.5 to 2.8, which are polarized plane waves, these are not, in fact, eigenvectors of the *discretized* version of Maxwell's equations applied to a uniform medium with $\epsilon' = \epsilon'_{I/III}$.

Formally, in order to construct a basis set of the eigenvectors of the discretized Maxwell's equations in regions I and III one must use the set of eigenvectors of the matrix \overleftrightarrow{M} in equation 2.68, defined by the equations 2.64 - 2.67, where the spatially constant value of ϵ'_I or ϵ'_{III} is used in equations 2.64 - 2.67.

Unfortunately, the matrix \overleftrightarrow{M} is not Hermitean. This means that its right eigenvectors, defined by:

$$\overleftrightarrow{M} \mathbf{v}^{(i)} = \lambda^{(i)} \mathbf{v}^{(i)} \quad (2.70)$$

and its left eigenvectors, defined by:

$$\mathbf{u}^{(i)H} \overleftrightarrow{M} = \lambda^{(i)} \mathbf{u}^{(i)H} \quad (2.71)$$

where the superscript H denotes the Hermitean conjugate, are not the same, and neither set is orthogonal. That is:

$$\mathbf{v}^{(i)H} \mathbf{v}^{(j)} \neq \delta_{i,j} \quad (2.72)$$

$$\mathbf{u}^{(i)H} \mathbf{u}^{(j)} \neq \delta_{i,j} \quad (2.73)$$

This nominally presents a problem when performing the projection operations. However, it is trivial to show that

$$\mathbf{u}^{(i)H} \mathbf{v}^{(j)} = \delta_{i,j} \quad (2.74)$$

and, therefore, the projection of an arbitrary $4N^2$ -vector, \mathbf{a} , *e.g.*, a wavefield integrated through the textured region, onto the basis of right eigenvectors is given by

$$\mathbf{a} = \sum_{j=1}^{4N^2} \eta_j \mathbf{v}^{(j)} \quad (2.75)$$

where

$$\eta_j = \mathbf{u}^{(j)H} \mathbf{a} \quad (2.76)$$

Thus, each right eigenvector, for which we seek an expansion coefficient, has a unique left eigenvector that can be used in equation 2.76 to find that expansion coefficient. Note that right and left eigenvectors have no correlation with right and left going plane waves. Both right and left going plane waves are right eigenvectors of the transfer matrix when there is no dielectric variation, and together constitute a complete basis. However, because these right eigenvectors are not orthogonal, the corresponding left eigenvectors are needed to efficiently carry out the expansion of an arbitrary vector in terms of the basis of plane waves.

Pendry [18] has shown that, to a good approximation, the right eigenvectors of \overleftrightarrow{M} in a uniform medium are given by the 2D in-plane Discrete Fourier Transform (DFT) of s and p polarized plane waves described in Fourier space as in equations 2.13 to 2.16, where $\boldsymbol{\kappa}$, the approximation made for \mathbf{k} in deriving the transfer matrix equations, is substituted for \mathbf{k} . That is, the right eigenvectors may be constructed as follows. First we define the two 3-vectors representing the Discrete Fourier Transform of the discretely sampled fields.

$$\tilde{\mathbf{E}}^{(s,\pm,I/III)}(\mathbf{G}_{l,m}) = \hat{\mathbf{n}} \times \boldsymbol{\kappa}_{l,m;\pm}^{I/III} \quad (2.77)$$

$$\tilde{\mathbf{H}}^{(s,\pm,I/III)}(\mathbf{G}_{l,m}) = \boldsymbol{\kappa}_{l,m;\pm}^{I/III} \times \tilde{\mathbf{E}}^{(s,\pm,I/III)}(\mathbf{G}_{l,m}) \quad (2.78)$$

$$\tilde{\mathbf{H}}^{(p,\pm,I/III)}(\mathbf{G}_{l,m}) = \hat{\mathbf{n}} \times \boldsymbol{\kappa}_{l,m;\pm}^{I/III} \quad (2.79)$$

$$\tilde{\mathbf{E}}^{(p,\pm,I/III)}(\mathbf{G}_{l,m}) = \boldsymbol{\kappa}_{l,m;\pm}^{I/III} \times \tilde{\mathbf{H}}^{(p,\pm,I/III)}(\mathbf{G}_{l,m}) \quad (2.80)$$

where the s or p superscript denotes the polarization of the plane wave, the I/III superscripts denote the region in which the plane wave is being defined (see figure 2.1), the \pm subscripts denote whether it is right-going or left-going, and the l, m subscripts label the reciprocal lattice vector.

To construct the $\kappa_{l,m;\pm}^{I/III}$ we begin with

$$k_x = (\mathbf{G}_{l,m} + \boldsymbol{\beta}) \cdot \hat{\mathbf{x}}; \quad k_y = (\mathbf{G}_{l,m} + \boldsymbol{\beta}) \cdot \hat{\mathbf{y}} \quad (2.81)$$

and use equations 2.33 and 2.34 to obtain the x and y components of $\kappa_{l,m;\pm}^{I/III}$. We then use the dispersion relation to solve for the two values of k_z corresponding to the right- and left-going waves, using $\epsilon'_{I/III}$ as appropriate for the particular region. Finally, for each such value of k_z , we use equation 2.35 to obtain the corresponding two values of the z -components of $\kappa_{l,m;\pm}^{I/III}$.

However, the dispersion relation that must be used is not precisely that for actual plane waves in a homogeneous medium given by equation 2.3. Rather, it is modified such that κ is again substituted for \mathbf{k} , as in the definition of the polarized basis set of plane waves itself (equations 2.13 – 2.16). This new dispersion relation is given by:

$$\omega^2 \mu_0 \epsilon_0 \epsilon'_{I/III} = \kappa^H \kappa = \frac{2}{a^2} [1 - \cos k_x a] + \frac{2}{b^2} [1 - \cos k_y b] + \frac{2}{g^2} [1 - \cos k_z g] \quad (2.82)$$

Explicitly, the two (\pm) solutions for k_z in each region (I/III) and for each reciprocal lattice vector $\mathbf{G}_{l,m}$ are given by:

$$\begin{aligned} k_z^{l,m,\pm,I/III} = & \pm \cos^{-1} \left\{ 1 - \frac{g^2}{2} \omega^2 \mu_0 \epsilon_0 \epsilon'_{I/III} \right. \\ & \left. + \frac{g^2}{a^2} [1 - \cos(a[\mathbf{G}_{l,m} + \boldsymbol{\beta}] \cdot \hat{\mathbf{x}})] + \frac{g^2}{b^2} [1 - \cos(b[\mathbf{G}_{l,m} + \boldsymbol{\beta}] \cdot \hat{\mathbf{y}})] \right\} \end{aligned} \quad (2.83)$$

Notice that we have dropped the normalization constants present in equations 2.13 – 2.16 since they are superfluous for vectors to be used as a basis set in subsequent calculations in which they cancel out. Consequently, the units of electric field here are the same as those for \mathbf{k} . Finally, notice that equations 2.77 – 2.80 refer to the reduced magnetic field, \mathbf{H}' , defined by equation 2.60, which is relevant to the transfer matrix defined by equations 2.64 – 2.67 and has the same units as electric field.

The \mathbf{E} and \mathbf{H}' fields are then grouped together and their z -components dropped to form the “right” 4-vectors:

$$\begin{bmatrix} \widetilde{\mathbf{E}}_x^{(s/p,\pm,I/III)}(\mathbf{G}_{l,m}) \\ \widetilde{\mathbf{E}}_y^{(s/p,\pm,I/III)}(\mathbf{G}_{l,m}) \\ \widetilde{\mathbf{H}}'_x^{(s/p,\pm,I/III)}(\mathbf{G}_{l,m}) \\ \widetilde{\mathbf{H}}'_y^{(s/p,\pm,I/III)}(\mathbf{G}_{l,m}) \end{bmatrix}^R \quad (2.84)$$

The real-space right eigenvectors are then obtained by projecting these onto the mesh points:

$$\begin{bmatrix} \begin{bmatrix} E_x(\boldsymbol{\varrho}_{1,1}; z_0) \\ E_y(\boldsymbol{\varrho}_{1,1}; z_0) \\ H'_x(\boldsymbol{\varrho}_{1,1}; z_0) \\ H'_y(\boldsymbol{\varrho}_{1,1}; z_0) \\ \vdots \end{bmatrix} \\ \begin{bmatrix} E_x(\boldsymbol{\varrho}_{j,n}; z_0) \\ E_y(\boldsymbol{\varrho}_{j,n}; z_0) \\ H'_x(\boldsymbol{\varrho}_{j,n}; z_0) \\ H'_y(\boldsymbol{\varrho}_{j,n}; z_0) \\ \vdots \end{bmatrix} \\ \begin{bmatrix} E_x(\boldsymbol{\varrho}_{N,N}; z_0) \\ E_y(\boldsymbol{\varrho}_{N,N}; z_0) \\ H'_x(\boldsymbol{\varrho}_{N,N}; z_0) \\ H'_y(\boldsymbol{\varrho}_{N,N}; z_0) \end{bmatrix} \end{bmatrix}^{R,I/III} = \begin{bmatrix} \begin{bmatrix} \widetilde{\mathbf{E}}_x^{(s/p,\pm,I/III)}(\mathbf{G}_{l,m}) \\ \widetilde{\mathbf{E}}_y^{(s/p,\pm,I/III)}(\mathbf{G}_{l,m}) \\ \widetilde{\mathbf{H}}'_x^{(s/p,\pm,I/III)}(\mathbf{G}_{l,m}) \\ \widetilde{\mathbf{H}}'_y^{(s/p,\pm,I/III)}(\mathbf{G}_{l,m}) \\ \vdots \end{bmatrix}^R \\ \begin{bmatrix} \widetilde{\mathbf{E}}_x^{(s/p,\pm,I/III)}(\mathbf{G}_{l,m}) \\ \widetilde{\mathbf{E}}_y^{(s/p,\pm,I/III)}(\mathbf{G}_{l,m}) \\ \widetilde{\mathbf{H}}'_x^{(s/p,\pm,I/III)}(\mathbf{G}_{l,m}) \\ \widetilde{\mathbf{H}}'_y^{(s/p,\pm,I/III)}(\mathbf{G}_{l,m}) \\ \vdots \end{bmatrix}^R \\ \begin{bmatrix} \widetilde{\mathbf{E}}_x^{(s/p,\pm,I/III)}(\mathbf{G}_{l,m}) \\ \widetilde{\mathbf{E}}_y^{(s/p,\pm,I/III)}(\mathbf{G}_{l,m}) \\ \widetilde{\mathbf{H}}'_x^{(s/p,\pm,I/III)}(\mathbf{G}_{l,m}) \\ \widetilde{\mathbf{H}}'_y^{(s/p,\pm,I/III)}(\mathbf{G}_{l,m}) \end{bmatrix}^R \end{bmatrix} \begin{matrix} e^{(i[\boldsymbol{\beta}+\mathbf{G}_{l,m}]\cdot\boldsymbol{\varrho}_{1,1})} \\ e^{(i[\boldsymbol{\beta}+\mathbf{G}_{l,m}]\cdot\boldsymbol{\varrho}_{j,n})} \\ e^{(i[\boldsymbol{\beta}+\mathbf{G}_{l,m}]\cdot\boldsymbol{\varrho}_{N,N})} \end{matrix} \quad (2.85)$$

$(\mathbf{G}_{l,m}, s/p, \pm)$

The corresponding left eigenvectors are also shown by Pendry to be constructed by

forming the “left” 4-vectors from the “right” 4-vectors according to:

$$\begin{bmatrix} \widetilde{\mathbf{E}}_x^{(s/p, \pm, I/III)}(\mathbf{G}_{l,m}) \\ \widetilde{\mathbf{E}}_y^{(s/p, \pm, I/III)}(\mathbf{G}_{l,m}) \\ \widetilde{\mathbf{H}}_x^{(s/p, \pm, I/III)}(\mathbf{G}_{l,m}) \\ \widetilde{\mathbf{H}}_y^{(s/p, \pm, I/III)}(\mathbf{G}_{l,m}) \end{bmatrix}^L = \begin{bmatrix} 0 & -1 & 0 & 0 \\ 1 & 0 & 0 & 0 \\ 0 & 0 & 0 & \frac{g^2\omega^2}{c^2\epsilon'_{I/III}} \\ 0 & 0 & -\frac{g^2\omega^2}{c^2\epsilon'_{I/III}} & 0 \end{bmatrix} \begin{bmatrix} \widetilde{\mathbf{E}}_x^{(p/s, \pm, I/III)}(\mathbf{G}_{l,m}) \\ \widetilde{\mathbf{E}}_y^{(p/s, \pm, I/III)}(\mathbf{G}_{l,m}) \\ \widetilde{\mathbf{H}}_x^{(p/s, \pm, I/III)}(\mathbf{G}_{l,m}) \\ \widetilde{\mathbf{H}}_y^{(p/s, \pm, I/III)}(\mathbf{G}_{l,m}) \end{bmatrix}^R \quad (2.86)$$

(notice the swapping of s and p subscripts).

The real space left eigenvectors may then be constructed in the same manner as in equation 2.85.

2.2.4 Significance of Using Pendry Modes

If we consider a uniform medium so that $\mathbf{D} = \epsilon_{\text{uni}}\mathbf{E}$ and $\mathbf{B} = \mu_0\mathbf{H}$, assume harmonically time-varying fields, and drop the time varying exponential, $e^{-i\omega t}$, from both sides of equations 2.25 and 2.26, they become :

$$\nabla \times \mathbf{E}(\mathbf{r}) = i\omega\mu_0\mathbf{H}(\mathbf{r}) \quad (2.87)$$

$$\nabla \times \mathbf{H}(\mathbf{r}) = -i\omega\epsilon_{\text{uni}}\mathbf{E}(\mathbf{r}) \quad (2.88)$$

Without making any approximations, we may again proceed as in section 2.2.2, carry out the curls, and eliminate the z -components of the fields to produce an equation, for example, for the E_y field:

$$\frac{\partial E_y(\mathbf{r})}{\partial z} = -i\mu H(\mathbf{r}) + \frac{i}{\epsilon_{\text{uni}}\omega} \left\{ \frac{\partial^2}{\partial y \partial x} H_y(\mathbf{r}) - \frac{\partial^2}{\partial y^2} H_x(\mathbf{r}) \right\} \quad (2.89)$$

For an s polarized plane wave it is a simple matter to show that the difference term in the curly braces in equation 2.89 is identically zero. This is because:

$$H_x^{(s)}(x, y, z) = \widetilde{H}_x^{(s)} e^{ik_x x} e^{ik_y y} e^{ik_z z} \quad (2.90)$$

$$H_y^{(s)}(x, y, z) = \widetilde{H}_y^{(s)} e^{ik_x x} e^{ik_y y} e^{ik_z z} \quad (2.91)$$

so that

$$\left\{ \frac{\partial^2}{\partial y \partial x} H_y(\mathbf{r}) - \frac{\partial^2}{\partial y^2} H_x(\mathbf{r}) \right\} = -k_y e^{ik_x x} e^{ik_y y} e^{ik_z z} [k_x \tilde{H}_y^{(s)} - k_y \tilde{H}_x^{(s)}] \quad (2.92)$$

but since from equations 2.5 - 2.8 we have

$$\tilde{H}_x^{(s)} = k_z k_x \quad (2.93)$$

$$\tilde{H}_y^{(s)} = k_z k_y \quad (2.94)$$

it follows that $\left\{ \frac{\partial^2}{\partial y \partial x} H_y(\mathbf{r}) - \frac{\partial^2}{\partial y^2} H_x(\mathbf{r}) \right\} = 0$.

When Maxwell's equations are discretized through the procedure described in section 2.2.2, the analogous equation to equation 2.89 is obtained by rearranging equation 2.65 to yield the difference equation corresponding to the z -derivative:

$$E_y(\mathbf{r} + \boldsymbol{\gamma}) - E_y(\mathbf{r} - \boldsymbol{\gamma}) = -\frac{g^2 \omega^2}{c^2} \mu'(\mathbf{r}) H'_x(\mathbf{r}) + \frac{g^2}{b} \left\{ \quad (2.95)$$

$$\begin{aligned} & \frac{H'_y(\mathbf{r} + \boldsymbol{\alpha} + \boldsymbol{\zeta}) - H'_y(\mathbf{r} - \boldsymbol{\alpha} + \boldsymbol{\zeta})}{\epsilon'(\mathbf{r} + \boldsymbol{\zeta})a} - \frac{H'_y(\mathbf{r} + \boldsymbol{\alpha} - \boldsymbol{\zeta}) - H'_y(\mathbf{r} - \boldsymbol{\alpha} - \boldsymbol{\zeta})}{\epsilon'(\mathbf{r} - \boldsymbol{\zeta})a} \\ & \frac{H'_x(\mathbf{r}) - H'_x(\mathbf{r} - 2\boldsymbol{\zeta})}{\epsilon'(\mathbf{r} - \boldsymbol{\zeta})b} + \frac{H'_x(\mathbf{r} + 2\boldsymbol{\zeta}) - H'_x(\mathbf{r})}{\epsilon'(\mathbf{r} + \boldsymbol{\zeta})b} \left\} \quad (2.96) \end{aligned}$$

For a plane wave in a uniform medium the translated fields, *e.g.*, $H'_y(\mathbf{r} + \boldsymbol{\alpha} - \boldsymbol{\zeta})$ in equation 2.95 may be rewritten in terms of a phase factor multiplying an untranslated field. Assuming a square array of mesh points, *i.e.*, $a = b$, we obtain:

$$E_y(\mathbf{r} + \boldsymbol{\gamma}) - E_y(\mathbf{r} - \boldsymbol{\gamma}) = -\frac{g^2 \omega^2}{c^2} \mu'(\mathbf{r}) H'_x(\mathbf{r}) + \frac{g^2}{\epsilon'_{uni}} \left\{ \quad (2.97)$$

$$\begin{aligned} & [e^{ik_x \alpha} e^{ik_y \zeta} H'_y(\mathbf{r}) - e^{-ik_x \alpha} e^{ik_y \zeta} H'_y(\mathbf{r})] \\ & - [e^{ik_x \alpha} e^{-ik_y \zeta} H'_y(\mathbf{r}) - e^{-ik_x \alpha} e^{-ik_y \zeta} H'_y(\mathbf{r})] \\ & + [H'_x(\mathbf{r}) - e^{-2ik_y \zeta} H'_x(\mathbf{r})] \\ & + [H'_x(\mathbf{r}) - e^{2ik_y \zeta} H'_x(\mathbf{r})] \left\} \quad (2.98) \end{aligned}$$

The term in curly braces can be further simplified to yield

$$4 \sin(k_y \zeta) [H'_x(\mathbf{r}) \sin(k_y \zeta) - H'_y(\mathbf{r}) \sin(k_x \alpha)] \quad (2.99)$$

and making use of the fact that

$$H'_x(\mathbf{r}) = \kappa_z \kappa_x; H'_y(\mathbf{r}) = \kappa_z \kappa_y \quad (2.100)$$

the term in curly braces becomes:

$$4 \sin(k_y \zeta) \kappa_z \{ \kappa_x \sin(k_y \zeta) - \kappa_y \sin(k_x \alpha) \} \quad (2.101)$$

which, using equations 2.33 - 2.34, reduces to

$$4 \sin(k_y \zeta) \kappa_z \left\{ \frac{2 \sin(k_x \alpha)}{a} \sin(k_y \zeta) - \frac{2 \sin(k_y \zeta)}{a} \sin(k_x \alpha) \right\} = 0 \quad (2.102)$$

Therefore, the terms in curly braces in equation 2.95, which represent the discrete analog to the double partial derivative terms in curly braces in equation 2.89, cancel to yield identically zero as was shown for the exact continuous case.

Thus these “Pendry” modes will propagate as eigenmodes of the discretized integration scheme and will not mix into one another as they propagate.

It is important to note that had we used “true” plane waves, that is,

$$H'_x(\mathbf{r}) = k_z k_x; H'_y(\mathbf{r}) = k_z k_y \quad (2.103)$$

then we would have obtained

$$4 \sin(k_y \zeta) k_z \{ k_x \sin(k_y \zeta) - k_y \sin(k_x \alpha) \} \approx 0 \quad (2.104)$$

which is only approximately equal to zero to the extent that $k_x a, k_y b \ll 1$. This means that these fields are not eigenstates of the discretized integration operation, and so they are “mixed” as they are propagated by equations 2.64 - 2.67. The same also holds true for all similar terms in curly braces in equations 2.64, 2.66, and 2.67 for the x component of the \mathbf{E} field of an s polarized mode and for the x and y components of the \mathbf{H} field of a p polarized mode, respectively.

2.2.5 Computation of Reflection and Transmission Coefficients

In what follows, the algorithm for the construction of the matrices $(T^{++})^{-1}$, $T^{-+}(T^{++})^{-1}$, and hence T^{++} , T^{-+} , T^{--} , T^{+-} is described in detail for the case of a square photonic lattice. The method can be generalized to accommodate other types of photonic lattices, and an outline for how this may be done is presented in Appendix A.

Of course, only a finite number of plane waves are included in the calculation, with there being an equal number of s and p polarized plane waves as well as an equal number of right-going and left-going plane waves. Thus if $N \times N$ reciprocal lattice vectors are included in two-dimensions, the size of the T matrices that result is $2N^2 \times 2N^2$.

We note that equations 2.64–2.67 require evaluation of the fields at \mathbf{r} , $\mathbf{r} \pm (\boldsymbol{\alpha} \pm \boldsymbol{\zeta})$, $\mathbf{r} \pm 2\boldsymbol{\zeta}$, $\mathbf{r} \pm 2\boldsymbol{\alpha}$, as well as evaluation of ϵ' and μ' at \mathbf{r} , $\mathbf{r} \pm \boldsymbol{\zeta}$, and $\mathbf{r} \pm \boldsymbol{\alpha}$. The scheme of real-space lattice points and reciprocal lattice vectors used for the square lattice is depicted in Figures 2.3 and 2.4, respectively.

Given β_{inc} , the value of k_z is calculated from the dispersion relation, for each reciprocal lattice vector, $\mathbf{G}_{l,m}$, using equation 2.82 with the value of the dielectric constant on the right hand side of the structure, ϵ'_{III} . As previously mentioned, there will be two solutions for k_z , each of which will be either purely real or purely imaginary for the case of lossless dielectrics (purely real ϵ'). One solution is labelled as right-going or (+), and the other as left-going or (−) according to the sign of the real or imaginary part of k_z . For the case of real k_z corresponding to propagating waves, its sign corresponds to that of the group velocity; for imaginary k_z corresponding to evanescent fields, its sign determines whether the fields are growing or decaying in the positive z direction. The right-going solution is selected and κ calculated according to equations 2.33–2.35. Then, the right eigenvector for a particular polarization is calculated by using equations 2.77 to 2.80 and, dropping the z components, is used to form the 4-vectors as in equation 2.84. These “plane waves” are then projected onto the $N \times N$ real-space mesh points on the unit cell depicted in figure 2.3 according to

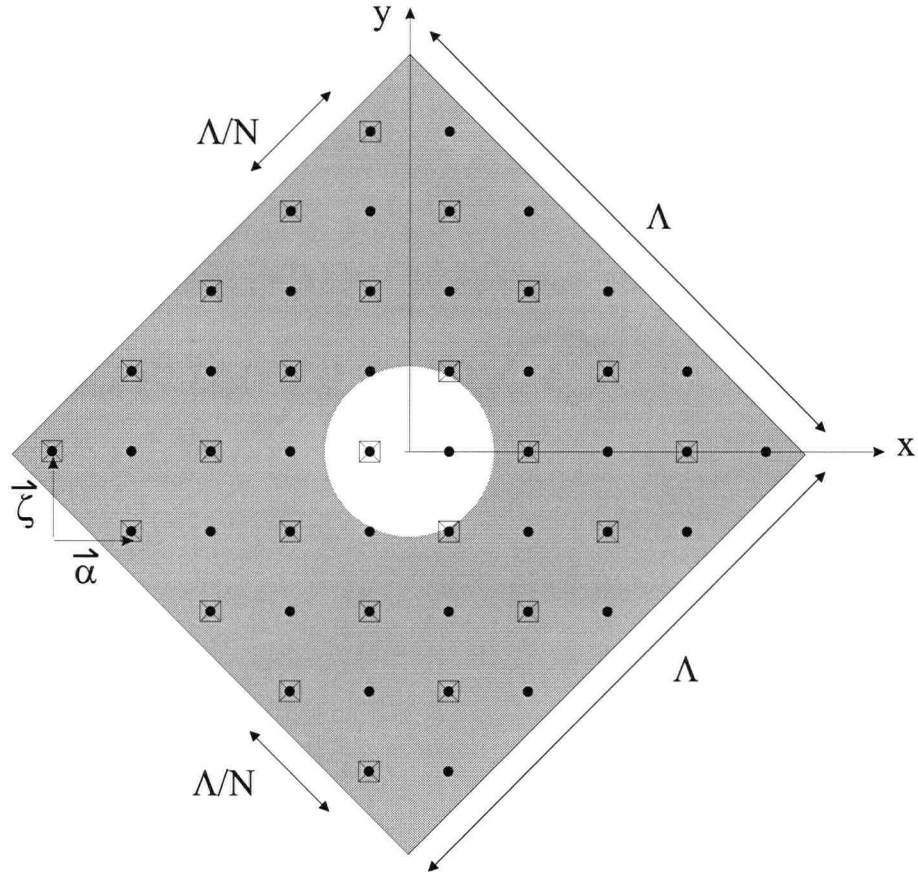


Figure 2.3: Scheme of real-space points on which the fields and dielectric constant are sampled on the unit cell. The dielectric constant is sampled at points represented by the black dots. The electric or magnetic fields are sampled only on those points with the crossed squares.

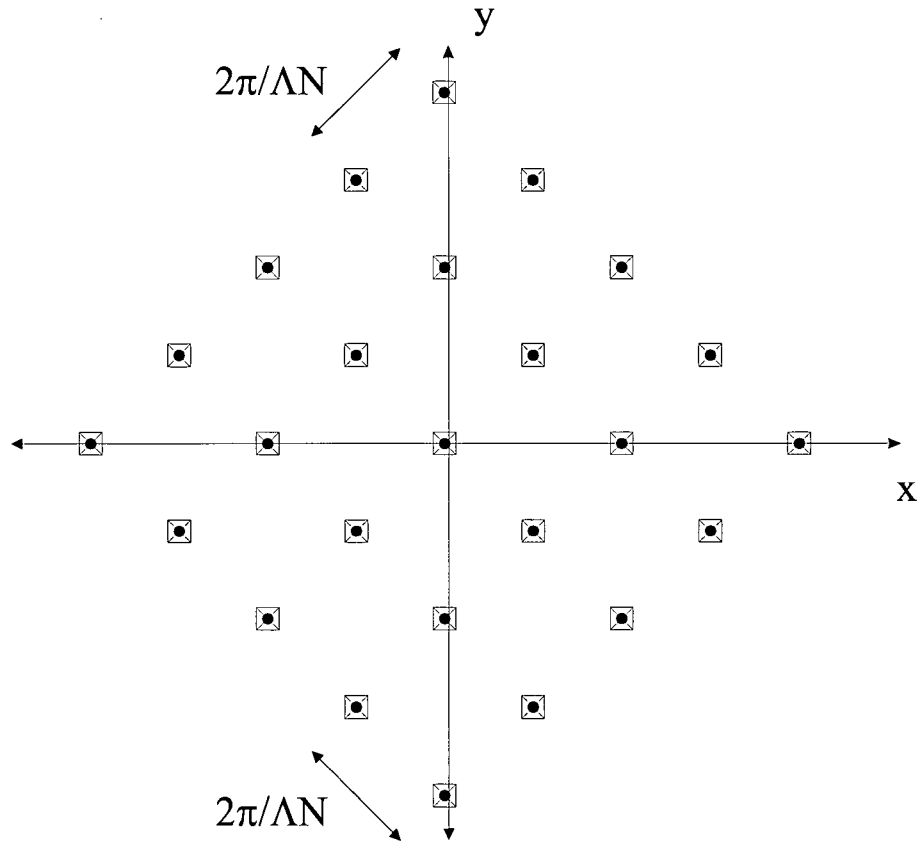


Figure 2.4: Scheme of reciprocal lattice vectors corresponding to in-plane wavevector of launched modes

$$\begin{aligned}
& \left[\begin{array}{c} \left[\begin{array}{c} E_x(\boldsymbol{\varrho}_{1,1}) \\ E_y(\boldsymbol{\varrho}_{1,1}) \\ H'_x(\boldsymbol{\varrho}_{1,1}) \\ H'_y(\boldsymbol{\varrho}_{1,1}) \end{array} \right]^{III} \\ \vdots \\ \left[\begin{array}{c} E_x(\boldsymbol{\varrho}_{j,l}) \\ E_y(\boldsymbol{\varrho}_{j,l}) \\ H'_x(\boldsymbol{\varrho}_{j,l}) \\ H'_y(\boldsymbol{\varrho}_{j,l}) \end{array} \right]^{III} \\ \vdots \\ \left[\begin{array}{c} E_x(\boldsymbol{\varrho}_{N,N}) \\ E_y(\boldsymbol{\varrho}_{N,N}) \\ H'_x(\boldsymbol{\varrho}_{N,N}) \\ H'_y(\boldsymbol{\varrho}_{N,N}) \end{array} \right]^{III} \end{array} \right]_{(\mathbf{G}_{m,n},s/p,+)} = \left[\begin{array}{c} \left[\begin{array}{c} \widetilde{\mathbf{E}}_x^{(s/p,+,III)}(\mathbf{G}_{m,n}) \\ \widetilde{\mathbf{E}}_y^{(s/p,+,III)}(\mathbf{G}_{m,n}) \\ \widetilde{\mathbf{H}}'_x^{(s/p,+,III)}(\mathbf{G}_{m,n}) \\ \widetilde{\mathbf{H}}'_y^{(s/p,+,III)}(\mathbf{G}_{m,n}) \end{array} \right]^R \\ \vdots \\ \left[\begin{array}{c} \widetilde{\mathbf{E}}_x^{(s/p,+,I/III)}(\mathbf{G}_{m,n}) \\ \widetilde{\mathbf{E}}_y^{(s/p,+,I/III)}(\mathbf{G}_{m,n}) \\ \widetilde{\mathbf{H}}'_x^{(s/p,+,I/III)}(\mathbf{G}_{m,n}) \\ \widetilde{\mathbf{H}}'_y^{(s/p,+,I/III)}(\mathbf{G}_{m,n}) \end{array} \right]^R \\ \vdots \\ \left[\begin{array}{c} \widetilde{\mathbf{E}}_x^{(s/p,+,I/III)}(\mathbf{G}_{m,n}) \\ \widetilde{\mathbf{E}}_y^{(s/p,+,I/III)}(\mathbf{G}_{m,n}) \\ \widetilde{\mathbf{H}}'_x^{(s/p,+,I/III)}(\mathbf{G}_{m,n}) \\ \widetilde{\mathbf{H}}'_y^{(s/p,+,I/III)}(\mathbf{G}_{m,n}) \end{array} \right]^R \end{array} \right] e^{[i(\boldsymbol{\beta}+\mathbf{G}_{m,n})\cdot\boldsymbol{\varrho}_{1,1}]} \\
& \qquad \qquad \qquad e^{[i(\boldsymbol{\beta}+\mathbf{G}_{m,n})\cdot\boldsymbol{\varrho}_{j,l}]} \\
& \qquad \qquad \qquad e^{[i(\boldsymbol{\beta}+\mathbf{G}_{m,n})\cdot\boldsymbol{\varrho}_{N,N}]}
\end{aligned} \tag{2.105}$$

where the superscript *III* indicates that it is a plane wave basis mode in region III. The subscripts $\mathbf{G}_{m,n}$ and $q(=s,p)$, identify the particular Fourier component and polarization launched, and the subscript (+) indicates the right-going mode (as distinct from the right eigenvector). The right eigenvectors are used regardless of whether the mode is right- or left- going.

Equation 2.68 is applied repeatedly to propagate the field backwards in discrete steps

to the left hand side of the textured layer to yield the fields on each mesh point $\boldsymbol{\varrho}_{j,l}$

$$\left[\begin{array}{c} \left[\begin{array}{c} E_x^{\text{prop}}(\boldsymbol{\varrho}_{1,1}) \\ E_y^{\text{prop}}(\boldsymbol{\varrho}_{1,1}) \\ H_x'^{\text{prop}}(\boldsymbol{\varrho}_{1,1}) \\ H_y'^{\text{prop}}(\boldsymbol{\varrho}_{1,1}) \end{array} \right]^{III} \\ \vdots \\ \left[\begin{array}{c} E_x^{\text{prop}}(\boldsymbol{\varrho}_{j,l}) \\ E_y^{\text{prop}}(\boldsymbol{\varrho}_{j,l}) \\ H_x'^{\text{prop}}(\boldsymbol{\varrho}_{j,l}) \\ H_y'^{\text{prop}}(\boldsymbol{\varrho}_{j,l}) \end{array} \right]^{III} \\ \vdots \\ \left[\begin{array}{c} E_x^{\text{prop}}(\boldsymbol{\varrho}_{N,N}) \\ E_y^{\text{prop}}(\boldsymbol{\varrho}_{N,N}) \\ H_x'^{\text{prop}}(\boldsymbol{\varrho}_{N,N}) \\ H_y'^{\text{prop}}(\boldsymbol{\varrho}_{N,N}) \end{array} \right]^{III} \end{array} \right]_{(\mathbf{G}_{m,n,q,+})} \quad (2.106)$$

where the superscript “prop” indicates that the fields are those that have been propagated back to the left hand side for the particular mode launched forward on the right hand side as indicated by the subscripts on the 4-vectors.

A Discrete Fourier Transform is then performed to extract, in turn, each Fourier component of the fields corresponding to each reciprocal lattice vector, $\mathbf{G}_{r,s}$, where the subscripts on the 4-vectors continue to identify the particular launched mode.

$$\left[\begin{array}{c} \tilde{E}_x^{\text{prop}}(\mathbf{G}_{r,s}) \\ \tilde{E}_y^{\text{prop}}(\mathbf{G}_{r,s}) \\ \tilde{H}_x'^{\text{prop}}(\mathbf{G}_{r,s}) \\ \tilde{H}_y'^{\text{prop}}(\mathbf{G}_{r,s}) \end{array} \right]_{\mathbf{G}_{m,n,q,+}}^{III} = \sum_{j,l} \exp[-i(\mathbf{G}_{r,s} + \boldsymbol{\beta}) \cdot \boldsymbol{\varrho}_{j,l}] \left[\begin{array}{c} E_x^{\text{prop}}(\boldsymbol{\varrho}_{j,l}) \\ E_y^{\text{prop}}(\boldsymbol{\varrho}_{j,l}) \\ H_x'^{\text{prop}}(\boldsymbol{\varrho}_{j,l}) \\ H_y'^{\text{prop}}(\boldsymbol{\varrho}_{j,l}) \end{array} \right]_{\mathbf{G}_{m,n,q,+}}^{III} \quad (2.107)$$

The matrix elements are then computed by projecting the resulting Fourier transformed 4-vector on the left hand side of equation 2.107 corresponding to each of the reciprocal lattice vectors, $\mathbf{G}_{r,s}$, onto the plane wave basis for the half-space on left side of the grating (region I). This is done by taking the inner product with each of the corresponding left eigenvectors for that basis.

Specifically, the elements of the matrix $(T^{++})^{-1}$ are obtained by projection onto the right-going modes on the left hand side of the structure (region I):

$$(T^{++})_{(\mathbf{G}_{r,s,u}),(\mathbf{G}_{m,n,q})}^{-1} = \left(\left[\begin{array}{c} \tilde{\mathbf{E}}_x^{(u,+,I)}(\mathbf{G}_{r,s}) \\ \tilde{\mathbf{E}}_y^{(u,+,I)}(\mathbf{G}_{r,s}) \\ \tilde{\mathbf{H}}_x^{(u,+,I)}(\mathbf{G}_{r,s}) \\ \tilde{\mathbf{H}}_y^{(u,+,I)}(\mathbf{G}_{r,s}) \end{array} \right]^L \right)^H \left[\begin{array}{c} \tilde{E}_x^{\text{prop}}(\mathbf{G}_{r,s}) \\ \tilde{E}_y^{\text{prop}}(\mathbf{G}_{r,s}) \\ \tilde{H}_x^{\text{prop}}(\mathbf{G}_{r,s}) \\ \tilde{H}_y^{\text{prop}}(\mathbf{G}_{r,s}) \end{array} \right]_{\mathbf{G}_{m,n,q,+}}^{III} \quad (2.108)$$

T^{++} may then be obtained by matrix inversion. The elements of the product matrix $T^{-+}(T^{++})^{-1}$ are obtained by projection onto the left-going modes in region I.

$$[T^{-+}(T^{++})^{-1}]_{(\mathbf{G}_{r,s,u}),(\mathbf{G}_{m,n,q})} = \left(\left[\begin{array}{c} \tilde{\mathbf{E}}_x^{(u,-,I)}(\mathbf{G}_{r,s}) \\ \tilde{\mathbf{E}}_y^{(u,-,I)}(\mathbf{G}_{r,s}) \\ \tilde{\mathbf{H}}_x^{(u,-,I)}(\mathbf{G}_{r,s}) \\ \tilde{\mathbf{H}}_y^{(u,-,I)}(\mathbf{G}_{r,s}) \end{array} \right]^L \right)^H \left[\begin{array}{c} \tilde{E}_x^{\text{prop}}(\mathbf{G}_{r,s}) \\ \tilde{E}_y^{\text{prop}}(\mathbf{G}_{r,s}) \\ \tilde{H}_x^{\text{prop}}(\mathbf{G}_{r,s}) \\ \tilde{H}_y^{\text{prop}}(\mathbf{G}_{r,s}) \end{array} \right]_{\mathbf{G}_{m,n,q,+}}^{III} \quad (2.109)$$

Hence T^{-+} may be obtained by matrix multiplication of the above result with T^{++} .

Similarly, the matrices T^{--} and $T^{-+}(T^{++})^{-1}$ are obtained by launching left-going modes on the left hand side (region I), projecting onto the real space lattice, integrating forward, Fourier analyzing the resulting wave field, and projecting onto the left eigenvectors on the right hand side(region III):

$$(T^{--})_{(\mathbf{G}_{r,s},u),(\mathbf{G}_{m,n},q)}^{-1} = \left(\left[\begin{array}{c} \tilde{\mathbf{E}}_x^{(u,-,III)}(\mathbf{G}_{r,s}) \\ \tilde{\mathbf{E}}_y^{(u,-,III)}(\mathbf{G}_{r,s}) \\ \tilde{\mathbf{H}}_x^{(u,-,III)}(\mathbf{G}_{r,s}) \\ \tilde{\mathbf{H}}_y^{(u,-,III)}(\mathbf{G}_{r,s}) \end{array} \right]^L \right)^H \left[\begin{array}{c} \tilde{E}_x^{\text{prop}}(\mathbf{G}_{r,s}) \\ \tilde{E}_y^{\text{prop}}(\mathbf{G}_{r,s}) \\ \tilde{H}_x^{\text{prop}}(\mathbf{G}_{r,s}) \\ \tilde{H}_y^{\text{prop}}(\mathbf{G}_{r,s}) \end{array} \right]^I_{\mathbf{G}_{m,n},q,-} \quad (2.110)$$

$$[T^{-+}(T^{--})^{-1}]_{(\mathbf{G}_{r,s},u),(\mathbf{G}_{m,n},q)} = \left(\left[\begin{array}{c} \tilde{\mathbf{E}}_x^{(u,+,III)}(\mathbf{G}_{r,s}) \\ \tilde{\mathbf{E}}_y^{(u,+,III)}(\mathbf{G}_{r,s}) \\ \tilde{\mathbf{H}}_x^{(u,+,III)}(\mathbf{G}_{r,s}) \\ \tilde{\mathbf{H}}_y^{(u,+,III)}(\mathbf{G}_{r,s}) \end{array} \right]^L \right)^H \left[\begin{array}{c} \tilde{E}_x^{\text{prop}}(\mathbf{G}_{r,s}) \\ \tilde{E}_y^{\text{prop}}(\mathbf{G}_{r,s}) \\ \tilde{H}_x^{\text{prop}}(\mathbf{G}_{r,s}) \\ \tilde{H}_y^{\text{prop}}(\mathbf{G}_{r,s}) \end{array} \right]^I_{\mathbf{G}_{m,n},q,-} \quad (2.111)$$

The matrix T^{--} , is obtained by matrix inversion, and T^{+-} is obtained by matrix multiplication.

2.2.6 Buried Gratings

It is also desirable to compute the scattering from a 2D grating buried in the middle of a dielectric stack as depicted in Figure 2.5. The extension of the model to allow for efficient calculation of scattering from such structures was performed by the author. In the description of the calculation that follows, the reader is referred to Figure 2.6. The calculation proceeds by first determining the matrices T^{++} , T^{-+} , T^{+-} , T^{--} for the textured layer, taking its adjacent untextured layers as the semi-infinite layers in the calculation described in the preceding section. These matrices are then combined with their diagonal counterparts, R^{++} , R^{-+} , R^{+-} , and R^{--} , which describe the scattering off the entire dielectric stack located to the right of the grating, in a multiple scattering calculation to yield intermediate matrices C^{++} , C^{-+} , C^{+-} , C^{--} , which describe scattering off the grating and dielectric stack to the right of the grating. These latter matrices are then combined with L^{++} , L^{-+} , L^{+-} , L^{--} , which describe the scattering from the entire

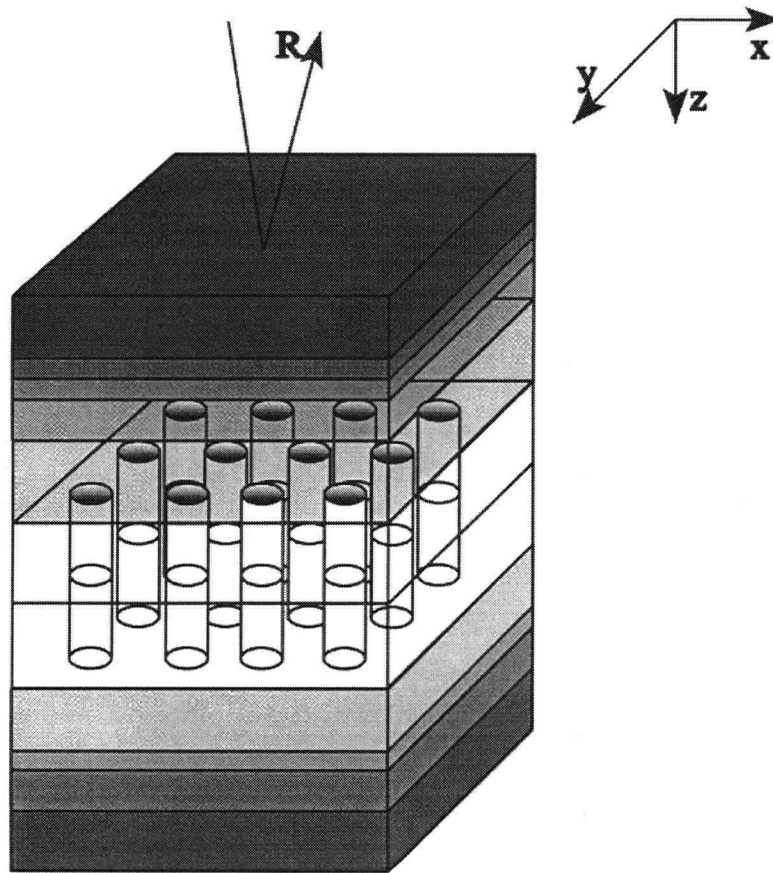


Figure 2.5: 2D grating embedded in an arbitrary multilayer dielectric stack

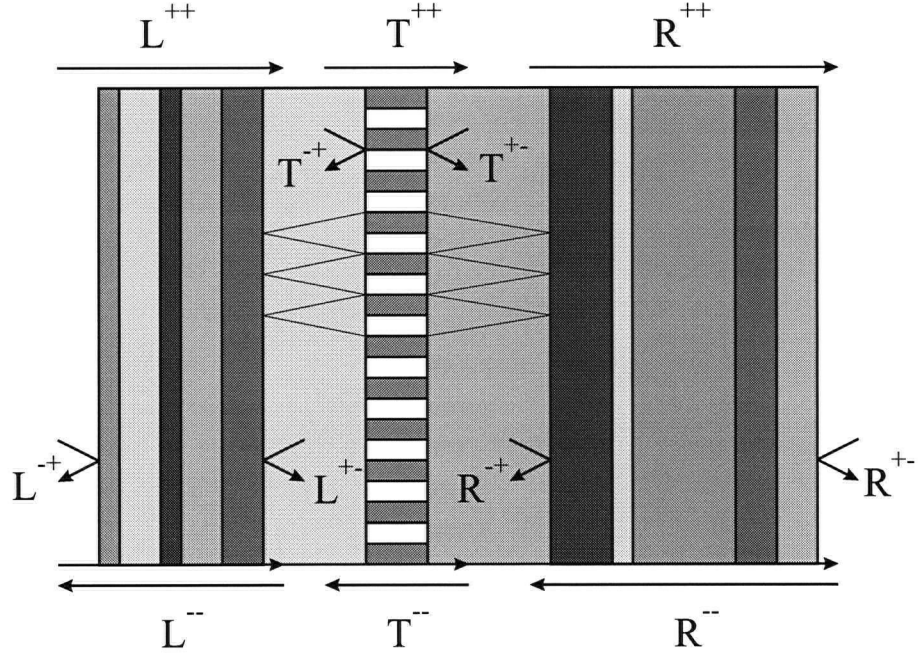


Figure 2.6: Component scattering matrices for calculation of overall reflection (scattering) matrix from grating embedded in an arbitrary multilayer dielectric stack.

dielectric stack to the left of the grating, in a multiple scattering calculation to yield F^{-+} , the matrix that describes reflection and diffraction from the entire buried grating structure.

The expression for C^{-+} is given by:

$$C^{-+} = T^{-+} + T^{--}[I - P_{g+1}^{-}R^{-+}P_{g-1}^{+}T^{+1}]^{-1}P_{g+1}^{-}R^{-+}P_{g-1}^{+}T^{++} \quad (2.112)$$

and the expression for F^{-+} is given by:

$$F^{-+} = L^{-+} + L^{--}[I - (P_{g-1}^{-}C^{-+}P_{g-1}^{+}L^{+-})]^{-1}P_{g-1}^{-}C^{-+}P_{g-1}^{+}L^{++} \quad (2.113)$$

where, the $P_{g\pm 1}^{\pm}$ are diagonal matrices accounting for the phase acquired or exponential growth or decay of the plane wave corresponding to each polarization and Fourier component in the calculation as it “propagates” right (+) or left (−) in the layers to the immediate left ($g - 1$) or right ($g + 1$) of the grating layer.

The untextured dielectric stacks specularly reflect and transmit but do not diffract light. Consequently, the matrices $L^{\pm\pm}$, $L^{\pm\mp}$, $R^{\pm\pm}$, $R^{\pm\mp}$ are diagonal, and their diagonal elements can be efficiently calculated in a multiple scattering calculation using Fresnel [42] reflection and transmission coefficients at each interface and plane wave propagation through each layer.

This multiple-scattering calculation avoids the need to integrate Maxwell's Equations through thick layers which becomes computationally expensive since the number of integration steps must increase linearly with layer thickness. Moreover, the multiple scattering calculation yields a result which is exact for all of the basis functions included in the calculation.

2.3 Results

2.3.1 Introduction

In this section we illustrate how reflectivity calculations can be used to reveal the nature of the photonic eigenmodes of two-dimensionally strongly-textured high-index contrast semiconductor waveguides. In order to introduce the various concepts involved, we proceed first through an investigation of the untextured, weakly and strongly one-dimensionally textured, and the weakly two-dimensionally textured cases.

2.3.2 Near-Normal Incidence Reflectivity from Untextured Uniform Slab

Figure 2.8 shows the specular reflectivity spectrum over a broad spectral range, for both the s and p polarizations, for light incident from air at an angle of $\theta = 10^\circ$ from the normal onto a 120 nm-thick piece of $\epsilon' = 12.25$ material. The structure is depicted in Figure 2.7. The s and p spectra are somewhat different, as expected, with both exhibiting fringes arising from the Fabry-Perot cavity formed within the high-index material due to reflections from the interfaces. The maxima in the reflectivity correspond to resonant leaky states where the fields are localized to some extent to the high-index region. A

discussion of the number of Fourier components included in the calculation, the number of in-plane mesh points, and intermediate planes (z -steps) that must be used to get well-converged results is deferred to section 2.4.

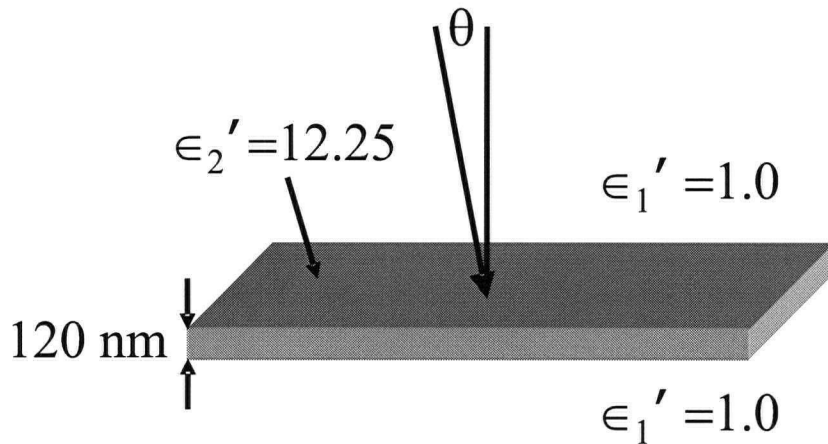


Figure 2.7: Waveguide consisting of 120 nm-thick slab of material with dielectric constant $\epsilon' = 12.25$

2.3.3 Bound Modes of Untextured Slab

The 120 nm-thick slab of material with dielectric constant $\epsilon_2' = 12.25$ constitutes a slab waveguide which supports bound electromagnetic modes. These modes have fields in the cladding layers above and below the slab that decay exponentially away from the slab and thus carry away no energy. Bound modes have a dispersion curve falling between the light lines for the refractive index of the core and cladding layers, as depicted in Figure 1.7. These modes are, in a sense, bare modes that will be mixed by a 2D texture to form the renormalized eigenstates of the planar 2D photonic crystal.

One way to determine the frequency of such a mode for a given in-plane wavevector is by computing the specular reflectivity spectrum for light with that particular wavevector. The specular reflectivity spectrum will then exhibit a pole when the energy and in-plane wavevector match the dispersion of one of these bound modes. This corresponds to

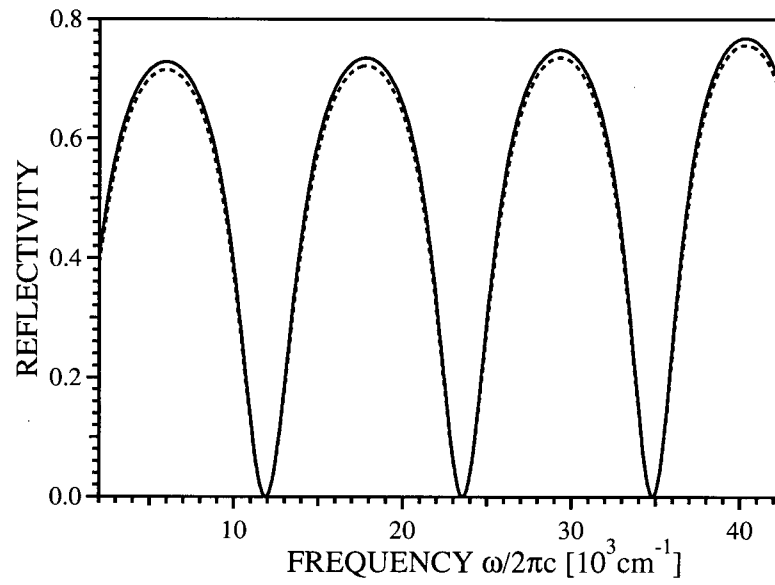


Figure 2.8: Specular reflectivity spectrum for light incident at 10^0 (from the normal) on a 120 nm-thick slab of material of dielectric constant $\epsilon' = 12.25$. The solid curve depicts the spectrum for the s polarization; the dashed curve depicts the spectrum for the p polarization.

performing the specular reflectivity calculation with an evanescent incident field.

An example of this is given below. Figure 2.9 depicts dispersion curves for the lowest order TE and TM bound modes supported by the slab structure of Figure 2.7. Figure 2.10 depicts the specular reflectivity spectrum obtained when an incident field having an in-plane propagation constant of $20,000 \text{ cm}^{-1}$ impinges on the slab. This spectrum corresponds to probing $\omega - \beta$ space along the line depicted in Figure 2.9. A feature (pole) appears in each of the s , and p polarized spectra, when the frequency matches that of corresponding TE or TM bound mode, as indicated by the dots in Figure 2.9.

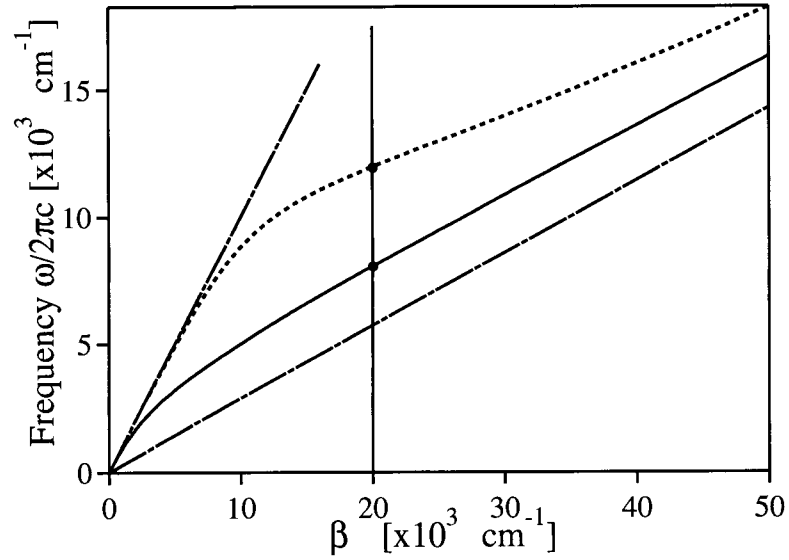


Figure 2.9: Plot of mode frequency versus in-plane wavevector, β , for the lowest order TE (solid curve) and TM (dotted curve) modes of a planar waveguide consisting of a 120 nm slab of material with $\epsilon' = 12.25$, clad above and below by air ($\epsilon' = 1$). The dot-dashed lines represent the lightlines for these materials. The solid vertical line depicts the part of $\omega - \beta$ space that is explored in the calculation of the spectra shown in Figure 2.10 below. The dots at the intersection of the vertical line with the dispersion curves indicate the appearance of a resonant feature in the spectra.

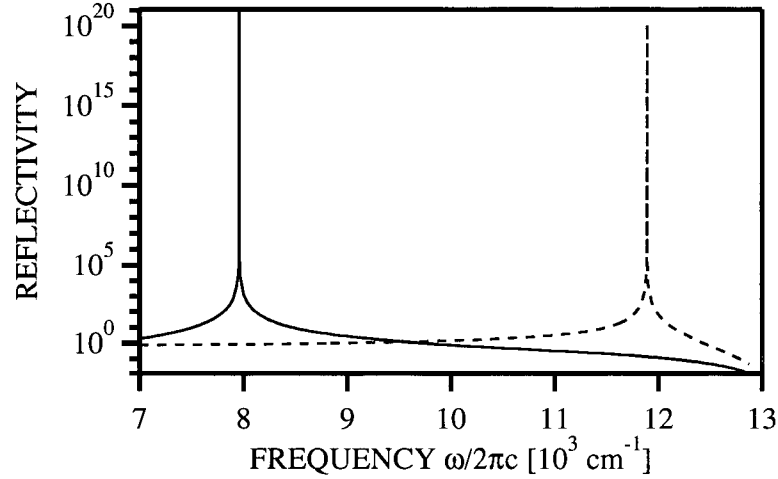


Figure 2.10: Specular reflectivity spectrum for evanescent field incident on 120 nm slab of material with $\epsilon' = 12.25$, with in-plane wavevector of $20,000 \text{ cm}^{-1}$. The solid line is for s polarized light, the dashed line is for p polarized light.

2.3.4 Slab Waveguide with 1D Grating

Figure 2.11 schematically depicts the effect on the dispersion of the electromagnetic modes when a shallow 1D grating is etched into the guide as shown in Figure 2.12. Gaps open up at the Brillouin zone boundaries as the various orders ($\beta_G, 2\beta_G$) of the dielectric modulation couple together the bound modes which existed in degenerate pairs at $\pm\beta_G/2$ and $\pm\beta_G$ for the untextured structure. It should be noted that one such dispersion plot exists for each of the TE and TM polarized modes, with the TM dispersion plot shifted higher in frequency. Finally, we note that the periodicity of the dielectric allows us to describe the mode dispersion in a zone-folded scheme in the first Brillouin zone.

When the specular reflectivity calculations are performed with incident (evanescent) light having in-plane wavevector given by $(\beta_G/2)\hat{x}$, two features are seen to occur in each polarization as shown in Figure 2.13. These occur again as poles in the reflectivity spectra indicating that the excitations remain completely bound to the guide.

The eigenmodes in the vicinity of the second order gap at in-plane wavevector $\beta_G\hat{x}$,

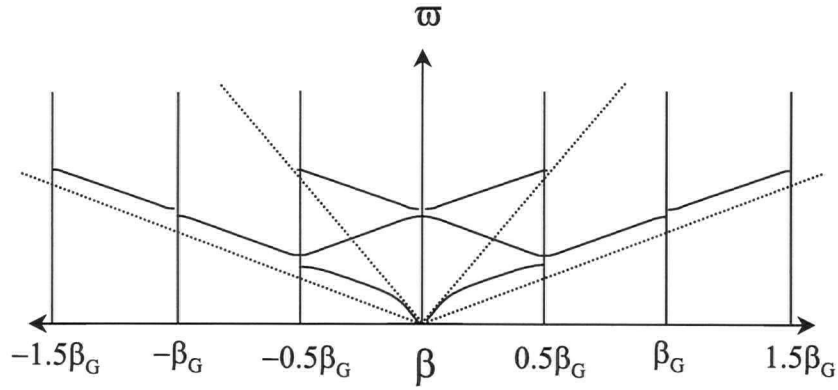


Figure 2.11: Schematic dispersion plot for single-mode slab waveguide with shallow 1D grating etched into its surface. The dashed lines represent the light lines for the low-index cladding layer (larger slope) and the high-index core layer (smaller slope). The solid lines represent the dispersion of Bloch states in the presence of the grating.

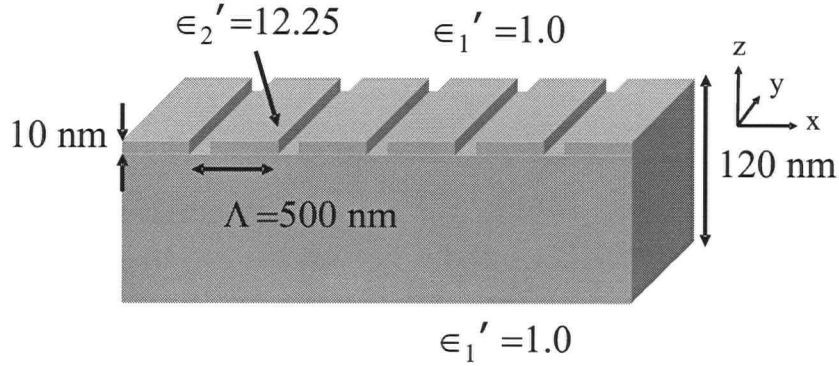


Figure 2.12: Slab waveguide with “weak” 1D texture: the structure consists of a 120 nm-thick slab of $\epsilon' = 12.25$ material, clad above and below by air, with a 10 nm deep 1D square-toothed grating having a pitch $\Lambda = 500$ nm and an air filling fraction of 25% etched into the surface.

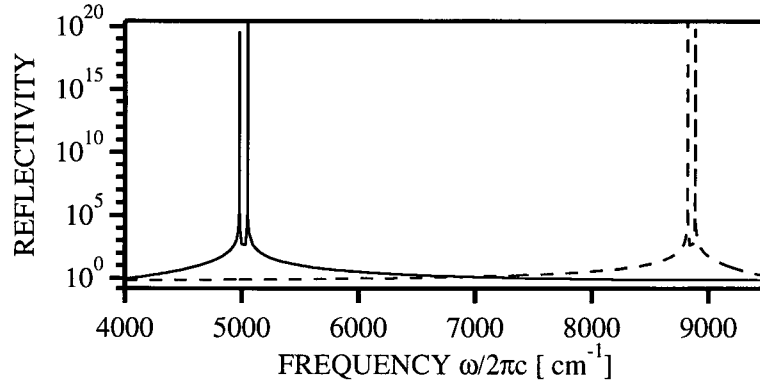


Figure 2.13: Calculated specular reflectivity spectrum for evanescent light incident with in-plane wavevector $\beta = (\beta_G/2)\hat{x} = (\pi/\Lambda)\hat{x}$. The solid curve is for s polarized light, the dashed curve is for p polarized light. The corresponding waveguide structure is depicted in Figure 2.12.

although primarily composed of superpositions of field components at $\pm\beta_G\hat{x}$, are nevertheless coupled *via* the $\pm\beta_G\hat{x}$ component of the dielectric modulation, to a component at $\beta = 0$ which can radiate into the semi-infinite layer, thereby rendering them leaky (or lossy). Figure 2.14a depicts the specular reflectivity spectrum for evanescent light incident with in-plane wavevector, $\beta = 1.01\beta_G\hat{x}$, *i.e.*, slightly detuned from the boundary between the 2nd and 3rd Brillouin zones, for both the s and p polarizations. The Bloch states again manifest themselves as resonant features in the spectra, however, they are no longer true poles. They have non-zero linewidths owing to their leaky nature.

The zeroth order radiative component of the Bloch states in the vicinity of the 2nd order gap allows us to excite them with a propagating field incident from above the grating. Figure 2.14b depicts the specular reflectivity spectra for light incident from above the grating at near-normal incidence for both the s and p polarizations. Once again, two features per polarization occur in the specular reflectivity spectra when the energy and in-plane wavevector match the dispersion of the modes. Here, the features occur as bipolar resonances in the specular reflectivity spectra, which are bounded by unity as required by energy (flux) conservation for propagating incident and reflected

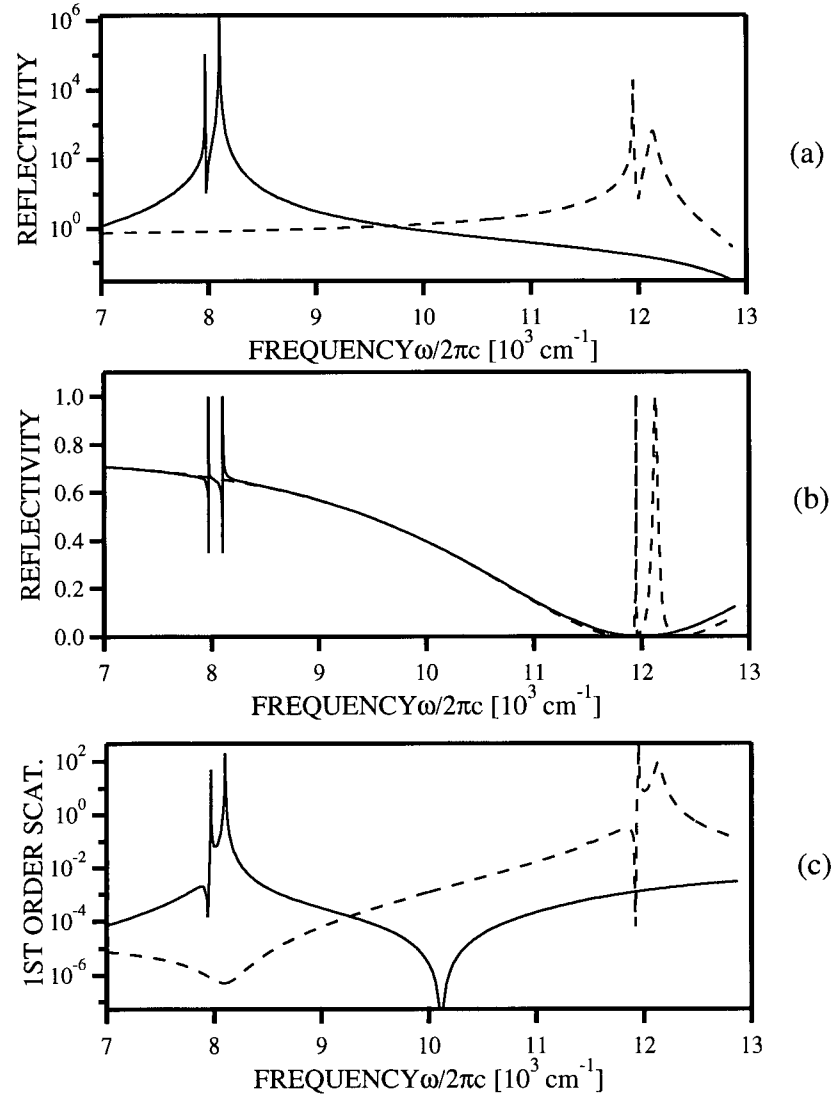


Figure 2.14: (a) Calculated specular reflectivity spectrum for evanescent light incident with in-plane wavevector, $\beta = 1.01\beta_G\hat{x}$, *i.e.*, slightly detuned from the boundary between the 2nd and 3rd Brillouin zones. (b) Calculated specular reflectivity spectrum for light incident with in-plane wavevector, $\beta = 0.01\beta_G\hat{x}$, *i.e.*, slightly detuned from the Brillouin zone-centre. (c) Calculated 1st order diffraction coefficient, *i.e.*, coefficient for scattering from a field component at $\beta = 0.01\beta_G\hat{x}$ to a field component at $\beta = 1.01\beta_G\hat{x}$. The solid curves are for *s* polarized light; the dashed curves are for *p* polarized light. The waveguide structure under study is depicted in Figure 2.12.

fields.

This is like hitting a diffraction grating near-normal incidence but with a wavelength such that there are no propagating diffracted orders. The diffraction is only into these evanescent “bound” modes.

Figure 2.14 (c) depicts the calculated 1st order scattering coefficient. This is the coefficient for scattering from a field component at $\beta = \beta_{\text{incident}}\hat{x}$ to a field component at $\beta = \beta_{\text{incident}}\hat{x} + \beta_G\hat{x}$. In this case this corresponds to scattering from $\beta = 0.01\beta_G\hat{x}$ to $\beta = 1.01\beta_G\hat{x}$. This is the amount of the incoming radiation at near-normal incidence, with in-plane wavevector $\beta = 0.01\beta_G\hat{x}$, that is scattered by the grating to light having \mathbf{E} , and \mathbf{H} fields which are evanescent in the direction normal to the slab (\hat{z}) and which vary sinusoidally in the \hat{x} direction with an in-plane wavevector of $\beta = 1.01\beta_G\hat{x}$. It essentially represents the coupling between the zeroth order, radiating component, and the field component resembling a bound mode of the untextured slab. This scattering coefficient also displays resonant features when the energy and in-plane wavevector match the dispersion of the Bloch states.

It is important to note that, in all of the spectra shown in Figure 2.14, one of each pair of features is narrow compared to the other. In fact, precisely at normal incidence, the narrow feature vanishes completely from the normal-incidence specular reflectivity and first-order scattering spectra, but not from the evanescent specular reflectivity spectrum. This occurs because symmetry requires an exact cancellation of the radiative component of that particular state at the precise centre of the Brillouin zone. Figure 2.15 shows the results of the reflectivity calculations carried out exactly at the zone-centre ($\beta = 0$). There are still two distinct Bloch states at zone-centre, as evidenced by the two features in the evanescent specular reflectivity spectrum. However, only one of them has a non-zero, zeroth order, radiative component which allows us to couple to it with radiation from above the grating. Nevertheless, we can still couple to the other Bloch state with an evanescent field, phase matched to the field component of the Bloch state at $\sim \beta_G\hat{x}$.

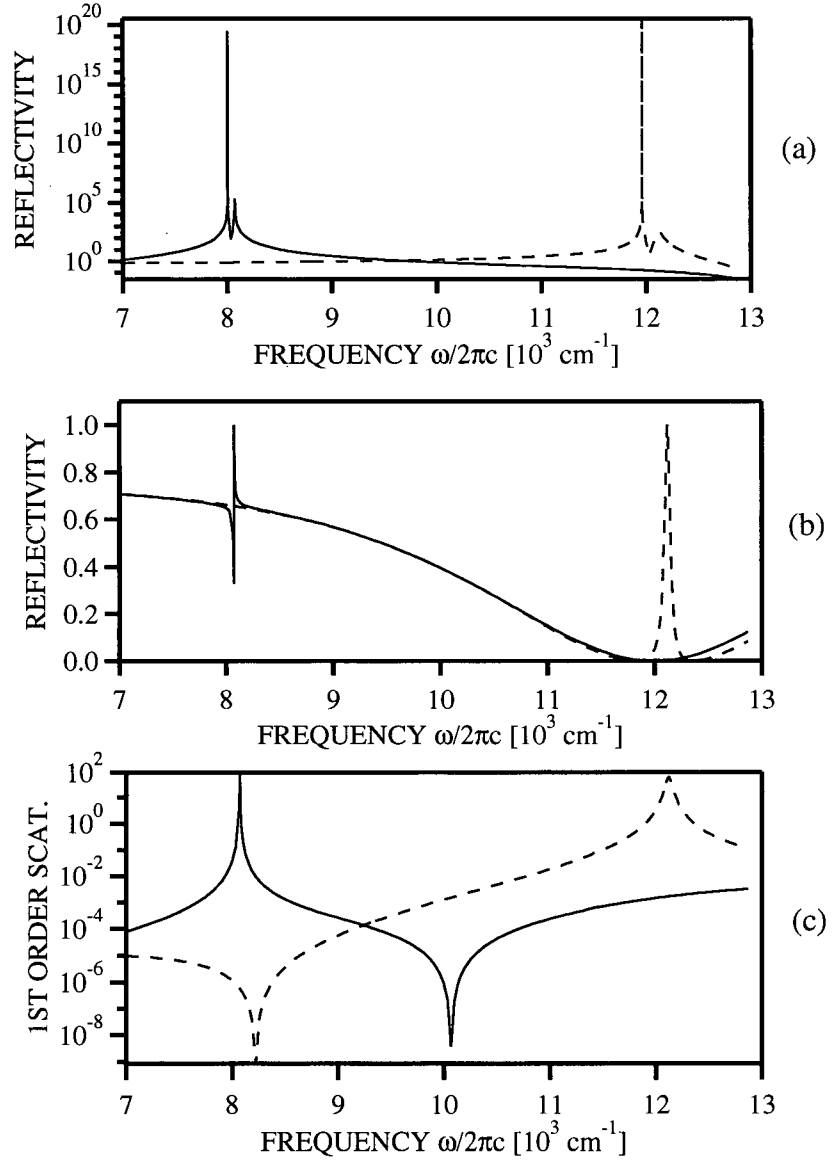


Figure 2.15: (a) Calculated specular reflectivity spectrum for evanescent light incident with in-plane wavevector, $\beta = \beta_G \hat{x}$, at the edge of the 1st Brillouin zone. (b) Calculated specular reflectivity spectrum for radiation incident with zero in-plane wavevector, *i.e.*, at the Brillouin zone-centre. (c) Calculated 1st order diffraction coefficient, *i.e.*, coefficient for scattering from a field component at $\beta = 0.01\beta_G \hat{x}$ to a field component at $\beta = 1.01\beta_G \hat{x}$. The solid curves are for *s* polarized light; the dashed curves are for *p* polarized light. The waveguide structure under study is depicted in Figure 2.12.

Figure 2.16 shows the near-normal incidence specular reflectivity spectrum for the same structure but with the grating having an air filling fraction of 75% rather than 25%. Notice that the broader mode is now the lower-frequency mode. The frequency (energy) ordering of the lossy, and non-lossy modes are dependent upon the duty cycle (air filling fraction) of the grating. The frequency ordering is basically due to the differing distributions of the real space field intensities of the eigenmodes in the high and low-index regions of the unit cell. This effect is discussed in greater detail in Chapter 6 (section 6.5) where a schematic depiction is given of the in-plane field intensity for the resonant eigenmodes at zone-centre.

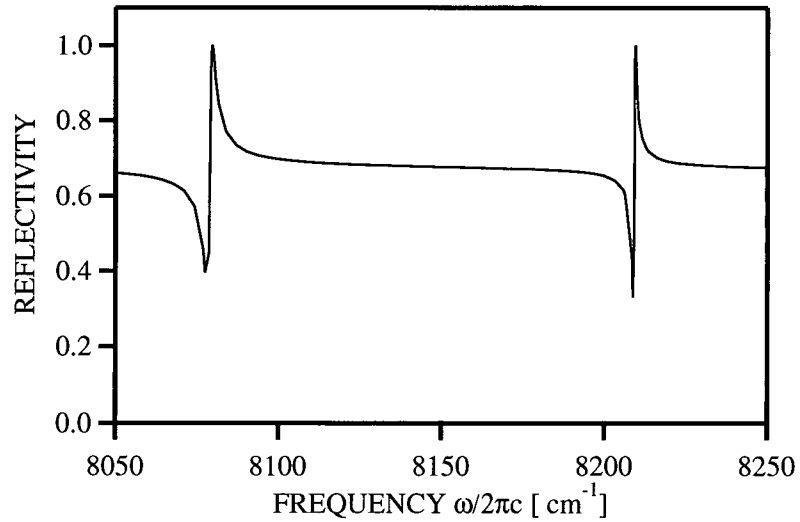


Figure 2.16: Calculated near-normal incidence specular reflectivity spectrum for light incident with in-plane wavevector, $\beta = 0.01\beta_G\hat{x}$, for s polarized light. The waveguide structure is identical to the one specified in Figure 2.12 except that the grating has an air filling fraction of 75% rather than 25%.

It should be mentioned that, in comparison to the photonic crystals discussed later, these structures are considered “weakly textured” because although the dielectric contrast between the teeth and trenches in the gratings is large, the grating itself occupies

a small fraction ($\sim 20\%$) of the total core thickness, resulting in a relatively small interaction of the mode with the grating. The width of the gap is approximately 1.5 percent of its centre frequency, which, nevertheless, is still larger than that corresponding to gratings used in typical DFB's, which is on the order of 0.1%.

We now consider the situation when the 1D grating is made to completely penetrate the guiding layer. Such a structure is depicted in Figure 2.17. Figure 2.18 shows the specular reflectivity spectrum for s polarized light incident from above the grating at 5° from normal. We consider only the spectrum for the s polarization. We notice that the gap between the modes has increased substantially, indicating stronger coupling between the $\pm\beta_G$ Fourier components. In fact, the gap is now $\sim 20\%$ of the centre frequency, indicating a very strong influence of the texture on the photonic eigenstates.

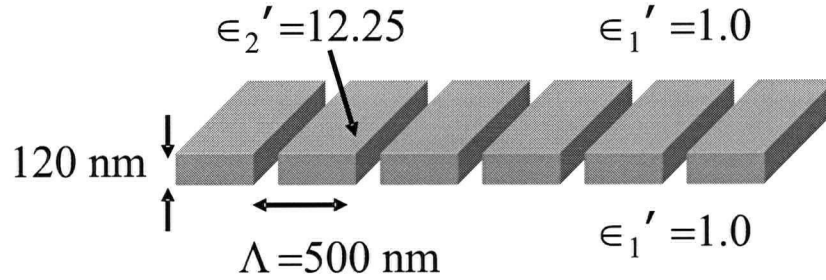


Figure 2.17: Slab waveguide with “strong” 1D texture: the structure consists of a 120 nm thick slab of $\epsilon' = 12.25$ material, clad above and below by air, with a 1D square-toothed grating that completely penetrates the slab. The grating has a pitch, $\Lambda = 500$ nm, and an air filling fraction of 25%.

2.3.5 Waveguide with 2D weak 2nd order grating

Next, we consider the situation where a weak 2D square grating is etched into a waveguide. One example of such a structure is that where a 2D array of cylindrical airholes, 10 nm deep, is buried in the core of our 125 nm waveguide of $\epsilon' = 12.25$ material. The structure, which is depicted schematically in Figure 2.19, also illustrates the ability of the model to perform calculations incorporating buried gratings.

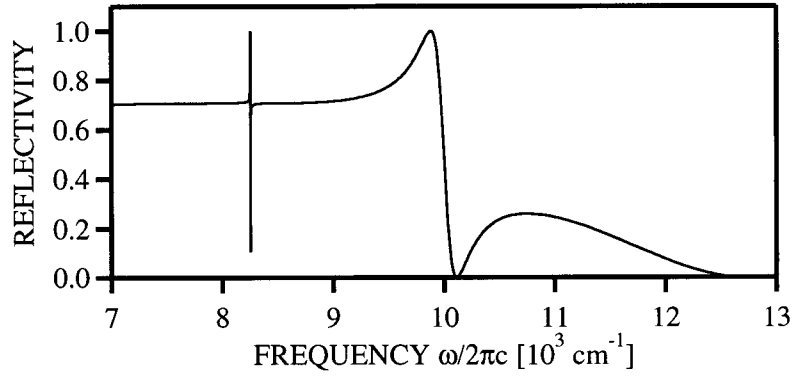


Figure 2.18: Calculated near-normal incidence specular reflectivity spectrum for *s* polarized light incident with in-plane wavevector, $\beta = 0.01\beta_G\hat{x}$. The waveguide structure, depicted in Figure 2.17, consists of a 120 nm thick slab of $\epsilon' = 12.25$ material, clad above and below by air, completely penetrated by 1D square-toothed grating having a pitch, $\Lambda = 500$ nm, and an air filling fraction of 25%.

With a 2D grating, in the vicinity of the 2D Brillouin zone-centre, there are now *four* field components resembling bound modes of the waveguide with in-plane propagation constants of $\pm\beta_G\hat{x}$ and $\pm\beta_G\hat{y}$, that are coupled together *via* the $\pm 2\beta_G\hat{x}$ and $\pm 2\beta_G\hat{y}$ Fourier components of the dielectric modulation. Additionally, all four of these couple to a zeroth order component, which radiates out normally from the structure, as in the 1D case, *via* the $\pm\beta_G\hat{x}$ and $\pm\beta_G\hat{y}$ components of the texture. Figure 2.20 schematically depicts the expected 2D bandstructure in the vicinity of the zone-centre as consisting of four band sheets shown in the reduced 2D Brillouin zone. There are actually two sets of these clusters of four sheets, centred at two different frequencies, corresponding to those of the TE and TM modes of the untextured slab. The radiative, zeroth order component of the Bloch state once again allows us to probe these modes with radiation incident from above the grating in a specular reflectivity calculation.

Figure 2.22 depicts the specular reflectivity spectrum for light incident from above this structure with in-plane wavevector along the $\Gamma - X$ symmetry direction. The symmetry directions for the square lattice are depicted in Figure 2.21. Three clusters

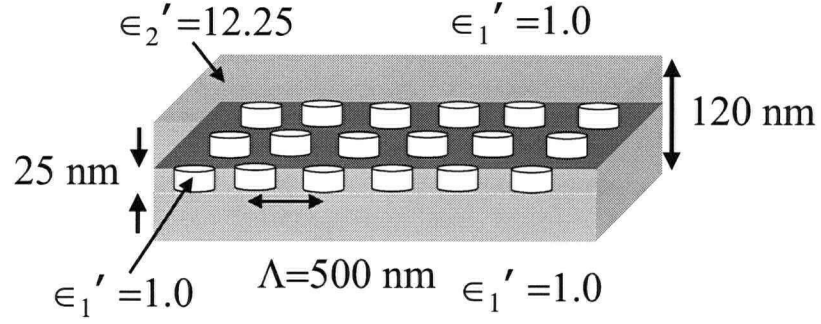


Figure 2.19: Slab waveguide consisting of 125 nm of $\epsilon' = 12.25$ material with air above and below, having a square lattice of cylindrical airholes, 25 nm deep, embedded at its centre. The lattice has a pitch of $\Lambda = 500$ nm, and the radius, r , of the holes is $r/\Lambda = 0.10$.

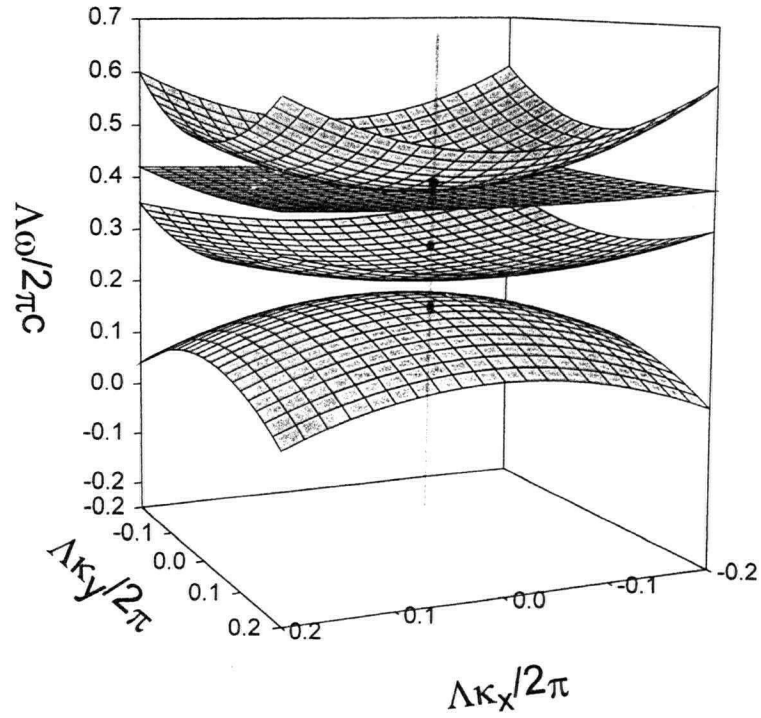


Figure 2.20: Schematic in-plane bandstructure of resonant modes of waveguide with a square grating shown in 1st 2D Brillouin zone.

of four bipolar features appear corresponding to Fano resonances [38] resulting from the four leaky modes described above. The precise Fano lineshape function is described in Chapter 5 (section 5.6.1), and a physical explanation of the reason behind the bipolar nature of the Fano lineshape is given in Chapter 6 (section 6.2). The cluster occurring at the lowest frequencies corresponds to the modes arising primarily from the combination of the four TE field components at $\pm\beta_G\hat{x}$ and $\pm\beta_G\hat{y}$. The cluster of four modes occurring at the highest frequencies corresponds to the modes arising from the combination of the four TM field components at $\pm\beta_G\hat{x}$ and $\pm\beta_G\hat{y}$. There is an additional cluster of four modes occurring at an intermediate frequency. These correspond to modes arising from the combination of TE field components at $\pm\beta_G\hat{x} \pm \beta_G\hat{y}$.

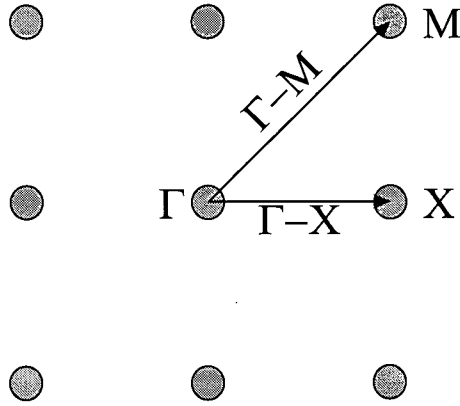


Figure 2.21: Symmetry directions for the square lattice.

Figure 2.23 shows an expanded view in the vicinity of each cluster. We note that in the lowest frequency cluster (where the modes are comprised primarily of TE field components) three features occur in the s polarization, while one occurs in the p polarization. Conversely, in the highest frequency cluster (where the modes are comprised primarily of TM field components) three features occur in the p polarization while one occurs in the s polarization.

We now examine the properties of the modes occurring in the lowest frequency cluster in greater detail. Figure 2.24 shows reflectivity spectra for light incident with zero

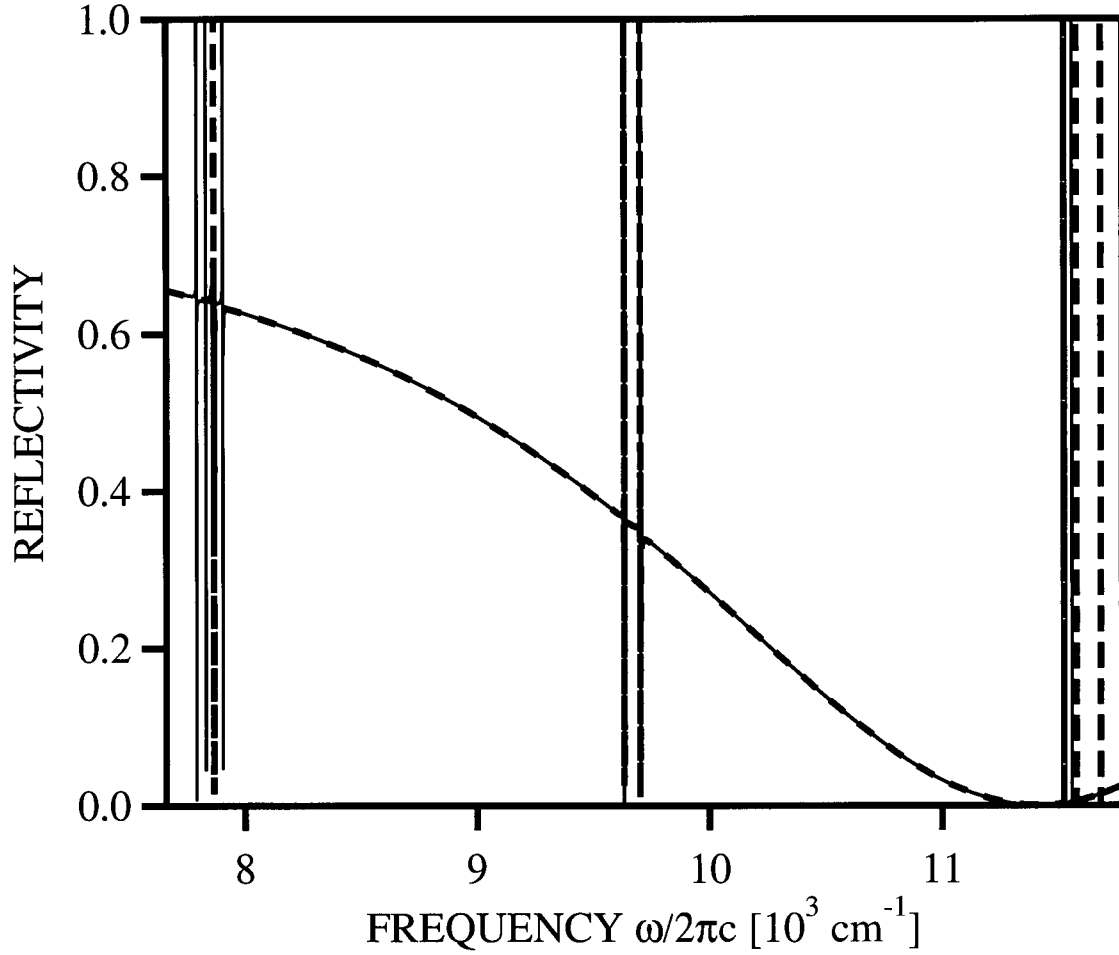


Figure 2.22: Calculated specular reflectivity spectrum for light incident on a 125 nm slab waveguide of $\epsilon' = 12.25$ material with air above and below, and a square lattice of cylindrical airholes, 25 nm deep, embedded at its centre. The lattice has a pitch of $\Lambda = 500$ nm, and the radius, r , of the holes is $r/\Lambda = 0.10$. Solid lines are for the s polarization, while dashed lines depict the p polarization. The spectra were calculated for light incident with in-plane wavevector fixed at $\beta/\beta_G = 0.01$ in the $\Gamma - X$ direction, which is defined in Figure 2.21.

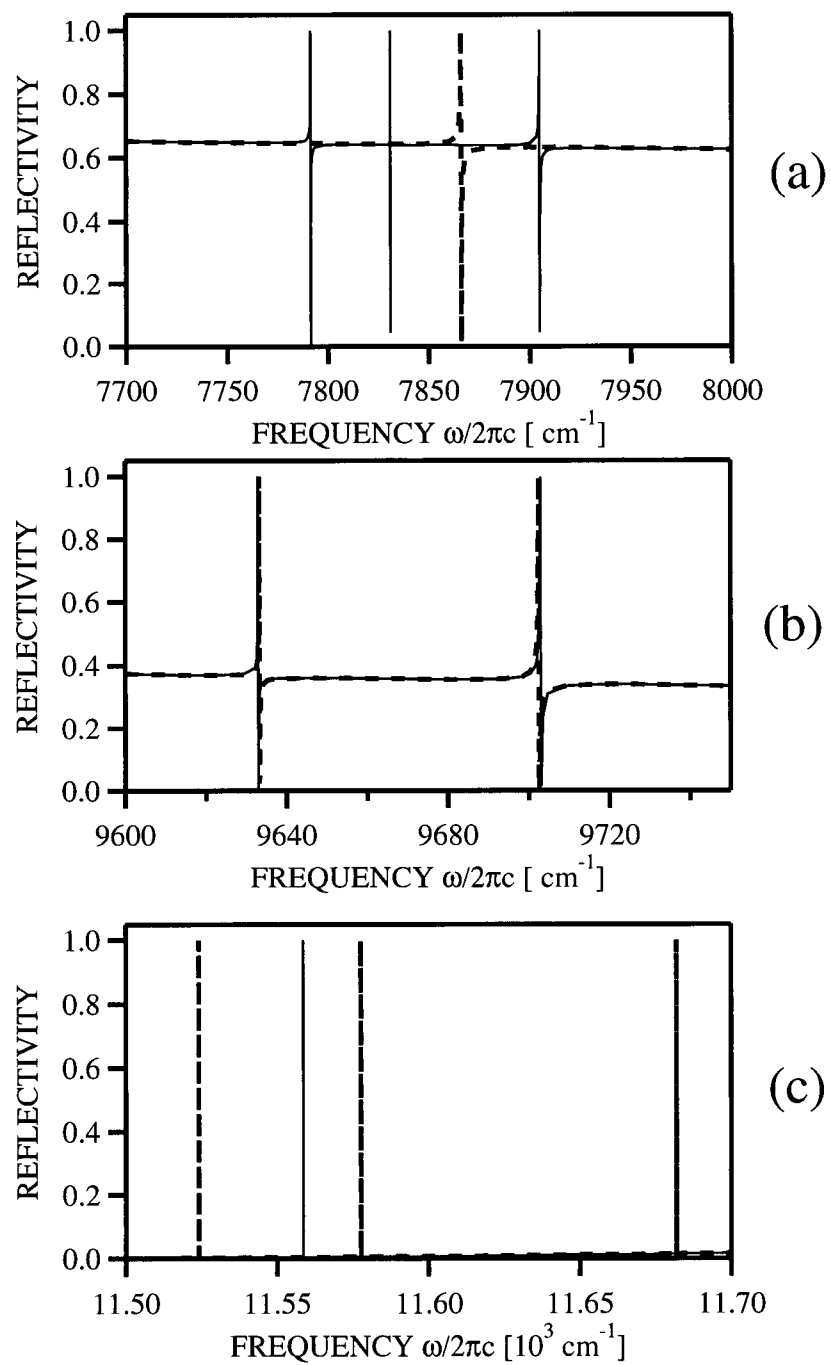


Figure 2.23: Expanded view of the spectrum depicted in Figure 2.22: (a) lowest frequency cluster (b) intermediate frequency cluster (c) high frequency cluster

in-plane wavevector (zone-centre), corresponding to normal incidence. The s and p polarized spectra, which now merely correspond to x and y polarization of the electric field, are identical, as expected from symmetry considerations, and each contains a lone feature. Thus, precisely at zone-centre, the narrow features vanish from the spectra, and the surviving, broad features, one in each of the s and p (or rather, x and y) polarized spectra, become degenerate.

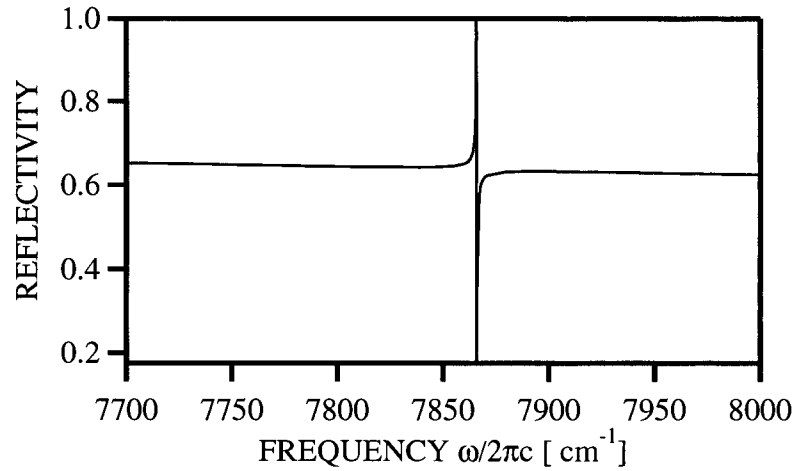


Figure 2.24: Calculated specular reflectivity spectrum from same structure as in Figure 2.23. The spectra were calculated for light incident with zero in-plane wavevector, $\beta/\beta_G = 0.00$, corresponding to normal incidence.

Figure 2.25 depicts reflectivity spectra for light incident with in-plane wavevector oriented along the direction $[\hat{x} + \hat{y}]$ (M symmetry direction). In this case, two resonances appear in each polarization (s and p).

Figure 2.26 depicts three specular reflectivity spectra, in the vicinity of the TE gap, for off-normal incident light along the X direction, for three different diameters of the airholes. The result illustrates the fact that the precise ordering of the broad and narrow features corresponding to the frequency ordering of the leaky and less leaky modes is dependent on the details of the unit cell of the square lattice. These polarization and symmetry properties are discussed further in Chapter 6.

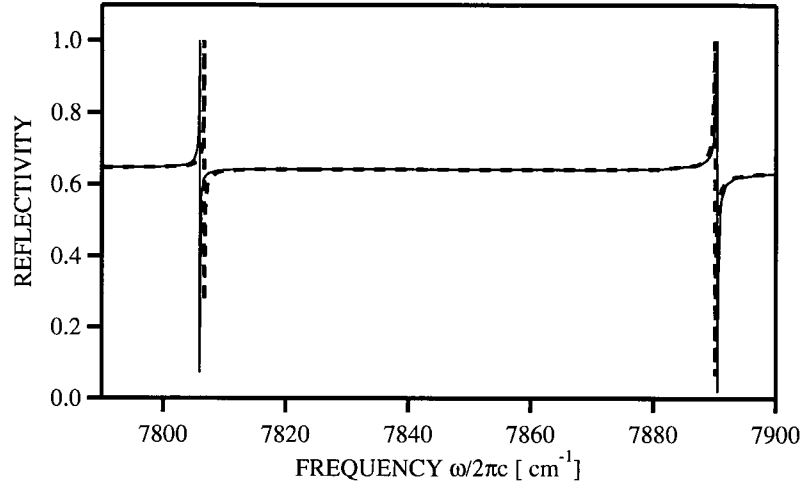


Figure 2.25: Calculated specular reflectivity spectrum from same structure as in Figure 2.23. The spectra were calculated for light incident with in-plane wavevector fixed at $\beta/\beta_G = 0.01$ in the $[\hat{x} + \hat{y}]$ direction (*i.e.*, along the $\Gamma - M$ symmetry direction).

2.3.6 2D Strong Texture

We now investigate structures with a “strong” 2D grating. As in the 1D case, this can be realized by having the dielectric texture extend all the way through the core of the waveguide. Figure 2.27 schematically depicts one such structure which is very similar to those investigated experimentally in the present work. The waveguide structure consists of a 80 nm thick slab of $\epsilon' = 12.25$ material which forms the guiding core, clad above by air and below by 2 μm of material with $\epsilon' = 2.25$. The semi-infinite half-plane below is also composed of $\epsilon' = 12.25$ material. The core waveguide layer is penetrated by a 2D square array of holes on a pitch, $\Lambda = 500$ nm, and with hole radii given by $r/\Lambda = 0.5$.

Due to the significant reduction of the average refractive index of the core layer, the guiding properties, *i.e.*, the frequencies of the TE and TM modes having $\beta = \beta_G$, can no longer be safely approximated by those of the untextured slab. Based on a calculation using the air-filling-fraction-averaged refractive index of the core, the effective untextured structure is seen to support only TE guided modes, with the TM modes being below the

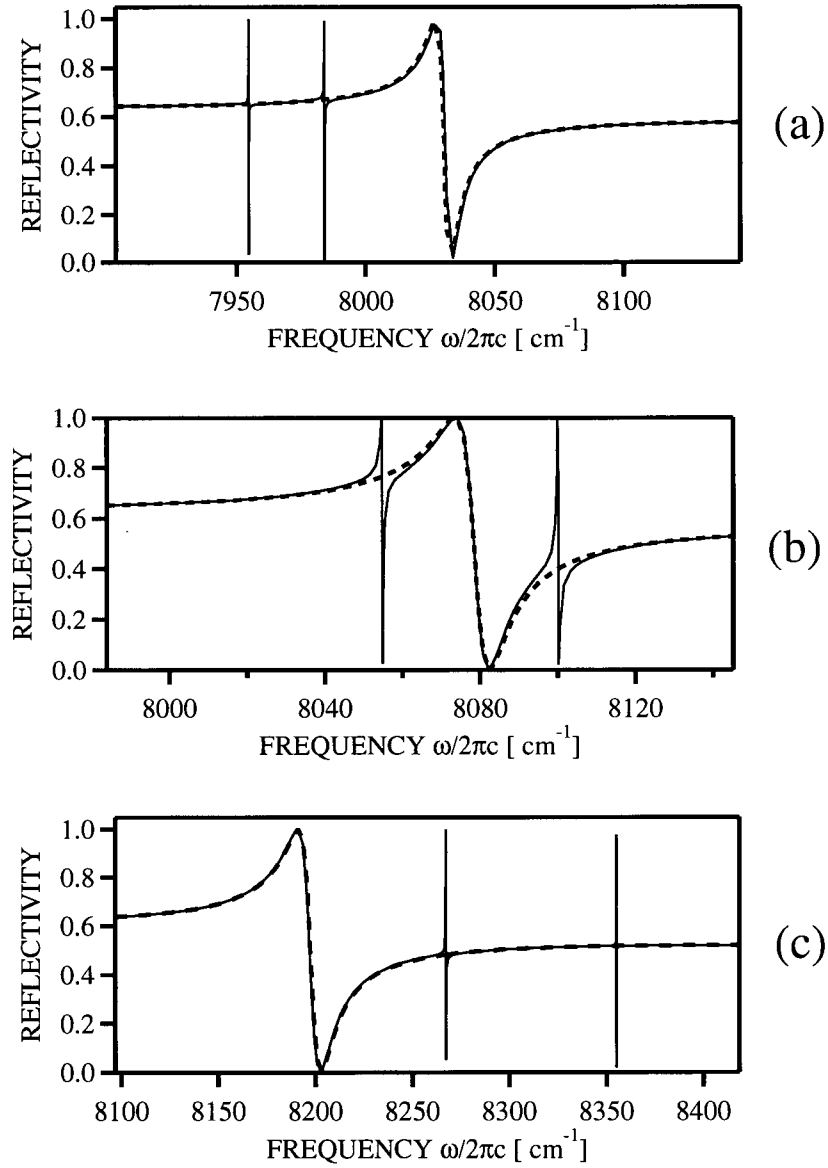


Figure 2.26: Calculated specular reflectivity spectrum for light incident on a 125 nm slab waveguide of $\epsilon' = 12.25$ material with air above and below, and a square lattice of cylindrical airholes, 25 nm deep embedded at its centre. The spectra were calculated for light incident with in-plane wavevector fixed at $\beta/\beta_G = 0.001$ in the \hat{x} direction (X symmetry direction). The lattice has a pitch of $\Lambda = 500$ nm, and the radius, r , of the holes is: (a) $r/\Lambda = 0.25$ (b) $r/\Lambda = 0.32$ (c) $r/\Lambda = 0.40$

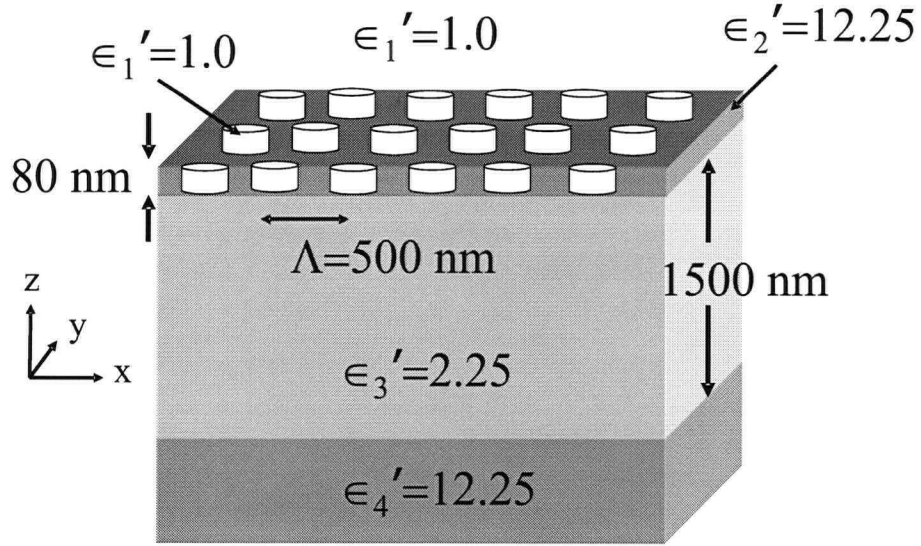


Figure 2.27: Strongly 2D textured thin asymmetric slab waveguide: the structure consists of a 80 nm-thick slab of $\epsilon' = 12.25$ material which forms the guiding core, clad above by air and below by $2\ \mu\text{m}$ of material with $\epsilon' = 2.25$. The semi-infinite half-plane below is composed of $\epsilon' = 12.25$ material. The core waveguide layer is penetrated by a 2D square array of holes on a pitch, $\Lambda = 500\ \text{nm}$, and with hole radii given by $r/\Lambda = 0.5$.

low frequency cutoff. Consequently, spectra are shown only in the vicinity of the second order TE gap.

Figures 2.28 and 2.29 show reflectivity spectra for light incident on the structure depicted in Figure 2.27 along the two symmetry directions.

The specular reflectivity spectra for this structure exhibit the same symmetry and polarization properties as in the case of weak texture. However, the range over which the features occur is now much larger. This is as expected owing to the much stronger scattering induced by the holes that now completely penetrate the waveguide core.

Figure 2.30 (a) shows the specular reflectivity spectrum on the same structure at normal incidence. As in the case of weak texture, a lone feature appears, as the two narrow features vanish and the broad features overlap exactly. Finally, as in the 1D case, we confirm the presence of the lossless features at zone-centre by calculating the reflectivity for evanescent light incident at $\beta = \beta_G \hat{x}$, which comprises one of the dominant field

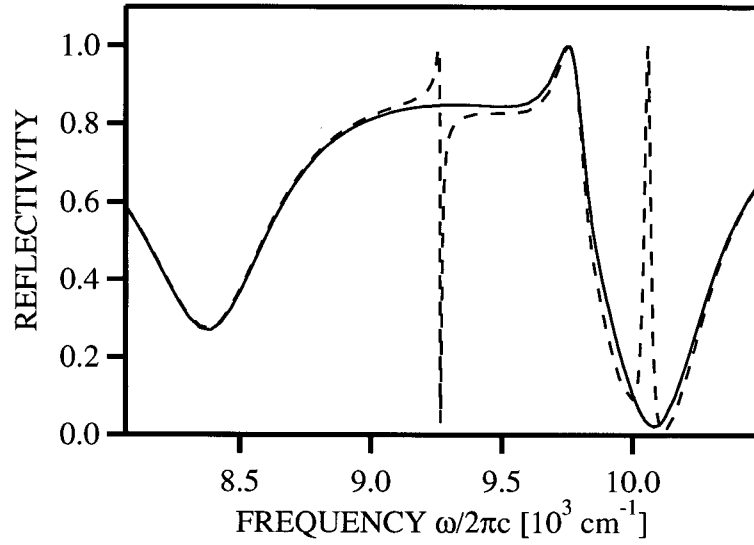


Figure 2.28: Calculated near-normal incidence specular reflectivity spectrum for light incident with in-plane wavevector, $\beta = 0.03\beta_G$, along the $\Gamma-X$ direction for the structure depicted in Figure 2.27 with $r/\Lambda = .2821$. The solid line represents the s polarized spectrum, the dashed line depicts the p polarized spectrum.

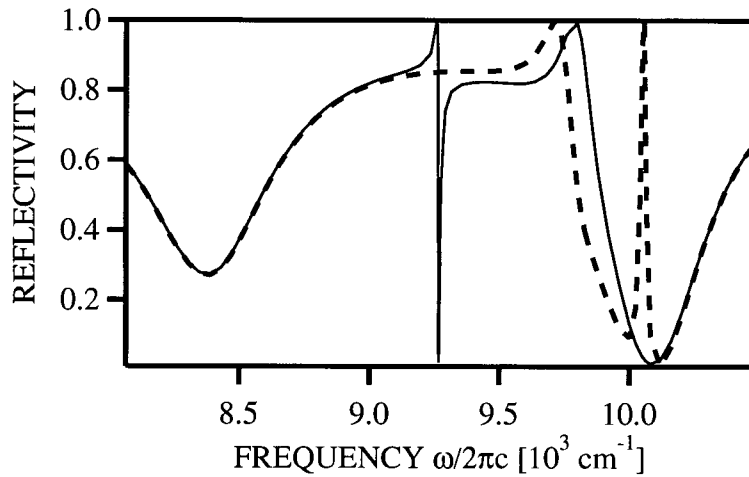


Figure 2.29: Calculated near-normal incidence specular reflectivity spectrum for light incident with in-plane wavevector, $\beta = 0.03\beta_G$, along the $\Gamma-M$ direction for the structure depicted in Figure 2.27 with $r/\Lambda = .2821$. The solid line represents the s polarized spectrum, the dashed line depicts the p polarized spectrum.

components in all four modes at zone-centre. This spectrum is shown in Figure 2.30 (b). The two lossless modes manifest themselves as poles while the two lossy modes appear as degenerate resonances with finite linewidth.

The nature of the various photonic eigenstates corresponding to each of the resonant features in the specular reflectivity spectra is described in Chapter 6.

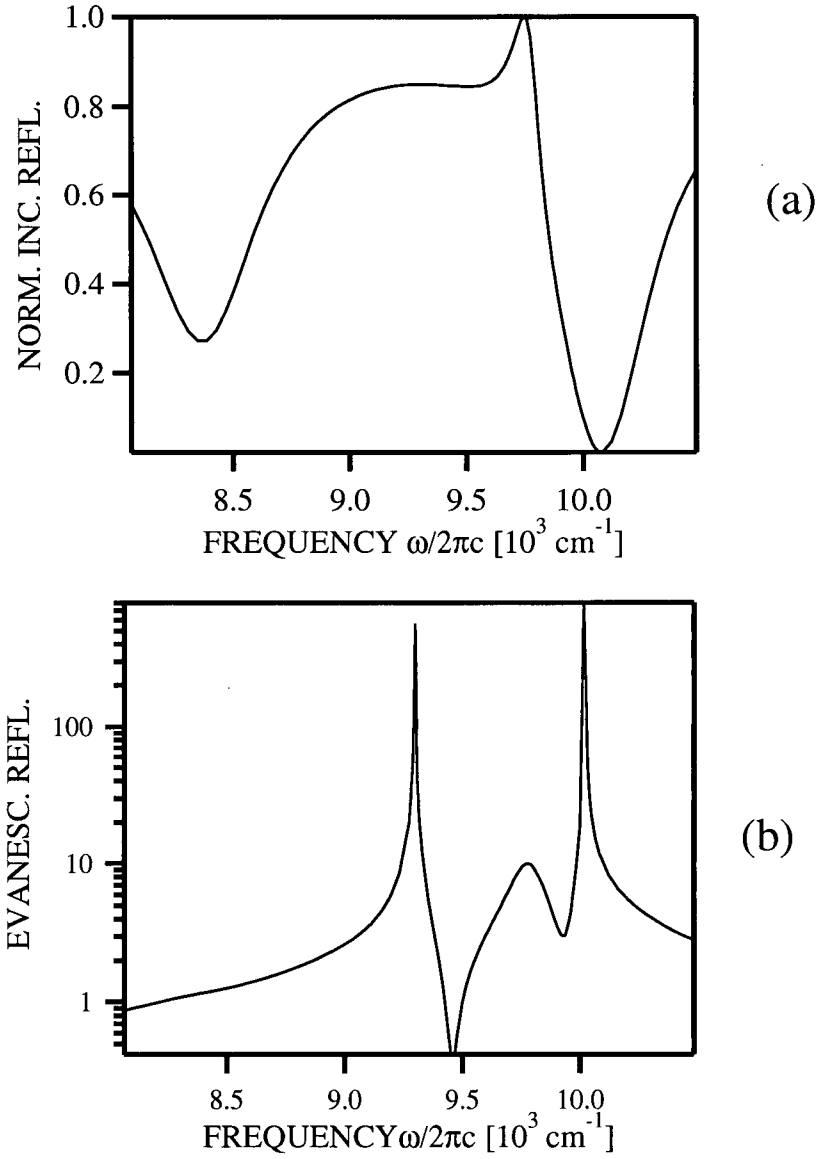


Figure 2.30: Calculated specular reflectivity spectra for light incident on the structure depicted in Figure 2.27 with $r/\Lambda = .2821$. (a) Normal incidence specular reflectivity, *i.e.*, light incident with $\beta = 0$. (b) Reflectivity for *s* polarized evanescent light incident with $\beta = \beta_G \hat{x}$.

2.4 Convergence

We recall that in the FDRS algorithm described above the structure being modelled is described by a finite, discrete, 3D mesh of the electric susceptibility and magnetic permeability constants. The components of the electric and magnetic fields are computed on a finite, discrete, 3D mesh, and a scattering matrix is computed for a finite, discrete set of plane wave like basis functions. There are, in principle, several distinct issues with respect to convergence having to do with the choice of the number of mesh points, and the number of basis wave functions to include in the calculation.

Firstly, for any given basis state, the accuracy of the propagation algorithm is limited by the sizes of the in-plane and z direction meshes relative to the wavevector of the basis state, as expressed by equations 2.36–2.38.

The second issue relates to the number of plane wave-like basis functions included in the calculation. Even for thin sinusoidal gratings, higher order scattering requires, in principle, that an infinite number of plane waves be included. Of course, for any given structure, there will only be *significant* scattering to a finite subset of these. The end result is that the number of plane waves to be included, either to capture the essential physics, or further, to give acceptable quantitative results will depend on the structure.

The third issue has to do with the relationship between the number of mesh points used for the field and the number of basis functions used in the calculation. We recall that the basis functions are essentially plane waves with a particular in-plane wavevector; they represent the different discrete in-plane Fourier components of the fields. The Nyquist criterion requires that the number of mesh points in each direction (x and y) be at least equal to the number of Fourier components (or basis functions) in that direction. This simply allows the basis functions to be represented on the real-space mesh without aliasing. However, if the number of in-plane mesh points exceeds the number of basis functions included in the calculation, then the fields at the end of the integration may contain significant higher spatial frequency content than that included in the plane wave

basis states onto which the fields are projected. This leads to a “scattering out of the basis” and quantitative errors. Because the problem is cast as an *inverse* scattering calculation requiring the transfer matrix to be inverted to yield the scattering matrices, one flagrant manifestation of this inconsistency is that the computed specular reflectivity spectra contain values that exceed unity for propagating waves and thus violate the principle of flux conservation.

Ideally, to insure self-consistency, it is preferable to perform the calculation with the same number of mesh points as basis functions. However, this would mean that the basis functions with the highest in-plane propagation vectors are not integrated very accurately because $k_{x/y}a_{x/y} = (\frac{N}{2} \frac{2\pi}{\Lambda})(\frac{\Lambda}{N}) = \pi \not\ll 1$. Since these higher order field components are relatively small, the significance of this error should be small. However, in the waveguide structures of interest here, these higher order components sometimes become erroneously enhanced and thereby introduce false modes in the reflectivity spectra. In some cases, this leads to spurious features appearing in the spectral range in the vicinity of the second order TE gap. One solution is to simply increase the number of basis functions and mesh points simultaneously such that the spurious features gradually move up and out of the range of interest. This is computationally very expensive. However, it turns out that by having the number of mesh points exceed the number of basis functions by one or two, the spurious features are quickly moved up and out of the frequency range of interest. This comes at the cost of the violation of flux conservation. However, the excess reflected flux in this regime on the structures studied is only in the range of a couple of percent. No such spurious features arise in the spectra presented in this section and so the calculations were carried out with the same number of mesh points as basis functions.

A fourth issue concerns the inherent pitfalls in attempting to represent the continuous permittivity and permeability functions, often containing sharp transitions, on a discretely sampled mesh. We recall that, as a result of equations 2.64 to 2.67, the number

of mesh points used to describe the structure in terms of its permittivity and permeability ($\epsilon' - \mu'$ -mesh) is related to that of the mesh points for the fields, as indicated by figure 2.2. This means that adjusting the $\epsilon' - \mu'$ -mesh necessarily requires adjusting the field mesh as well.

The remainder of this section describes the various tests performed to determine the convergence properties of the FDRS calculations and discusses the results with a view to the issues raised above.

2.4.1 Convergence of the Integration Scheme Alone

A simple, basic test of the accuracy and convergence of the code was performed by using it to determine the frequency of the bound modes of an untextured slab from the appearance of the poles in the evanescently probed specular reflectivity for large in-plane propagation vector. Such a test is attractive because an exact answer can be calculated independently by using Fresnel coefficients [42]. It should also be noted that since the problem possesses *continuous* translational symmetry in the in-plane directions, the size of the in-plane unit cell for the calculation, may, in principle, be chosen arbitrarily. Thus, the size of the in-plane mesh on which the fields are integrated may be varied continuously. Additionally, since there is no scattering to higher order in-plane Fourier components in the case of the untextured waveguide, it is sufficient to include only one plane wave corresponding to the in-plane Fourier component of the field having the in-plane propagation constant for which it is desired to find the bound mode frequency in the calculation. This further allows only one mesh-point per unit cell to be used in the integration of the fields. As a result the FDRS code becomes much less computationally expensive than in the textured case.

However, purely for convenience, in the studies on the convergence properties of the untextured waveguide mode frequencies presented here, the FDRS parameters were set as follows. The in-plane unit cell was set to a square of side $\Lambda = 500$ nm, which

was typical of the actual textured structures studied and modelled in the present work. Only one plane wave was used but the number of in-plane mesh points per unit cell and the number of z -mesh points were varied. The in-plane wave vector of the incident evanescent light was set to $\beta_{\text{inc}} = 2\pi/\Lambda$. The untextured waveguide structure used in the calculation consisted of a 120 nm slab of material with $\epsilon' = 12.25$ clad above and below by air ($\epsilon' = 1.0$).

Figure 2.31 depicts a logarithmic plot of the absolute value of the error as a function of the number of mesh points that were included in the calculation in each of the \hat{x} and \hat{y} directions. The different curves (lines) from top to bottom on the graph are for increasing numbers (specifically: 12, 22, 32, 42, 62, and 122) of mesh points in the \hat{z} direction. As the number of z steps increases the curves approach a straight line, with a slope of -2 on the logarithmic plot, indicating that for sufficiently fine z -mesh, the error decreases as the inverse square of the number of mesh points in each of the \hat{x} and \hat{y} directions.

Since there is no scattering to higher order in-plane Fourier components in the case of the untextured waveguide, it is sufficient to include in the calculation only the one in-plane Fourier component having the in-plane propagation constant for which it is desired to find the bound mode frequency. The error here may arise only from the coarseness of the mesh on which Maxwell's equations are integrated. Therefore, the preceding analysis tests only the convergence of the integration scheme, itself.

2.4.2 Overall Convergence Behaviour for Textured Structures

In the case of a textured waveguide, the eigenmodes contain, in principle, an infinite number of in-plane Fourier components of the fields. It is expected that only a finite subset of these are significant, and so the issue arises of how many need be included in the calculation to yield quantitatively accurate results. As in the untextured case, the number of mesh points in the in-plane ($x-y$), as well as in the normal (z) direction may

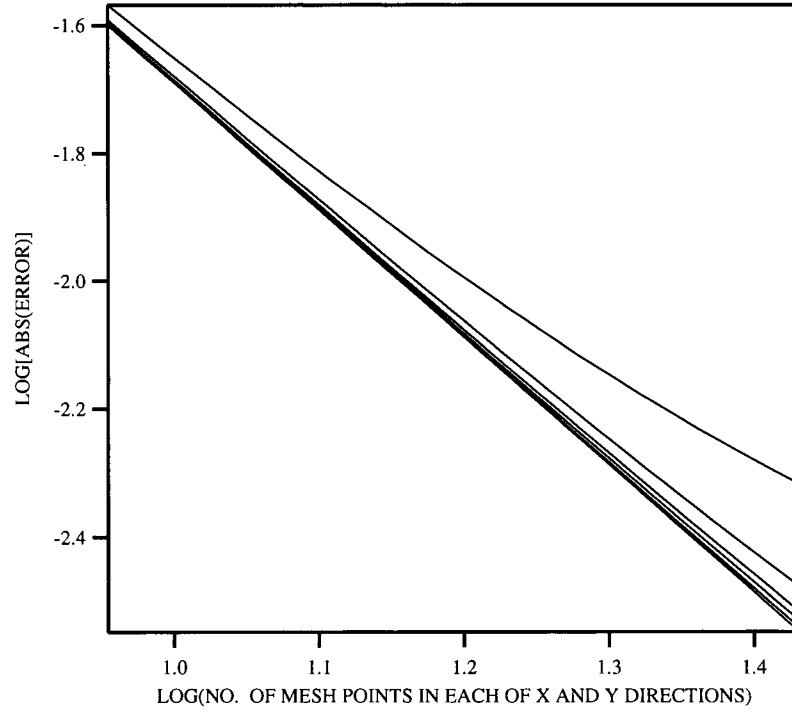


Figure 2.31: Logarithmic plot of the absolute value of the error on the bound mode frequencies of an untextured slab waveguide as calculated by the FDRS method as a function of the number of mesh points in each of the \hat{x} and \hat{y} directions included in the calculation. The (artificial) unit cell for the FDRS method was set to a square of side $\Lambda = 500$ nm, and the in-plane wave vector of the incident evanescent light was set to $\beta_{\text{inc}} = 2\pi/\Lambda$. The structure used for the calculation consisted of a 120 nm slab of material with $\epsilon' = 12.25$ clad above and below by air ($\epsilon' = 1.0$). The different curves (lines) are for increasing numbers, (specifically: 12, 22, 32, 42, 62, and 122), from top to bottom on the graph, of mesh points in the \hat{z} direction.

also be varied. Rather than exploring the entire parameter space, which is computationally expensive, particularly for two-dimensionally textured structures, the approach adopted in the work described below is to vary these parameters in a related fashion. This is done as follows. We define N to be the number of reciprocal lattice vectors (or Fourier components of the field) used per reciprocal-space direction, as shown in figure 2.4. Thus, in 2D, there will be $N \times N$ reciprocal lattice vectors. We also set equal to N the number of field mesh points per real-space direction, so that there are $N \times N$ field mesh points in 2D. Finally, we set to $N + 2$ the number of *pairs* of planes on which the electric and magnetic field are alternately defined (see figure 2.3). The additional two pairs of planes account for the fact that one pair of planes is required in each of the untextured regions, so that the number of planes in the textured region remains N . Therefore, in this scheme, the aspect ratio of the three-dimensional mesh or “element” remains unchanged as N is varied. We note that for the 2D square lattice, the mesh sizes for the approximations defined in equations 2.33–2.35 are given by:

$$a = b = \sqrt{2} \frac{\Lambda}{N} \quad (2.114)$$

$$g = \frac{d}{N} \quad (2.115)$$

where d is the thickness of the textured region. The FDRS calculation may then be performed several times for the same physical structure but for increasing values of this one parameter, N , called the “number of elements”, with respect to which the convergence properties of the mode frequencies and widths may be studied.

Figure 2.33 shows the results of such a study for the strongly one-dimensionally textured slab waveguide depicted in Figure 2.32 with slab and grating thickness, $d = 80$ nm. The plots with the square markers and dashed lines in Figure 2.33a and Figure 2.33b represent the frequency and width respectively of the lossy mode at the zone-centre ($\beta = 0$) as a function of the number of elements used in the FDRS calculation. These plots indicate that the convergence behaviour of this model with respect to both the

mode frequency and linewidth possesses a strong oscillatory component.

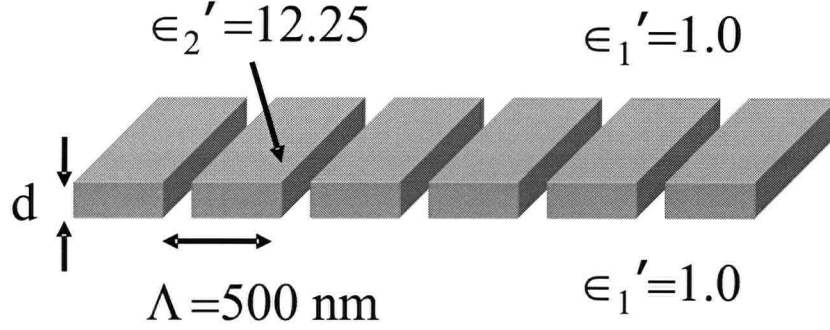


Figure 2.32: Slab waveguide with “strong” 1D texture: the structure consists of a slab of thickness d of $\epsilon' = 12.25$ material, clad above and below by air, with a 1D square-toothed grating having a pitch, $\Lambda = 500 \text{ nm}$, and an air filling fraction of 25% that completely penetrates the slab.

By damping out this oscillatory component, the convergence properties of the model can be improved. This can be achieved by spectrally filtering the underlying $\epsilon' - \mu'$ mesh such that it contains no higher spatial Fourier components than that permitted by the Nyquist criterion for the $x - y$ mesh employed for the particular calculation as dictated by the number of elements used therein. In other words, an anti-aliasing filter must be applied to the underlying $\epsilon' - \mu'$ profile of the ideal structure that is appropriate for the coarseness of the mesh on which the fields are to be sampled for the particular calculation. The filter used in this work is a Kaiser window [43] with $\beta_{\text{Kaiser}} = 2.3$ and N_{Kaiser} set equal to the number of elements used in the FDRS calculation (in order to optimally satisfy the Nyquist criterion).

The plots with the round markers and solid lines in Figure 2.33a and Figure 2.33b represent the corresponding results of the FDRS calculations when they are carried out with this spectral pre-filtering of the $\epsilon' - \mu'$ profile implemented. Monotonic convergence with respect to the number of elements is now exhibited.

In order to obtain an estimate of the upper bound on the error of the FDRS calculation it is useful to re-plot the above convergence results with spectral pre-filtering as

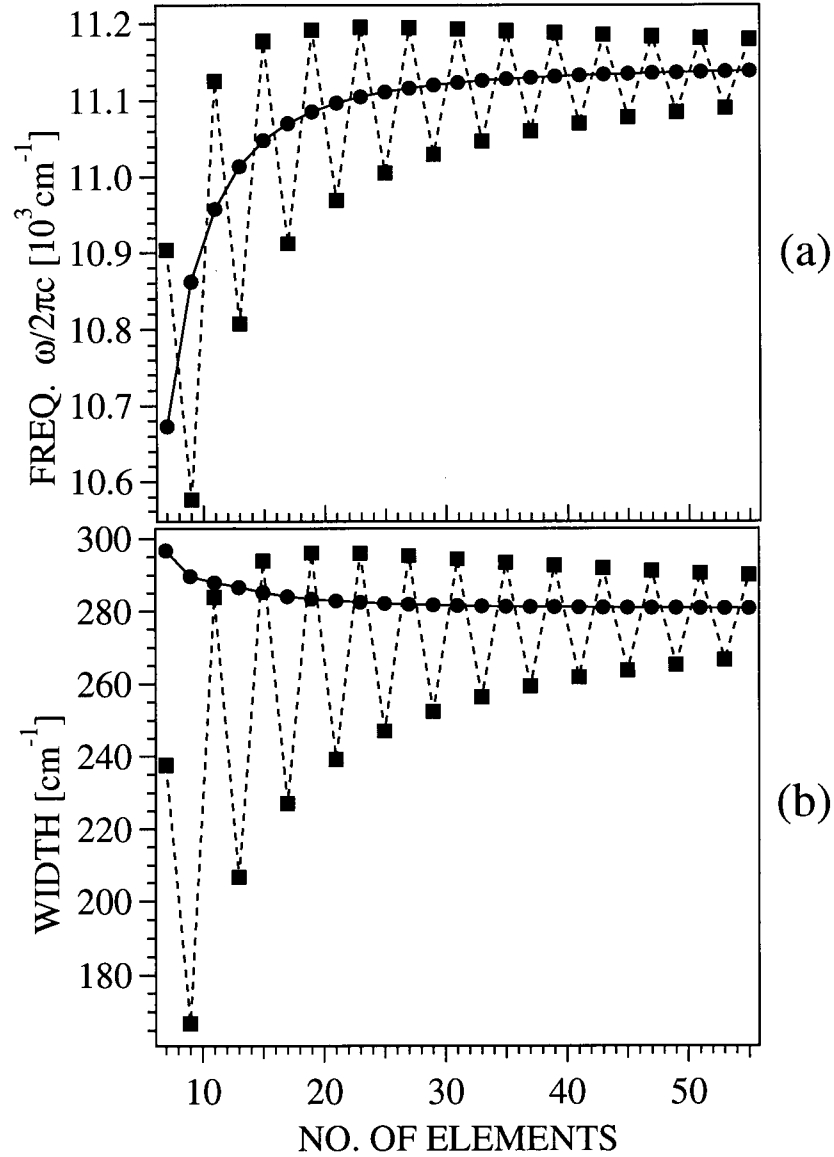


Figure 2.33: Mode frequency (a) and width (b) *vs.* the "number of elements" (see text) used in FDRS calculation for the structure depicted in Figure 2.32 with $d = 80$ nm. The results are for the second-order lossy mode at the zone-centre. Plots with round markers and solid lines depict results with anti-aliasing spectral filtering of the $\epsilon' - \mu'$ profile implemented; plots with square markers and dashed lines depict results without filtering of the $\epsilon' - \mu'$ profile.

a function of the square of the mesh size normalized by the size of the unit cell (grating pitch). This plot is shown in Figure 2.34. The dashed lines represent the best fit line obtained from a least-squares fit. The y-intercept of the best fit line may be taken as an estimate of the final converged value, and, hence, an estimate of the error for a particular calculation may be obtained by subtracting it from the value of the calculation. In the case of the width, there was a regime at the larger mesh sizes (fewer elements used) where the convergence was not very linear with respect to the square of the mesh size, but when the mesh size squared decreases below a certain point ($\sim 10 \times 10^{-3}$ on the graph, corresponding to 15 elements), both the linearity and rate of convergence improve. Therefore, the fitting was only carried out using the results for these smaller mesh sizes as indicated by the presence of the dashed line.

For this structure it was found that a computation with 15 elements was sufficient to produce results that are converged to within 1% for the mode frequencies, and to within 1.7% for the width.

Similar convergence behaviour is exhibited in the case of two-dimensional strong texture. Figure 2.36 depicts the convergence of the mode frequency and width for the second-order lossy mode at the zone-centre for the structure depicted in Figure 2.35. This structure is very similar to those used in the experimental work described later in this thesis. Here it is found that a computation with 17 elements, requiring approximately two hours of runtime on a current PC (*AMD Duron 1600* 1.6 GHz, 1GB RAM), produces results that are converged to within 1% for the mode frequency and to within 7% for the width.

Finally, it is perhaps not surprising that the FDRS calculations converge roughly linearly with the square of the mesh size since this is the leading error term in the approximations in equations 2.33 to 2.35.

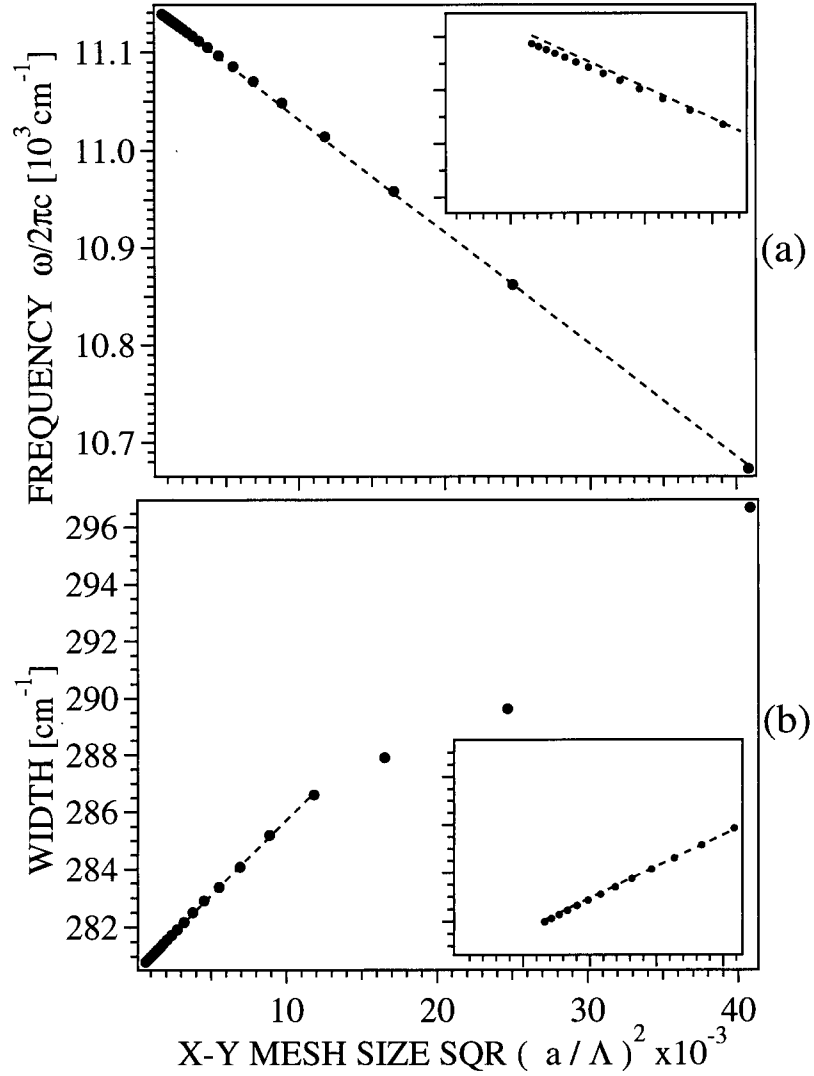


Figure 2.34: (a) Mode frequency and (b) width, *vs.* square of the $x - y$ mesh size normalized by the unit cell size (or grating pitch) used in the FDRS calculation for the structure depicted in Figure 2.32 with $d = 80$ nm. The results are for the second-order lossy mode at the zone-centre. The insets provide a magnified view of the small mesh size regions of their respective graphs. The FDRS calculation was carried out with anti-aliasing spectral filtering of the $\epsilon' - \mu'$ profile implemented. The dashed lines represent the best fit line obtained from a linear least squares fit. In (b) the rightmost three points were ignored in the fitting.

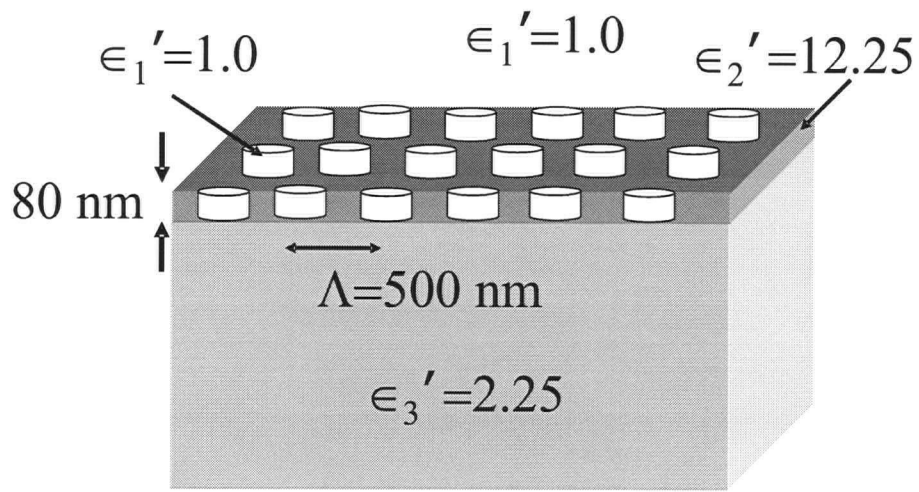


Figure 2.35: Strongly 2D textured thin asymmetric slab waveguide: the structure consists of a 80 nm-thick slab of $\epsilon' = 12.25$ material which forms the guiding core, clad above by air and below by material with $\epsilon' = 2.25$. The core waveguide layer is penetrated by a 2D square array of holes on a pitch, $\Lambda = 500$ nm, and with hole radii given by $r/\Lambda = 0.2821$.

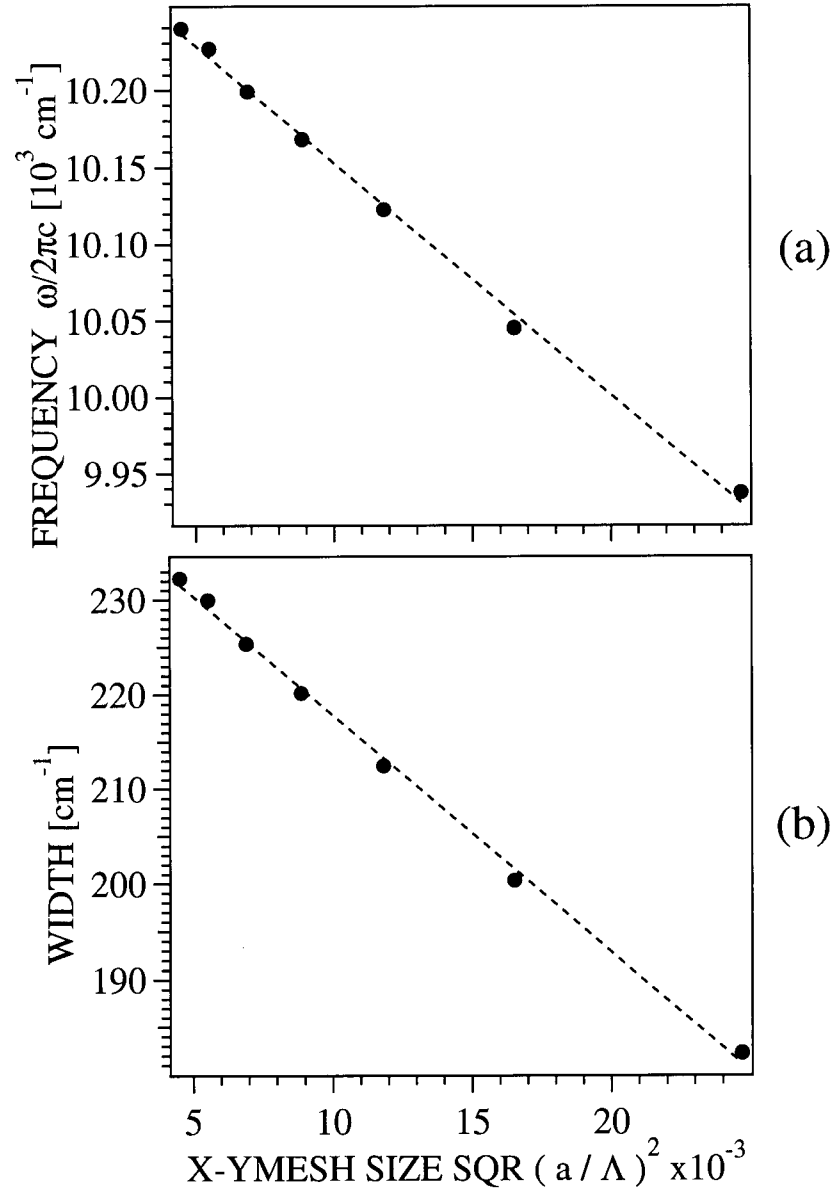


Figure 2.36: Mode frequency (a) and width (b) *vs.* square of the $x - y$ mesh size normalized by the unit cell size (or grating pitch) used in the FDRS calculation for the structure depicted in Figure 2.35. The results are for the second-order lossy mode at the zone-centre. The FDRS calculation was carried out with anti-aliasing spectral filtering of the $\epsilon' - \mu'$ profile implemented. The mesh sizes correspond (from left to right in the graph) to 21×21 , 19×19 , 17×17 , 15×15 , 13×13 , 11×11 , and 9×9 elements used in the calculation.

2.5 Comparison with Green's Function Based Model

Due to run times of several hours required to produce well-converged, resolved spectra over a broad frequency range for comparison to those obtained experimentally, the FDRS model presented in this thesis was used for validation of the more computationally efficient Green's Function (GF) based model [40, 41] which was then used for extensive fitting to the experimental spectra.

In the GF model, the 1D or 2D grating is treated as a modification to the linear susceptibility, $\Delta\chi$, of some untextured slab waveguide structure. Maxwell's equations are then arranged so that the polarization arising from $\Delta\chi$ is isolated as a driving term on the right hand sides. In this formulation, the homogeneous solution is merely the known solution for the case of an untextured waveguide. Using a Green's function formalism, a particular solution may then be found for the spatial Fourier transform of the electric field. The solution takes the form of an integral of the polarization generated by $\Delta\chi$ times the Green's function. The polarization is then re-expressed in terms of $\Delta\chi$ times the electric field to yield an integral equation. Due to the discrete translational symmetry of the problem, $\Delta\chi$ may be expanded in an infinite but discrete Fourier series over the reciprocal lattice vectors of the grating. Also, due to Bloch's theorem, only the corresponding discrete set of spatial Fourier components of the field need be computed. Using the fact that $\Delta\chi$ is non-zero only in the grating layer, and making the approximation that the fields do not vary significantly over the thickness of the grating (thin grating approximation), the integral equation is converted to a set of algebraic equations which couple the various Fourier components of the fields through the various Fourier components of $\Delta\chi$. A full, detailed description of the GF model is beyond the scope of this thesis and is given elsewhere [40, 41]. However, from the brief description given above, it is important to note: 1) that the number of reciprocal lattice vectors included in any actual calculation will be finite and may, therefore, affect the accuracy of the results; and 2) that the accuracy of the results will also be affected by the extent

to which the fields remain constant over the thickness of the grating. In the remainder of this section we demonstrate the accuracy of this Green's function-based reflectivity calculation, when applied to a thin slab, by comparing it with results from the FDRS model.

Figure 2.37 compares the near-normal ($\beta = 0.02\beta_G$ along the $\Gamma - X$ direction) specular reflectivity spectra from a 2D textured slab, as calculated using the GF model (upper plot), and using the FDRS model (lower plot). The structure used in the comparison is the same as that depicted in Figure 2.35 and is intended to be a somewhat simplified version of that used in the experimental work described in this thesis. It consists of an 80 nm slab of material with $\epsilon' = 12.25$ completely penetrated by a 2D square array of cylindrical holes on a 500 nm pitch and 25% air filling fraction, all sitting on a semi-infinite substrate with $\epsilon' = 2.25$. The number of mesh points and plane waves used for the FDRS model are as described in section 2.4.2 using 17 elements. The GF calculation included the nine reciprocal lattice vectors at $\vec{0}$, $\pm\beta_G\hat{x}$, $\pm\beta_G\hat{y}$, $\pm\beta_G\hat{x} \pm \beta_G\hat{y}$.

The computation time required for the GF model is approximately 1/2000 of the time required for the FDRS approach. In Figure 2.37 it is clear that the spectra are in excellent agreement, both with respect to the locations and widths of the resonances. The absolute frequencies of the modes differ by less than 1.5%, which is smaller than uncertainties arising from grating fabrication tolerances (pitch, filling fraction, etch profile), epitaxial growth tolerances (layer thickness and alloy composition), uncertainties in literature values of refractive indices, as well as experimental uncertainties on the in-plane wavevector of the probing beam. Furthermore, the widths of the broad, p polarized features were extracted from the results of both calculations and found to agree to within 6.6%. Similar calculations on the same structure at precisely normal incidence ($\beta = 0$) using both models yielded spectra, exhibiting, as expected, a single broad degenerate feature in each of the s and p polarized spectra. Here, the agreement between the two models was within 1.0% with respect to the absolute frequency, and to within

6.5% with respect to the width.

To address the limitations imposed by the thin-grating approximation made in the GF model we consider a symmetric planar waveguide consisting of a slab of varying thickness of $\epsilon' = 12.25$ -material, with air ($\epsilon' = 1.0$) above and below, completely penetrated by a 1D grating having an air-filling fraction of 25%. The structures are similar to that depicted in Figure 2.17. Figure 2.38 plots the location of the upper and lower edges of the 2nd order gap as calculated with the GF model (dotted curve), and FDRS model (solid curve) for varying thickness of the grating (=slab). The FDRS model was verified to be converged to within 1% for the upper band and 0.2% for the lower band (using 17 “elements” in the calculations). The GF calculation included the three reciprocal lattice vectors at $\vec{0}$ and $\pm\beta_G\hat{x}$. It is clear that for thin gratings the two methods agree well. When the waveguide-grating is 80 nm thick the two methods agree to within 1.4% for the upper edge, and 0.27% for the lower edge. However, when the waveguide is 250 nm thick (a thickness greater than those that are usually of interest in the context of studying photonic crystal membranes, which is the object of the present work) the two methods agree to within 6.2% for the upper edge, and 0.8% for the lower edge. The percent difference between the two methods increases as the thickness of the grating and slab-waveguide increases.

However, it is not possible, in general, to specify a simple relationship between the GF model’s accuracy and the grating thickness. For a given structure, the accuracy depends on the mode being studied, as demonstrated in this example. Furthermore, different layer structures may result in different errors for a fixed grating thickness. The FDRS model is, therefore, useful for benchmarking and verifying the accuracy of the GF model for each type of structure.

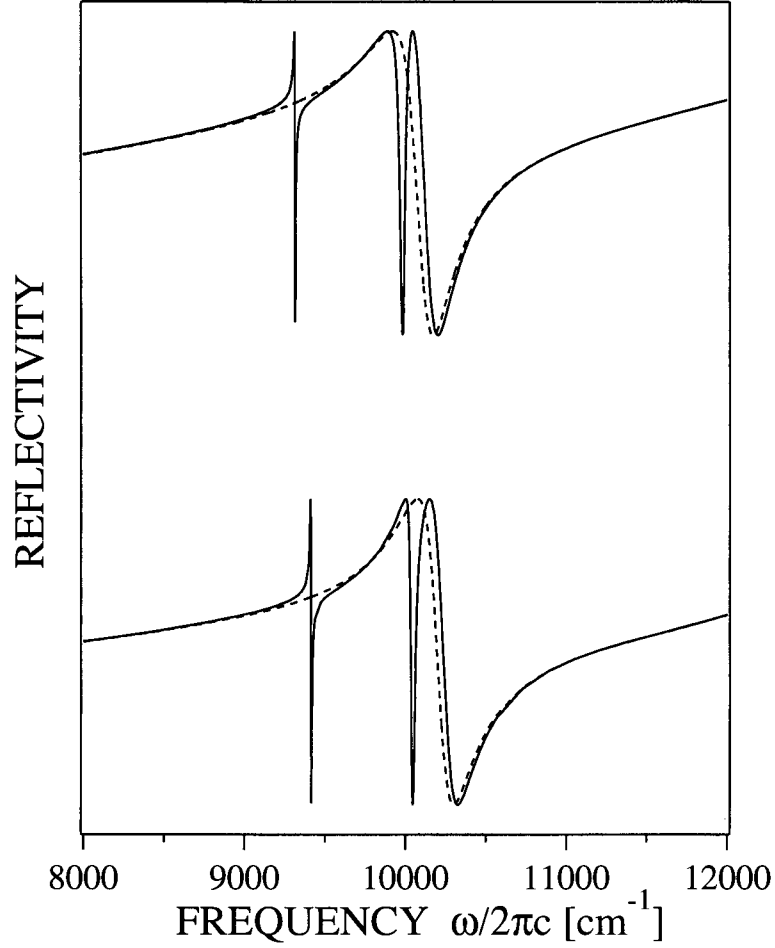


Figure 2.37: Near-normal incidence specular reflectivity spectra for light incident with in-plane wavevector $\beta = 0.02\beta_G$ along the $\Gamma - X$ direction calculated with the FDRS model (lower plot) and the GF model (upper plot). The parameters used for the FDRS model are as described in section 2.4.2 using 17 elements. The GF calculation included the nine reciprocal lattice vectors at $\vec{0}$, $\pm\beta_G\hat{x}$, $\pm\beta_G\hat{y}$, $\pm\beta_G\hat{x} \pm \beta_G\hat{y}$. The solid lines represent the s polarized spectra, and the dashed lines represent the p polarized spectra. The structure being modelled is the same as the one depicted in Figure 2.27. The resonance widths and shape are in excellent agreement. The mode frequencies agree to within 1.5%.

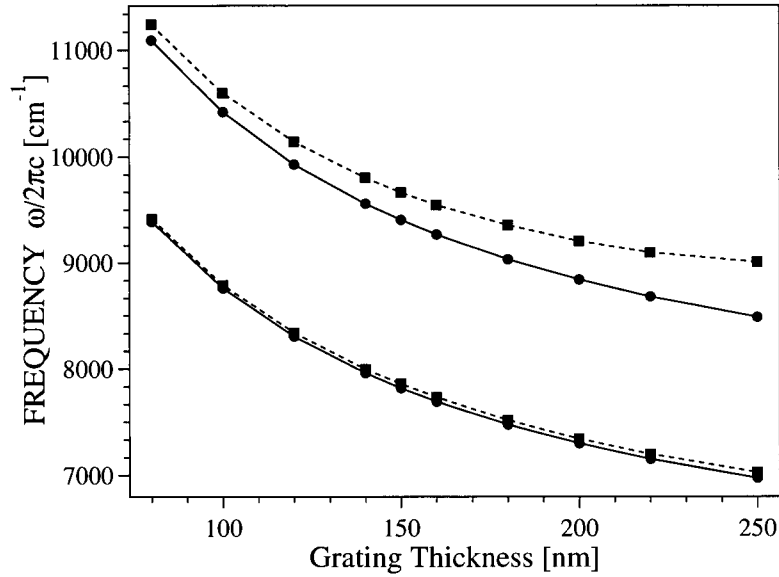


Figure 2.38: Location of the upper and lower edge of the 2nd order gap in a 1D textured symmetric waveguide as a function of guide and grating thickness, d (see Figure 2.32). The waveguide core is made of material with $\epsilon' = 12.25$ and clad above and below by air ($\epsilon' = 1.0$). The grating, which completely penetrates the waveguide core, has an air filling fraction of 25%. The dashed lines are for the calculation with the GF model, the solid lines with the FDRS model which was verified to be converged to within 1% for the upper band and 0.2% for the lower band (using 17 “elements” in the calculations). The GF calculation included the three reciprocal lattice vectors at $\vec{0}$ and $\pm\beta_G\hat{x}$.

2.6 Significance of Modification to Pendry's Method

As previously mentioned, this scheme for integration of Maxwell's equations on a discrete mesh is a modified version of a similar scheme published by J.B Pendry [44]. The principal difference lies in the approximations Pendry makes for the wavevector. Instead of equations 2.33 to 2.35, Pendry defines two approximate wavevectors:

$$\begin{aligned} k_x &\approx [\exp(ik_x a) - 1]/ia = \kappa_x^E \\ k_y &\approx [\exp(ik_y b) - 1]/ib = \kappa_y^E \\ k_z &\approx [\exp(ik_z g) - 1]/ig = \kappa_z^E \end{aligned} \quad (2.116)$$

and

$$\begin{aligned} k_x &\approx -[\exp(-ik_x a) - 1]/ia = \kappa_x^H \\ k_y &\approx -[\exp(-ik_y b) - 1]/ib = \kappa_y^H \\ k_z &\approx -[\exp(-ik_z g) - 1]/ig = \kappa_z^H \end{aligned} \quad (2.117)$$

Substitution of (2.116) into (2.31) and (2.117) into (2.32), Fourier transformation to real space, and elimination of the z components in a manner similar to the derivation presented in section 2.2 yields, for example, for the E_x component of the fields:

$$\begin{aligned} E_x(\mathbf{r} + \mathbf{g}) &= E_x(\mathbf{r}) + \frac{g^2 \omega^2}{c^2} \mu'(\mathbf{r}) H'_y(\mathbf{r}) + \frac{g^2}{a} \{ \\ &\quad + \frac{H'_x(\mathbf{r} + \mathbf{a} - \mathbf{b}) - H'_x(\mathbf{r} + \mathbf{a})}{\epsilon'(\mathbf{r} + \mathbf{a})b} - \frac{H'_x(\mathbf{r} - \mathbf{b}) - H'_x(\mathbf{r})}{\epsilon'(\mathbf{r})b} \\ &\quad + \frac{H'_y(\mathbf{r} - \mathbf{a}) - H'_y(\mathbf{r})}{\epsilon'(\mathbf{r})a} - \frac{H'_y(\mathbf{r}) - H'_y(\mathbf{r} + \mathbf{a})}{\epsilon'(\mathbf{r} + \mathbf{a})a} \} \end{aligned} \quad (2.118)$$

Comparing this with equation 2.64 derived in section 2.2:

$$\begin{aligned} E_x(\mathbf{r} + \boldsymbol{\gamma}) &= E_x(\mathbf{r} - \boldsymbol{\gamma}) + \frac{g^2 \omega^2}{c^2} \mu'(\mathbf{r}) H'_y(\mathbf{r}) + \frac{g^2}{a} \{ \\ &\quad - \frac{H'_x(\mathbf{r} + \boldsymbol{\alpha} + \boldsymbol{\zeta}) - H'_x(\mathbf{r} + \boldsymbol{\alpha} - \boldsymbol{\zeta})}{\epsilon'(\mathbf{r} + \boldsymbol{\alpha})b} + \frac{H'_x(\mathbf{r} - \boldsymbol{\alpha} + \boldsymbol{\zeta}) - H'_x(\mathbf{r} - \boldsymbol{\alpha} - \boldsymbol{\zeta})}{\epsilon'(\mathbf{r} - \boldsymbol{\alpha})b} \\ &\quad - \frac{H'_y(\mathbf{r}) - H'_y(\mathbf{r} - 2\boldsymbol{\alpha})}{\epsilon'(\mathbf{r} - \boldsymbol{\alpha})a} + \frac{H'_y(\mathbf{r} + 2\boldsymbol{\alpha}) - H'_y(\mathbf{r})}{\epsilon'(\mathbf{r} + \boldsymbol{\alpha})a} \} \end{aligned} \quad (2.119)$$

we see that both contain the four terms in braces corresponding to discrete, numerical derivatives arising from $\nabla \times \mathbf{H}$ in Maxwell's Equations. However, Pendry's approximations for \mathbf{k} lead to forward or backward difference terms for the derivatives rather than the centred difference terms that arise in the approximations for \mathbf{k} used in the present work.

This introduces an artificial chirality for the scattering to Fourier components in the $\pm x$ and $\pm y$ directions in the plane, and this asymmetry prevents the model from producing specular reflectivity spectra with features that exhibit the expected degeneracies at points of high symmetry, such as zone-centre.

Figures 2.39 and 2.40 compare the specular reflectivity spectra produced by the model using Pendry's original approximations for \mathbf{k} to those from the model implemented in this work. The specular reflectivity spectra are for light incident from air on a 80 nm film of material having a refractive index of 3.5, textured with a square array of 300 nm diameter cylindrical holes filled with a material having a refractive index of 1.5, all on a substrate of refractive index 1.5. Figure 2.39 is for the case of normal incidence, while Figure 2.40 is for the case of light incident with in-plane wavevector of $\beta/\beta_G = 0.01$ along the $\Gamma - X$ direction.

At normal incidence, Pendry's original scheme does produce identical spectra for both the s and p reflectivity. However, it produces three distinct features in each of these spectra rather than one degenerate feature. More generally, for the case of radiation incident with a wavevector $\beta = 0.01\beta_G$ along the $\Gamma - X$ symmetry direction, Pendry's original scheme yields three features in each polarization rather than the $3s+1p$ combination required by the symmetry of the 2D square lattice.

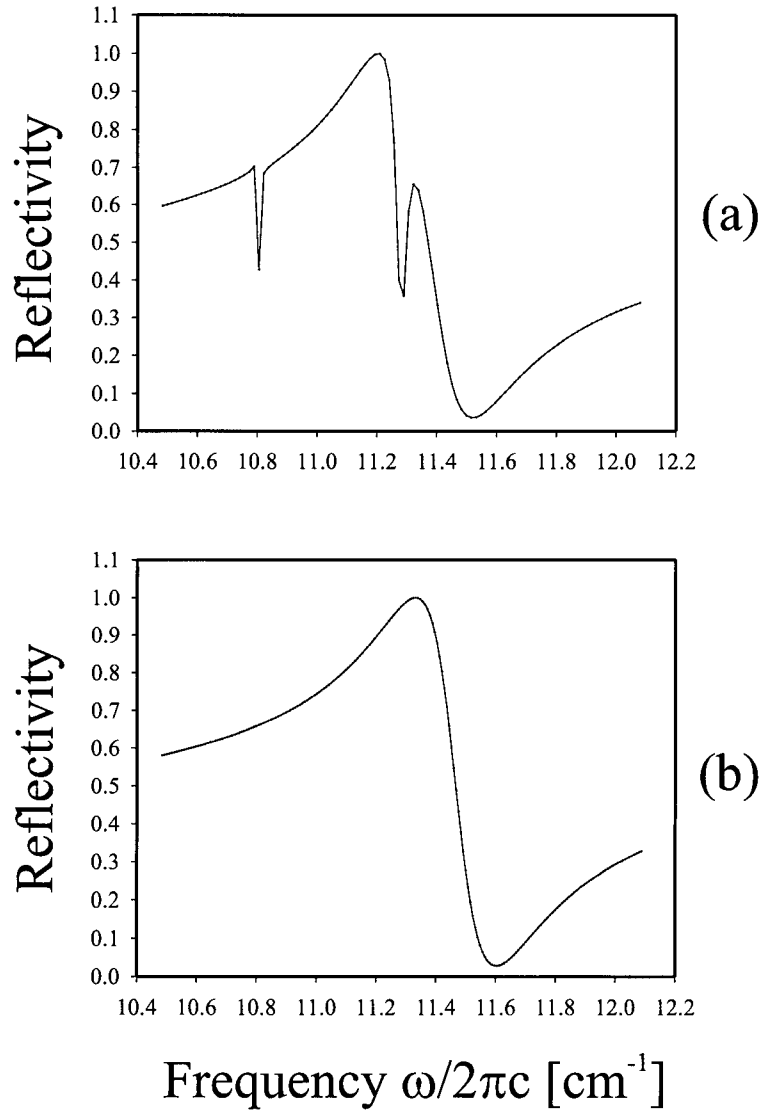


Figure 2.39: Calculated normal incidence specular reflectivity spectra for light incident with zero in-plane wavevector. The calculation is performed (a) using Pendry's original approximations for \mathbf{k} and (b) the approximations for \mathbf{k} implemented in this work. The solid and dashed lines, which overlap completely here, represent the *s* polarized and *p* polarized spectra respectively. The light is incident on a film of material having a dielectric constant of 12.25 textured with a square array of 300 nm diameter cylindrical holes filled with a material having a dielectric constant of 2.25, all on a substrate with a dielectric constant of 2.25. The pitch of the grating is 500 nm.

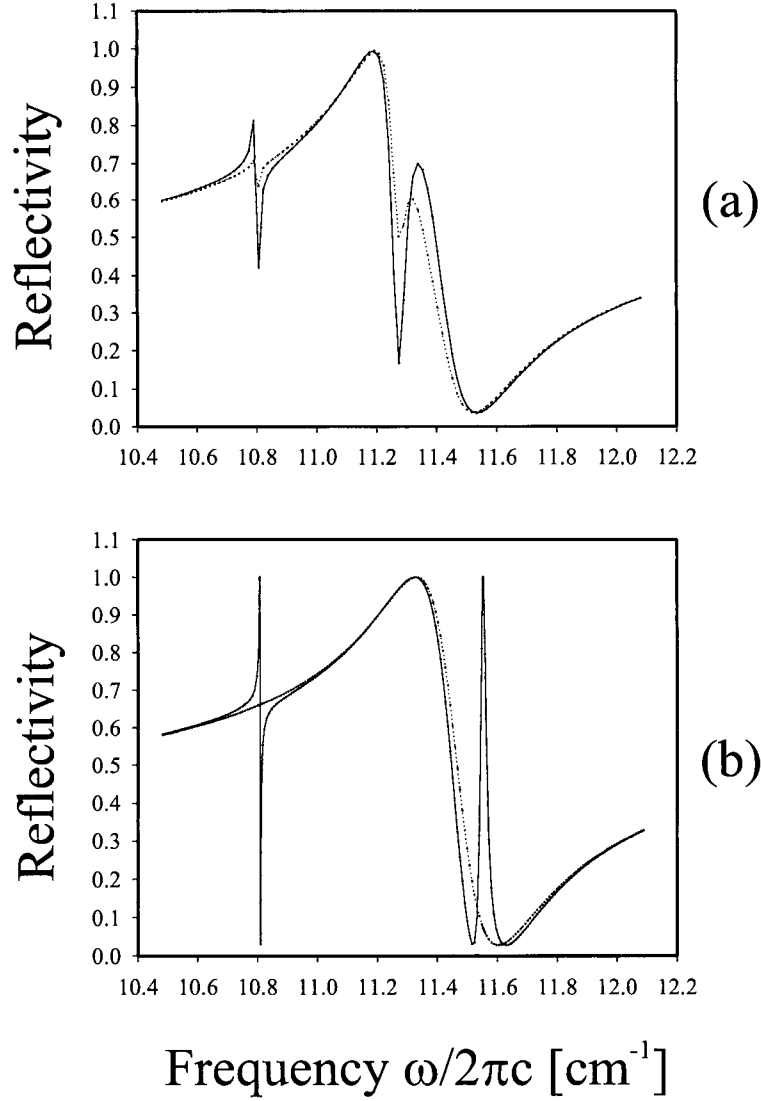


Figure 2.40: Calculated near-normal incidence specular reflectivity spectrum for light incident with in-plane wavevector, $\beta = 0.01\beta_G$, along the $\Gamma - X$ direction. The calculation is performed (a) using Pendry's original approximations for \mathbf{k} and (b) the approximations for \mathbf{k} implemented in this work. The solid lines represent the s polarized spectra, the dashed lines depict the p polarized spectra. The light is incident on a film of material having a dielectric constant of 12.25 textured with a square array of 300 nm diameter cylindrical holes filled with a material having a dielectric constant of 2.25, all on a substrate with a dielectric constant of 2.25. The pitch of the grating is 500 nm.

2.7 Summary

This chapter has described a numerical model for calculating optical scattering from an arbitrary slab waveguide structure with an embedded 2D photonic crystal. The algorithm involves the projection of plane wave-like basis functions onto a real-space mesh and integration of each of these functions through the structure in the direction perpendicular to the slab, using an approximate, discretized version of Maxwell's equations in real space, followed by projection back onto the basis of plane wave functions, so as to form a transfer matrix. The plane wave-like basis functions are the actual eigenfunctions for the translation operation on the discrete mesh using the approximate, discretized Maxwell's equations in a bulk, untextured medium. The model is capable of computing efficiently the scattering from structures with buried photonic lattices by combining the real-space integration scheme for the textured layer with Fresnel coefficients computed for the untextured layers, using a transfer matrix formalism. Scattering spectra that were generated using this numerical model for various planar waveguide structures with both strong and weak, 1D and 2D photonic lattices were presented interpreted, and discussed in terms of the dispersion, lifetimes, and polarization properties of the slab modes of their various respective structures. Results of an investigation of the convergence behaviour of the numerical algorithm were presented for the thin "hard" waveguide photonic crystals of interest in this work which showed that convergence was greatly improved with the application of anti-aliasing pre-filtering to the dielectric profile. The results also showed that by using a mesh size and set of basis functions that required a run time of only a couple of hours on a current PC (*AMD Duron 1600* 1.6 GHz, 1GB RAM) the mode frequencies were converged to within approximately 1% and the widths to within 7%. Mode frequencies and widths were calculated using a more efficient Green's function (GF) based method specific to the thin "hard" waveguide photonic crystal geometry and found to agree with the results from the method presented here to within 1.5% for the frequencies and 7% for the widths. Results were presented

which indicated that the agreement between the two models decreased as the depth of the textured layers was increased. Finally an explanation was given of how the incorrect polarization properties and lack of degeneracies expected at high crystal symmetry points exhibited by spectra using Pendry's original approximations were attributable to the introduction of an artificial chirality into the equations, and how this was rectified in the model presented in this work.

Chapter 3

Fabrication

3.1 Introduction and Overview

One of the author's early attempts at realizing a robustly guiding waveguide with strong 2D texture is depicted in the micrograph shown in Figure 3.1 taken using a scanning electron microscope (SEM). A view taken at higher magnification is shown in Figure 3.2.

The structure consists of a 100 nm GaAs film sitting on a $2.0\text{ }\mu\text{m}$ layer of $\text{Al}_{0.6}\text{Ga}_{0.4}\text{As}$ on a GaAs substrate. It was grown by Metal Organic Vapour Phase Epitaxy by Simon Watkins' group at Simon Fraser University. A $20\text{ }\mu\text{m} \times 100\text{ }\mu\text{m}$ array of holes of diameter 350 nm and period 480 nm was etched through the top GaAs layer using aqueous citric acid/hydrogen peroxide solution and an etch-mask of PMMA made by electron beam lithography. After removal of the mask, the structure was dipped in an aqueous hydrofluoric acid solution, which penetrated through the etched holes in the GaAs layer to selectively etch away the underlying $\text{Al}_{0.6}\text{Ga}_{0.4}\text{As}$ film while leaving the GaAs layers intact. The structure, therefore, constitutes a "freestanding", air/GaAs/air waveguide with high-index-contrast 2D texture embedded directly in the guiding core. Figure 3.2 also serves to illustrate the extent to which these thin, diaphanous structures represent the extreme non-perturbative limit of textured slab waveguides.

The problem with this approach is the lack of robustness, which additionally places an upper limit on the size of the freestanding area that can be produced before the whole structure buckles and collapses. In an attempt to fabricate a batch of ten such structures, each having a length of $90\text{ }\mu\text{m}$ and widths varying from $10\text{ }\mu\text{m}$ to $100\text{ }\mu\text{m}$, only one structure, having a width of $10\text{ }\mu\text{m}$, survived.

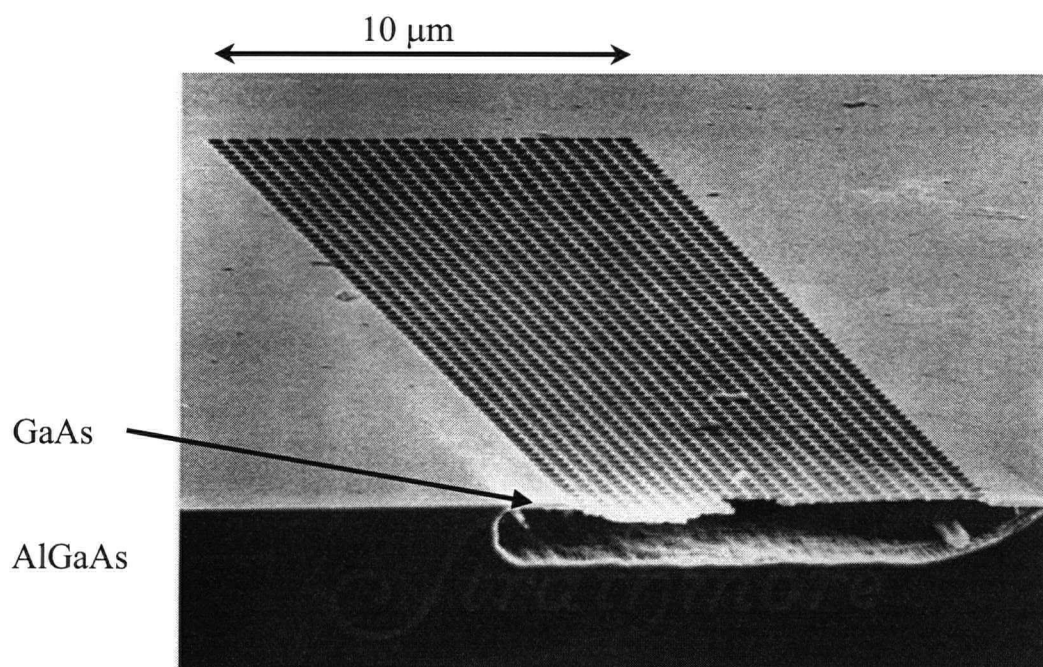


Figure 3.1: Scanning electron microscope (SEM) image of freestanding air/GaAs/air slab waveguide patterned with 2D square lattice of airholes.

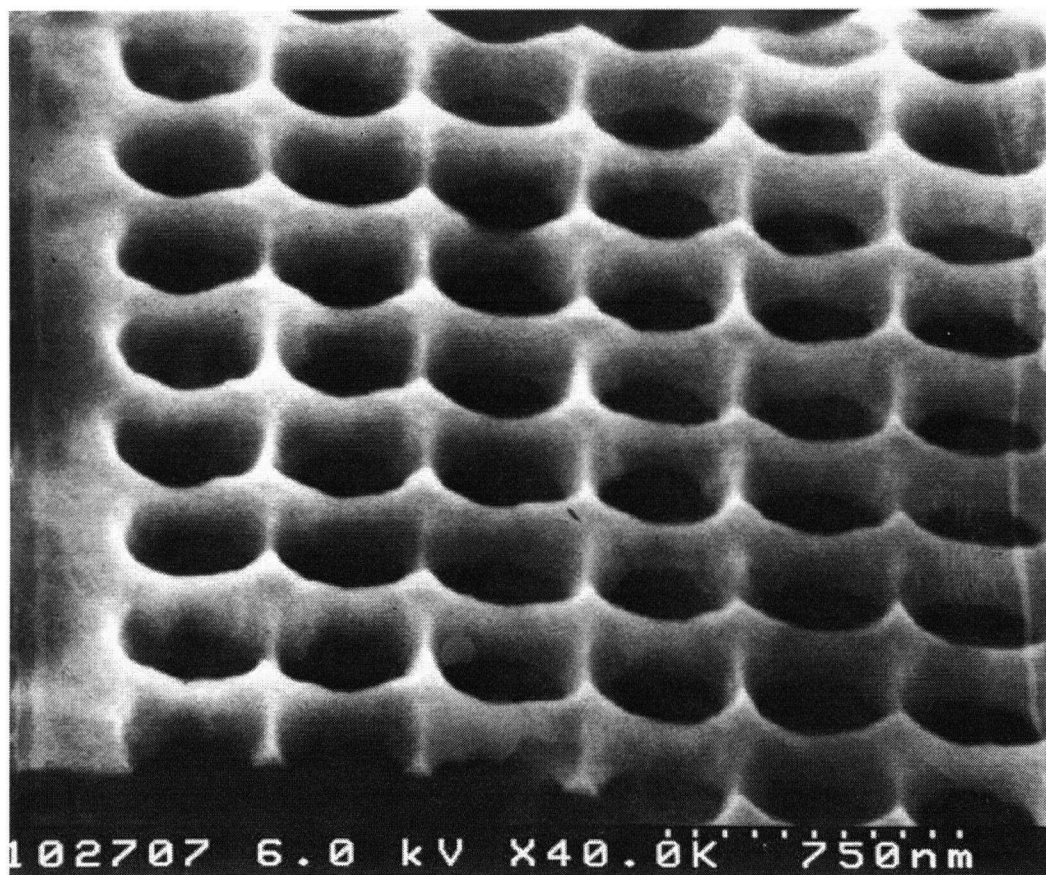


Figure 3.2: High magnification (SEM) image of the same structure as in Figure 3.1

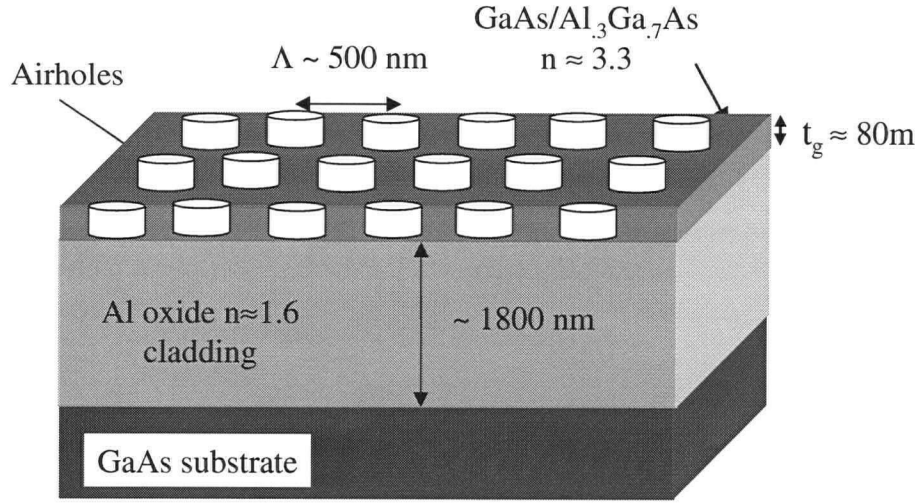


Figure 3.3: Schematic diagram of oxide-based high-index contrast waveguide with strong 2D texture

With the advent of wet-lateral oxidation techniques [45, 46, 47] for oxidizing AlGaAs to produce aluminum oxide, an alternative approach was developed. It consists of oxidizing, rather than etching away, an underlying $\text{Al}_x\text{Ga}_{1-x}\text{As}$ layer through the 2D array of airholes that penetrate the waveguide core. The refractive index of aluminum oxide, $n_{\text{oxide}} \approx 1.6$, which forms the underlying cladding layer in this scheme, is sufficiently low to maintain robust guiding even in the presence of airholes in the waveguide core. Such an oxide-based structure was fabricated by the author and is depicted schematically in figure 3.3.

The sample was grown by Molecular Beam Epitaxy by Shane Johnson at the Center for Solid State Electronics Research, Arizona State University. The oxidation process requires $\text{Al}_x\text{Ga}_{1-x}\text{As}$ with high aluminium composition in order to proceed. Therefore, $\text{Al}_{0.98}\text{Ga}_{0.02}\text{As}$ was grown as the cladding layer below the waveguide core. $\text{Al}_{0.30}\text{Ga}_{0.70}\text{As}$ was grown to form the lower 35 nm of the core, adjacent to the layer to be oxidized. This was done on the basis of reports in the literature [48] that a better interface quality is achieved between this alloy and aluminium oxide than with pure GaAs. As with the

“freestanding” sample, the underlying cladding layer was made thick enough so that the value of the electric field in the evanescent tail of the bound mode is insignificant at the GaAs substrate, thereby making negligible any coupling to substrate modes.

The remainder of the fabrication process was developed and carried out by the author. The holes were made by dry etching the waveguide through a 225 nm-thick PMMA mask created using electron-beam lithography. The PMMA mask was then removed. The oxide layer was formed by placing the etched sample in an atmosphere comprised of nitrogen gas and water vapour at 425°C for 20 minutes. Atomic force microscopy was used to determine the uniformity of the pitch and the hole diameters.

The following section describes the techniques and equipment used in fabricating the oxide-based structure described above, while section 3.3 lays out the sequence of processing steps carried out. Finally, section 3.4 presents results from subsequent inspection of the fabricated structures using optical, scanning electron, and atomic force microscopy.

3.2 Processing Techniques and Equipment

3.2.1 Electron Beam Lithography

Overview

Electron beam lithography consists of selectively bombarding areas of an organic polymer mask with an electron beam that can be swept in a controlled fashion across a certain “field of view”. The electron beam modifies the polymer in one of two ways. In the case of a “positive” resist, the beam breaks bonds and creates smaller polymer chains, while in the case of a “negative” resist, it induces the formation of cross linked bonds. When an exposed positive resist is dipped into a developer solution, the developer dissolves the smaller chains, thereby removing the portion of the resist subjected to the electron beam. Conversely, in the case of a “negative” resist, the exposed area is impervious to the developer so that the pattern of resist that is dissolved is the negative of the pattern swept

by the electron beam. The remainder of this subsection provides a general description of the processing steps, techniques, and equipment used to create the polymer mask by electron beam lithography. A more detailed description of the specific recipes used to produce the samples used in the optical experiments is deferred to section 3.3.

Resist Application

A positive resist, Polymethylmethacrylate (PMMA), was used in the present work. A thin film of the resist was applied to the sample by a technique known as “spin coating”. This involves placing a few drops of the resist, dissolved in highly volatile solvent (chlorobenzene), in the centre of the sample and spinning it at 500 – 10,000 rotations per minute (rpm). The centrifugal force distributes the fluid over the sample until a uniform thickness of the resist layer is achieved in steady state. The resulting thickness of the resist coating depends primarily on the spin rate (500-10,000 rpm). The sample is subsequently heated to just beyond the PMMA’s glass temperature in order to relieve stress in the resist and to promote evaporation of the solvent.

Exposure

The system used to create and deliver an electron beam to the polymer resist is comprised of a scanning electron microscope (SEM) interfaced to a computer running specialized nanolithography software. The microscope used in this work is a Hitachi model S-4100.

The main components of the scanning electron microscope are an electron source, beam deflection system, electromagnetic lenses, and apertures. These are shown in Figure 3.4. The top electromagnetic lens is used to provide a demagnified image of the source, approximately 1 nm in diameter, which is then imaged onto the target by a second (objective) electromagnetic lens. The advantage of having a two-lens system, in conjunction with beam limiting apertures, lies in its ability to deliver a monochromatic beam of electrons as well as to provide for flexibility in the “working distance” between

the sample and the scan coils. The beam-limiting apertures also control the maximum angle, α , subtended by the beam in order to limit aberrations and to minimize the beam spot size.

The electron source is a cold cathode field emission tip. It consists of a small piece of crystalline tungsten etched to a point and welded onto a tungsten filament. A large negative voltage is applied to the tip with respect to the walls of a small surrounding chamber. This induces a large potential gradient (electric field) in the vicinity of the pointed tip, which reduces the width of the potential barrier confining electrons to the tungsten, thus allowing them to quantum mechanically tunnel out. Field emission tips are brighter than those based on thermionic emission, thereby allowing for shorter exposure times. However, adsorption of individual atoms of gas onto the tip leads to fluctuations in current. Longer term downward drift of the emitted current occurs as several atomic layers build up on the tip, and eventually the current becomes unusably low and the tip must be "flashed" to clean it. This is done by briefly passing a large current through the tungsten filament and tip. As a result, one must wait two to three hours after flashing for the current to become stable, after which it is usable for about four to eight hours before it has decayed by nearly an order of magnitude.

Once extracted, the electron beam is accelerated towards the specimen by an accelerating potential difference, V_{acc} . The electrons are then focussed onto the sample by the pair of electromagnetic lenses, and the entire beam can be deflected in the x and y directions by the deflection coils.

During lithography the signals that control the amount of current fed to the deflection coils are provided by a 80486 50 MHz IBM-AT computer running the "NPGS" nanolithography software (from J.C Nabity Lithography Systems) *via* a 16 bit Digital-to-Analog / Analog-to-Digital (D/A-A/D) interface card.

The software allows the user to specify the required pattern of exposure using a computer aided design package, "Design Cad", as well as the desired exposure for each

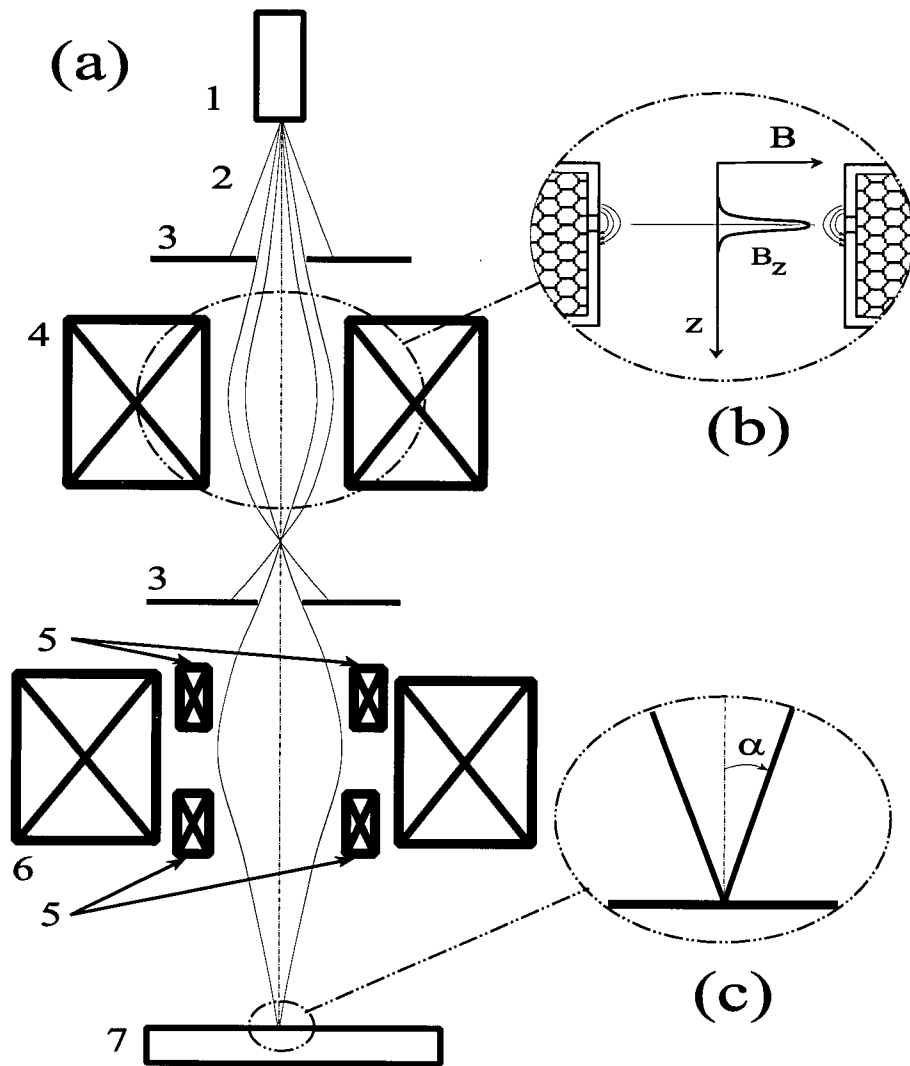


Figure 3.4: (a) Field emission scanning electron microscope column, corresponding to the column of the Hitachi S-4100 SEM: (1) Electron source (2) Beam paths showing the effect of successive apertures in the column, (3) Apertures (4) Condenser Lens (5) Deflection Coils (6) Objective lens (7) Specimen; (b) Magnetic Lens detail showing how the magnitude of the axial magnetic component B_z varies in the lens region; (c) Detail showing geometry of beam aperture angle α at the sample.

pattern element. The software then transforms the information to a series of (x, y) points and dwell times. In order to convert the required dose to a dwell time, the software requires the beam current. This is obtained by measuring the current entering a Faraday cup inserted into the beampath just before the sample (see Figure 3.4). The Faraday cup is a small conducting chamber with a pinhole entrance for the electrons, and the current is measured using a sensitive picoammeter. Due to the gradual degradation of the emitted current described above, this measurement must be done immediately prior to writing each pattern.

Upon entering the thin resist layer, the high-energy electron beam ($\sim 20 - 30$ keV) spreads slightly due mainly to inelastic, small-angle, forward scattering. After having traversed the resist layer, the electrons continue losing energy through inelastic processes but also experience large-angle, elastic scattering, which causes some electrons to re-enter the resist with lower energy, where they multiply scatter and give up more energy to the polymer over an extended lateral area. The result is that the radial distribution of total energy deposited in the resist is much broader than the waist of the focused electron beam incident on the surface, which is on the order of a nanometre. The distribution of deposited energy, therefore, has a tail that extends beyond the typical sub-micron lengthscale of the features to be written. This leads to what is called the “proximity effect” whereby the energy deposited to create a certain pattern element contributes to the total absorbed energy dose of nearby pattern elements. In addition to increasing the minimum feature sizes attainable, scattering also renders the requisite doses pattern-dependent. In the present work, this means that the dose required to produce holes of a certain diameter depends on the pitch of the array of holes to be created.

3.2.2 Etching

After the array of holes is created in the resist layer by electron beam lithography, an etching process is used to transfer it onto the core layer of the waveguide.

Conventional wet chemical etching techniques involve immersing the sample into a liquid reactive solution. However, wet-etching tends to be isotropic; this leads to undercutting of the mask which makes the minimum feature sizes considerably larger than those attainable in the etch-mask.

“Dry” etching techniques, which involve bombardment of the sample with reactive ion species in a rarefied atmosphere, allow for greater anisotropy and higher aspect ratios of the etched sidewalls, which, in turn, allow for feature sizes virtually limited by the mask.

An electron-cyclotron resonance (ECR) plasma etcher was used in this work. It consists of a cylindrical process chamber, approximately 12 inches in diameter and 20 inches tall, with multiple optical ports, gas inlet and outlet ports, and adjacent airlock. A system computer is interfaced to D/A-A/D boards which read out various transducers and remotely control valves and power supplies. A schematic diagram of the ECR etcher is shown in figure 3.5.

The reactive ions are obtained by igniting a plasma in the reactor vessel at low pressure, *i.e.*, 1-100 mTorr. The ions are then driven down onto the sample by an electric field induced normal to the sample surface. The electron cyclotron resonance (ECR) plasma etching system used in this work creates a plasma by delivering microwave radiation resonant with the cyclotron frequency of electrons in the presence of an applied magnetic field. The magnetic confinement in an ECR plasma enhances the degree of ionization, and thereby enables operation at low pressures. The long ionic mean free paths attainable allow for high directionality of the bombarding ions with lower ionic kinetic energies. The result is that anisotropic etching can be achieved without the excessive damage induced by energetic ions.

The ions are accelerated towards the sample by the DC component of an electric field created in its vicinity by applying an 13.56 MHz RF potential between the reactor walls and an electrode placed just below the sample. The DC component of the electric

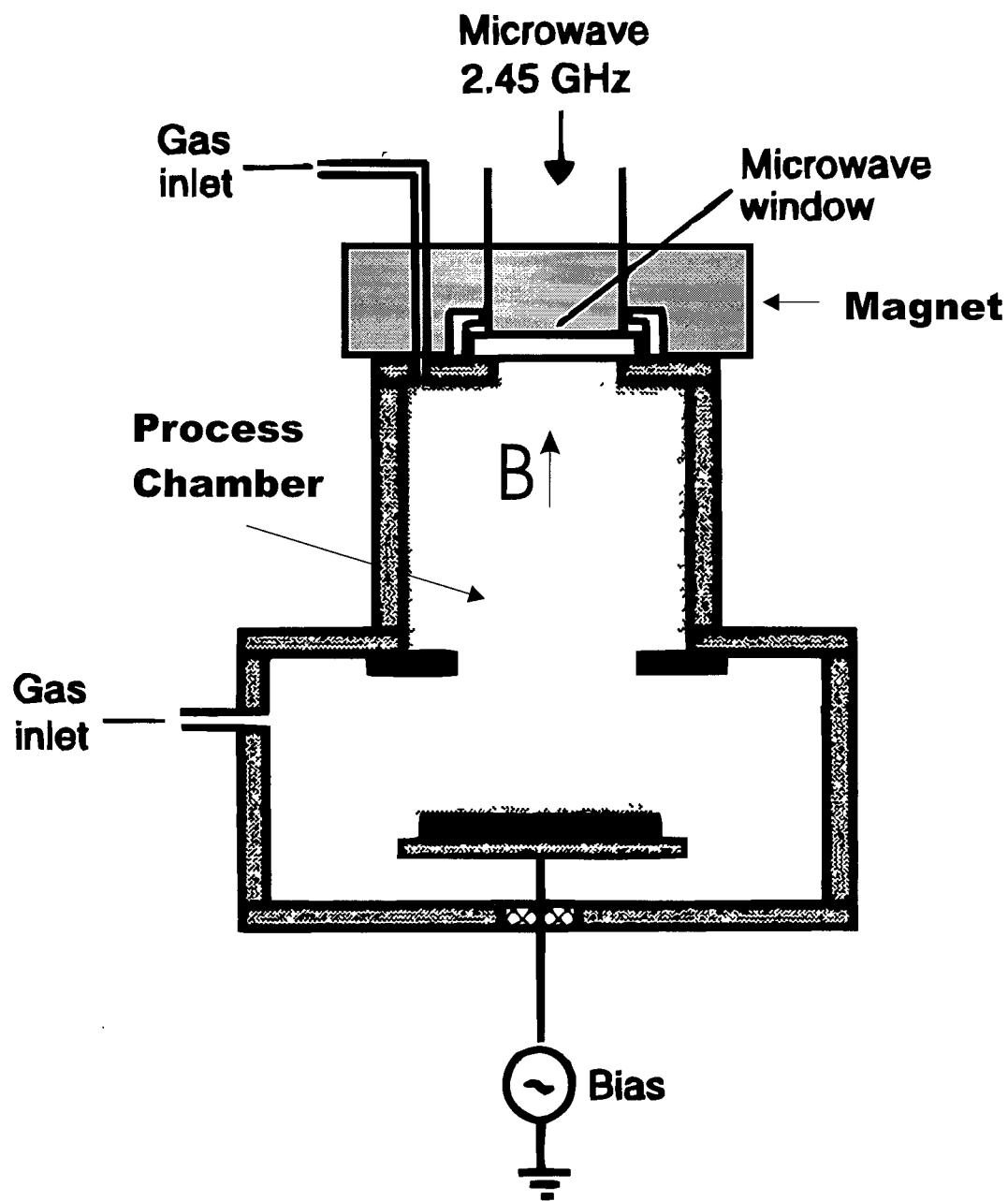


Figure 3.5: Schematic diagram of ECR plasma etcher

field arises from the difference in mobility between the negatively charged electrons and positively charged ions, which leave the plasma at different rates at the anode and cathode. The DC bias can be controlled by varying the amount of RF power delivered. However, the RF power required to achieve high directionality of the ions is still low enough to have little effect on the plasma ionization, which is essentially controlled by the amount of microwave power delivered. Thus, this system allows for almost independent control of these two important plasma etching parameters.

The corrosive process gases are stored in gas bottles housed in exhausted gas cabinets just outside the clean room and delivered to the etcher through electro-polished stainless steel tubing. For safety reasons, gas sensors are placed inside the gas cabinets as well as in the vicinity of the etcher, itself, inside the cleanroom.

For a typical etch process, the sample is placed on a sample holder in the airlock. The airlock is then pumped down, and a motorized load arm loads the sample holder onto the chuck in the middle of the reaction vessel. During etching, the sample sits on a liquid cooled chuck; the temperature of the chuck is measured by a thermocouple monitored by the system computer. A helium flow is maintained on the backside of the wafer to increase thermal conductivity and thereby improve temperature control during the etch process.

The process vacuum system for evacuating the reaction chamber consists of a *Pfeiffer* corrosive service turbomolecular pump backed by a mechanical pump package. A *VAT Series 64* throttling gate valve mounted between the process chamber and the turbo pump is used to control process pressures in the reactor chamber. It is controlled by computer through a *VAT PM5* pressure controller. Process chamber pressure is monitored by an *MKS Baratron* capacitance manometer. Process gas flow, itself, is regulated by *MKS* mass flow controllers under control of the system computer.

The reactor is configured with an Nd-Fe-B permanent magnet which is used to generate the electron cyclotron resonance zone. The magnet produces a maximum field of

approximately 4600 G at the top of the reactor vessel.

Microwaves are transmitted from a magnetron to the ECR through a mil spec #WR-284 waveguide with mil spec. #CPR-284 G flanges. The output frequency of the microwave power supply is 2.455 GHz. The output power is continuously variable and is normally controlled remotely by the system computer. Impedance matching to the plasma load is allowed for by partial insertion of three stubs mounted on three different translation stages into the hollow waveguide cavity.

The RF source is AC coupled to the electrode through an autotuning impedance matching network that matches the $50\ \Omega$ output impedance of the source to the impedance presented by the plasma. The sample wafer is electrically isolated from the chuck and the RF electrode so that its potential floats. The RF source is a *Plasma Therm Type HFS 500E*. It operates at a frequency of 13.56 MHz. The matching network is a *Plasma Therm AMNS-500E* modified and repaired by the UBC Physics & Astronomy Electrical Shop.

The gas mixture employed in this work consisted of argon (Ar), chlorine (Cl_2), and boron trichloride (BCl_3). This combination was selected based on reports in the literature that it provided good anisotropy, little damage to the substrate as well as low etch selectivity between GaAs and AlAs [49].

Low selectivity was particularly important in the present work as the waveguide core to be etched was comprised of a GaAs layer as well as an $\text{Al}_{0.3}\text{Ga}_{0.7}\text{As}$ layer. One problem that tends to arise in etching AlGaAs is that it has a high affinity for any residual O_2 or H_2O in the chamber and readily oxidizes to form Al_2O_3 , which cannot be easily etched by Cl_2 . This causes the formation of a step in the etch profile since the $\text{Al}_{0.3}\text{Ga}_{0.7}\text{As}$ etches more slowly. The BCl_3 works as a scavenger for any residual O_2 or H_2O in the chamber. Secondly, it readily etches any Al_2O_3 as soon as it is formed, thus allowing the chlorine ions to etch both layers evenly. The Ar is used mainly as a carrier gas and to stabilize the plasma, as Ar ion etching is purely a kinetic process with a much lower

etch rate.

3.2.3 Oxidation

The process known as “wet lateral oxidation” of AlGaAs, discovered in the early 1990’s [45, 46, 47], simply entails exposing the face of a film of $\text{Al}_x\text{Ga}_{1-x}\text{As}$ with $x > .84$ to a damp but otherwise inert atmosphere at high temperature. The oxygen in the water reacts to form an oxide with aluminum and gallium, while the arsenic and hydrogen combine to form arsine gas. The reaction proceeds from an exposed face at a constant rate which depends on the precise conditions but which increases with the aluminium composition of the alloy.

The exact nature of the oxide formed is an outstanding issue in the literature, and possibly dependent on oxidation temperature and other conditions. Potential candidates include: $(\text{Al}_x\text{Ga}_{1-x})_2$ in a similar form to $\gamma\text{-Al}_2\text{O}_3$, crystalline phases such as $\alpha\text{-Al}_2\text{O}_3$, $\beta\text{-Al}_2\text{O}_3$, $\delta\text{-Al}_2\text{O}_3$, amorphous alumina AlO_y , hydrates $(\text{Al}_2\text{O}_3) \cdot n\text{H}_2\text{O}$, and hydroxides $\text{Al}_m(\text{OH})_n$. Nevertheless, the oxides so produced have refractive indices that lie between 1.5 and 1.75, which is sufficient to provide the low-index waveguide cladding layer required in the present work.

Figure 3.6 depicts the setup used for oxidation. It was designed and assembled by the author and Francois Sfigakis, a former Master’s student. Stainless steel piping is used throughout as it is relatively inert (compared with copper or brass) up to 500°C . A quartz oven tube is used in order to support temperatures up to 525°C . The valves and other Pyrex glassware used away from the oven are capable of withstanding temperatures up to 200°C . Nitrogen (N_2), which does not react with GaAs or AlGaAs at a temperature below 600°C , is used as the carrier gas.

Nitrogen gas from the building supply is bubbled through the boiler (BL), which consists of a sealed flask of de-ionized water maintained at 95°C , and then delivered to the quartz tube sitting inside a three-zone *Lindberg* furnace (model 5500 series)

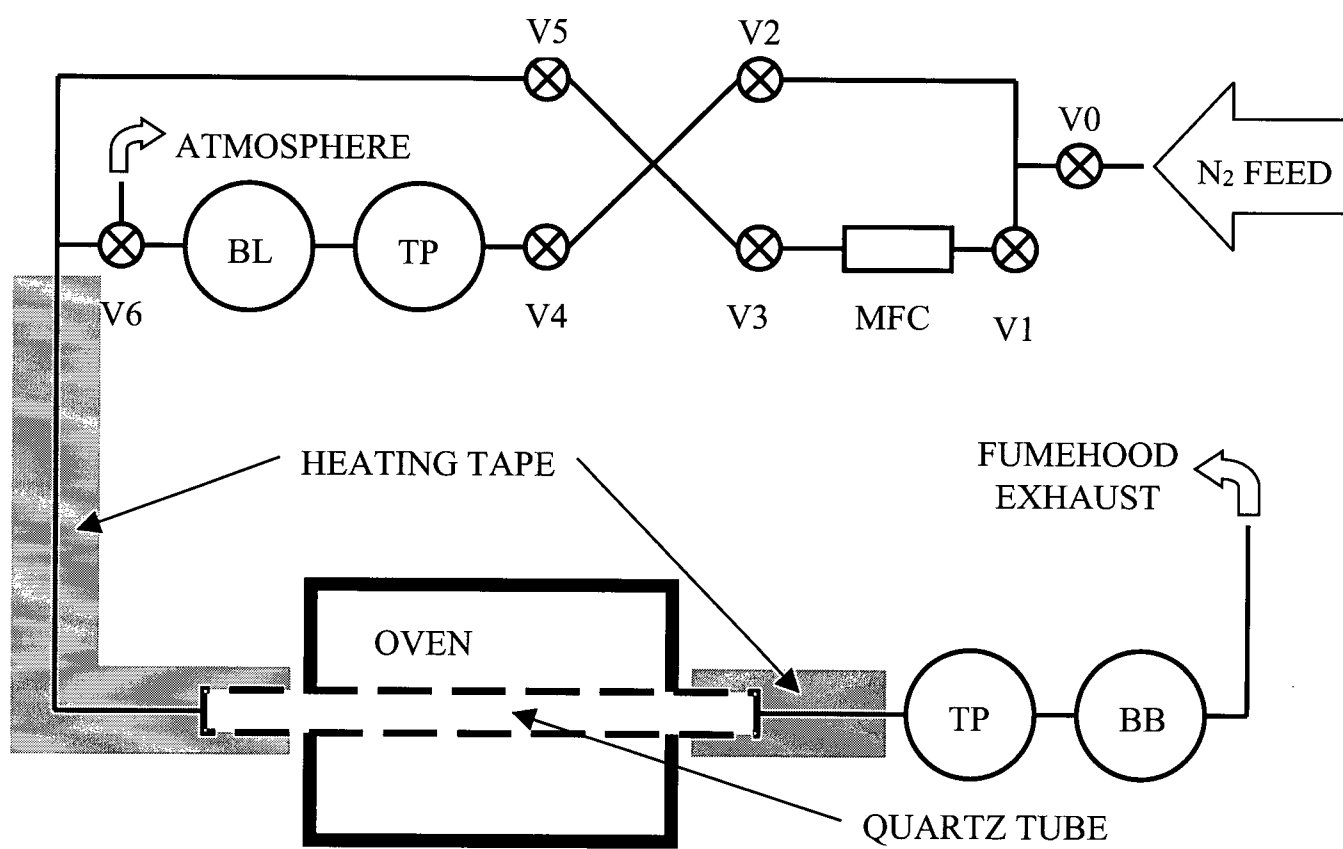


Figure 3.6: Oxidation Setup

maintained at $400^{\circ}\text{C} - 425^{\circ}\text{C}$.

The flow rate of the carrier gas, N_2 , is controlled by a pair of mass flow controllers, each comprised of a *Vacuum General* valve (model *CV2 31S01*) and a *Tylan Corp.* mass flow meter (model *FM-360*). Two parallel controllers were used in order to increase the maximum controlled gas throughput possible. The boiler is heated by the combination of hemispherical heating mantle and heating tape. The temperature of the boiler is measured using a calibrated thermocouple and maintained by manually varying the AC voltage applied to the heating elements by using a variable transformer. Heating tape is wrapped around the stainless steel tubing, bellows, and around the parts of the quartz tube lying outside the oven.

The oven temperature is automatically regulated by a *Lindberg* Proportional-Integral-Derivative (PID) programmable controller based on a temperature measurement fed back to it from a thermocouple in contact with the quartz tube in the centre of the oven.

The exhaust gases containing toxic arsine are bubbled through a flask of water, dubbed the bubbler (BB), to partially dissolve and remove arsine, before being vented up the fumehood exhaust. Two empty flasks act as water traps (TP). One is placed between the oven and bubbler to prevent water from being sucked into the oven by the pressure differential as the oven cools. The other trap is placed before the boiler to prevent water from being sucked into the gas lines.

3.2.4 Optical Microscopy

Immediately after oxidation, the patterns were viewed under the optical microscope. The holes in the patterns are not resolvable optically. On the other hand, the presence of aluminum oxide can be detected from the colour difference between the region around and under the patterns and the rest of the sample. This colour difference is due to the different optical lengths of the cavities formed by either the $\text{Al}_{0.98}\text{Ga}_{0.02}\text{As}$ or aluminum oxide sandwiched between the waveguide core and substrate.

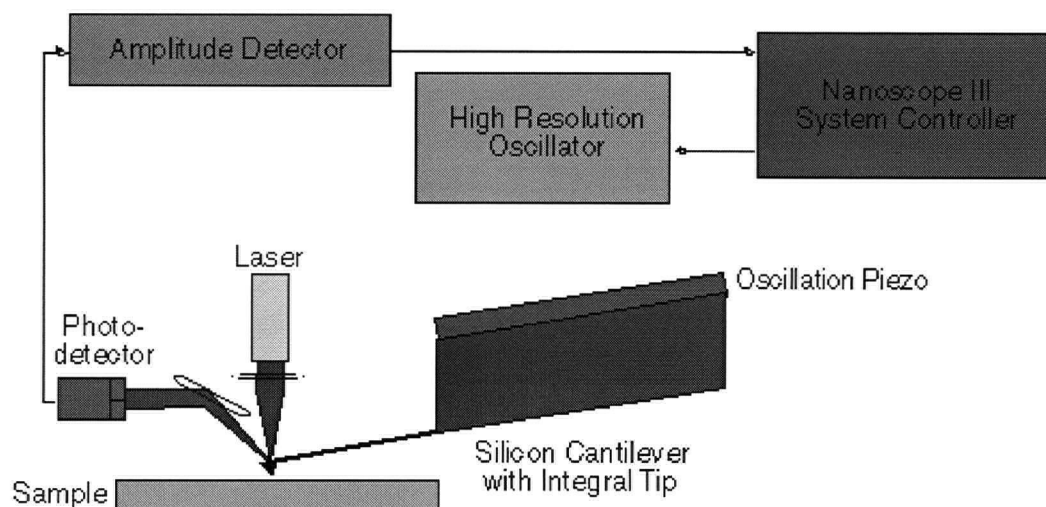


Figure 3.7: Schematic diagram of AFM tip operation and position detection

The optical microscope was also used to detect patterns that were unusable due to particulate matter that had been deposited on the sample surface prior to or during processing, or due to non-uniformity of the resist thickness.

3.2.5 Atomic Force Microscope

Atomic force microscopy was used after fabrication to measure the uniformity, pitch, and air filling fraction of the 2D gratings. The atomic force microscope (AFM) used was a *Digital Instruments model MMAFM-2* operating in “Tapping Mode”.

Atomic force microscopy consists of scanning a pointed probe mounted on a cantilever across the sample surface. The tip position is measured with the use of a laser beam which is reflected off the backside of the cantilever, near the tip, and onto an array of four photodetectors as depicted in Figure 3.7. The vertical position of the tip is inferred from the difference signal between the top and bottom pairs of photodetectors.

In “Tapping Mode” operation, oscillation is induced near the cantilever’s resonant frequency using a piezoelectric crystal. When the oscillating tip comes in close proximity to a surface, the tip begins to intermittently contact it, and the cantilever oscillation is

reduced due to energy loss caused by the tip contacting the surface. The *tendency* for reduction in oscillation amplitude is used to identify and measure surface features. The cantilever oscillation amplitude is actually maintained constant by a feedback loop, and the surface features are inferred from the amplitude of the error signal.

The advantage of “Tapping Mode” is that it inherently prevents the tip from sticking to the surface and causing damage during scanning. It should also be noted that “Tapping Mode” AFM was selected over SEM in order to avoid damage to these very porous structures by the prolonged electron bombardment of small areas which is required for filling fraction measurements.

Finally, it should be noted that both the radius of curvature of the very end of the tip and its aspect ratio limit the resolution of the images obtained. It should also be emphasized that the image obtained cannot always simply be considered to be a convolution of the tip shape with the topography of the sample since some portions of the sample may be inaccessible to the tip due to its non-zero width and non-vertical profile.

3.3 Fabrication Procedure

3.3.1 SEM measurement of Layer Structure

The layer structure for the as-grown sample is depicted in Figure 3.8. By viewing a cleaved edge of the sample using the field emission SEM, it was possible to measure the thickness of the $\text{Al}_{0.98}\text{Ga}_{0.02}\text{As}$ layer as well as the combined thickness of the GaAs and $\text{Al}_{0.7}\text{Ga}_{0.3}\text{As}$ layers. These measured thicknesses, along with their nominal values, are given in Table 3.1.

3.3.2 Cleaving

A small, approximately $5\text{mm} \times 5\text{mm}$, piece of sample was cleaved off the quarter wafer by scribing the wafer at the desired cleave locations, placing it over a thin wire aligned

1. GaAs
2. $\text{Al}_{0.30}\text{Ga}_{0.70}\text{As}$
3. $\text{Al}_{0.98}\text{Ga}_{0.02}\text{As}$
4. GaAs substrate and buffer layer

Figure 3.8: As grown sample layer structure for ASU 721

Layer No.	Material	Nominal Thickness [nm]	Measured Thickness [nm]
1	GaAs	45	90 ± 10
2	$\text{Al}_{0.7}\text{Ga}_{0.3}\text{As}$	35	
3	$\text{Al}_{0.98}\text{Ga}_{0.02}\text{As}$	1600	
4	GaAs	substrate	substrate

Table 3.1: Nominal and measured thicknesses of layers in sample ASU 721

with the scribe, and applying pressure to one side of the sample.

3.3.3 Lithography

Resist Application and Pre-bake

The sample was manually rinsed to remove particles from the surface. It was held with tweezers while deionized (DI) water from a gun was sprayed on the surface. It was subsequently sprayed liberally with acetone from a squirt bottle to remove the water, and then sprayed with methanol to remove the acetone. Finally, the sample surface was blown with dry nitrogen gas.

After cleaning, the sample was placed on the chuck of the photo-resist spinner. The resist used was Polymethylmethacrylate (PMMA) 950K molecular weight. It is shipped by the supplier, *Olin*, in 4% solution in chlorobenzene. Using a pipette and bulb, a single drop of the resist solution was applied to the centre of the sample, and the sample was spun at 8000 rpm for 30 seconds to produce a uniform 225 nm-thick coating. After spin-on, the sample was removed from the spinner and placed on a hot-plate, pre-heated to 175°C, and left to bake overnight in a fumehood.

Exposure

The sample was then fixed to a ~ 7 mm stainless steel stub using a carbon based conductive glue with the resist-coated side facing up. In order to provide greater electrical contact and mechanical support, two thin strips of aluminum foil were placed across two diagonally opposing corners of the sample. Small pieces of graphite were deposited on the resist near the edges of the sample by rubbing a 2B pencil gently against them. These provided small features useful in subsequent focussing of the electron beam on the resist surface.

The stub holding the sample was mounted onto a holder and inserted into the SEM

main chamber through the air-lock and locked into place on the translation/rotation/tilt-stage. The tip was then flashed and left for 2.5 hours to allow the adsorption on the tip to reach its stable configuration. The electron beam was then turned on. The electron beam and apertures were aligned and the astigmatism adjustment performed as per the procedures specified in the SEM manual.

The edge of the sample was then translated into the field of view, taking care not to expose any of the more central parts of the sample to the electron beam. The resist surface was moved into the focal plane of the electron beam so as to bring the graphite pieces lying on the surface into focus. The sample was then translated such that each of its edges was, in turn, brought into the field of view. By thus verifying that all of the edges remained in focus, it was possible to ensure that the sample was sitting flat and was, in fact, oriented normal to the beam. Finally, for convenience, the sample was rotated to align its edges with those of the field of view.

Next, the movable Faraday cup was inserted into the beam path; the beam current was measured, and its value was entered into the nanolithography software. The sample was then translated to bring the desired exposure area under the beam, the $x - y$ raster control switched to computer control, the Faraday cup blocking the beam removed, and a key depressed on the computer to command the software to start writing the pattern. Once the pattern was written, the sample was translated to bring another portion of it under the field of view, and the procedure in this paragraph was repeated for each of the patterns defined in the nanolithography software run file.

After all the patterns were written, the electron beam was turned off, the sample was removed from the SEM and returned to the clean room for development and etching.

Development

First, the sample was flushed with dry nitrogen gas to remove the graphite particles. It was then immersed in developer solution (from OCGY Inc.) consisting principally of

methyl isobutyl ketone (MIBK) diluted in isopropyl alcohol (IPA), MIBK:IPA 1:3, for 90 seconds. The development process was stopped by immersing the sample in an IPA rinse for 60 seconds. This was followed by immersion of the sample in DI water for 30 seconds followed by drying with nitrogen gas. The sample was then immersed in a high-contrast developer solution consisting of ethoxy ethanol (EE) diluted in methanol, EE:methanol 3:7, for 15 seconds to remove any thin film of PMMA remaining at the bottom of the developed holes. This final development process was stopped by immersing the sample in methanol for 30 seconds. This was followed, once again, by rinsing of the sample in DI water for 30 seconds followed by drying with nitrogen gas.

After a brief inspection under the optical microscope, to confirm the appearance of $90 \times 90 \mu\text{m}$ patterns, the sample was transferred to the etcher.

3.3.4 Etching

The sample holder that shipped with the etcher is designed to hold 3"-diameter wafers. Consequently, a 3" silicon wafer was placed in the sample holder, and the sample was fixed to the centre of the silicon wafer using a drop of conductive paint obtained from *Astex-PlasmaQuest*.

The load-lock cover was closed and the load-lock pumped down. The sample was then inserted into the reaction chamber by the motorized load arm. The steps and conditions programmed into the etcher system control computer are given in Table 3.2.

After the chamber was pumped down to a base pressure of $\sim 1 \times 10^{-7}$ Torr, the process gases were allowed to flow for 30 seconds before the microwave source was activated to ignite the plasma. Simultaneously, the RF source was manually activated to induce the DC bias.

After the etch, the chamber was purged with nitrogen gas for 30 seconds in order to help clear out the toxic process gases before the sample was transferred back to the air lock by the motorized load arm.

Process Pressure	10 mTorr
Ar flow rate	20.1 sccm
Cl ₂ flow rate	1.6 sccm
BCl ₃ flow rate	2.2 sccm
Microwave power	100 Watts
RF Bias	100 Volts
Chuck temperature	5°C
Backside He pressure	5 Torr
Pre-etch purge time	45 seconds
Etch time	160 seconds

Table 3.2: Etch conditions

The sample was then removed from the air lock, rinsed, and left in a beaker of acetone for two hours in order to remove the remaining PMMA mask. This was immediately followed by rinsing in methanol and DI water for 30 seconds, each followed by drying with nitrogen gas.

3.3.5 Oxidation

With reference to Figure 3.6, the sample was placed on a quartz boat that was introduced into the quartz tube and carefully pushed to the centre of the tube and oven using a rod.

The system was then purged with nitrogen gas for one hour by opening valves V2, V4, V5, and setting the three-way valve V6 to vent to atmosphere.

With the nitrogen purge still on, the oven was turned on and the PID controller was programmed to ramp the temperature up to 400°C in 30 minutes. Meanwhile the boiler was filled with fresh DI water, and the hemispherical heating mantle was turned on to slowly heat the water up to 95°C. The power to the heating tape was also turned on at this point. Once the oven had reached 400°C, valves V2 and V5 were closed, the mass flow controllers were turned on and set to provide a flow of 100 sccm (standard cubic centimetres per minute), and valve V3 was opened. Finally, the three-way valve, V6,

was switched to deliver the moist nitrogen gas into the oven tube.

After the desired oxidation time had elapsed (usually twenty to sixty minutes), valves V6 and V4 were closed, and valve V5 was opened to deliver 100 sccm of dry nitrogen gas while the oven was ramped down to 200°C in two hours. The boiler, heating tape, and oven were turned off, and the sample and oven were allowed to cool overnight with the controlled 100 sccm nitrogen purge on. The sample was then removed from the oxidation oven.

3.4 Fabrication Results

Lithography, etching, and oxidation were performed, as described previously in this chapter, on sample ASU 721 so as to produce twenty-four patterns arranged on a 0.5 mm grid in 6 rows of 4 gratings each. The doses and pitches programmed into the lithography software are given in Table 3.3. Note that two copies of each pitch-dose combination were produced for the sake of redundancy. The sample was oxidized for twenty minutes. Figure 3.9 shows a magnified view of one of these, grating 22, and its vicinity. The dark, square box is the grating itself. Surrounding it is a region that is slightly darker than the rest of the sample. This region was oxidized outward from the grating, and we can see that it extends out approximately 10 μm from the edges of the grating.

Table 3.4 summarizes the yield and extent of oxidation around each of the gratings.

After the optical spectroscopy measurements were completed, atomic force microscopy was carried out on gratings 20, 22, 23, 24 to verify pattern uniformity as well as the air filling fraction of the holes produced. A 4 μm \times 4 μm image of grating 22 is shown in Figure 3.10. The lateral scales were calibrated by comparing the value obtained from an AFM measurement of the pitch of a grating to that obtained from a diffraction measurement using a helium-neon laser, and from observation in the SEM. The image shows good uniformity in both the hole size and pitch over its field of view. This was also the

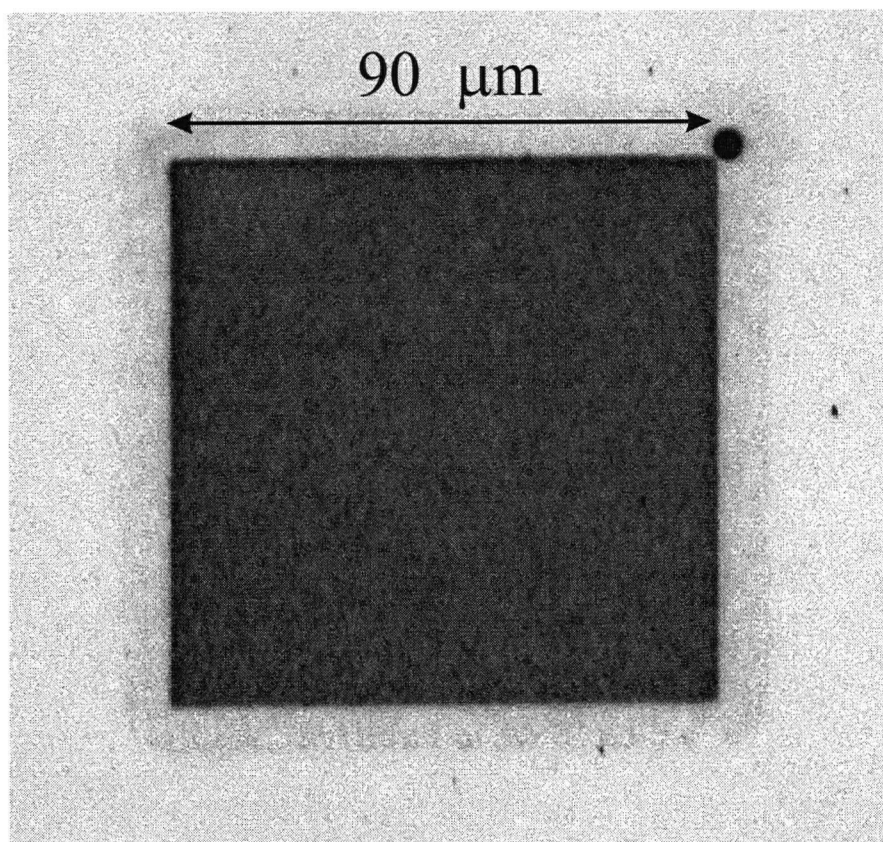


Figure 3.9: Top view of grating 22 on sample ASU 721 as imaged by the optical microscope. The size of the grating is $90\text{ }\mu\text{m} \times 90\text{ }\mu\text{m}$. Some processing was performed on the image to enhance the contrast between the oxidized region, which extends out around the grating and is slightly darker compared to the unoxidized parts of the sample.

Grating	Dose [fC]	Pitch [nm]
g1	35	550
g2	50	550
g3	65	550
g4	25	500
g5	35	500
g6	45	500
g7	30	525
g8	45	525
g9	60	525
g10	45	575
g11	60	575
g12	75	575
g13	30	550
g14	50	550
g15	65	550
g16	25	500
g17	35	500
g18	45	500
g19	30	525
g20	45	525
g21	60	525
g22	45	575
g23	60	575
g24	75	575

Table 3.3: Pitches and doses specified for e-beam lithography

Grating	Extent of oxidation out from edge [μm]	Condition
g1	—	bad
g2	—	bad
g3	—	bad
g4	—	bad
g5	12	top left corner bad
g6	12	2 bad patches
g7	6	good
g8	12	good
g9	14	good
g10	8	good
g11	—	good
g12	15	good
g13	3	spot on left edge
g14	9	good
g15	13	good
g16	12	good
g17	9	good
g18	12	good
g19	9	good
g20	10	good
g21	15	spot on left edge
g22	10	good
g23	11	good
g24	10	good

Table 3.4: Extent of oxidation and yield

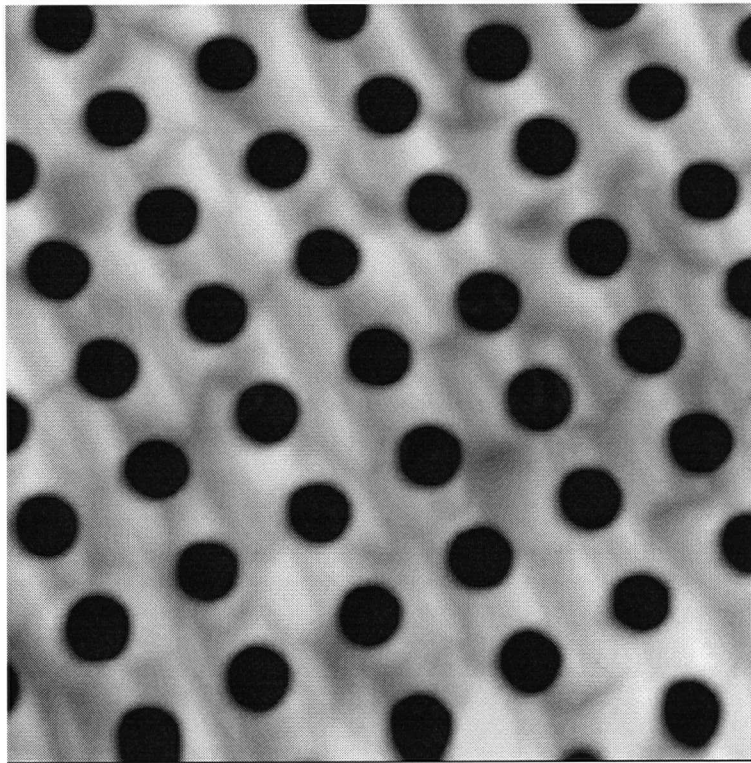


Figure 3.10: $4\ \mu\text{m} \times 4\ \mu\text{m}$ AFM image of grating 22.

case in images taken from other regions of this and other gratings.

Figure 3.11 shows a slice of the above image for grating 22 taken through the diameters of the holes. The profile and radius of the AFM tip preclude drawing any conclusions regarding the profile and depth of the holes. However, the diameter of the holes at the surface may be inferred from the measured profile by taking the distance between the leading and trailing edges as indicated by the arrows in Figure 3.11. Table 3.5 gives the measured hole diameters and pitches of the gratings as well as their air filling fractions, calculated with the assumption of cylindrical holes.

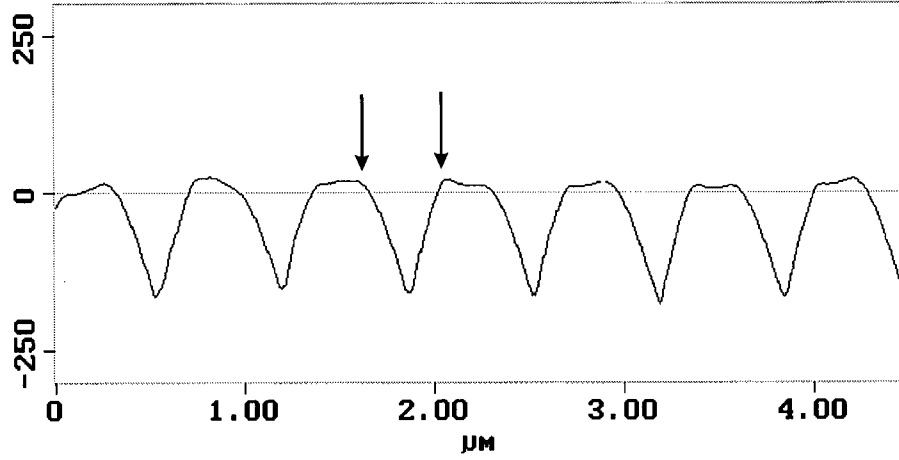


Figure 3.11: Section through diameter of holes in image in Figure 3.10. The arrows indicate the leading and trailing edges of the depression in the profile, which are used to obtain a measurement of the diameter of the holes at the surface.

Grating	Pitch, Λ [nm]	Hole radius, r [nm]	r/Λ	Filling fraction
g22	571 ± 17	170 ± 10	0.300 ± 0.020	0.278 ± 0.027
g23	576 ± 16	187 ± 11	0.325 ± 0.021	0.331 ± 0.026
g24	573 ± 16	226 ± 14	0.394 ± 0.026	0.489 ± 0.045

Table 3.5: Pitches and hole radii and corresponding air filling fractions estimated from AFM profiles from three gratings having nominally the same pitch but different electron beam exposure times.

Chapter 4

Optical Experiments

4.1 Introduction

The experimental setup described in this chapter was used to collect specular reflectivity spectra from the gratings in the geometry depicted in Figure 4.1 below. For each grating, data were collected for a series of incidence angles θ , for each of $\phi = 0$ and $\phi = 45^\circ$, and for each of s and p polarizations of the reflected light.

This was done by focusing white light from a tungsten quartz-halogen bulb delivered by an optical fiber down to a $200\text{ }\mu\text{m}$ diameter spot on the sample, which over-filled the $90\text{ }\mu\text{m} \times 90\text{ }\mu\text{m}$ two-dimensional grating under study. The specularly reflected light was collected and focussed onto the input aperture of a Fourier Transform Spectrometer after passing through a polarizer to discriminate between s and p polarized light, and an aperture to eliminate light coming from outside the patterned area. Reflective optics were used throughout to avoid chromatic aberrations. To aid in alignment, a CCD camera could be inserted into the beam path, at the intermediate focus, to image the surface of the sample.

This chapter describes the experimental apparatus, the procedure used for initial alignment of its optical components, the angular resolution obtainable, and the procedure used for obtaining spectra on each grating. The optical set-up was designed and constructed by W.J. Mandeville. The optical experiments to collect the data used in the present work were carried out by the author.

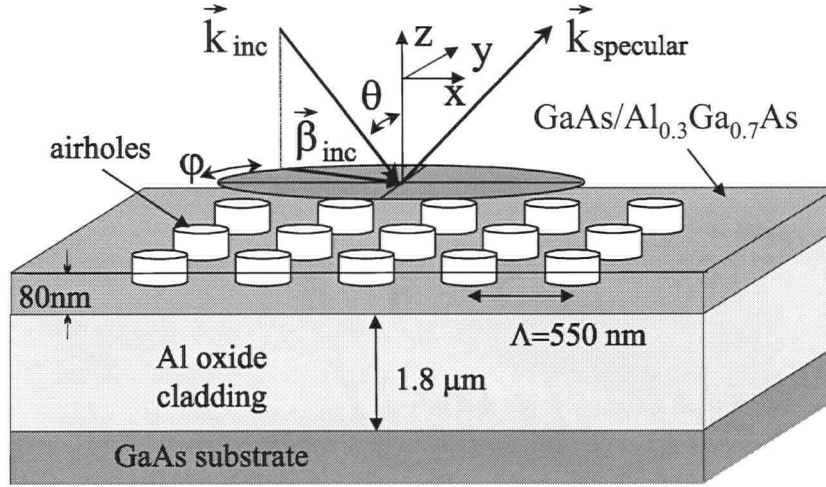


Figure 4.1: Schematic diagram of scattering geometry used in specular reflectivity measurement. The dimensions of the sample and pattern depicted are the nominal values for grating 22 on sample ASU 721.

4.2 Experimental Apparatus

Figure 4.2 depicts the experimental optical apparatus used. All of the components were assembled on an optical table, except for the self-contained Fourier Transform Interferometer (FTIR) which was placed adjacent to the table.

The light source used was a commercially available optical fiber illuminator consisting of a 100W quartz halogen light bulb with the tungsten element emitting at 3200K.

A pair of 1" diameter lenses of focal lengths 2.54 cm and 3.76 cm collimate and then focus the light onto the end of the optical fiber mounted on the fiber chuck and inserted into the fibre holder on the illuminator.

The optical fibre used to deliver the light onto the turntable ring is a 2 meter long 100 μm -core multimode visible/near-IR fibre. The total power delivered by the fiber was measured to be approximately 1mW using a *Spectra Physics 404* power meter with a spectral range 0.45 μm – 0.9 μm . Assuming a blackbody spectrum, this corresponds to approximately 4 mW of total power delivered by the fibre, and to approximately 2

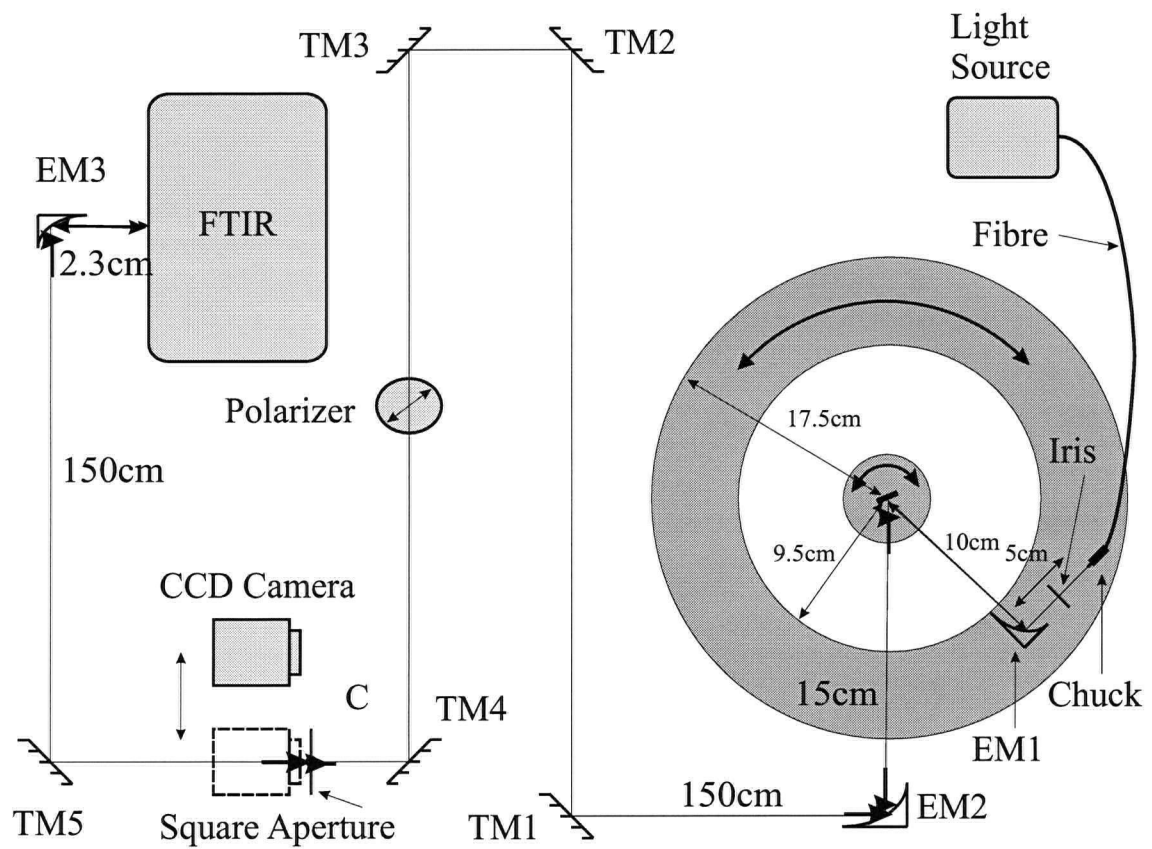


Figure 4.2: Schematic diagram of experimental setup

mW in the spectral range $0.77\ \mu\text{m} - 1.67\ \mu\text{m}$ ($6000\ \text{cm}^{-1} - 13,000\ \text{cm}^{-1}$) for which data were collected in this work.

The $\theta - 2\theta$ apparatus is composed of two rotating stages. The output facet of the illuminating fibre, iris diaphragm, and the focusing ellipsoidal mirror are placed on a rotating annulus (with inner and outer diameter of 19 cm and 35 cm respectively) positioned to be concentric with the rotating sample-holder which is described in detail below.

Three ellipsoidal mirrors were used to image from focal point to focal point. The sections of the ellipsoid were chosen for the mirrors such that the beam is turned by 90° .

The first ellipsoidal mirror, EM1, images the output facet of the fibre onto the sample, creating a 2X magnified spot. This produces a $200\ \mu\text{m}$ spot on the sample that slightly overfills the $90\ \mu\text{m} \times 90\ \mu\text{m}$ gratings.

The second ellipsoidal mirror, EM2, creates a 10X magnified image of the sample surface at the point C, 150 cm from the mirror. A square aperture is placed in this image plane to ensure that only light reflected off the patterns is passed to the spectrometer. The aperture is so adjusted by viewing the image formed at this point using a CCD camera inserted into the beampath just downstream of the aperture.

A polarizer cube is used to select a particular polarization of the collected light. Since the plane of incidence for the reflectivity measurement is parallel to the optical table, turning the polarizer such that it transmits light polarized with the electric field perpendicular to the optical table corresponds to selecting the *s*-polarization. Conversely, having the polarizer axis parallel to the optical table selects the *p*-polarization.

The third ellipsoidal mirror, EM3, then images the real image formed at point C onto the input aperture of the FTIR.

Figure 4.3 shows a schematic diagram of the sample holder assembly. In addition to rotation concentric with the outer ring, this assembly permits us to vary the angle made by the plane of incidence with respect to the crystal axes of the photonic lattice,

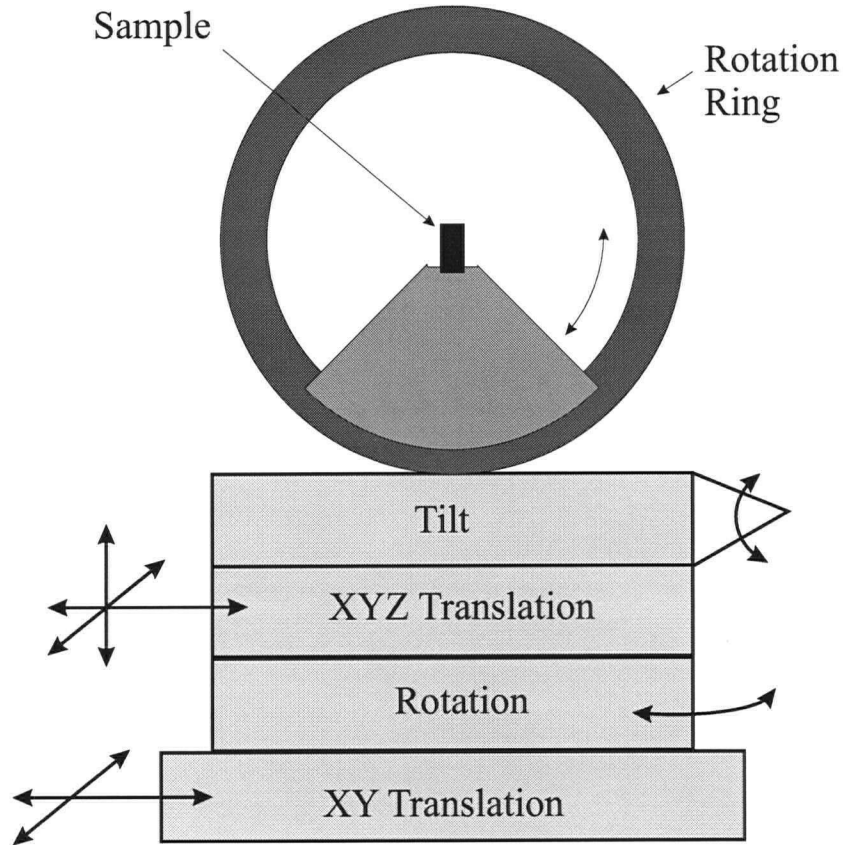


Figure 4.3: Schematic diagram of sampleholder

without having to reposition the sample and re-align the setup. The translation and tip-tilt stages provide for convenient alignment.

4.2.1 Fourier Transform Spectrometer

A *BOMEM model DA8* Fourier Transform Interferometer was used in this work . Fourier transform spectroscopy allows for large bandwidth data acquisition with a large range of spectral resolutions. The broad bandwidth feature is of particular value in the present work where scans over a minimum range of 2000 cm^{-1} are essential for efficient data collection.

The system essentially consists of a Michelson interferometer augmented with a thermally stabilized He-Ne laser, electro-optic transducers, and electromechanical actuators

to allow for automatic calibration and alignment of the optical components. Input and output optics are provided to introduce parallel radiation into the interferometer, and to subsequently couple parallel radiation out and focus it down onto a detector. Figure 4.4 shows a schematic diagram of the principal optical components.

The parallel beam at the input of the interferometer is divided into two equal-amplitude beams at the beamsplitter which, after travelling through different path lengths, are then superimposed and focussed onto a detector. As the moveable mirror is scanned, the intensity falling on the detector is recorded as a function of the optical path delay between the two arms to form an interferogram. The power spectral density of the input light is obtained by (cosine) Fourier transformation of the interferogram.

An InGaAs detector and a quartz beamsplitter combine to provide a spectral range of approximately 6000 cm^{-1} to $14,000\text{ cm}^{-1}$. Most spectra were obtained at a resolution of 7 cm^{-1} .

4.3 Alignment

A pointed piece of polished GaAs was mounted on the sample holder for alignment purposes. Using a level Helium-Neon laser beam, the fibre and ellipsoidal mirrors, EM1 and EM2, were levelled and placed in their approximate positions.

In order to ensure that the sample was at the centre of rotation of the sample rotation stage, the following procedure was used. The fibre was pulled back from the focus of the elliptical mirror, EM1, in order to illuminate the test sample with a broad, defocussed spot such that the sample cast a shadow on a small screen placed behind it. The sample was then translated using the upper XYZ translation stage on the sample holder assembly until the point of the shadow did not move as the sample was rotated.

Having assured that the sample tip was aligned with the rotation axis of the sample rotation stage, the centres of rotation of the sample rotation stage and turntable ring were aligned by adjusting the lower XY translation stage until the shadow of the pointed tip

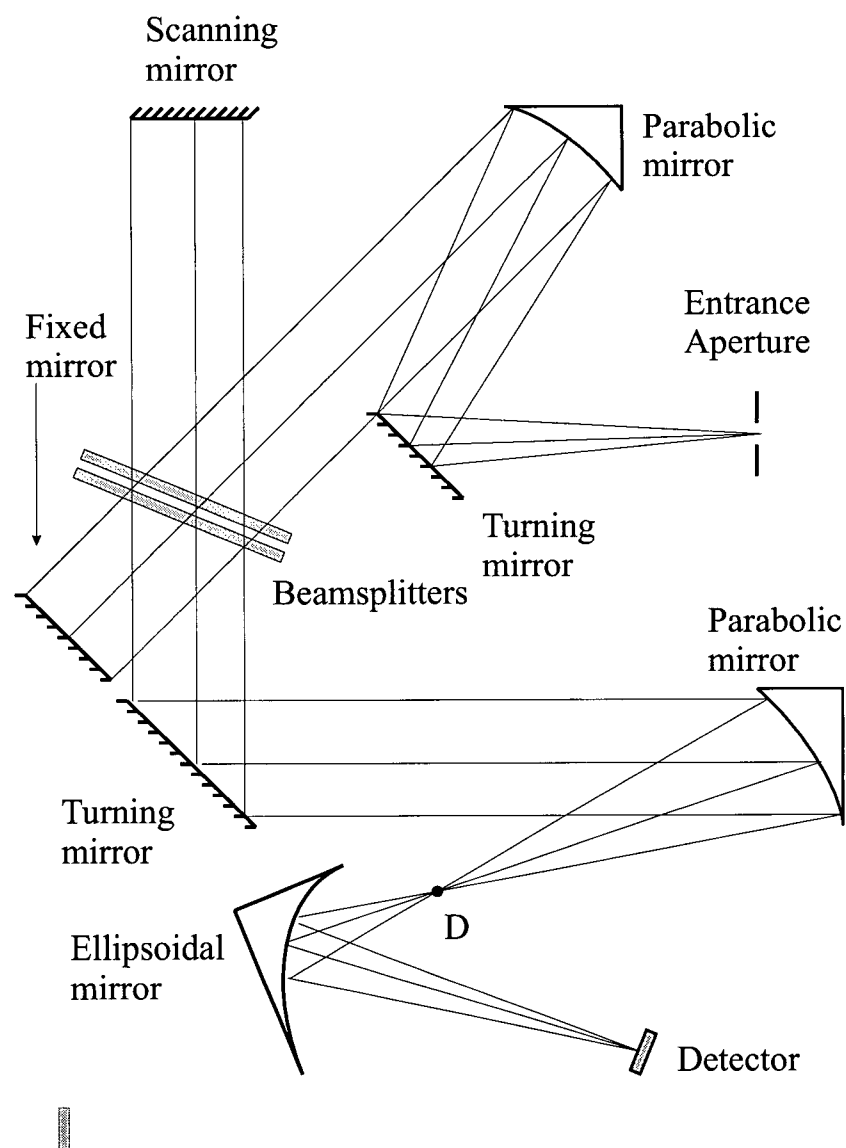


Figure 4.4: Schematic diagram of FTIR spectrometer

remained stationary on the screen fixed to the turntable when the turntable and sample holder were rotated through 360° .

The ellipsoidal mirror, EM2, was then adjusted using the following procedure. The CCD camera was placed a focal distance away, and the mirror was adjusted until a feature (divot or scratch) on the sample was in focus on the CCD camera.

The ellipsoidal mirror, EM1, and fibre were then positioned such that a round, well-focussed light spot was imaged by the CCD camera.

Subsequently, the square aperture was set to the correct height using the He-Ne laser and placed on the optical table at the long focus of the ellipsoidal mirror, EM3. The square aperture was then illuminated and the ellipsoidal mirror adjusted such that the image of the square aperture was focussed down to a point at the entrance aperture of the FTIR.

Another illuminated aperture serving as a point source was then placed at the focal point of the detector collection mirror in the FTIR (point D in figure 4.4). The turning mirror, TM5 was positioned and adjusted such that a sharp image, centred on the square aperture, was produced. Also, the center of the illuminated spot on the turning mirror TM5 was verified to be aligned and level with the square aperture using the Helium-Neon laser. The specularly reflected signal off a piece of GaAs was then verified to be falling near the centre of the of the spot produced by and co-aligned with the light coming from the back-illuminated aperture inside the FTIR over the 1.5 m span between the aperture and TM5.

Finally, the remaining turning mirrors were inserted, and the mirrors, TM2 and TM3, were moved to adjust the path length such that the spot of white light was focussed at the position of the square aperture, as viewed using the CCD camera placed at that point.

4.4 Angular Resolution

Because it is a *focussed* beam of light impinging on the grating, which is used to excite the modes of the structure, for a fixed frequency ω , there is, in actuality, an angular distribution of \mathbf{k} vectors incident on the sample at once. Consequently, this results, again, in an angular distribution of specularly reflected light about the nominal angle of reflection.

The angular spread of \mathbf{k} vectors incident on the sample can have a maximal value of $\pm 4^\circ$ which is defined by the size of the mirror EM1. During data collection this value was reduced by closing down the iris aperture, placed midway between the fibre and mirror, to a maximum of 3mm in diameter. This allowed a $\Delta\theta$ of $\pm 3^\circ$.

Of the cone of light reflecting off the sample, only that falling within the detector acceptance angle is analyzed by the FTIR. This acceptance angle is limited by the $f/\#$ ($f/4$) of the off-axis parabolic collimating mirror in the FTIR. This was calculated, by ray tracing, to correspond to an acceptance angle of $\pm 1^\circ$ about the nominal angle of specular reflection off the sample.

The result of the finite angular resolution is to smear out the sharp features expected in the collected spectra. A quantitative analysis of this effect is deferred to the next chapter.

4.5 Experimental Procedure

A series of specular reflectivity spectra was collected from each of the gratings at incident angles of 2.5° , 5° , 10° , 15° , 20° , 25° , 30° , 40° , and 50° , with the polarizer rotated first in the s , then in the p position, for both $\phi = 0^\circ$ and $\phi = 45^\circ$ (see Figure 4.1). The following procedure was used to position the sample for each incident angle. The CCD was inserted into the beam path and the grating translated until it appeared in the field of view on the monitor. The input mirror, EM1, was rotated to position 2θ , and the

sample rotated until the signal on the detector, as monitored by a digital voltmeter, was maximized. The square aperture was then closed down until only light from the grating was imaged on the CCD. The CCD camera was then swung out of the way and a spectrum taken. With the system properly aligned initially, it was possible to take spectra at all the incident angles for a particular polarization without having to adjust any of the optics, including the position of the square aperture.

A series of specular reflectivity spectra were also taken off a piece of GaAs polished on one side. These were used to normalize out the input spectrum, the detector response, and absorption lines due to atmospheric molecules.

Chapter 5

Results

5.1 Introduction

The experimental setup described in Chapter 4 was used to collect specular reflectivity spectra from the ten 2D gratings fabricated on sample ASU 721. The spectra from three of these gratings (grating numbers 22,23,24) exhibited features indicative of the photonic bandstructure expected near the second order gap. For grating 22, in particular, all of these features remained clearly identifiable and within the detector's spectral range over a large range of incident angles and for both polarizations. Consequently, the bulk of this chapter presents the data obtained on grating 22. Spectra from gratings 23 and 24, which have the same pitch but larger hole sizes, are also presented in order to show the effects of filling fraction on the ordering of the broad and narrow spectral features associated with lossy modes.

5.2 Resonant Reflectivity

Figure 5.1 depicts the experimental and model specular reflectivity spectra obtained for p polarized light incident at 5° along the X ($\phi = 0^\circ$) direction of the square lattice. The spectra are plotted as a function of a “reduced frequency” or wavenumbers (in units of cm^{-1}) which we denote as

$$\tilde{\omega} \triangleq \omega/2\pi c \tag{5.1}$$

where c is the speed of light in free space. The experimental spectrum was obtained and normalized according to the procedure described in the previous chapter. The resulting spectrum was then normalized again, this time, to its maximum value within the range

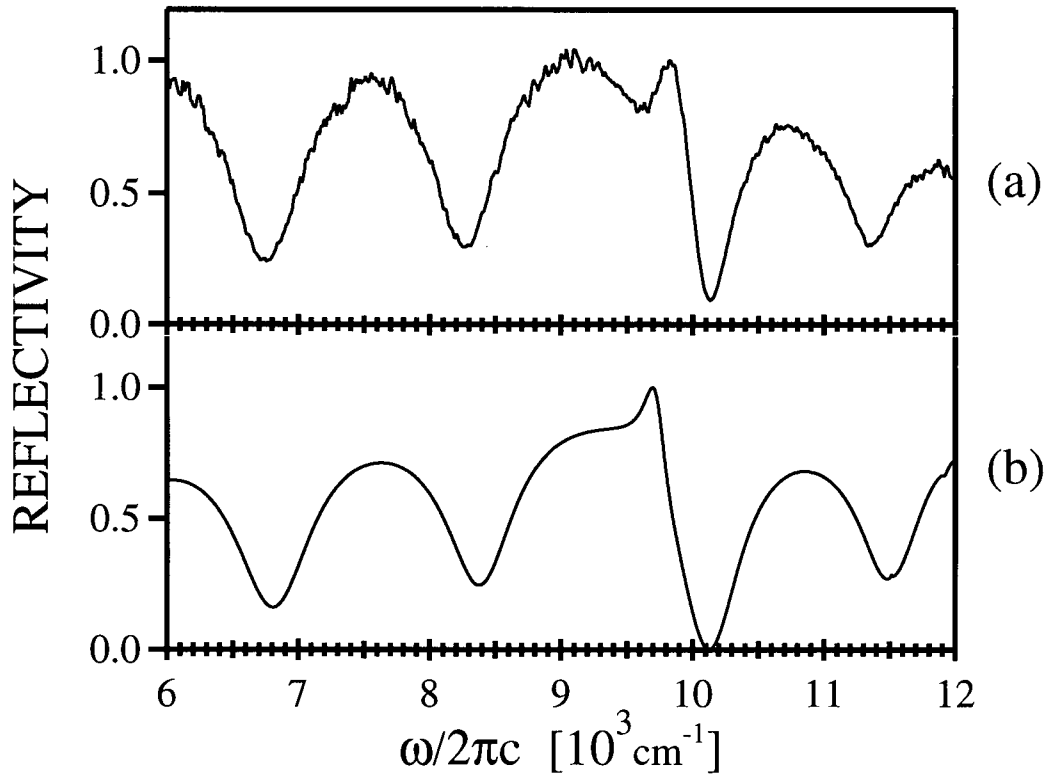


Figure 5.1: Experimental (a) and calculated (b) specular reflectivity spectra on grating 22 at incidence angle of $\theta = 5^\circ$ and $\phi = 0^\circ$ for p-polarization of reflected light.

6000 cm^{-1} to 14,000 cm^{-1} . The model spectrum was calculated using the Green's function code referred to in Chapter 2. The exact values of the parameters input to the program to describe the structure under study are discussed later in this chapter.

The broad features in the spectra spaced at $\sim 1000 \text{ cm}^{-1}$ are Fabry-Perot fringes arising from the optical cavity formed by the Al oxide layer. They would be present even in the absence of the grating. The sharp, bipolar feature is a Fano resonance [38], which indicates resonant coupling to a leaky slab mode attached to the textured waveguide structure. It is these Fano resonances that are used to probe the dispersion and lifetimes of the resonant modes of the textured waveguide. The precise Fano lineshape function is described in section 5.6.1. A physical explanation of the reason behind the bipolar

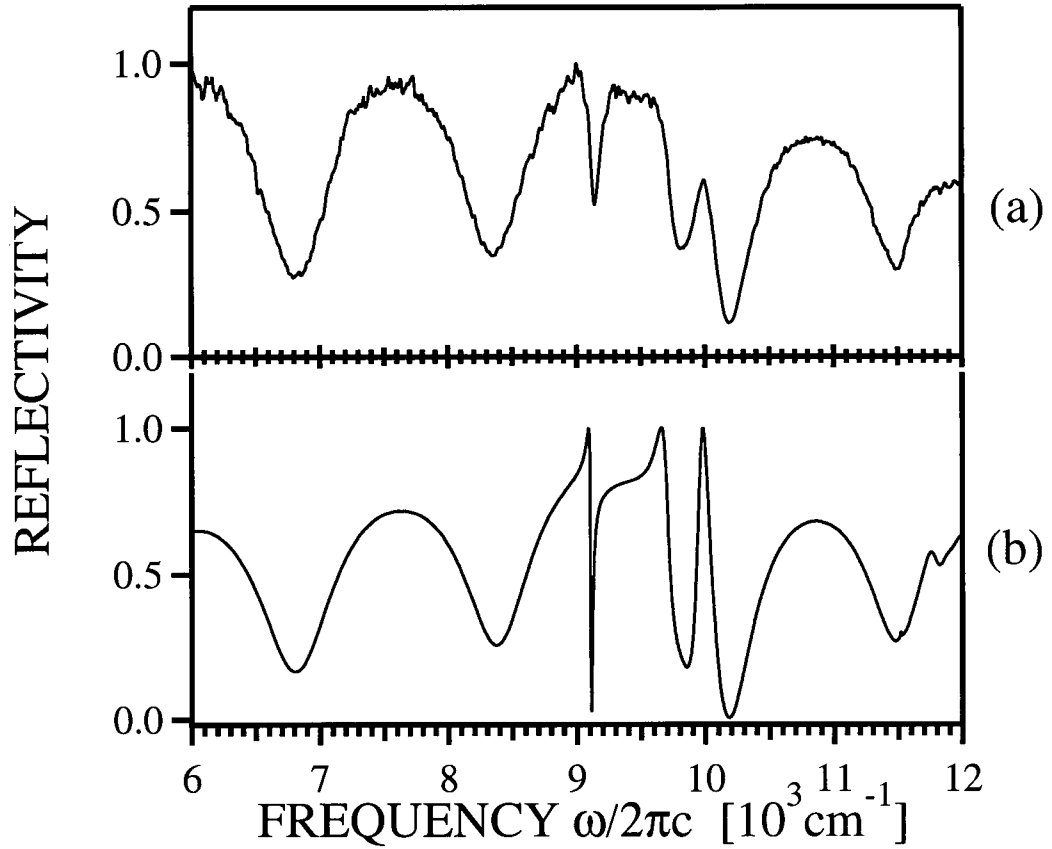


Figure 5.2: Experimental (a) and calculated (b) specular reflectivity spectra on grating 22 at incidence angle of $\theta = 5^\circ$ and $\phi = 0^\circ$ for s -polarization of reflected light.

nature of the Fano lineshape is again deferred to Chapter 6 (section 6.2).

5.3 Polarization Properties

Figure 5.2 shows the experimental and model spectra for reflected s polarized light. In this case, there are three sharp features superimposed on the Fabry-Perot fringes, giving a total of four features in either polarization.

Figures 5.3 and 5.4 show the experimental and model spectra for light incident at $\theta = 5^\circ$ along the $\Gamma - M$ direction of the photonic crystal ($\phi = 45^\circ$) for the p and

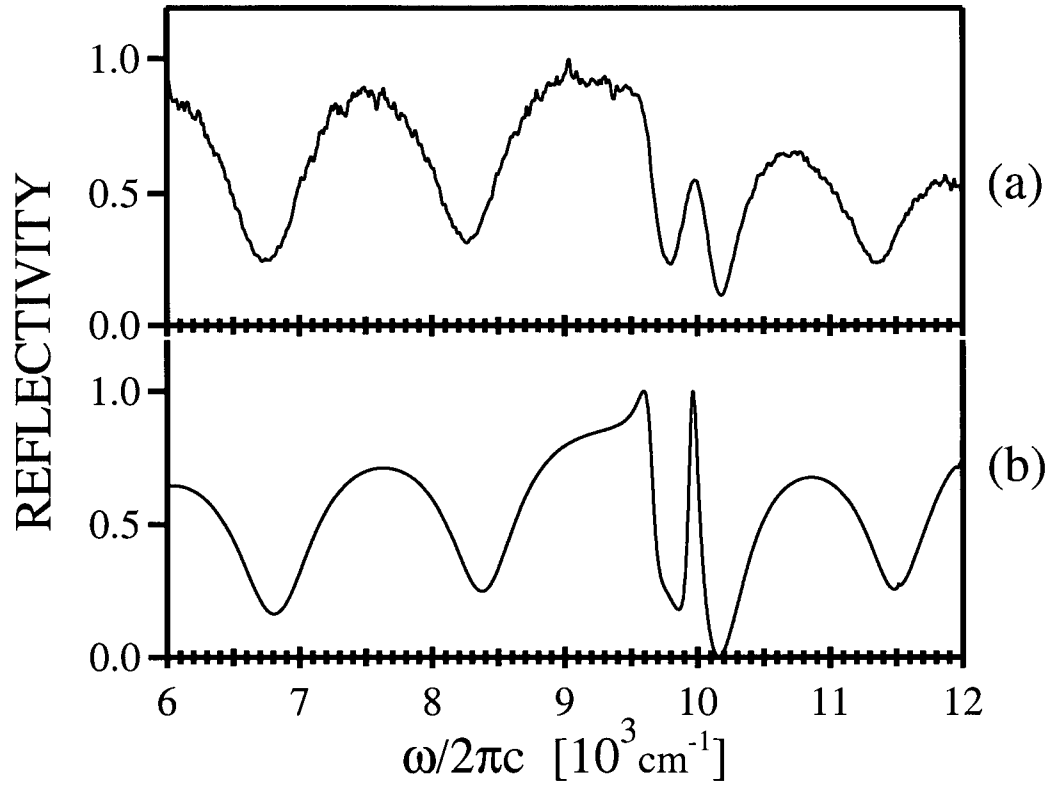


Figure 5.3: Experimental (a) and calculated (b) specular reflectivity spectra on grating 22 at incidence angle of $\theta = 5^\circ$ and $\phi = 45^\circ$ for p-polarization of reflected light.

s polarizations respectively. The specular reflectivity spectra again exhibit four Fano resonances, but, in this case, two features occur in each polarization.

In summary, then, the spectra exhibit well-defined polarization selection rules which are dependent on the orientation of the plane of incidence.

5.4 Dispersion

Figure 5.5 shows a series of s polarized specular reflectivity spectra, taken at various angles of incidence with the in-plane propagation vector always oriented along the $\Gamma - X$ direction (*i.e.*, $\phi = 0$). The plots have been offset from one another for the sake of clarity,

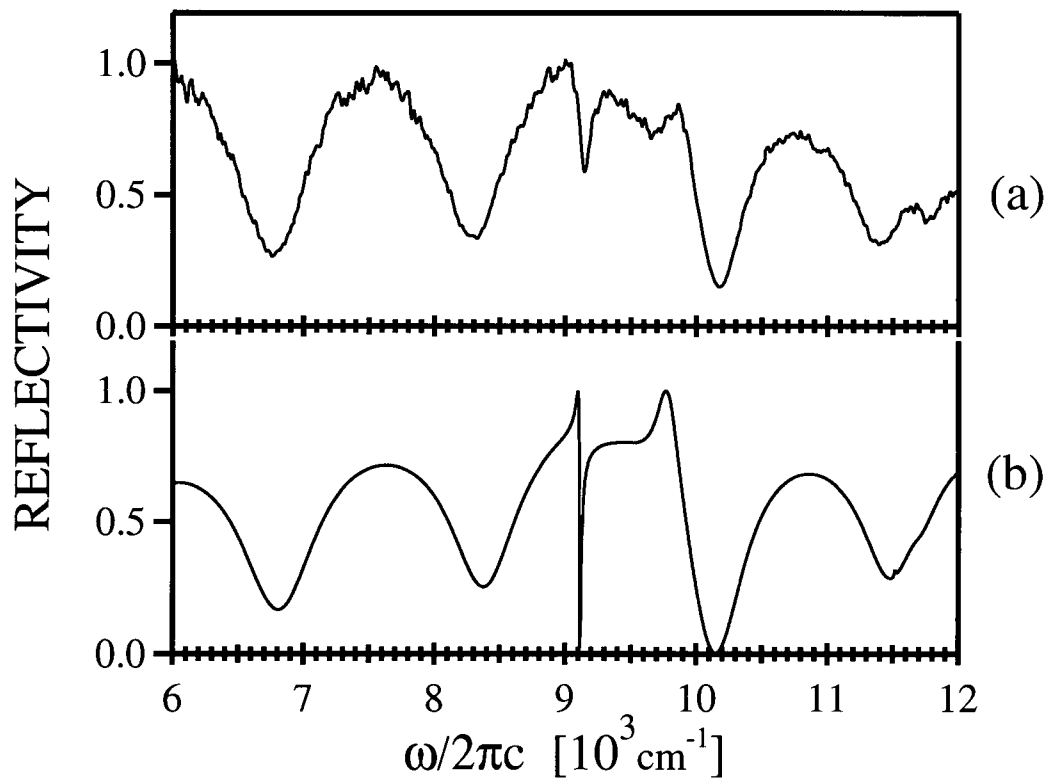


Figure 5.4: Experimental (a) and calculated (b) specular reflectivity spectra on grating 22 at incidence angle of $\theta = 5^\circ$ and $\phi = 45^\circ$ for s -polarization of reflected light.

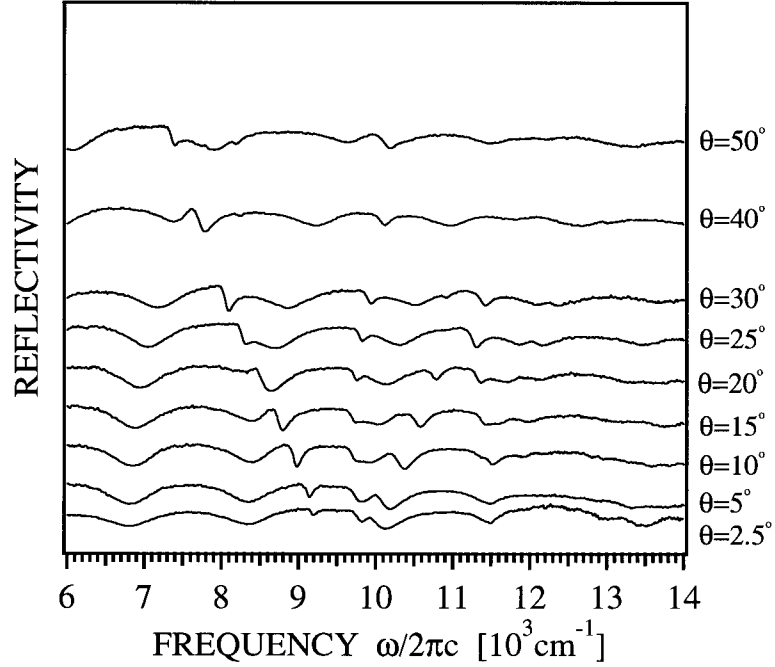


Figure 5.5: Experimental specular reflectivity spectra for s polarization at various incident angles, θ , along the $\Gamma - X$ direction ($\phi = 0$). The plots have been offset from one another for the sake of clarity; the vertical scale on the reflectivity traces is linear.

and each spectrum has been normalized to its maximum value in the displayed spectral range. The basic dispersion of various bands leaking s polarized radiation is manifestly evident. There is a clear gap, or avoided crossing, near zone-centre (*i.e.*, at small angles of incidence) where the bands flatten out. The size of the gap near zone-centre is approximately 900 cm^{-1} which is of the order of 10% of the centre frequency. There is also a fourth band occurring higher in energy which anti-crosses with the third band at about 25° . The linewidth of the modes varies from band to band and within bands.

5.5 Fitting with Model

The GF model requires the following as input parameters: the layer thicknesses and materials of the slab waveguide structure, the grating pitch, hole radii and material filling the holes, the incidence angle or in-plane wavevector, and the frequency range for the calculation. One limitation of this model is that there can only be one type of host material for the textured layer, whereas the core layer of the ASU 721 waveguide studied is nominally composed of a 45 nm thick GaAs layer as well as a 35 nm $\text{Al}_{0.3}\text{Ga}_{0.7}\text{As}$ layer. Consequently, a single material with dielectric constant given by an average of those for GaAs and $\text{Al}_{0.3}\text{Ga}_{0.7}\text{As}$, weighted according to thickness, was used in the model for the core layer. That is:

$$\epsilon'_g(\tilde{\omega}) = a_{\text{GaAs}}\epsilon'_{\text{GaAs}}(\tilde{\omega}) + [1 - a_{\text{GaAs}}]\epsilon'_{\text{Al}_{0.3}\text{Ga}_{0.7}\text{As}}(\tilde{\omega}) \quad (5.2)$$

$$a_{\text{GaAs}} = t_{\text{GaAs}}/(t_{\text{GaAs}} + t_{\text{Al}_{0.3}\text{Ga}_{0.7}\text{As}}) \quad (5.3)$$

Also, the 2D array of holes that comprise the grating was etched part of the way into the cladding layer in order to aid in the oxidation. As a result, an additional layer with dielectric constant given by an average of aluminium oxide and air, weighted according to the air filling fraction of the holes, was placed between the core and uniform oxide layer in the model. The nominal thickness for this layer was estimated to be 350 nm based on the etch time. The semiconductor dielectric constants, including dispersion, were taken from the literature [50]. The dielectric constant of the oxide was measured by our group, independently, to be 2.56 [51].

Altogether, the parameters that were allowed to vary in the model were the pitch (Λ), the air filling fraction of the (assumed cylindrical) holes (f), the thicknesses of the core (t_g), oxide (t_{oxide}), and air-oxide layer (t_{ao}), and the admixture of GaAs and $\text{Al}_{0.3}\text{Ga}_{0.7}\text{As}$ in the core layer (a_{GaAs}).

For each combination of these parameters a *full* set of reflectivity spectra were calculated for the series of incidence angles depicted in figure 5.5, for both the s and p

polarizations in the $\Gamma - X$ direction. These were compared manually with those from the experiment. The model parameters yielding the best fit to all of the data are presented in Table 5.1 along with their nominal and/or measured values. The pitch of the photonic lattice was 550 nm, and the air filling fraction of the holes was 27%. These compare favourably (to within 3.5%) to the nominal and measured values. The total thickness of the GaAs/Al_{0.3}Ga_{0.7}As core layer from the best fit model results compares favourably with both the SEM measurement and the nominal value supplied by the sample grower. As stated above, the GF model can not handle variation in the grating layer in the transverse direction other than by averaging the dielectric constant of the layer. A 60% weight to the Al_{0.3}Ga_{0.7}As content yielded the best result. This corresponds to thicknesses of 33 nm and 50 nm for the GaAs and Al_{0.3}Ga_{0.7}As layers respectively, which are somewhat off from their respective nominal values of 45 nm and 35 nm. No more can be said since we are unable to measure the layer structure within the core. The total thickness of the oxide layer used in the model is in good agreement with the measured value. Best agreement was obtained when it was assumed that the 2D array of holes penetrated 350 nm into the oxide layer. This was modelled as a layer with a reduced dielectric constant according to the air fill fraction of the holes which were assumed to have vertical sidewalls. This penetration into the oxide is not inconsistent with the depths registered by the probe during AFM microscopy, which were in excess of 200 nm, when it is considered that the non-vertical probe prevents the probe tip from reaching the bottom of the holes. In summary, the parameters describing the physical waveguide geometry and composition that were input to the model to provide the best agreement with the measured spectra were within 3.5% of the measured values where measurement was possible.

This same set of parameters was then used to generate spectra at various angles of incidence oriented along the $\Gamma - M$ direction ($\phi = 45^\circ$). The excellent agreement with the corresponding experimental data suggested that no further iteration of the parameters

Parameter	Model value	Nominal value	Measured value
grating pitch	550 nm	575 nm	(571 ± 17) nm
air filling fraction	0.27	none	(0.278 ± 0.027) nm
GaAs thickness	33 nm	45 nm	none
$\text{Al}_{0.3}\text{Ga}_{0.7}\text{As}$ thickness	50 nm	35 nm	none
total core thickness	83 nm	80 nm	(90 ± 10) nm
oxide layer total thickness	1900 nm	1600 nm	(1800 ± 80) nm
air-oxide layer thickness	350 nm	none	> 200 nm

Table 5.1: Model, Nominal, and Measured sample structure parameters for grating 22 on sample ASU 721

was necessary. The bandstructure generated using these best-fit model results and that obtained from the experimental spectra are both plotted in Figure 5.8, which is presented later in this chapter in section 5.7.

5.6 Extraction of Mode Frequency and Linewidth from Spectra

5.6.1 Extraction of Frequency and Linewidth from Experimental Spectra

The specular reflectivity spectra in the vicinity of the relevant resonant features were fit with a function comprised of the sum of an Airy function [42], which models the Fabry-Perot fringes, and a Fano resonance, which models the feature associated with the Bloch state of the photonic crystal.

The Airy-like function is given by:

$$A(\tilde{\omega}) = b + s \times \frac{2r^2[1 - \cos(d\tilde{\omega} + \psi)]}{1 + r^4 - 2r^2 \cos(d\tilde{\omega} + \psi)} \quad (5.4)$$

For a simple 3-layer structure the parameters r and d would represent the reflectivity of the interfaces and the optical path through the cavity respectively. An offset, b , scale factor, s , and phase factor, ψ , were added to account for the fact that there are additional layers above the oxide cladding layer that is primarily responsible for the Fabry-Perot fringes. This function was used to fit the spectra for the values of the parameters in

a region away from any Fano resonances. It was combined with the Fano lineshape function given by:

$$F(\tilde{\omega}) = F_0 \frac{(q + 2(\tilde{\omega} - \tilde{\omega}_0)/\Gamma)^2}{1 + (2(\tilde{\omega} - \tilde{\omega}_0)/\Gamma)^2} \quad (5.5)$$

to yield:

$$R(\tilde{\omega}) = A(\tilde{\omega}) + F(\tilde{\omega}), \quad (5.6)$$

which was fit to the entire spectrum, allowing only the Fano lineshape parameters, q , Γ , $\tilde{\omega}_0$, F_0 to vary. Finally, a fit was performed using $R(\tilde{\omega})$ but allowing all of the parameters to vary. This procedure usually resulted in a good fit to the experimental spectrum.

One such fit to an experimental spectrum obtained from grating 22 is depicted in Figure 5.6. Only the lower frequency Fano-like resonance was fit over the range ($6000 \text{ cm}^{-1} - 9000 \text{ cm}^{-1}$). From this fitting procedure the mode was found to lie at 7450 cm^{-1} and to have a linewidth of 105 cm^{-1} .

5.6.2 Extraction of Mode Parameters from Model Spectra

A slightly different approach was used in order to extract the widths and positions of the resonances from the GF model. In addition to specular reflectivity spectra, the model is also capable of generating scattering spectra for the four field components with in-plane propagation constants $\beta_{\text{inc}} \pm \beta_G \hat{x}$ and $\beta_{\text{inc}} \pm \beta_G \hat{y}$.

The quasi-bound modes of the system again manifest themselves as Fano resonances in the spectra, but this approach has the advantage that the modes appear *almost background-free*. This is the case because the non-resonant background is first order in the dielectric texture for these components, while it is of order unity in the specular component. Figure 5.7 shows sample fits to first order scattering spectra with the Fano lineshape function $F(\tilde{\omega})$, together with the corresponding specular spectrum. Notice that the first order spectra contain only a weak background, which simplifies and reduces the number of parameters required to obtain good fits. Furthermore, as discussed

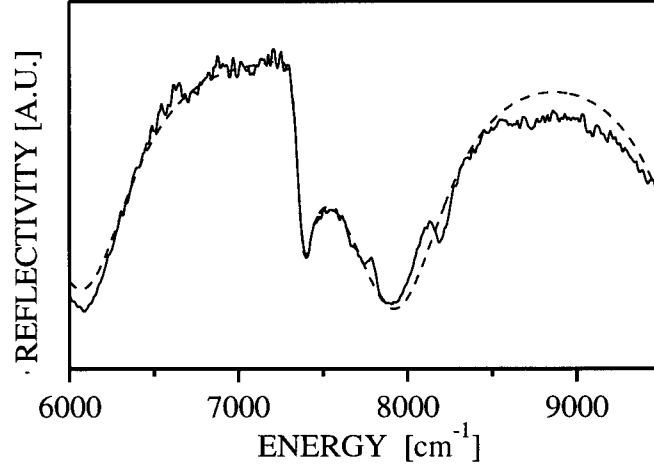


Figure 5.6: Fit to specular reflectivity spectrum obtained from grating 22 obtained with light incident at $\theta = 50^\circ$ along the $\Gamma - X$ direction. The solid line represents the experimental spectrum while the dashed line represents the “best fit” spectrum generated by a Fano lineshape function summed with an Airy function. The initial fit to the Fabry-Perot fringes was performed over a wider range of energies (6000 cm^{-1} to $11,500 \text{ cm}^{-1}$) not shown here. The fit using a Fano lineshape and Airy function was performed using data points in the range $6000 \text{ cm}^{-1} - 9000 \text{ cm}^{-1}$.

above, away from zone-centre, each of the bands are rapidly dominated by a particular Fourier component. Consequently, by fitting to the dominant component for the band in question, the neighbouring resonances associated with the other bands remain small. And therefore, the estimates for the errors on the mode frequency and linewidth arising from the first-order fitting procedure are much smaller than the errors associated with fitting the experimental specular reflectivity spectra.

It should be mentioned here that while these first-order diffracted spectra provide “cleaner” signals for extracting mode frequencies and linewidths from model calculations, such first-order diffracted spectra are considerably more difficult to obtain experimentally than specular reflectivity spectra. The first-order diffracted light must travel down the thin untextured waveguide core to the edge of the sample, and since the waveguide core is on the surface of the sample there is considerable loss due to scattering from surface

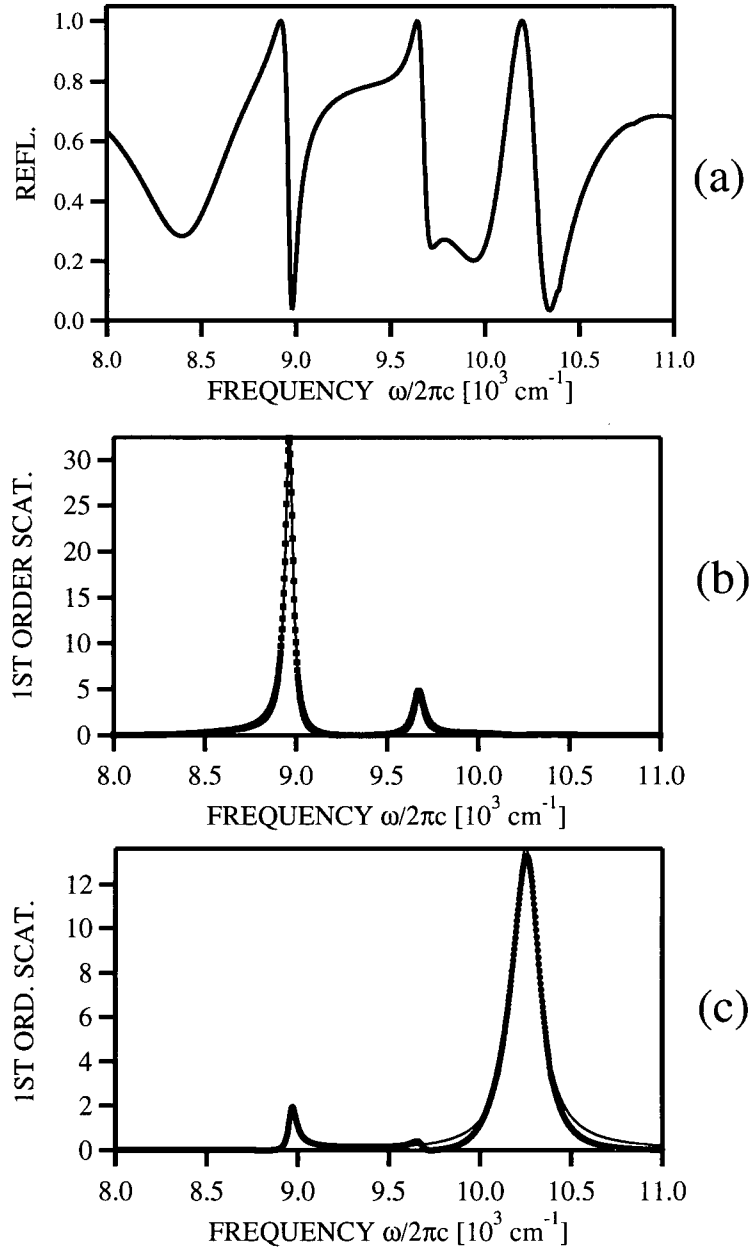


Figure 5.7: Fit to spectra generated by the GF model. (a) Specular reflectivity spectrum for reference (b) 1st order scattering to $-\beta_G \hat{x}$ field component (c) 1st order scattering $+\beta_G \hat{x}$ field component. In (b) and (c) the symbols correspond to the model values, and the smooth lines are the result of a fit with a Fano lineshape function. The spectra are for 10^0 angle of incidence along the $\Gamma - X$ direction.

debris. Also, since there is no lateral confinement, the diffracted beam spreads in the in-plane directions. This all necessitates creating a cleaved edge whence the diffracted light is to be extracted very near the textured region. Making such precisely positioned cleaves without destroying the grating proved to be extremely challenging, especially since aluminum oxide flakes and crumbles upon cleaving.

5.7 Bandstructure

The bandstructure for these modes was obtained by extracting the energies, ω_i , at which the resonant features occur and plotting these as a function of the magnitude of the in-plane propagation vector, given by $\beta^i = \frac{\omega_i}{c} \sin(\theta)$. Figure 5.8 shows the dispersion of the resonant modes of the structure along the $\Gamma - X$ and $\Gamma - M$ symmetry directions of the square Brillouin zone. For comparison, the inset schematically depicts the bandstructure for a similar structure had the array of holes been etched only a small fraction of the way through the guiding core. In that case, the corresponding dispersion curves would effectively represent the bare TE polarized slab modes, zone-folded to the first Brillouin zone by the in-plane Fourier components of the square grating.

The polarization of the features in the reflectivity measurement and in the calculations, remains the same within each band along a given symmetry direction of the crystal, and so the curves in Figure 5.8 have been labelled as either s or p polarized. Along the $\Gamma - X$ direction, there are a total of 5 curves, with four labelled s and one labelled p . In the vicinity of the zone-centre, there are three s polarized curves and one p polarized curve. Two of these exhibit large dispersion, with one having positive dispersion (frequency increasing with β) and the other having negative dispersion. The remaining s polarized curve and the p polarized curve both have little dispersion.

Away from zone-centre, in the $\Gamma - X$ direction, the fourth and fifth curves, which are both s polarized, anti-cross near $\beta/\beta_G \approx 0.25$. The frequency gap at the point of closest approach is comparable to the gap which occurs at zone-centre.

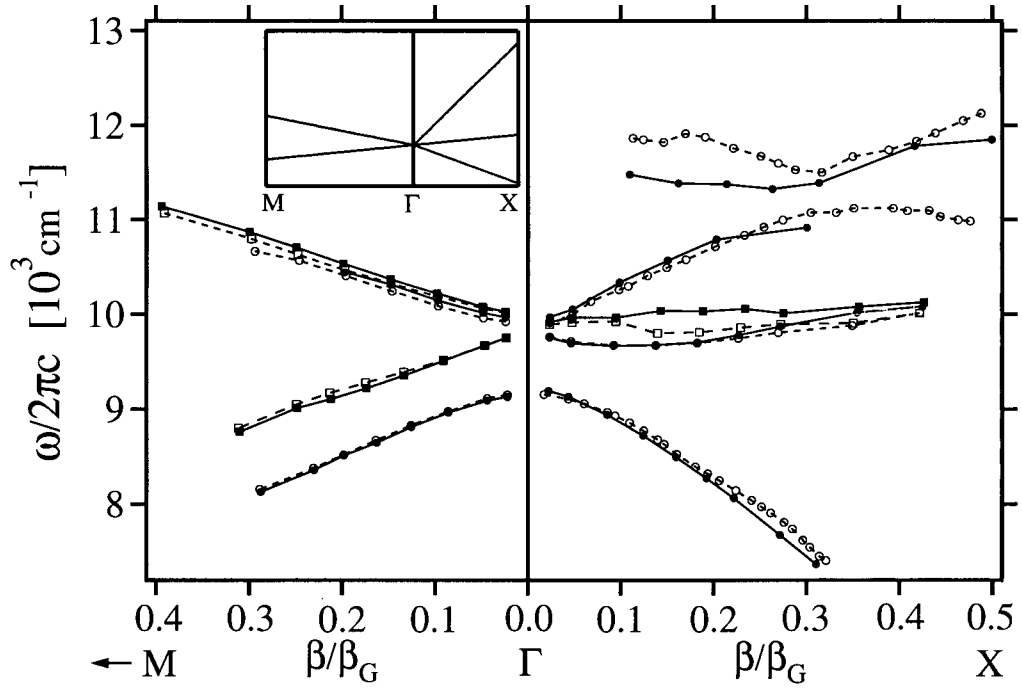


Figure 5.8: Mode frequency versus magnitude of in-plane wavevector for experiment (solid lines and markers) and model (dotted lines and hollow markers) for *s* (circles) and *p* (squares) polarized radiation. The inset schematically depicts the bandstructure for the case of weak texture.

Along the $\Gamma - M$ direction, there are two moderately dispersive pairs of curves with each pair containing one s and one p polarized band. One pair have a positive dispersion while the other pair have a negative dispersion.

There is excellent agreement between the model and experiment except for the fifth curve in the $\Gamma - X$ direction. This is partly due to the fact that it lies at or above the electronic bandgap of GaAs ($11,450 \text{ cm}^{-1}$), which forms half of the waveguide core. In this region, the model used for the dielectric constant of GaAs neglects the imaginary part and is not strictly valid even for the real part. The discrepancy is also due to the omission from the model of higher order Fourier components of the field, which become significant at higher energies.

5.8 Linewidths

5.8.1 Linewidth of Lowest Energy Band

Figure 5.9 shows the variation of the linewidth of the lowest energy band as a function of the in-plane propagation vector for both experiment and theory. Except very near the zone-centre, where the calculated value approaches zero, the measured linewidth agrees with the model to within a factor of two. Away from zone-centre, the experimental and calculated linewidths both exhibit a non-monotonic variation. It should be noted that while the calculation assumes pure plane waves incident with well-defined \mathbf{k} vectors, and an infinite, perfectly periodic photonic crystal that is free from imperfections, none of these assumptions is strictly true in the experiment.

The finite size of the photonic crystal, the non-zero detector acceptance angle $\Delta\theta$, and non-uniformities in the photonic crystal will all contribute to a smearing out of the spectra, in a convoluted manner, that limits the resolution of the experiment. Qualitatively, these factors account for the fact that the experimental linewidth does not seem to be approaching zero at the zone-centre as it does in the calculation and as dictated by symmetry considerations. An approximate quantitative treatment of their effects on

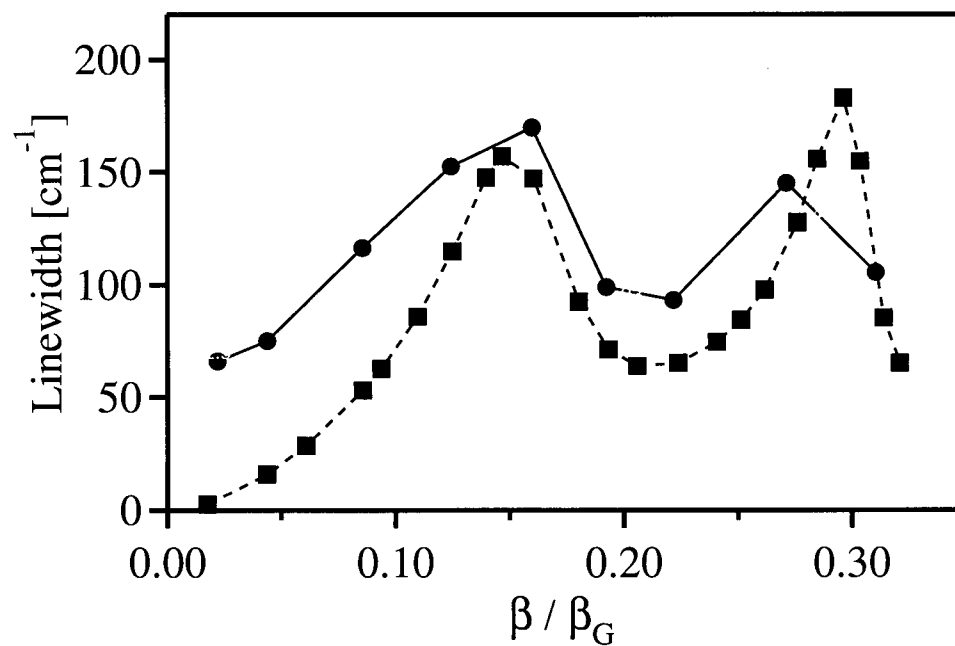


Figure 5.9: Experimental (filled circles and solid lines) and model (filled squares and dotted lines) linewidths of the lowest frequency band appearing along the Γ - X direction in Figure 5.8.

the measured linewidths is given below.

In Chapter 4 it was stated that there is an angular spread of $\pm 3^\circ$ of \mathbf{k} vectors exciting the modes of the structure and that the detector acceptance is $\pm 1^\circ$. Since $\beta = \tilde{\omega} \sin(\theta)$, this corresponds to $\Delta\beta = \tilde{\omega} \cos(\theta) \Delta\theta$. Consequently, one would expect the reflectivity spectrum to contain a continuous spread of Fano resonances corresponding to modes within a frequency band:

$$\Delta\tilde{\omega}_{\text{spr}} = \tilde{\omega} \cos(\theta) \Delta\theta \frac{d\tilde{\omega}}{d\beta}. \quad (5.7)$$

Furthermore, because the photonic crystal is of finite size, the Fourier Transform of the dielectric modulation is not just a series of delta functions translated in Fourier space by the reciprocal lattice vectors of the crystal. For a finite crystal, this function must be convolved in each of the x and y directions with the *sinc* function, $\frac{\sin(D\tilde{\omega})}{D\tilde{\omega}}$, where D is the size of the crystal. For the value, $D = 90 \mu\text{m}$, corresponding to the size of the photonic crystals in this work, the main lobe of the *sinc* function has a full width at half maximum of approximately $\Delta\beta_G = 60 \text{ cm}^{-1}$. The effect on the eigenstates of the crystal is that they are no longer made up of discrete field components with in-plane propagation vectors given by $\pm n\beta_G \hat{x} \pm m\beta_G \hat{y}$ for integer m and n . Rather, to a good approximation, they contain significant field components in a range spanning $\Delta\beta_G$ in each of the x and y directions, centred at $\pm n\beta_G \hat{x} \pm m\beta_G \hat{y}$. The components in the band near zero in-plane wavevector will be phase-matched to radiating components in the cladding air layer. When white light is used to probe along $\beta = \tilde{\omega} \sin \theta$, reflectivity will be enhanced when the in-plane wavevector is matched to the near-zone-centre field components of the eigenstates of the finite-sized crystal. This occurs in the frequency range:

$$\Delta\tilde{\omega}_{\text{fin}} = \Delta\beta_G \frac{d\tilde{\omega}}{d\beta} \quad (5.8)$$

The experimental linewidth can be approximated by adding in quadrature $\Delta\tilde{\omega}_{\text{spr}}$ and $\Delta\tilde{\omega}_{\text{fin}}$ to the inherent width of the mode. Near the zone-centre, this adds approximately

50 cm⁻¹ to the inherent linewidth, bringing it into much better agreement with the experiment¹.

Away from zone-centre, the dispersion increases then becomes roughly constant. However, this is largely offset by the ω and $\cos\theta$ factors in equation 5.7, which both decline, so that the net effect is to add about 80 – 90 cm⁻¹ to the inherent linewidth leaving it in reasonable agreement with the experiment.

Finally, it should be re-iterated that non-uniformities in both the periodicity, as well as in the sizes and shapes of the airholes that comprise the photonic crystal are also expected to have the effect of smearing out the spectra. However, the lack of any available quantitative characterization of these non-uniformities precludes any further comment in this regard.

5.8.2 Linewidths of 4th and 5th Bands

Figure 5.10 shows the experimental and model linewidths as a function of in-plane wavevector along the $\Gamma - X$ direction for the fourth and fifth lowest bands. The feature associated with the fifth band remains resolved for all of the incident angles, and the associated linewidth varies smoothly in both the experiment and the model. The model predicts that, for the fourth band, the linewidth of the associated feature vanishes at the anti-crossing and varies considerably on either side of it. The experiment is qualitatively consistent with this: there is a larger variation in the linewidth in the fourth band than in the fifth band, and the resonance associated with the fourth band vanishes at $\theta = 25^\circ$. Once again, due to averaging effects, we expect the linewidth to vanish from the spectrum when it becomes too small ($\lesssim 80 \text{ cm}^{-1} - 90 \text{ cm}^{-1}$, see footnote above).

¹This treatment would be rigorous if the resonances in reflection were strictly Lorentzian in character. The fact that they are generally Fano-like complicates the situation. In particular the averaging of Fano lineshapes tends to diminish the visibility of the features as much as it increases their apparent widths. This is consistent with the experimental results that consistently have the resonant features "disappear" when their line widths decrease below the instrumentally limited resolution calculated as above. More realistic (and complicated) averaging of the theoretical spectra bear this out but this is beyond the scope of this thesis.

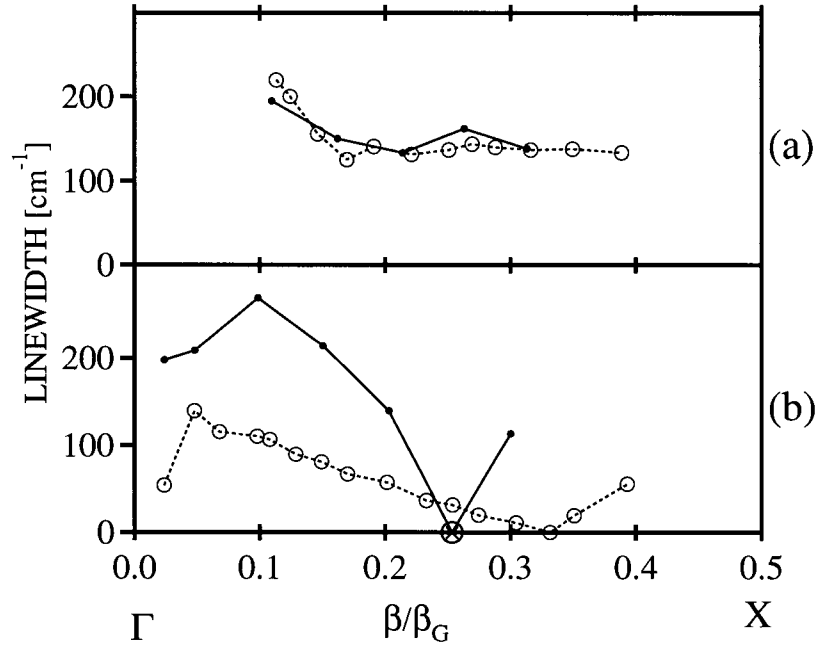


Figure 5.10: Experimental (dots and solid lines) and model (open circles and dotted lines) linewidths of 5th lowest (a), and 4th lowest (b) bands in Figure 5.8 *vs.* in-plane wavevector along the Γ - X direction. The crossed circle represents a zero linewidth that was inferred from the absence of any feature in the spectrum.

A crossed circle has, therefore, been used for the experimental data point in the fourth band at $\beta/\beta_G \approx 0.25$, which corresponds to $\theta = 25^\circ$, in order to indicate an unknown but small linewidth.

Thus, both model and experiment are consistent in demonstrating that one band involved in an anti-crossing away from zone-centre shows no dramatic variations in linewidth, while the other band exhibits a widely varying linewidth that vanishes near the point in the Brillouin zone where maximum coupling of the bands occurs.

5.9 Effect of Filling Fraction

Figure 5.11 depicts *s* polarized experimental spectra for different incident angles obtained using the grating analyzed above (no. 22) and two other gratings (nos. 23, 24)

having the same pitch but larger hole sizes. The spectra have been offset vertically from one another for the sake of clarity. All the samples yield a series of Fano resonances that exhibit qualitatively similar dispersion, but there are obvious quantitative differences due to the differing fill fractions. The resonance associated with the lowest energy band has been highlighted in each set of spectra: it shifts up in energy with increasing air filling fraction, as expected. In fact, all four bands shift to higher energy with more air in the crystal. Subtle differences in the precise dispersion of the bands in these other samples were not pursued due to the difficulty in extracting accurate fits to nearly overlapping Fano features in many of the spectra.

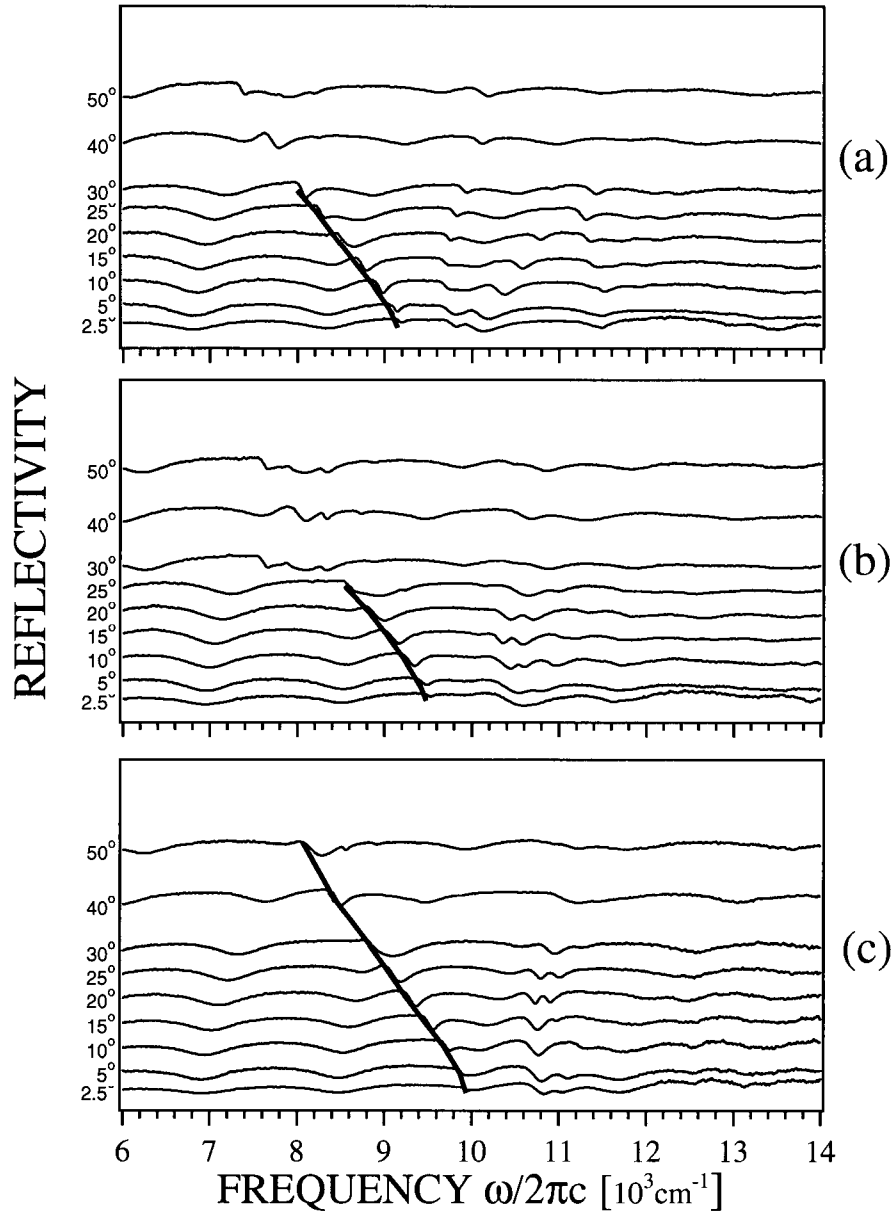


Figure 5.11: Experimental specular reflectivity spectra for *s* polarized light (solid lines) and *p* polarized lines (dotted lines) (a) grating 22 (b) grating 23 (c) grating 24 which have the same pitch but different air filling fractions of (a) 0.28 (b) 0.33 (c) 0.49. The spectra have been offset vertically from one another for the sake of clarity. The vertical scale on the reflectivity traces is linear. The dark, thick lines have been drawn in by hand to serve as a guide to the eye.

Chapter 6

Discussion

6.1 Introduction

This chapter provides an interpretation of the experimental data presented in the previous chapter based on symmetry considerations as well as knowledge gained from the numerical models. The results can be interpreted entirely in terms of renormalized (coupled) bound slab modes of some effective slab waveguide. The effective waveguide can be thought of as one where the dielectric constant in the textured guiding core is averaged according to the air filling fraction of the holes. In the spectral range of interest, the effective waveguide supports only a single, TE polarized mode, the frequency and in-plane wavevector of which follows some dispersion relation:

$$\tilde{\omega}_{guide} = f(\beta_{guide}) \quad (6.1)$$

where β_{guide} is the magnitude of the in-plane wavevector, $\boldsymbol{\beta}_{guide}$, of the guided mode, and $\tilde{\omega}$ is given by equation 5.1. The dispersion relation is isotropic within the plane of the guide. Light incident from above the grating at some frequency $\tilde{\omega}$ at incident angle, θ , and azimuthal angle, ϕ , will have an in-plane momentum given by:

$$\boldsymbol{\beta}_{inc} = \tilde{\omega} \sin(\theta) \cos(\phi) \hat{x} + \tilde{\omega} \sin(\theta) \sin(\phi) \hat{y} \quad (6.2)$$

The presence of the square grating causes this light to be scattered by the reciprocal lattice vectors of the photonic crystal, $\boldsymbol{G}_{j,l} = j\beta_G \hat{x} + l\beta_G \hat{y}$, where $\beta_G = 2\pi/\Lambda$, and j and l are integers. That is, $\boldsymbol{\beta}_{inc} \rightarrow \boldsymbol{\beta}_{inc} + \boldsymbol{G}_{j,l}$. The significant reciprocal lattice vectors for our structure in the spectral range of interest are: $\pm\beta_G \hat{x}$, $\pm\beta_G \hat{y}$, $\pm\beta_G \hat{x} \pm \beta_G \hat{y}$. A resonant feature appears in the specular reflectivity spectrum whenever the frequency

of incident radiation is such that one (or more) of the scattered components fall on the dispersion curve for the *renormalized* guided mode at that same frequency.

Many of the interesting properties revealed in this study can be qualitatively explained by ignoring the renormalization of these slab mode energies and focusing just on the restrictions imposed by symmetry. Therefore, many of the following features also apply to weakly 2D textured slab waveguides, where the renormalization is minimal.

6.2 Resonant Features in Reflectivity

The reflectivity spectrum is comprised of both resonant and non-resonant components. The non-resonant, slowly varying, component can be thought of as reflection off the “average waveguide structure”. That is, by treating the textured layer as a uniform layer with a dielectric constant taken to be the average of the dielectric constants of the semiconductor and air, weighted by their respective filling fractions. Because the layer structure is such that it contains a cavity formed by the oxide layer sandwiched between two semiconductors (namely, the substrate and the “average waveguide layer”), this slowly varying component exhibits Fabry-Perot fringes. The resonant, bipolar and asymmetric feature in the reflectivity is a Fano [38] resonance. The asymmetric and bipolar lineshape arises from interference between contributions to the reflected field from the directly scattered component described above and from a component which is doubly-scattered from the incoming radiation from above the grating to a bound mode supported by the guide and back to radiation scattered out the top of the grating. The phase of the doubly-scattered contribution varies by π radians as the frequency is tuned through the phase-matching condition for coupling to the bound mode, whereas the phase of the directly scattered contribution varies very little. Thus the two contributions sum constructively on one side of the phase-matching condition and destructively on the other side, thereby giving rise to a bipolar and asymmetric lineshape.

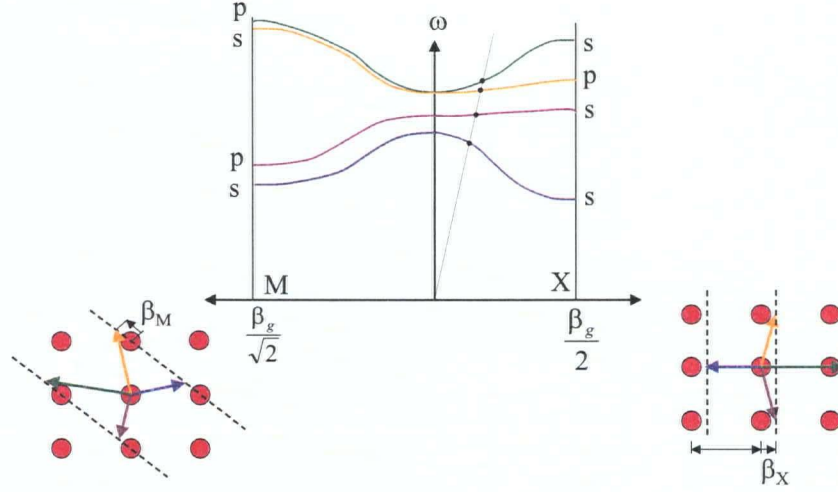


Figure 6.1: Schematic dispersion of resonant states attached to the core of a slab waveguide with square photonic lattice.

6.3 Polarization Properties and Basic Dispersion

From the fits to the Fano resonances obtained for a wide range of incident angles and polarizations, the photonic bandstructure along the two high-symmetry directions in the second Brillouin zone was obtained as in Figure 5.8. Concentrating on the four prominent bands emanating from the zone-centre in Figure 5.8, their dispersion and polarization properties can be schematically summarized as in Figure 6.1.

Starting along the $\Gamma - X$ direction, three bands have s polarization and one has p polarization. The modes associated with all four of these bands are primarily composed of a superposition of *TE polarized* field components with in-plane spatial variation given by $(\beta_{inc}\hat{x} \pm \beta_G\hat{x})$ and $(\beta_{inc}\hat{x} \pm \beta_G\hat{y})$. These field components are depicted in Figure 6.2.

Away from zone-centre, the upwardly dispersing band along $\Gamma - X$ is primarily composed of a TE slab mode at $(\beta_{inc} + \beta_G)\hat{x}$, which can only radiate s polarized radiation. Similarly, the downwardly dispersing, lowest energy band is dominated by the TE polarized $(\beta_{inc} - \beta_G)\hat{x}$ slab mode which also can only radiate in the s polarization. The two flat bands are composed principally of either symmetric or antisymmetric superpositions of

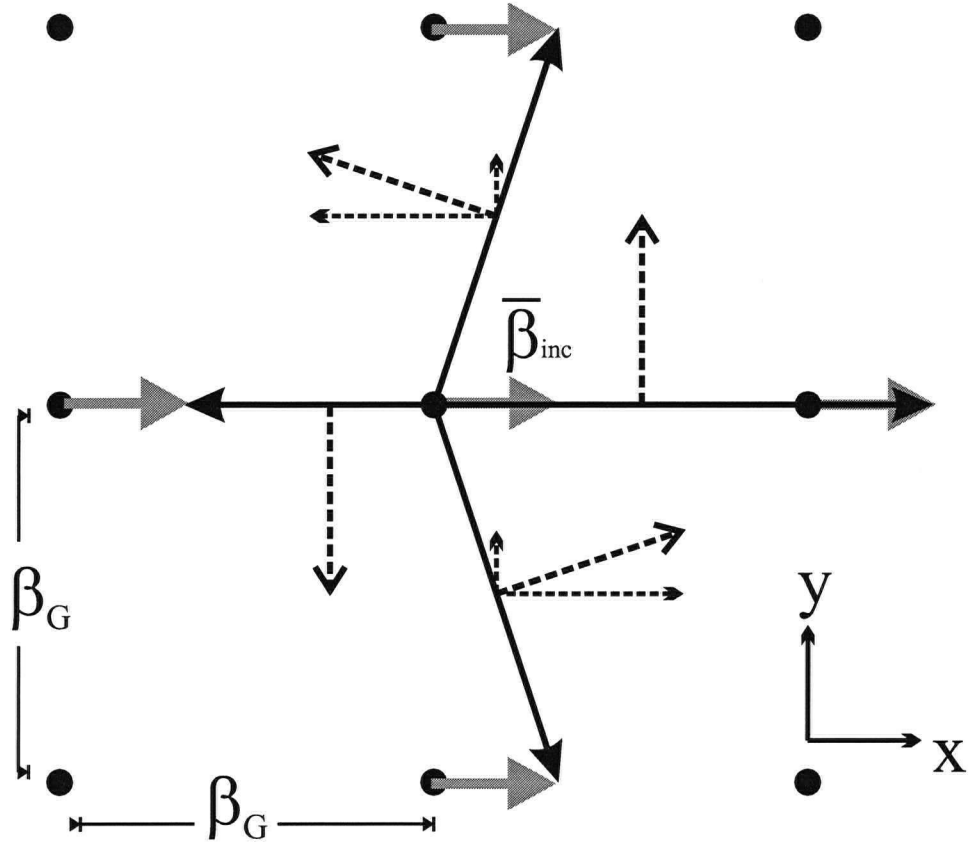


Figure 6.2: Dominant Fourier field components of eigenmodes in lowest four bands along the $\Gamma - X$ ($\theta = 0$) direction depicted in Figure 5.8: the solid black arrows represent the propagation vectors associated with the in-plane variation of the field components; dashed lines represents the electric fields and their x and y components; the grey arrows represent the incident in-plane wavevector, *i.e.*, detuning from zone-centre

the TE slab modes at $(\beta_{inc}\hat{x} \pm \beta_G\hat{y})$. The symmetric combination will generate a zeroth-order polarization with no \hat{x} component, since the principal \hat{x} components of the two respective TE slab modes cancel exactly, again leaving only an s polarized residual field that can couple to the emitted radiation. On the other hand, the antisymmetric superposition will have the \hat{y} components cancel, yielding a field entirely along the \hat{x} direction that can only couple to p polarized radiation. This fully explains both the dispersion and polarization of the four bands along the $\Gamma - X$ direction using only symmetry and the fact that the photonic eigenstates represented by these bands are composed primarily of TE slab modes.

With the aid of Figure 6.3, a similar analysis explains why in the $\Gamma - M$ direction there are two pairs of moderately dispersive bands, with one pair having positive and the other negative dispersion with respect to detuning away from zone-centre, and with each pair being comprised of one s and one p polarized band.

In this case, the four relevant field components, $(\frac{\beta_{inc}}{\sqrt{2}}[\hat{x} + \hat{y}] \pm \beta_G\hat{x})$, $(\frac{\beta_{inc}}{\sqrt{2}}[\hat{x} + \hat{y}] \pm \beta_G\hat{y})$, occur in pairs lying symmetrically about the in-plane direction of propagation of the exciting field. Here, the symmetric (anti-symmetric) superpositions of the modes at $(\frac{\beta_{inc}}{\sqrt{2}}[\hat{x} + \hat{y}] + \beta_G\hat{x})$ and $(\frac{\beta_{inc}}{\sqrt{2}}[\hat{x} + \hat{y}] + \beta_G\hat{y})$ give resultant fields polarized perpendicular (parallel) to the direction of propagation of the radiating field, $(\frac{\beta_{inc}}{\sqrt{2}}[\hat{x} + \hat{y}])$, and thus can couple only to s (p) polarized radiation. It is also evident from the diagram that as the detuning from zone-centre, β_{inc} , increases, the in-plane wavevector of these modes increases so that they and the pair of eigenstates of the photonic crystal they principally comprise, exhibit positive dispersion.

The same applies to the modes at $(\frac{\beta_{inc}}{\sqrt{2}}[\hat{x} + \hat{y}] - \beta_G\hat{x})$ and $(\frac{\beta_{inc}}{\sqrt{2}}[\hat{x} + \hat{y}] - \beta_G\hat{y})$. However, in this case, the in-plane wavevector of these modes decreases when the detuning from zone-centre increases so that these modes comprise the pair of eigenstates exhibiting negative dispersion.

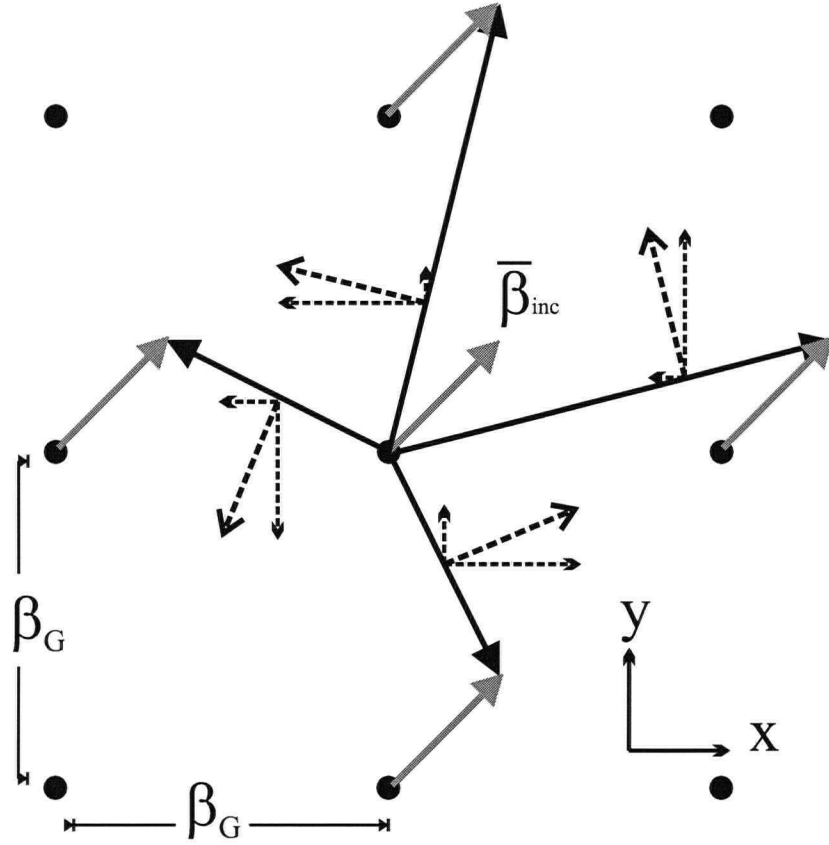


Figure 6.3: Dominant Fourier field components of eigenmodes in the four bands along the $\Gamma - M$ direction depicted in Figure 5.8: the solid arrows represent the propagation vectors associated with the in-plane variation of the field components; the grey arrows represent the incident in-plane wavevector, *i.e.*, detuning from zone-centre; the dashed lines represents the electric fields and their x and y components.

More generally, the polarization of leaked radiation will only be either s or p polarized for excitation along directions that possess mirror symmetry. This can be seen from the following argument. Along such directions, parity requires that field components of the eigenmode lying symmetrically about the plane of symmetry occur in either symmetric or anti-symmetric pairs of equal amplitude. Such pairs necessarily superimpose to give resultant electric fields which are either perpendicular or parallel to the symmetry direction and hence can only drive polarization in the zeroth order which is either purely s or p polarized. The remaining field components, which lie along the line of mirror symmetry, can only drive purely s or p polarization at zeroth order according to whether they are TE or TM, respectively.

Thus, it is an important property of these structures that, for light incident along the crystal symmetry directions ($\phi = 0^\circ$ and $\phi = 45^\circ$ in the present case), there is no s - p or p - s scattering in the specular direction. That is to say that the polarization of the radiative component of the eigenmodes is a “good quantum number”.

Since the preceding arguments did not refer at all to the magnitude of the in-plane wavevector, it follows that the polarization of the radiative component of the eigenmodes remains the same within a curve along a given symmetry direction in the bandstructure plot of Figure 5.8. Notice, however, that a given *band* cannot be given a unique polarization label because, away from directions of high symmetry, leaky eigenmodes will, in general, radiate an elliptically polarized field. Indeed, the fourth highest energy band shown in Figure 5.8 radiates s polarized light along the Γ -X direction and p polarized light along the Γ -M direction.

Finally, although beyond the scope of the experimental results presented in this work, it is important to note that none of the above arguments depends upon the radiative nature of the exciting and reflected fields. The same arguments apply equally well to the truly bound eigenmodes below the light line, for example, in the vicinity of the first order gap of a similar structure with 2D square lattice. Thus, we can generalize the

preceding statement to say that along directions of the photonic crystal which possess mirror symmetry, the polarization of the field component lying in the first Brillouin zone is a “good quantum number” for the Bloch states in that band.

6.4 Gaps and Symmetry Influences on Linewidths

The s polarized spectra around the second order gaps near zone-centre contain two narrow features and one broad feature which has approximately the same width and energy as the lone feature occurring in the p polarization. As shown by the model results in 2.3.5, it is expected that, at normal incidence, the two broad features become degenerate and retain a non-zero width whereas the narrow features become infinitely narrow and vanish. This behaviour may also be arrived at by the following symmetry argument.

Right near zone-centre, the modes in the four bands being considered here cannot be dominated by just one or two slab modes. Rather, they have to be made up of appropriate combinations of all four TE slab modes at $\pm\beta_G\hat{x}$ and $\pm\beta_G\hat{y}$ that preserve the required symmetry. Two of these modes necessarily generate polarization with no radiative component due to the perfect cancellation of the TE slab modes’ contributions to the zeroth order polarization at $\beta = 0$. The other two modes have a net non-zero zeroth order polarization, and they are necessarily degenerate at the zone-centre since there can be no preferred polarization for such leaked radiation at $\beta = 0$. Thus, non-degenerate modes at zone-centre must be infinitely long-lived, and finite-lifetime modes must be degenerate at zone-centre.

The size of the gaps at zone-centre (for extremely weak 2D square texture, all four of the zone-centre modes would have almost identical energies) are a measure of how much the zone-centre eigenmodes differ in their respective amounts of localization in the dielectric versus the air. The size of the gap and the energetic ordering of degenerate and non-degenerate modes at zone-centre are both influenced considerably by the air

filling fraction of the photonic lattice.

6.5 Effect of Filling Fraction

As mentioned in the previous chapter (section 5.9), the lowest energy feature shifts up in Figure 5.11 as the air-filling fraction of the 2D grating is increased. This is because the frequencies of the bound slab modes of the “effective untextured” waveguide will tend to increase as more low-index material is introduced into the core, guiding layer, thereby reducing its average dielectric constant. These bound modes also become less tightly bound to the (textured) guiding core, and therefore, interact less with the grating. Consequently the width of the gap, which is a measure of the scattering induced by the grating, will also be reduced for gratings with larger filling fraction. Hence, the effect of having a larger air-filling fraction on the gap is to increase its centre-frequency and decrease its size. Both of these effects result in an increase of the frequency of the lowest band, which is consistent with the experimental results.

Figure 6.4 depicts model specular reflectivity spectra for light incident along the $\Gamma - X$ direction at $\theta = 10^\circ$ for two different fill fractions. As the hole radius is increased, the lossy mode is clearly seen to shift from the highest to the middle s polarized feature. Increasing the hole radius further would, in principle, shift it to the lowest feature. However, this is not possible in our structure; since the holes completely penetrate the guiding core, increasing the normalized hole radius (r/Λ) much beyond 0.35 reduces the average index of the guiding core so much that it ceases to support any bound modes.

We can conclude that the hole size for our structure is such that the lossy mode is the one that is either second highest or third highest in frequency of the s polarized modes.

The frequency ordering of the lossy and non-lossy modes at zone-centre comes about as a result of the real-space field intensity distribution of the eigenmode over the unit cell. For simplicity we revert to consideration of the specular reflectivity spectra from

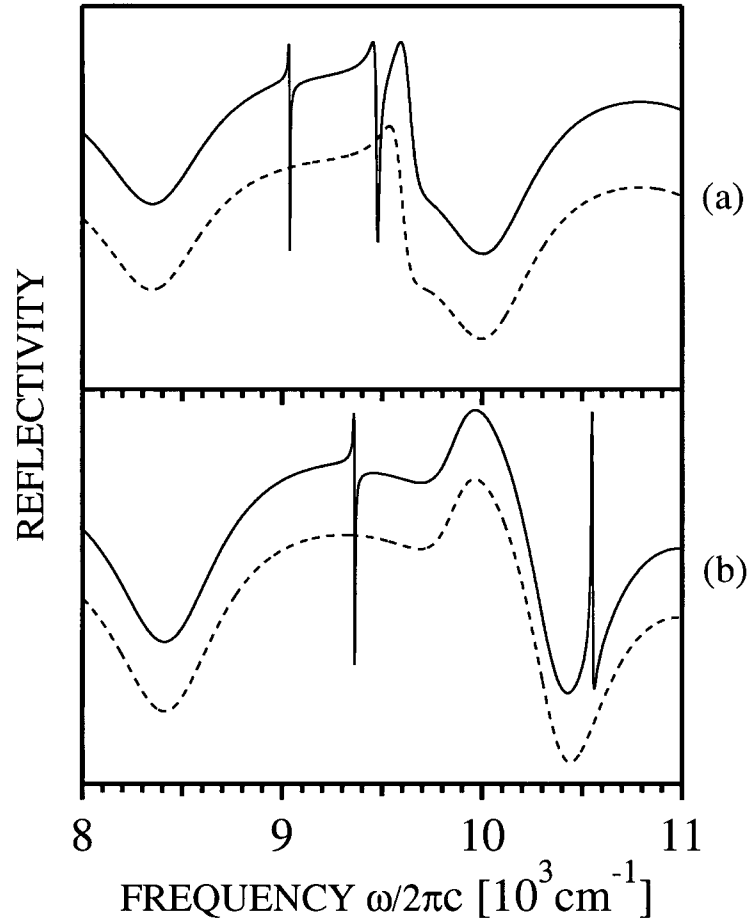


Figure 6.4: Calculated specular reflectivity spectra for s polarized (solid lines) and p polarized (dotted lines) for $\theta = 2^\circ$, $\phi = 0$ with (a) $r/\Lambda = 0.29$ and (b) $r/\Lambda = 0.33$. The other parameters in the model are as the fitted results for grating 22. The curves have been shifted vertically for clarity.

the waveguide structures with 1D texture presented in section 2.3.4.

Right at zone-centre, for a grating having reflection symmetry, such as the square grating under consideration, parity requires that the eigenmodes be composed of a symmetric or anti-symmetric superposition of field components having in-plane variation given by $e^{\pm i\beta_G x}$. At the second order TE gap, the \mathbf{E} field is in the \hat{y} direction and dominated by components at $\pm\beta_G$:

$$\mathbf{E}(x, z) = [E_{y0}e^{i\beta_G x}\hat{y} \pm E_{y0}e^{-i\beta_G x}\hat{y}]\psi(z). \quad (6.3)$$

However, each of the $\pm\beta_G$ components can scatter with the same scattering amplitude, to a zeroth order Fourier component which is phase matched to radiate away into the cladding regions. In the case of the eigenmode comprised of the symmetric superposition, the fields scattered back to zeroth order will add, thereby enhancing the radiated field and giving rise to a lossy eigenmode. Conversely, for the eigenmode comprised of the anti-symmetric superposition, the fields scattered back to the zeroth order component will cancel exactly, so that no radiating field is produced and the mode remains lossless. Slightly, away from zone-centre the cancellation ceases to be exact so that the “lossless” mode appears as a very narrow feature with small loss.

The frequency ordering arises from the fact that the in-plane intensity profile is different for the two eigenmodes. Figure 6.5 schematically depicts the electric field intensity profile arising from symmetric and antisymmetric superpositions of field components having in-plane variation given by $e^{\pm i\beta_G x}$ over a unit cell of a 1D grating. This is done for three different gratings having air filling fractions of 25%, 50%, and 75%. For the case of 25% fill fraction, the lossy, symmetric superposition (left), has a greater proportion of its field energy (area under the curve) concentrated in the low dielectric portion than does the lossless eigenmode comprised of the anti-symmetric superposition (right). Consequently, the lossy mode appears as the high-frequency (or high-energy) mode. Conversely, at a filling fraction of 75%, the situation is reversed and hence the lossy mode appears at low frequency. The transition occurs at a filling fraction of 50%. Here,

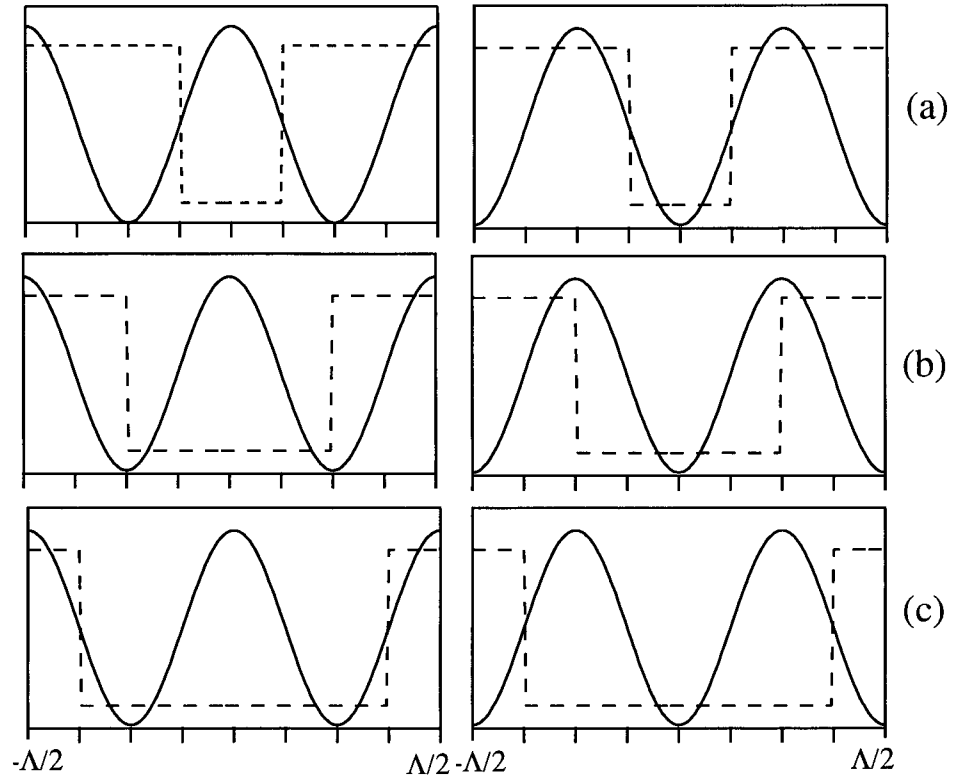


Figure 6.5: Schematic depiction of the in plane electric field intensity distribution over the unit cell for a 1D grating of the symmetric, lossy (left) and anti-symmetric, non-lossy (right) band edge states for a grating with (a) 25% (b) 50% (c) 75% air filling fraction. In (b) the lossy and lossless modes both modes have the same fraction of their total field energy (area under the curve) in the high-index region. The dielectric profile is indicated by the dashed line.

the lossy and lossless modes both modes have the same fraction of their total field energy in the high-index region, and are, therefore, degenerate.

6.6 Gaps Away from Zone-Centre

Figure 5.10 shows the experimental and model linewidths as a function of in-plane wavevector along the $\Gamma - X$ direction for the fourth and fifth lowest bands. Both the experiment and model exhibit a linewidth going to zero well away from the zone-centre

and boundary. This corresponds to the anti-crossing of these bands which occurs near $\beta_{inc}/\beta_G \approx 0.25$ in Figure 5.8. The energy of closest approach is comparable to the gap which occurs at zone-centre. This implies that the corresponding modes are strongly mixed.

As described above, away from the zone-centre, the 4th band is dominated by the $\beta_{inc}\hat{x} + \beta_G\hat{x}$ TE-like Fourier component corresponding to a bound mode traveling in the $+\hat{x}$ direction. From kinematic considerations, one would expect the next higher set of modes at zone-centre to be symmetric and anti-symmetric superpositions of TE polarized field components at $\beta_{inc}\hat{x} \pm (\beta_G\hat{x} \pm \beta_G\hat{y})$. This is because these reciprocal lattice vectors have the next largest magnitude and the dispersion of the untextured slab modes, which is isotropic in the in-plane directions, is monotonically increasing, and also because the lowest order TM modes occur at much higher frequency, owing to the thinness of the waveguide core. For these modes, symmetry considerations for detuning in the $\Gamma - X$ direction are similar to those for detuning in the $\Gamma - M$ direction for the modes at the “second order” ($\pm\beta_G\hat{x}$ and $\pm\beta_G\hat{y}$) gap. Consequently, these modes will appear as two pairs of bands having positive and negative dispersion, with each pair having one band leaking s polarized radiation and one band leaking p polarized radiation. The 5th band must be one of the modes with negative dispersion, which, in turn, implies that it must be composed of in-phase or out of phase superpositions of $\beta_{inc}\hat{x} - \beta_G(\hat{x} \pm \hat{y})$. Since it is leaking only s polarized radiation, the superposition must be such that it cancels out the E_y field, which implies that it must be the symmetric superposition (see Figure 6.6.)

Therefore, in the vicinity of the anti-crossing away from zone-centre, the modes in the 4th and 5th bands must be comprised of a significant admixture of TE polarized field components at $\beta_{inc}\hat{x} - \beta_G(\hat{x} \pm \hat{y})$ and $\beta_{inc}\hat{x} + \beta_G\hat{x}$. Right at the anti-crossing, *i.e.*, the point of closest approach of the 4th and 5th bands, which occurs experimentally at $\beta/\beta_G \approx 0.25$, these three components scatter back to $\beta_{inc}\hat{x}$ with appropriate amplitudes so as to produce a zero net field. Consequently, the leaky component vanishes, as

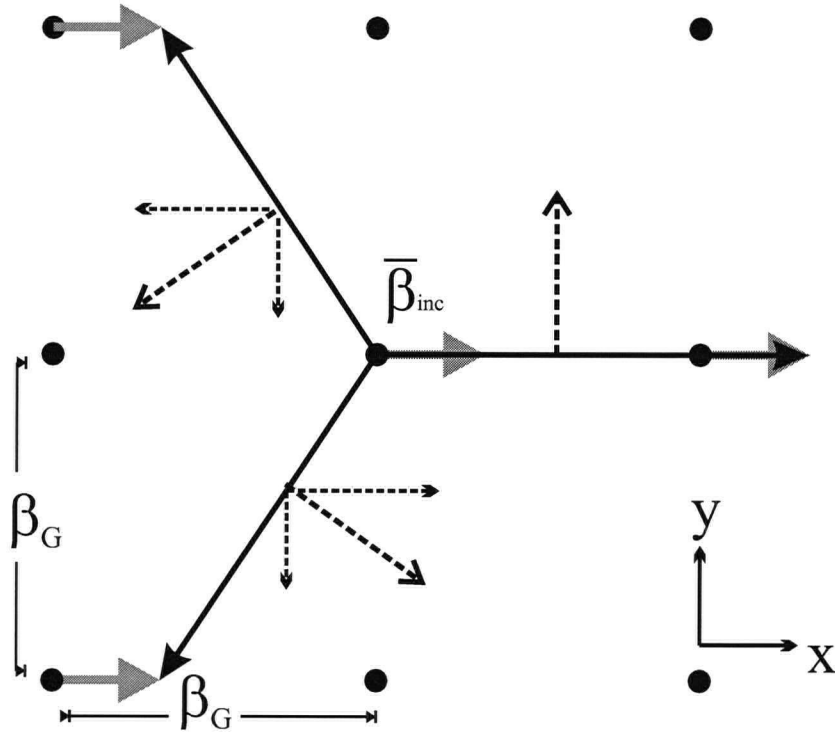


Figure 6.6: Dominant Fourier field components of eigenmodes in the 4th and 5th lowest energy bands along $\Gamma - X$ direction in Figure 5.8 in the vicinity of their anti-crossing: the solid arrows represent the propagation vectors associated with the in-plane variation of the field components; the grey arrows represent the incident in-plane wavevector, *i.e.*, detuning from zone-centre; dashed lines represents the electric fields and their x and y components.

evidenced by the disappearance of the Fano resonance in the specular reflectivity spectra. At the anti-crossing the mode in the 4th band is completely bound to the slab and has infinite lifetime.

The above description was verified by looking at scattering coefficients produced by the FDRS model. The dominant components of the mode correspond to the dominant scattering amplitudes from $\beta_{inc}\hat{x}$ to $\beta_{inc}\hat{x} + (n\hat{x} + m\hat{y})\beta_G$. Figure 6.7 depicts the spectra of the various scattering amplitudes calculated with in-plane wavevector value of $\beta_{inc}/\beta_G \approx 0.25$, corresponding to $\theta = 25^\circ$, at which the anti-crossing occurs as inferred from the fact that the resonant feature in the 4th band disappears from the reflectivity spectrum in Figure 5.5. The results clearly show the largest amplitudes for the components at $\beta_{inc}\hat{x} - \beta_G(\hat{x} \pm \hat{y})$ and $\beta_{inc}\hat{x} + \beta_G\hat{x}$, with those for the former two being equal as expected from symmetry considerations.

6.7 Extrinsic Influences on Linewidths

Referring now to Figure 5.9, the calculated width is clearly seen to be approaching zero at zone-centre; therefore, this mode becomes completely bound there. The oscillating behavior of the linewidth is due to the presence of the substrate and would not exist in the case of a three layer air/AlGaAs/Al oxide guide. This can be understood in terms of a simple model wherein the grating is taken to be a thin source emitting radiation leaked by the mode downward toward the substrate with the perpendicular component of the propagation vector given by:

$$k_{\perp}^2 = \left(\frac{n_{\text{oxide}}\tilde{\omega}}{c}\right)^2 - \beta^2. \quad (6.4)$$

This component is reflected at the oxide/substrate boundary with a π phase change. Consequently, when the product $k_{\perp}d_{\text{oxide}}$ is such that it returns in phase with the field in the grating, the radiation is enhanced, the mode becomes more leaky and the linewidth is increased. Conversely, when the reflected field returns out of phase with the field in

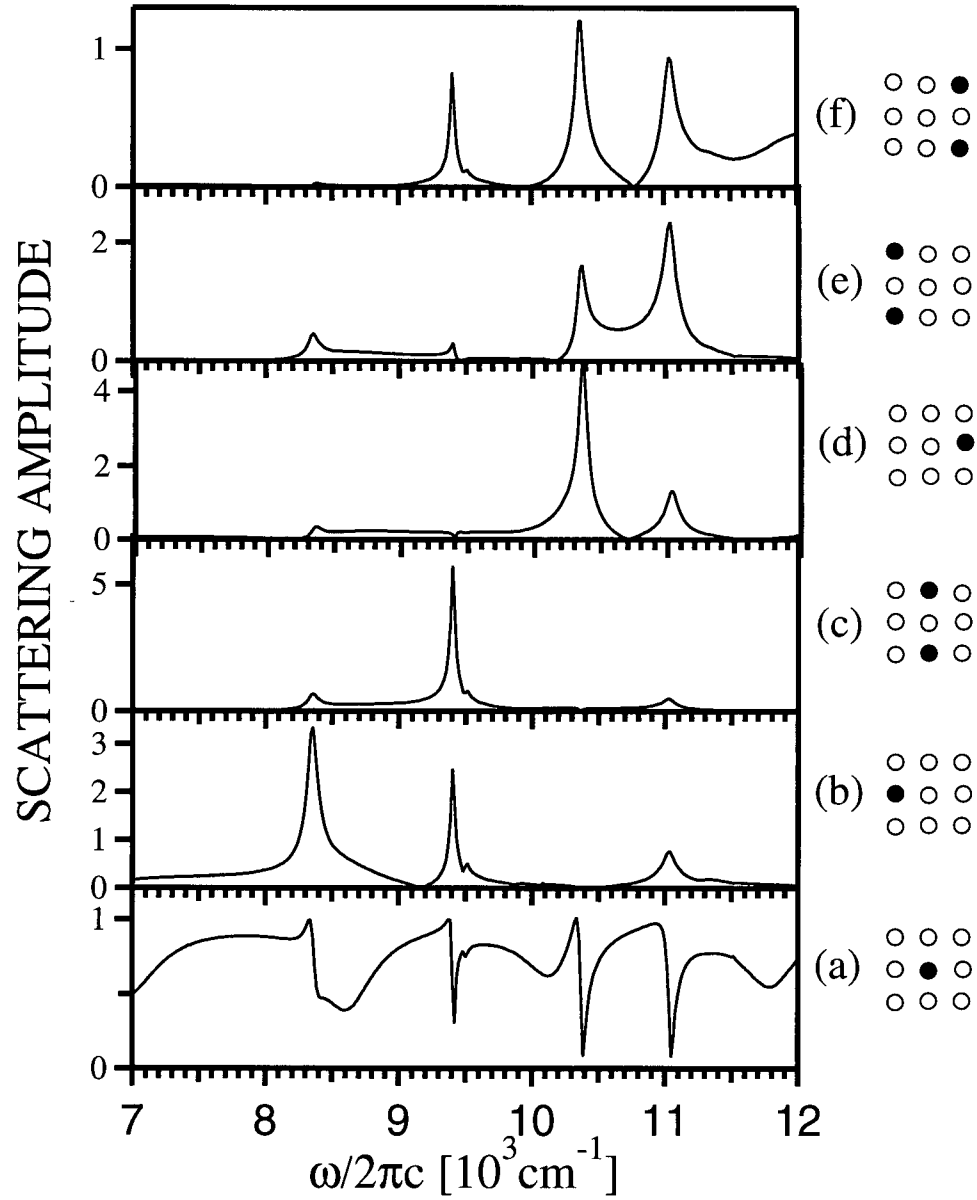


Figure 6.7: Scattering amplitudes calculated using the FDRS Code for s polarized light incident at $\beta_{inc} \approx 0.25\beta_G\hat{x}$ corresponding to $\theta = 25^\circ$ along the $\Gamma-X$ direction, where the anti-crossing occurs. The various plots depict the scattering amplitudes to s polarized light with in-plane wavevector: (a) β_{inc} (b) $\beta_{inc} - \beta_G\hat{x}$ (c) $\beta_{inc} \pm \beta_G\hat{y}$ (d) $\beta_{inc} + \beta_G\hat{x}$ (e) $\beta_{inc} + \beta_G[-\hat{x} \pm \hat{y}]$ (f) $\beta_{inc} + \beta_G[\hat{x} \pm \hat{y}]$. The structure is the same as that for grating 22 with the parameters as obtained from fitting with the GF code.

the grating, radiation is suppressed, the mode becomes less leaky and the linewidth is decreased. This effect has previously been predicted by Benisty *et al.* [52].

It should also be noted that since the only other significant Fourier components of the Bloch state in this band are evanescent in the cladding layer and hence are not appreciably influenced by the oxide layer thickness when it exceeds 500 nm, the thickness of the cladding layer could be used to tune the mode lifetime without significantly altering its energy.

For these bands, then, the first order Fourier component of the dielectric modulation couples the vertical oxide cavity to the 2D in-plane “cavity” formed by the distributed feedback. When a high-index-contrast photonic lattice is used, the first-order Fourier component of the “scattering potential” is larger than in the weakly textured case. The larger diffraction rate which results manifests itself not only in broader linewidths but also an enhanced coupling between the vertical and distributed in-plane cavities.

Chapter 7

Summary and Conclusions

7.1 Summary

A numerical model was developed for calculating specular reflectivity and scattering from an infinite 2D photonic crystal embedded in an arbitrary dielectric slab waveguide structure. A discrete set of plane wave-like basis functions is integrated through the textured structure using Maxwell's equations on a discrete real-space mesh. Resonant features in the reflectivity and scattering spectra are used to obtain information regarding the dispersion, polarization, and lifetimes of the bound and resonant electromagnetic modes of the textured waveguide. With run-times on the order of two hours on a current PC (*AMD Duron 1600* 1.6 GHz, 1GB RAM) the model is found to converge to within 1% for the mode frequencies and to within 7% for the linewidths.

A fabrication procedure was developed for making structurally robust and robustly guiding thin semiconductor slab waveguides with 2D square photonic lattices of air-holes that completely penetrate the core layer. The procedure involved using electron beam lithography and ECR plasma etching to define the texture in an 80 nm thick GaAs/Al_{0.3}Ga_{0.7}As core on the surface of a $\sim 1.8\mu m$ layer of Al_{0.98}Ga_{0.02}As grown on a GaAs substrate using Molecular Beam Epitaxy. The texture consisted of a square lattice of cylindrical airholes. These varied in pitch from 500 nm to 575 nm and in air filling fraction from 0.28 to 0.49. The sample was then placed in a warm, moist environment to oxidize the Al_{0.98}Ga_{0.02}As layer in the region beneath the 2D lattice through the holes.

Polarized, angle-resolved specular reflectivity spectra were measured at a series of incident angles for energies between 6000 cm⁻¹ and 14,000 cm⁻¹. The experimental

spectra bear a strong resemblance to those calculated using the numerical models. Both the experimental and model spectra were fit with a combination of an Airy function and Fano-lineshape function in order to extract the energy and lifetimes of the modes excited at each angle of incidence. These were used to plot the dispersion of mode frequencies and lifetimes. The bandstructure so obtained exhibits large (1000 cm^{-1} at 9500 cm^{-1}) gaps and drastic modification of the dispersion over a large portion of the Brillouin zone. Both of these effects are much more pronounced than those that are typical of weakly textured slab waveguides.

The spectra exhibited well-defined polarization properties along the symmetry directions of the crystal in that the polarization of leaked radiation was either purely *s* or purely *p*. Near zone-centre, in the vicinity of the second order gap, and for detuning along the $\Gamma - X$ direction of the crystal, three modes appeared in the *s* polarization and one in the *p* polarization. One of each of the *s* and *p* polarized modes exhibited little dispersion over a large portion of the 1st Brillouin zone. For detuning along the $\Gamma - M$ direction, two moderately dispersive pairs of features appeared, with one of each pair appearing in the *s* and *p* polarization.

There was also generally good agreement between the model and experiment for the linewidths of the resonant features associated with the modes, except where the linewidths were predicted to vanish (or become narrower than $\sim 80\text{ cm}^{-1}$); in this case the lower limit on the experimental resolution made a quantitative comparison impossible. Nevertheless, linewidths (lifetimes) were observed that varied considerably within a given band and between bands in a manner that agreed qualitatively with the model. In particular, for one of the modes, there was an oscillation of the linewidth as a function of the in-plane wavevector which was clearly evident in both the model and experimental spectra.

Finally, an anti-crossing was observed away from any high symmetry points of the

crystal, simultaneously with the vanishing of the linewidth of one of the features associated with the anti-crossing bands.

7.2 Conclusions

Features in specular reflectivity spectra from 2D textured semiconductor slab waveguide-based photonic crystals can be used to study the intrinsic properties of resonant electromagnetic modes localized in the vicinity of the textured core.

By comparing model calculations with the experimental results, it has been clearly shown that in order to fully characterize these electromagnetic excitations their dispersion, lifetimes, and polarization must be determined.

Analysis of the results indicates that for the “membrane-like” structures studied in this work (thin, high-index core, low-index cladding and texture, $\Delta n \approx 1.8$) the electromagnetic excitations can be largely interpreted as renormalized (mixed) TE and TM polarized slab modes characteristic of a fictitious effective slab waveguide where the core has a uniform refractive index given by the volume-averaged refractive index of the textured core of the actual structure. The degree of mixing introduced by the 2D texture, as inferred from the width of the anti-crossings, is $\sim 10\%$.

The polarization properties can be explained entirely in terms of symmetry arguments regarding the coupling of the zeroth order radiative component with the bound-slab-mode-like TE field components at $\pm\beta_G\hat{x}$ and $\pm\beta_G\hat{y}$. The gross dispersion properties can be explained qualitatively from kinematical considerations.

The oscillation of the linewidth with in-plane wavevector was explained by the coupling of the Bloch states of the photonic crystal embedded in the waveguide to the Fabry-Perot modes of the cavity formed by the oxide layer *via* the zeroth order Fourier component of the Bloch state that radiates down into the oxide and undergoes multiple reflections there.

More generally, the detailed shape of the bandstructure and the variation of the

resonant mode lifetimes is rich, and affords considerable flexibility for future device designers.

All bands exhibit zero group-velocity at zone-centre, and small group velocity out to at least 10% of the zone boundary. It has been shown that the lifetimes of degenerate bands at zone-centre are, in general, finite. These degenerate bands at zone-centre offer small group velocity and strong coupling to external radiation modes. This makes them interesting for detector, emitter, and coupling applications. Isolated bands at zone-centre are necessarily infinitely-long-lived right at the zone-centre, and have relatively long lifetimes out to $\sim 10\%$ of the way to the zone boundary. This combination of small group velocity and long lifetimes is of particular interest in active laser devices that incorporate 2D photonic crystals.

The anti-crossing observed away from the zone-centre, is in a certain respect, “accidental” in that it depends on the details of the bare slab mode dispersion and, unlike the gaps (anticrossings) occurring at high symmetry points of the photonic lattice, could not be predicted purely from symmetry considerations of the 2D lattice alone.

In summary, the complete understanding of the complex (energy and lifetime) dispersion and polarization properties of this interesting new class of materials, obtained by developing and using a numerical solution of Maxwell’s equations to interpret broadband specular reflectivity spectra, has shown that this bandstructure for photons can be qualitatively explained by applying symmetry and kinematical considerations to the renormalization of the slab waveguide modes by the high index contrast 2D scattering potential.

7.3 Future Directions

Work in this area is proceeding along several lines. One is the inclusion of electronic resonances through incorporation of quantum wells, wires, and dots in appropriately designed slab waveguide-based photonic crystals. Some theoretical work has also been

done [53] on simultaneously texturing the magnetic permeability of materials. In addition to allowing for greater scattering, this also allows an additional degree of freedom in engineering photonic bandstructure, as well as tunability *via* application of an external magnetic field.

Yet another direction involves the search for purely photonic effects through the design and realization of more elaborate structures, such as the integration of several layers of slab waveguide crystals and the inclusion of periodic defects. Work is already underway in our group using the latter strategy. A modified version of both the FDRS code and the GF code, capable of modelling infinite photonic lattices with periodic defects embedded in slab waveguides, has been developed. These structures hold promise for engineering very weakly dispersive bands predicted to play important roles in enhancement of non-linear optical cross-sections [11].

Bibliography

- [1] J.D. Joannopoulos, Robert D. Meade, and Joshua N. Winn. *Photonic Crystals: Molding the Flow of Light*. Princeton University Press, New Jersey, 1995.
- [2] E. Yablonovitch, T.J. Gmitter, and K.M. Leung. Photonic band structure: The face-centered-cubic case employing nonspherical atoms. *Phys. Rev. Lett.*, 67:2295–2298, 1991.
- [3] E. Yablonovitch. Inhibited spontaneous emission in solid-state physics and electronics. *Phys. Rev. Lett.*, 58:2059–2062, 1987.
- [4] S. John. Strong localization of photons in certain disordered dielectric superlattices. *Phys. Rev. Lett.*, 58:2486–2489, 1987.
- [5] N.W. Ashcroft and N.D. Mermin. *Solid State Physics*. Holt, Reinhart and Winston, New York, 1976.
- [6] C. Kittel. *Introduction to Solid State Physics*. Wiley, New York, 1996.
- [7] S. John and J. Wang. Quantum electrodynamics near a photonic band gap: photon bound states and dressed atoms. *Phys. Rev. Lett.*, 64:2418–2421, 1990.
- [8] S. John and J. Wang. Quantum optics of localized light in a photonic band gap. *Phys. Rev. B*, 43:12772–12789, 1991.
- [9] S. John and V. Rupasov. Multiphoton localization and propagating quantum gap solitons in a frequency gap medium. *Phys. Rev. Lett.*, 79:821–824, 1997.
- [10] S. Jamal and J.C. Cartledge. Performance of 10-gb/s multispan lightwave systems using dispersion-compensating fiber Bragg gratings. *Proc. SPIE Int. Soc. Opt. Eng.*, 4087:417, 2000.
- [11] K. Sakoda and K. Ohtaka. Optical response of three-dimensional photonic lattices: solutions of inhomogeneous Maxwell’s equations and their applications. *Phys. Rev. B*, 54:5732–5741, 1996.
- [12] K. Inoue, M. Sasada, J. Kawamata, K. Sakoda, and J. W. Haus. A two-dimensional photonic crystal laser. *Japanese Journal of Applied Physics*, 38:L157–L159, 1999.
- [13] J.D. Joannopoulos, Pierre R. Villeneuve, and Shannui Fan. Photonic crystals: putting a new twist on light. *Nature*, 386:143–149, 1997.
- [14] K.M. Ho, C.T. Chan, and C.M. Soukoulis. Existence of a photonic gap in periodic dielectric structures. *Phys. Rev. Lett.*, 65:3125–3155, 1990.

- [15] R.D. Meade, A. M. Rappe, K. D. Brommer, J. D. Joannopoulos, and O. L. Alerhand. Accurate theoretical analysis of photonic band-gap materials. *Phys. Rev. D*, 48:8434–8436, 1993.
- [16] Pierre R. Villeneuve and Michel Piche. Photonic bandgaps in periodic dielectric structures. *Prog. Quant. Electr.*, 18:153–200, 1994.
- [17] E. Yablonovitch. Photonic band-gap structures. *J. Opt. Soc. Am. B*, 10:283–295, 1993.
- [18] A. S. McLean and J.B. Pendry. A polarized transfer matrix for electromagnetic waves in structured media. *J. Mod. Opt.*, 41:1781–1802, 1994.
- [19] K. Agi, E.R. Brown, O.B. McMahon, C. Dill III, and K.J. Malloy. Design of ultrawideband photonic crystals for broadband antenna applications. *Electron. Lett.*, 30:2166, 1994.
- [20] C.C. Cheng and A. Scherer. Fabrication of photonic band gap crystals. *J. Vac. Sci. Technol. B*, 13:2696, 1995.
- [21] C. Zhang, L. Zavieh, A. Mitra, and T.S. Mayer. Fabrication of GaAs based 3D photonic bandgap materials. In *Proc. IEEE Cornell Conf. Adv. Concepts High Speed Semicond. Dev. Circ.*, Ithaca, N.Y., 1997. IEEE.
- [22] Y.A Vlasov, V. N. Astratov, O. Z. Karimov, A. A. Kaplyanskii, V. N. Bogomolov, and A. V. Prokofiev. Existence of a photonic pseudogap for visible light in synthetic opals. *Phys. Rev. B*, 55:13357, 1997.
- [23] T. Tamir, editor. *Guided-Wave Optoelectronics*. Springer Series in Electronics and Photonics 26. Springer-Verlag, New York, 1990.
- [24] J.R. Wendt, G.A. Vawter, P.L. Gourley, T.M. Brennan, and B.E. Hammons. Nanofabrication of photonic crystal structures in GaAs/AlGaAs. *J. Vac. Sci. B*, 11:2637, 1993.
- [25] D. Labilloy, H. Benisty, C. Weisbuch, C. J. M. Smith, R. Houdr, and U. Oesterle. Finely resolved transmission spectra and band structure of two-dimensional photonic crystals using emission from InAs quantum dots. *Phys. Rev. B*, 59:1649–1652, 1999.
- [26] P. Paddon and Jeff F. Young. Simple approach to coupling in textured planar waveguides. *Opt. Lett.*, 23:1529, 1998.
- [27] P. Paddon and Jeff F. Young. Two-dimensional vector-coupled-mode theory for textured planar waveguides. *Phys. Rev. B*, 61:2090–2101, 2000.

- [28] O. Painter, R. K. Lee, A. Scherer, A. Yariv, J. D. O'Brien, P. D. Dapkus, and I. Kim. Two-dimensional photonic band-gap defect mode laser. *Science*, 284:1819, 1999.
- [29] J.S. Foresi, P.R. Villeneuve, J. Ferrera, E.R. Thoen, G. Steinmeyer, S. Fan, J.D. Joannopoulos, L.C. Kimerling, Henry I. Smith, and E.P. Ippen. Photonic bandgap microcavities in optical waveguides. *Nature*, 390:143, 1997.
- [30] P.R. Villeneuve, S. Fan, J. D. Joannopoulos, K-Y Lim, G. S. Petrich, L. A. Kolodziejski, and R. Reif. Air-bridge microcavities. *Appl. Phys Lett.*, 67:167–169, 1995.
- [31] Attila Mekis, J. C. Chen, I. Kurland, Shanhui Fan, Pierre R. Villeneuve, and J. D. Joannopoulos. High transmission through sharp bends in photonic crystal waveguides. *Phys. Rev. Lett.*, 77:3787–3790, 1996.
- [32] A. Yariv. Coupled-mode theory for guided wave optics. *IEEE J. Quantum Electron.*, QE-9:919–933, 1973.
- [33] W. Streifer, D. Scifres, and R. Burnham. Coupled wave analysis of DFB and DBR lasers. *IEEE J. Quantum Electron.*, QE-13:134–141, 1977.
- [34] R.F. Kazarinof and C. Henry. Second order distributed feedback lasers with mode selection provided by first-order radiation losses. *IEEE J. of Quant. Electron.*, QE-21:144–150, 1985.
- [35] V. N. Astratov, J.S. Culshaw, R.M. Stevenson, D.M. Whittaker, M.S. Skolnick, T.F. Krauss, and R.M. de la Rue. Resonant coupling of near-infrared radiation to photonic band structure waveguides. *J. Lightwave Tech.*, 17:2050–2056, 1999.
- [36] V. Pacradouni, J. Mandeville, A. R. Cowan, P. Paddon, and Jeff F. Young. Photonic bandstructure of dielectric membranes periodically textured in two dimensions. *Phys. Rev. B*, 62:4204–4207, 2000.
- [37] V. Pacradouni, W.J. Mandeville, A.R. Cowan, S.R. Johnson, and Jeff F. Young. Dispersion and lifetimes of electromagnetic modes attached to strongly textured slab waveguides. *Optical and Quantum Electronics*, 34:161–169, 2002.
- [38] U. Fano. Effects of configuration interaction on intensities and phase shifts. *Phys. Rev.*, 124:1866–1878, 1964.
- [39] M. Kanskar, P. Paddon, V. Pacradouni, R. Morin, A. Busch, J. F. Young, S. R. Johnson, J. Mackenzie, and T. Tiedje. Observation of leaky slab modes in air-bridge semiconductor waveguides with a two-dimensional photonic lattice. *Appl. Phys. Lett.*, 70:1438–1440, 1997.

- [40] A. Cowan, P. Paddon, V. Pacradouni, and J.F. Young. Resonant scattering and mode coupling in two-dimensional textured planar waveguides. *J. Opt. Soc. Am. A*, 18:1160–1170, 2001.
- [41] A. Cowan. Periodically textured planar waveguides. Master's thesis, University of British Columbia, Vancouver, Canada, September 2000.
- [42] M. Born and E. Wolf. *Principles of Optics: Electromagnetic theory of propagation, interference and diffraction of light*. Cambridge University Press, Cambridge and New York, 1999.
- [43] A.V. Oppenheim and R.W. Schaefer. *Discrete-Time Signal Processing*. Prentice Hall, New Jersey, 1989.
- [44] P.M. Bell, J.B. Pendry, L.M. Moreno, and A.J. Ward. A program for calculating transmission coefficients of complex structures. *Computer Physics Communications*, 85:306–322, 1994.
- [45] J. M. Dallesasse, N. Holonyak Jr., A. R. Sugg, T. A. Richard, and N. El-Zein. Hydrolyzation oxidation of $\text{Al}_x\text{Ga}_{1-x}\text{As}$ -AlAs-GaAs quantum well heterostructures and superlattices. *Appl. Phys. Lett.*, 57:844, 1990.
- [46] D. L. Huffaker, D. G. Deppe, K. Kumar, and T. J. Rogers. Native-oxide defined ring contact for low threshold vertical-cavity lasers. *Appl. Phys. Lett.*, 65:97, 1994.
- [47] K. D. Choquette, R. P. Schneider Jr., K. L. Lear, and K. M. Geib. Low threshold voltage vertical-cavity lasers fabricated by selective oxidation. *Electron. Lett.*, 30:2043–2044, 1994.
- [48] J. A. Kash, B. Pezeshki, F. Agahi, and N. A. Bojarczuk. Recombination in GaAs at the AlAs-oxide-GaAs interface. *Appl. Phys. Lett.*, 67:2022, 1995.
- [49] R. E. Sah, J. D. Ralston, S. Weisser, and K. Eisele. Characteristics of a two-component chemically-assisted ion-beam etching technique. *Appl. Phys. Lett.*, 67:927, 1995.
- [50] S. Adachi. Optical properties of $\text{Al}_x\text{Ga}_{1-x}\text{As}$ alloys. *Phys. Rev. B*, 38:12345, 1988.
- [51] F. Sfigakis, P. Paddon, V. Pacradouni, M. Adamcyk, C. Nicoll, A.R. Cowan, T. Tiedje, and J.F. Young. Near-infrared refractive index of thick, laterally oxidized AlGaAs layers. *J. Lightwave Tech.*, 18:199, 2000.
- [52] H. Benisty, D. Labilloy, C. Weisbuch, C.J.M. Smith, T. F. Krauss, D. Cassagne, A. Braud, and C. Jouanin. Radiation losses of waveguide-based two-dimensional photonic crystals: positive role, of the substrate. *Appl. Phys. Lett.*, 76:532, 2000.
- [53] M. M. Sigalas, C. M. Soukoulis, R. Biswas, and K. M. Ho. Effect of the magnetic permeability on photonic band gaps. *Phys. Rev. B*, 56:959, 1997.

Appendix A

Generalization of FDRS Method to an Arbitrary 2D Lattice

The most general 2D Bravais lattice of no particular symmetry is the oblique net, which may be specified by a pair of non-collinear primitive lattice vectors, \mathbf{A}_1 , \mathbf{A}_2 of arbitrary length and orientation.

As before, we define a mesh for taking difference terms, however, this time we use an oblique, *i.e.*, non-rectilinear, mesh given by:

$$\mathbf{a} = a\hat{x} \tag{A.1}$$

$$\mathbf{b} = b\hat{b} = b \cos \psi \hat{x} + b \sin \psi \hat{y} \tag{A.2}$$

$$\mathbf{g} = g\hat{z} \tag{A.3}$$

where:

$$\hat{b} = \cos \psi \hat{x} + \sin \psi \hat{y} \tag{A.4}$$

Here again, we presently make no assumption regarding the orientation of the 2D photonic crystal with respect to our coordinate axes. We now generalize equations 2.33 – 2.35 in accordance with our oblique mesh to:

$$\frac{\mathbf{k} \cdot \mathbf{a}}{|\mathbf{a}|} = k_x \approx [\exp(\frac{ik_x a}{2}) - \exp(\frac{-ik_x a}{2})]/ia \triangleq \kappa_x \tag{A.5}$$

$$\frac{\mathbf{k} \cdot \mathbf{b}}{|\mathbf{b}|} = k_b \approx [\exp(\frac{ik_b b}{2}) - \exp(\frac{-ik_b b}{2})]/ib \triangleq \kappa_b \tag{A.6}$$

$$\frac{\mathbf{k} \cdot \mathbf{g}}{|\mathbf{g}|} = k_z \approx [\exp(\frac{ik_z g}{2}) - \exp(\frac{-ik_z g}{2})]/ig \triangleq \kappa_z \tag{A.7}$$

so that we may write:

$$\boldsymbol{\kappa} = \kappa_x \hat{x} + \kappa_b \hat{b} + \kappa_z \hat{z} \tag{A.8}$$

We note from equation A.2 that:

$$\hat{y} = \frac{\mathbf{b}}{b} - \cot \psi \hat{x} \quad (\text{A.9})$$

so that we may write

$$k_y = \mathbf{k} \cdot \hat{y} = \frac{\mathbf{k} \cdot \mathbf{b}}{b} - \mathbf{k} \cdot \hat{x} \cot \psi = k_b - k_x \cot \psi. \quad (\text{A.10})$$

We may now proceed as before with equations 2.31 – 2.32, carrying out the cross-products, making the approximations for \mathbf{k} , and expanding component-by-component to get a set of six equations similar to equations 2.40 – 2.45. We take as an example the equation for the x component of the \mathbf{B} field.

$$(\mathbf{k} \times \tilde{\mathbf{E}})_x = k_y \tilde{E}_z - k_z \tilde{E}_y = \omega \tilde{B}_x \quad (\text{A.11})$$

Using equation A.10 this becomes:

$$k_b \tilde{E}_z - k_x \tilde{E}_z \cot \psi - k_z \tilde{E}_y = \omega \tilde{B}_x. \quad (\text{A.12})$$

Now, making the approximations for \mathbf{k} using equations A.5 – A.7, we obtain:

$$\begin{aligned} \tilde{B}_x \approx & \frac{\exp(ik_b \frac{b}{2}) \tilde{E}_z}{ib\omega} - \frac{\exp(-ik_b \frac{b}{2}) \tilde{E}_z}{ib\omega} - \frac{\exp(ik_x \frac{a}{2}) \tilde{E}_z}{ia\omega} \cot \psi + \frac{\exp(-ik_x \frac{a}{2}) \tilde{E}_z}{ia\omega} \cot \psi \\ & - \frac{\exp(ik_z \frac{g}{2}) \tilde{E}_y}{ig\omega} + \frac{\exp(-ik_z \frac{g}{2}) \tilde{E}_y}{ig\omega} \end{aligned} \quad (\text{A.13})$$

We now note that:

$$\exp(\pm ik_b \frac{b}{2}) = \exp(\pm i\mathbf{k} \cdot \frac{\mathbf{b}}{2}) = \exp[\pm i\mathbf{k} \cdot \frac{(b \cos \psi \hat{x} + b \sin \psi \hat{y})}{2}] = \exp[\pm i\mathbf{k} \cdot \frac{(b_x \hat{x} + b_y \hat{y})}{2}] \quad (\text{A.14})$$

and therefore, similarly to the second of expressions 2.46

$$\exp(\pm ik_b \frac{b}{2}) \tilde{F}_l \Leftrightarrow F_l(x \mp \frac{b_x}{2}, y \mp \frac{b_y}{2}, z) = F_l(\mathbf{r} \mp \boldsymbol{\zeta}) \quad (\text{A.15})$$

where, \tilde{F}_l denotes a component of the \mathbf{E} , \mathbf{D} , \mathbf{B} or \mathbf{H} field, \Leftrightarrow denotes Fourier transformation, and $\boldsymbol{\zeta}$ is now defined as:

$$\boldsymbol{\zeta} = \frac{\mathbf{b}}{2} \quad (\text{A.16})$$

We now take the inverse Fourier transform of equation A.13, making use of equation A.15 and the first and third of equations 2.46, to yield:

$$B_x(\mathbf{r}) \approx -\frac{E_z(\mathbf{r} + \boldsymbol{\zeta}) - E_z(\mathbf{r} - \boldsymbol{\zeta})}{ib\omega} + \cot \psi \frac{E_z(\mathbf{r} + \boldsymbol{\alpha}) - E_z(\mathbf{r} - \boldsymbol{\alpha})}{ia\omega} + \frac{E_y(\mathbf{r} + \boldsymbol{\gamma}) - E_y(\mathbf{r} - \boldsymbol{\gamma})}{ig\omega} \quad (\text{A.17})$$

Isolating the E_y terms in the preceding equation, we obtain:

$$\frac{E_y(\mathbf{r} + \boldsymbol{\gamma}) - E_y(\mathbf{r} - \boldsymbol{\gamma})}{ig\omega} \approx \mu(\mathbf{r})H_x(\mathbf{r}) + \frac{E_z(\mathbf{r} + \boldsymbol{\zeta}) - E_z(\mathbf{r} - \boldsymbol{\zeta})}{ib\omega} + \cot \psi \frac{E_z(\mathbf{r} + \boldsymbol{\alpha}) - E_z(\mathbf{r} - \boldsymbol{\alpha})}{ia\omega} \quad (\text{A.18})$$

In order to obtain an equation resembling equation 2.65 we need to eliminate the z-fields. Consequently, using the same procedure as for B_x above, we first obtain the expression for the D_z component given by:

$$D_z(\mathbf{r}) \approx \frac{H_y(\mathbf{r} + \boldsymbol{\alpha}) - H_y(\mathbf{r} - \boldsymbol{\alpha})}{ia\omega} - \frac{H_x(\mathbf{r} + \boldsymbol{\zeta}) - H_x(\mathbf{r} - \boldsymbol{\zeta})}{ib\omega} + \cot \psi \frac{H_x(\mathbf{r} + \boldsymbol{\alpha}) - H_x(\mathbf{r} - \boldsymbol{\alpha})}{ia\omega} \quad (\text{A.19})$$

so that:

$$E_z(\mathbf{r}) \approx \frac{H_y(\mathbf{r} + \boldsymbol{\alpha}) - H_y(\mathbf{r} - \boldsymbol{\alpha})}{ia\omega\epsilon(\mathbf{r})} - \frac{H_x(\mathbf{r} + \boldsymbol{\zeta}) - H_x(\mathbf{r} - \boldsymbol{\zeta})}{ib\omega\epsilon(\mathbf{r})} + \cot \psi \frac{H_x(\mathbf{r} + \boldsymbol{\alpha}) - H_x(\mathbf{r} - \boldsymbol{\alpha})}{ia\omega\epsilon(\mathbf{r})} \quad (\text{A.20})$$

In this manner, expressions similar to those given in equations 2.64 – 2.67 may be obtained that again allow for the \mathbf{E} and \mathbf{H} fields defined on a discrete mesh on a pair of planes to be propagated forward or backward in the z direction. As before, these equations require evaluation of the fields at \mathbf{r} , $\mathbf{r} \pm (\boldsymbol{\alpha} \pm \boldsymbol{\zeta})$, $\mathbf{r} \pm 2\boldsymbol{\zeta}$, $\mathbf{r} \pm 2\boldsymbol{\alpha}$, as well as evaluation of ϵ' and μ' at \mathbf{r} , $\mathbf{r} \pm \boldsymbol{\zeta}$, and $\mathbf{r} \pm \boldsymbol{\alpha}$. However, now $\boldsymbol{\alpha}$ and $\boldsymbol{\zeta}$ are no longer defined to be orthogonal to one another.

Figure A.1 depicts the mesh points within the unit cell of the photonic crystal on which evaluation of the fields (squares) and ϵ' and μ' (black dots) are required. Notice that in this scheme (as before), we take \mathbf{a} and \mathbf{b} along the body diagonals of the primitive cell of (the underlying Bravais lattice of) the photonic crystal we wish to model.

Explicitly:

$$\mathbf{a} = (\mathbf{A}_1 + \mathbf{A}_2)/N \quad (\text{A.21})$$

$$\mathbf{b} = (\mathbf{A}_1 - \mathbf{A}_2)/N \quad (\text{A.22})$$

where N^2 (N along each primitive lattice vector) is the number of mesh points we desire for the fields. We then orient our rectilinear coordinate axes such that \hat{x} lies along \mathbf{a} .

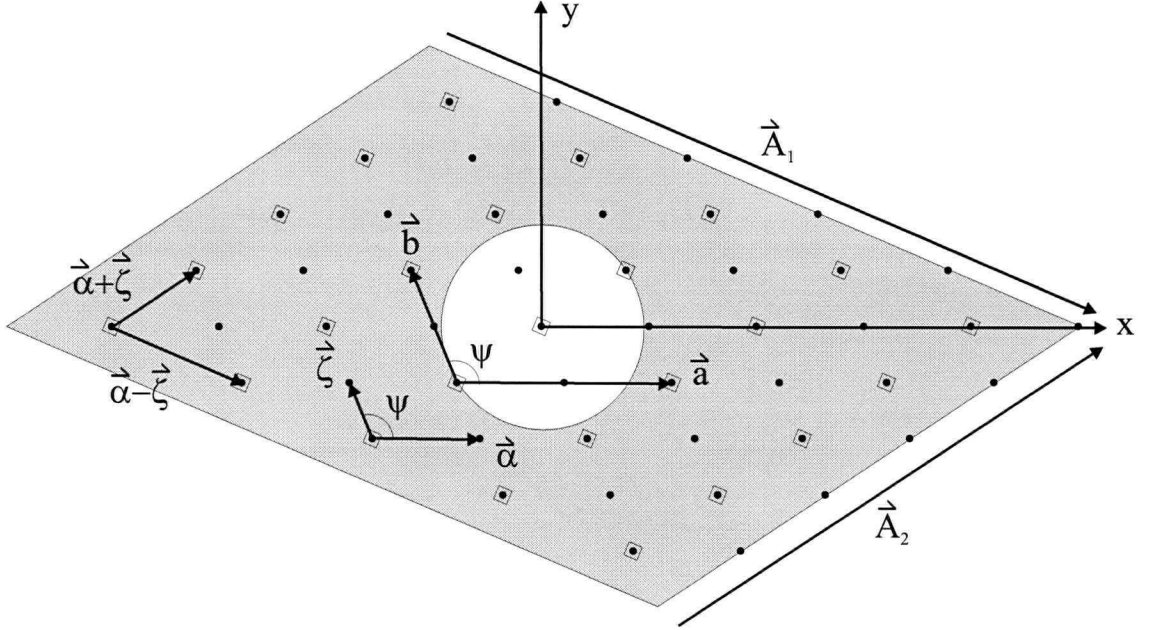


Figure A.1: Scheme of real-space points on which the fields and dielectric constant are sampled on the unit cell. The dielectric constant is sampled at points represented by the black dots. The electric or magnetic fields are sampled only on the points with squares. \mathbf{A}_1 and \mathbf{A}_2 represent the primitive lattice vectors of the photonic crystal.

The reciprocal lattice vectors for the general 2D oblique lattice with primitive lattice vectors, \mathbf{A}_1 , \mathbf{A}_2 , are given by:

$$\mathbf{G}_1 = \frac{2\pi}{A_{1x}A_{2y} - A_{2x}A_{1y}}(A_{2y}\hat{x} - A_{2x}\hat{y}) \quad (\text{A.23})$$

$$\mathbf{G}_2 = \frac{2\pi}{A_{1x}A_{2y} - A_{2x}A_{1y}}(A_{1y}\hat{x} - A_{1x}\hat{y}) \quad (\text{A.24})$$

The reciprocal lattice is similar to the direct lattice but rotated by 90 degrees. It is depicted in figure A.2. As before, the polarized plane wave like basis modes may be

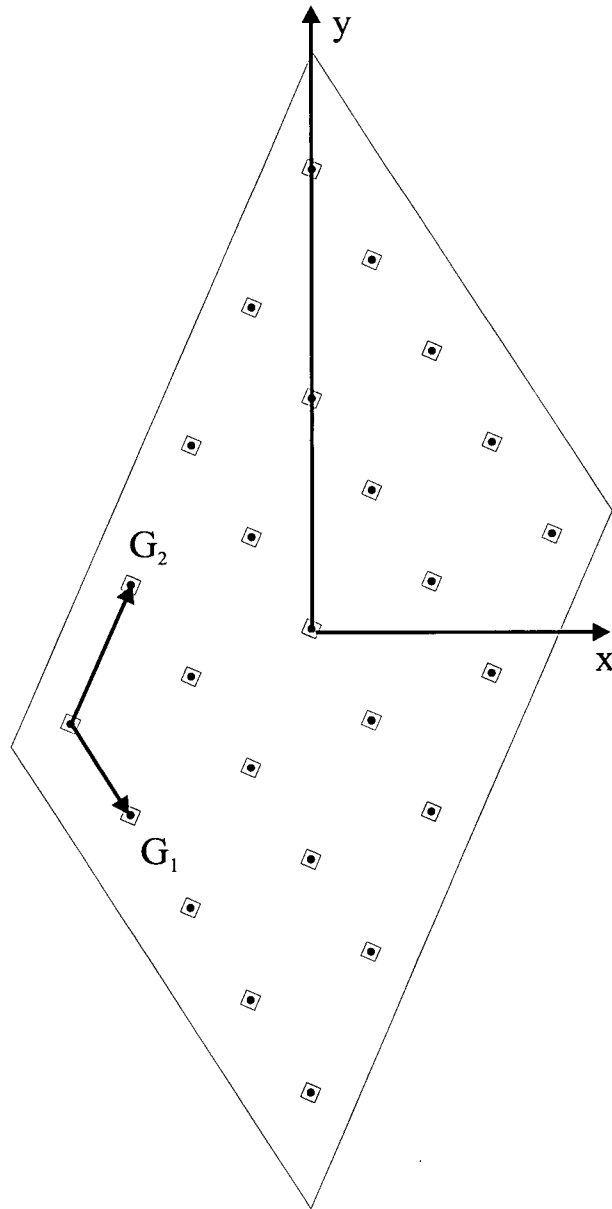


Figure A.2: Scheme of reciprocal lattice vectors corresponding to in-plane wavevector of launched modes for photonic crystal with oblique 2D lattice.

formed from a finite set of the reciprocal lattice vectors using equations 2.77 – 2.80, where the expression for κ in equation A.8 may be used, and where

$$k_b = (\mathbf{G}_{l,m} + \beta) \cdot \hat{b}. \quad (\text{A.25})$$

The dispersion relation for this mesh is obtained from:

$$\omega^2 \mu_0 \epsilon_0 \epsilon'_{I/III} \kappa^H \kappa = \frac{2}{a^2} [1 - \cos k_x a] + \frac{2}{b^2} [1 - \cos k_b b] + \frac{2}{g^2} [1 - \cos k_z g] + \frac{8}{ab} \cos \psi \sin \frac{k_x a}{2} \sin \frac{k_b b}{2} \quad (\text{A.26})$$

where:

$$\cos \psi = \frac{|\mathbf{A}_1|^2 - |\mathbf{A}_2|^2}{|\mathbf{A}_1 + \mathbf{A}_2| |\mathbf{A}_1 - \mathbf{A}_2|} \quad (\text{A.27})$$

This dispersion relation may be solved, as before, for k_z to yield two solutions which are then used to generate κ_z 's corresponding to incoming and outgoing plane waves.